Design of the Physical Layer for Future Sub-TeraHertz Communication Systems

Simon Bicaïs

Université Grenoble Alpes

THÈSE

Pour obtenir le grade de

DOCTEUR DE LA COMMUNAUTÉ UNIVERSITÉ GRENOBLE ALPES

Spécialité : **Signal, Image, Parole, Télécoms**

Arrêté ministériel : 25 mai 2016

Présentée par

Simon Bicaïs

Thèse dirigée par **José Luis Gonzalez Jimenez**
et encadrée par **Jean-Baptiste Doré**

Préparée au sein du **CEA-LETI**
dans l'École Doctorale **d'Électronique, Électrotechnique, Automatique et Traitement du Signal (EEATS)**

Design of the Physical Layer for Future Sub-TeraHertz Communication Systems

Thèse soutenue le 12 novembre 2020, devant le jury composé de :

Pr. Laurent ROS
Professeur des universités à Grenoble-INP, président

Pr. Inbar FIJALKOW
Professeure à ENSEA Cergy-Pontoise, rapportrice

Pr. Jean-Marie GORCE
Professeur des universités à l'INSA de Lyon, rapporteur

Pr. Ana GARCIA-ARMADA
Professeure à l'université Carlos III de Madrid, examinatrice

Pr. Mérouane DEBBAH
Professeur des universités à l'université Paris-Saclay, examinateur

Dr. José Luis GONZALEZ JIMENEZ
Ingénieur de recherche au CEA Leti , directeur de thèse

Dr. Jean-Baptiste DORÉ
Ingénieur de recherche au CEA Leti, encadrant

Acknowledgments

Les travaux rapportés dans ce manuscrit sont le résultat de trois années de doctorat menées au sein du CEA Leti, à Grenoble. Je souhaite ici remercier toutes les personnes qui ont contribué à ces recherches et à cette thèse.

En premier lieu, je remercie chaleureusement Dr. Jean-Baptiste Doré. Je le remercie pour son encadrement, tous ses conseils et tout le temps qu'il a consacré à ces travaux. J'ai eu beaucoup de chance d'avoir un encadrant aussi ouvert qui a su m'accorder toute sa confiance ; en plus d'être toujours disponible et d'une expertise indéniable. J'ai considérablement appris à ses côtés tout au long de ce doctorat. Ce fut un réel plaisir de travailler avec lui et je considère notre collaboration comme une expérience très riche tant sur le plan professionnel que personnel. Je remercie aussi mon directeur thèse Dr. José Luis Gonzalez Jimenez pour avoir dirigé cette thèse et pour la confiance qu'il m'a accordée.

Je tiens également à témoigner toute ma reconnaissance aux membres du jury. Merci au président du jury Pr. Laurent Ros, aux rapporteurs Pr. Inbar Fijalkow et Pr. Jean-Marie Gorce, et aux examinateurs Pr. Ana Garcia Armada et Pr. Mérouane Debbah pour avoir accepté d'examiner ces travaux de recherches et pour l'intérêt qu'ils ont porté à cette thèse.

Je remercie tous les membres du service technologies sans-fil du CEA Leti qui ont fait partie de cette expérience. Nombreux sont ceux qui m'ont aidé par leur soutien, leurs conseils et leur relectures. Merci à l'ensemble de ces personnes de m'avoir accueilli et intégré au sein du département. Partager ces années avec eux fut un plaisir et si mon passage au CEA fut aussi agréable c'est en grande partie grâce à eux.

Finalement, j'adresse un grand merci à tous mes proches. Je les remercie pour leur soutien, leur présence et leur affection.

Abstract

To deploy high-rate wireless services, future communication networks envisage the use of wide frequency bands. Still, the usual frequency bands in the sub-6 GHz spectrum are extremely limited and expensive. To expand its available spectrum, the forthcoming generation of mobile networks with 5G initiates the use of higher frequencies through the exploitation of millimeter-wave bands. In this search for frequency resources, the sub-THz spectrum from 90 to 300 GHz offers unprecedentedly large available bands, several tens of GHz. Wireless communications in sub-THz frequencies are therefore seen as a foremost solution to achieve Tbit/s data rates and meet the requirements of future wireless connectivity. Nevertheless, existing and mature wireless technologies cannot be directly transposed to the sub-THz bands as they do not consider the specific features of sub-THz communications. Additional research is hence required to design efficient communication systems adapted to the constraints of sub-THz frequencies. Some of the major technological challenges brought by using high carrier frequencies and large bandwidths include: the performance limitations caused by the strong phase impairments of high-frequency oscillators; and the problem of high sampling rates required by the analog-to-digital conversion. In this thesis, the conducted research focuses on the development of the physical layer for sub-THz communication systems and attempts to overcome these technological barriers. Our objective is twofold: to increase the communication data rate and to relax the constraints on radio-frequency architectures. To do so, our approach consists in jointly designing signal processing for the analog and digital domains.

The two main contributions of this work are: the optimization of coherent transceivers for strong phase noise channels; and the proposal of dedicated communication systems with non-coherent and high-rate architectures. First, we have proposed optimized transmission schemes for strong phase noise channels including: the modulation, the demodulation, and the link adaptation. The proposed solutions achieve high spectral efficiency communications with relaxed constraints on radio-frequency oscillators. Our results show that the use of optimized transmission schemes greatly contributes to mitigate the impact of phase noise on coherent transceivers. Consequently, our work describes valuable technical solutions to the development of physical layers with high spectral efficiency for the sub-THz spectrum. Second, we have also targeted low-complexity physical layers readily implementable in sub-THz frequencies. We have studied the design of communication systems specifically dedicated to the sub-THz bands using non-coherent architectures. In order to implement high-rate communications with non-coherent architectures, we have considered the use of spatial multiplexing and wide frequency bands. Our work on spatial multiplexing in sub-THz frequencies demonstrates that high-rate communications can be implemented with low complexity and low power architectures using multi-antenna systems and energy detection receivers. Besides, the use of wide bands strongly constrains the analog-to-digital conversion. In order to reduce the required sampling frequencies of converters and to simplify practical implementations, we have proposed a new receiver for high-rate impulse radio systems. We have shown that the proposed receiver architecture, using parallel projections of the received signal in the analog domain, leads to near-optimal performance with significantly reduced sampling frequencies.

Résumé

Les futurs réseaux de communications pour déployer des services sans-fil très haut-débit envisagent l'utilisation de larges bandes de fréquences. Alors que les bandes de fréquences habituelles dans le spectre sub-6 GHz sont extrêmement prisées et limitées, la future génération de réseaux mobile amorce une montée en fréquence en exploitant les bandes millimétriques. Dans cette quête de ressources fréquentielles, le spectre sub-THz, de 90 à 300 GHz, offre des bandes disponibles d'une largeur sans précédent. Les communications sans-fil dans les fréquences sub-THz sont donc considérées comme une solution privilégiée pour atteindre des débits de l'ordre du Tbit/s et ainsi répondre aux futurs besoins de la connectivité sans-fil. Néanmoins, bien qu'elles soient matures, les technologies sans-fil existantes ne peuvent être directement transposées aux bandes sub-THz car elles ne tiennent pas compte des caractéristiques spécifiques des communications sub-THz. Il est donc nécessaire de mener des recherches supplémentaires afin de concevoir des systèmes de communication performants et adaptés aux enjeux et contraintes de ce nouveau spectre. Parmi les principaux défis technologiques amenés par la montée en fréquence et l'utilisation de bandes larges se trouvent les limitations de performance dues aux oscillateurs générant un bruit de phase important et une problématique d'échantillonnage à très haute fréquence. Dans cette thèse, les recherches menées portent sur le développement de la couche physique pour les systèmes de communication sub-THz et tentent de lever ces verrous technologiques. Notre objectif est double : augmenter le débit de données de communication et assouplir les contraintes sur les architectures radiofréquences. Pour ce faire, notre approche consiste à concevoir conjointement le traitement du signal pour les domaines analogique et numérique.

Les deux principales contributions de ce travail sont les suivantes : l'optimisation d'émetteurs-récepteurs cohérents pour les canaux à fort bruit de phase ; et la proposition de systèmes de communication dédiés avec des architectures non-cohérentes et haut-débits. Tout d'abord, nous avons proposé des schémas de transmission optimisés pour les canaux à fort bruit de phase comprenant : la modulation, la démodulation, et l'adaptation de lien. Les solutions proposées permettent de réaliser des communications à haute-efficacité spectrale avec des contraintes relâchées sur les oscillateurs radiofréquences. Par conséquent, nos travaux décrivent des solutions techniques précieuses au développement de couches physiques à haute efficacité spectrale pour le spectre sub-THz. Dans un second temps, nous avons également ciblé les couches physiques de faible complexité et simple à mettre en œuvre dans les fréquences sub-THz. Nous avons ainsi étudié la conception de systèmes de communication spécifiquement dédiés au bandes sub-THz utilisant des architectures non cohérentes. Pour réaliser des communications haut-débit avec des architectures non-cohérentes, nous avons notamment considéré l'utilisation du multiplexage spatial et de larges bandes de fréquences. Nos travaux sur le multiplexage spatial dans les fréquences sub-THz démontrent que des communications haut-débit peuvent être réalisées sur des architectures de faible complexité et de faible puissance en utilisant des systèmes multi-antennaire et des récepteurs à détection d'énergie. Par ailleurs, utiliser de larges bandes de fréquences implique de fortes contraintes sur la conversion analogique-numérique. Afin de réduire les fréquences d'échantillonnage des convertisseurs et de simplifier la mise en œuvre pratique, nous avons proposé un nouveau récepteur pour les systèmes radio-impulsionnels haut-débit. Nous avons montré qu'une architecture de réception avec des projections parallèles du signal reçu dans le domaine analogique conduit à des performances quasi-optimales avec des fréquences d'échantillonnage considérablement réduites.

Contents

List of Publications **vii**

List of Acronyms **x**

List of Symbols **xiii**

I Prologue **1**

1 Introduction to Sub-TeraHertz Communications **2**
1.1 The Physical Layer of Digital Communication Systems . . . 2
1.2 The Sub-THz Spectrum: Motivations and Applications . . . 4
1.3 Requirements and Challenges . . . 8
1.4 Research Ambitions and Objectives . . . 12

2 Thesis Work on Sub-TeraHertz Physical Layer **16**
2.1 Thesis Vision: From Technological Constraints to Solutions . . . 16
2.2 Thesis Overview . . . 19
2.3 Main Contributions and Organization . . . 22

II Optimizations of Signal Processing for Coherent Transceivers **24**

3 From System Modeling to Optimized Receiver Algorithms **25**
3.1 Modeling Sub-THz Communication Systems . . . 25
3.2 Optimum Demodulation in the Presence of Phase Noise . . . 35
3.3 Synthesis and Discussions . . . 44

4 Transceiver Optimizations and Performance Analyses **48**
4.1 Polar-QAM: a Phase Noise Robust Modulation Scheme . . . 48
4.2 System-Level Optimizations and Performance Analyses . . . 59
4.3 Synthesis and Discussions . . . 63
4.4 Towards Dedicated Architectures . . . 64

III Propositions of Dedicated Architectures **66**

5 MIMO Systems with Energy Detection Receivers **67**
5.1 Introduction . . . 68
5.2 System Model . . . 69
5.3 Detection Algorithm Design . . . 71
5.4 Performance Analysis . . . 75
5.5 Synthesis and Discussions . . . 83

6 Parallelization of Envelope Detection Receivers **86**
6.1 An Algebraic Framework for Envelope Modulation . . . 86
6.2 RAFAE: A receiver architecture for high-rate impulse radio with reduced sampling rates 94
6.3 Synthesis and Discussions . . . 104
6.4 Dedicated Architectures: Retrospective and Opening . . . 105

IV Epilogue **107**

7 Conclusion and Perspectives **108**
7.1 Summary of Thesis Research . . . 108
7.2 Applications of Thesis Findings . . . 111
7.3 Discussions . . . 112
7.4 Perspectives . . . 113

V Appendices **115**

A Distribution of Received Symbols over the Non-Linear MIMO Channel **116**

B Channel Model for the RAFAE Architecture **119**

C Résumé Étendu **124**

Bibliography **130**

Publications

Patents

[P4] **"Neural Networks based Demodulation for MIMO Systems using Energy Detection Receivers"**
"Méthode de Démodulation basée sur les Réseaux de Neurones pour les Systèmes MIMO utilisant des Récepteurs à Détection d'Énergie"
Simon Bicaïs, Alexis Falempin, Jean-Baptiste Doré
Filed in June 2020

[P3] **"Receiver based on the Analog Fourier Analysis of the Envelope"**
"Récepteur basé sur l'Analyse Analogue de Fourier de l'Énergie
Simon Bicaïs, Jean-Baptiste Doré
Filed in June 2020

[P2] **"Coherent Quadratic Receiver with Low Intermediate Frequency"**
"Récepteur Quadratique Cohérent à Fréquence Intermédiaire Basse"
Simon Bicaïs, Jean-Baptiste Doré, Benoît Miscopein
Filed in January 2020

[P1] **"Digital High-Order Modulation Scheme Robust to Phase Noise"**
"Méthode de Modulation Numérique d'Ordre Élevé Robuste au Bruit de Phase"
Simon Bicaïs, Jean-Baptiste Doré, José Luis Gonzalez Jimenez
Filed in March 2019

Journal Articles

[J3] **"Scoring the Terabit/s Goal: Broadband Connectivity in 6G"**
Nandana Rajatheva, Italo Atzeni, Simon Bicaïs, Emil Bjornson, *et al.*
Submitted for publication in *IEEE Communications Surveys and Tutorials*, 2020

[J2] **"Design and Analysis of MIMO Systems using Energy Detectors for Sub-THz Applications"**
Simon Bicaïs, Alexis Falempin, Jean-Baptiste Doré, Valentin Savin
Submitted to *the IEEE Transactions on Wireless Communications*

[J1] **"Design of Digital Communications for Strong Phase Noise Channels"**
Simon Bicaïs, Jean-Baptiste Doré
Accepted for publication in *Special issue "6G Intelligent Communications" of the IEEE Open Journal of Vehicular Technology*, 2020

Conference Papers

[C13] **"Design of MIMO Systems Using Energy Detectors for Sub-TeraHertz Applications"**
Simon Bicaïs, Jean-Baptiste Doré, Valentin Savin
2020 International Symposium on Personal, Indoor and Mobile Radio Communications (PIMRC), August 2020, London, United-Kingdom

[C12] **"Optimized Single-Carrier Transceiver For Future Sub-TeraHertz Applications"**
Simon Bicaïs, Jean-Baptiste Doré, Grégory Gougeon, Yoann Corre
2020 45th International Conference on Acoustics, Speech, and Signal Processing (ICASSP), May 2020, Barcelona, Spain

[C11] **"Technology Roadmap for Beyond 5G Wireless Connectivity in D-band"**
Jean-Baptiste Doré, Didier Belot, Éric Mercier, Simon Bicaïs, Grégory Gougeon, Yoann Corre, Benoît Miscopein, Dimitri Kténas, Emilio Calvanese Strinatti
2020 2nd 6G Wireless Summit (6GSummit), March 2020, Levi, Finland

[C10] **"Assessment of sub-THz Mesh Backhaul Capabilities from Realistic Modelling at the PHY Layer"**
Grégory Gougeon, Yoann Corre, Mohammed Aslam, Simon Bicaïs, Jean-Baptiste Doré
2020 14th European Conference on Antennas and Propagation (EuCAP), March 2020, Copenhagen, Denmark

[C9] **"Phase Noise Model Selection for Sub-THz Communications"**
Simon Bicaïs, Jean-Baptiste Doré
2019 IEEE Global Communications Conference (Globecom), December 2019, Hawaii, U.S.A

[C8] **"Mitigation of Carrier Frequency Offset in a Sub-THz Channel Bonding Scenario"**
Simon Bicaïs, Jean-Baptiste Doré
2019 IEEE International Symposium on Personal, Indoor and Mobile Radio Communications (PIMRC), September 2019, Istanbul, Turkey

[C7] **"Algebraic Framework for Digital Envelope Modulation"**
Simon Bicaïs, Jean-Baptiste Doré
European Signal Processing Conference (EuSiPCo), September 2019, A Coruna, Spain

[C6] **"Modèles de Bruit de Phase pour les Communications Sub-TeraHertz"**
Simon Bicaïs, Jean-Baptiste Doré
XXVIIème colloque francophone de traitement du signal et des images (GRETSI), August 2019, Lille, France

[C5] **"Espaces de Hilbert pour les Modulations Numériques d'Enveloppe"**
Simon Bicaïs, Jean-Baptiste Doré
XXVIIème colloque francophone de traitement du signal et des images (GRETSI), August 2019, Lille, France

[C4] **"Sub-THz Spectrum as Enabler for 6G Wireless Communications up to 1 Tbit/s"**
Yoann Corre, Gregory Gougeon, Jean-Baptiste Doré, Simon Bicaïs, Benoit Miscopein, Emmanuel Faussurier, Majed Saad, Jacques Palicot, Faouzi Bader
2019 1st 6G Wireless Summit (6GSummit), March 2019, Levi, Finland

[C3] **"Adaptive PSK Modulation Scheme in the Presence of Phase Noise"**
Simon Bicaïs, Jean-Baptiste Doré, José Luis Gonzalez Jimenez
2018 IEEE 19th International Workshop on Signal Processing Advances in Wireless Communications (SPAWC), June 2018, Kalamata, Greece

[C2] **"Above 90-GHz Spectrum and Single-Carrier Waveform as Enablers for Efficient Tbit/s Wireless Communications"**
Jean-Baptiste Doré, Yoann Corre, Simon Bicaïs, Jacques Palicot, Emmanuel Faussurier, Dimitri Kténas, Faouzi Bader
2018 IEEE 25th International Conference on Telecommunications (ICT), June 2018, Saint-Malo, France

[C1] **"On the Optimum Demodulation in the Presence of Gaussian Phase Noise"**
Simon Bicaïs, Jean-Baptiste Doré, José Luis Gonzalez Jimenez
2018 IEEE 25th International Conference on Telecommunications (ICT), June 2018, Saint-Malo, France

List of Acronyms

3GPP	Third Generation Partnership Project
5G	Fifth Generation
5G-NR	New Radio
ADC	Analog-to-Digital Converters
ANR	French National Research Agency
APSK	Amplitude-Phase-Shift Keying
ARCEP	French agency in charge of regulating telecommunications
ASK	Amplitude-Shift Keying
AWGN	Additive White Gaussian Noise
BCH	Bose–Chaudhuri–Hocquenghem
BER	Bit Error Rate
BICM	Bit-Interleaved Coded Modulation
CDM	Code Division Multiplexing
CEPT	Conference of Postal and Telecommunications
CFO	Carrier Frequency Offset
CMOS	Complementary Metal–Oxide Semiconductor
CRLB	Cramer-Rao Lower Bounds
CSI	Channel-State Information
D2D	Device-to-Device
DAC	Digital-to-Analog Converters
FEC	Forward Error Correction
GPN	Gaussian Phase Noise
I/Q	In-phase/Quadrature
IR	Information Rate

ISI	Inter-Symbol Interference
ITU	International Telecommunication Union
LDPC	Low-Density Parity Check
LLR	Log-Likelihood ratio
LNA	Low Noise Amplifiers
LoS	Line-of-Sight
MIMO	Multi-Input Multi-Output
ML	Maximum Likelihood
MLD-GA	Maximum Likelihood Detector with a Gaussian Assumption
mm-Wave	millimeter-wave
NNC	Non-Negative Channel
NND	Neural-Networks based Detector
OFDM	Orthogonal Frequency Division Multiplexing
OOK	On-Off Keying
OSI	Open Systems Interconnection
PAM	Pulse-Amplitude Modulation
PAPR	Peak-to-Average Power Ratio
PCB	Printed Circuit Board
PER	Packet Error Rate
PLL	Phase-Locked Loop
PN	Phase Noise
PPM	Pulse-Position Modulation
PSD	Power Spectral Density
PSK	Phase-Shift Keying
PWM	Pulse-Width Modulation
QAM	Quadrature Amplitude Modulation
RF	Radio-Frequency
SEP	Symbol Error Probability
SER	Symbol Error Rate
SNR	Signal-to-Noise Ratio

TDMA	Time Division Multiple Access
ULA	Uniform Linear Arrays
URLLC	Ultra-Reliable Low-Latency Communications
UWB	Ultra-WideBand
VLC	Visible Light Communications
WLAN	Wireless Local Area Networks
WRC	World Radiocommunication Conference

List of Symbols

System parameters:

T_s	Symbol duration
B	System bandwidth
P_t	Power at the transmitter
f_c	Carrier Frequency
G, g	Antenna gain
H	Propagation gain
h	Channel coefficient
N_f	Noise figure
d	Propagation distance Tx Rx
P_r	Power at the receiver
M	Modulation order
$\mathcal{C}$	Constellation
η	Spectral efficiency

Communication signals:

τ	Discrete-time Index
$s[\tau]$	Sent symbols
$r[\tau]$	Received symbols
$w[\tau]$	Discrete-time thermal noise
σ_w^2	Thermal noise variance
$\phi[\tau]$	Discrete-ime phase noise
σ_ϕ^2	Phase noise variance

t	Continuous-time variable
$s(t)$	Sent signal (baseband)
$x(t)$	Output of the transmitter (passband)
$y(t)$	Input of the receiver (passband)
$r(t)$	Received signal (baseband)
$w(t)$	Continuous-time thermal Noise
N_0	Thermal noise spectral density
$\phi(t)$	Continuous-time phase noise

Mathematical Notations:

$\mathcal{N}(\mu, \sigma^2)$	Normal distribution
$\mathbf{C}\mathcal{N}(\mu, \sigma^2)$	Complex normal distribution
χ^2_N	Chi-square distribution
$E[\cdot]$	Expectation operator
$p(r\|s)$	Channel likelihood function
$\Pi(t)$	Rectangular function
$\mathcal{L}^2$	Square-integrable functions
ℓ^2	Square-summable sequences
$\langle \cdot, \cdot \rangle$	Inner product
$\|\cdot\|_2$	Euclidean norm
$Pr(\cdot)$	Probability
$p(\cdot)$	Probability density function
$\boldsymbol{u} = (u_1, \cdots, u_N)$	Vector
$S = \{s_n\}_{1 \geq n \geq N}$	Set

Part I

Prologue

Chapter 1

Introduction to Sub-TeraHertz Communications

The purpose of this chapter is to answer the following question: Why and how are communications in sub-THz frequencies envisaged for future wireless applications? Significant efforts from research institutes and industrial companies are currently devoted to the development of wireless communications in sub-THz frequencies. Indeed, the sub-THz spectrum, from 90 to 300 GHz, offers large available frequency bands which could be used to implement high-rate wireless services. For this reason, communication systems using the sub-THz bands are emerging and considered as a foremost solution for future wireless networks. To gain insight on the design of sub-THz communication systems and their requirements, a simple analysis is proposed using two fundamental tools of wireless communications: Shannon's capacity formula and Friis' transmission equation. The design limitations are cross-correlated to the contemplated applications to determine the characteristics of physical layers of future sub-THz systems. In doing so, we introduce the new design challenges brought by the specific propagation conditions and technological constraints of sub-THz communications. One of the main challenges for the physical layer is the design of wireless communication systems impacted by strong phase impairments and implemented with band-limited analog-to-digital converters. Finally, we present the ambitions of research and industrial projects in facing these new challenges. In particular, the expected outcomes are oriented towards novel communication technologies in sub-THz frequencies that could meet the requirements of future wireless applications.

1.1 The Physical Layer of Digital Communication Systems

This section introduces the physical layer for digital communication systems by describing the main blocks of the transmission chain[1]. Transmission of information between different systems is ruled by protocols to ensure successful communications and interoperability. The Open Systems Interconnection (OSI) model is a conceptual framework widely used to describe communication systems. It partitions communication systems into different abstraction layers to define the transmission and reception of information. Each layer has a specific communication function and can communicate only to the layer above and to the one under. The purpose of this conceptual framework is to simplify the design of protocols. Since layers are independent, errors and problems are contained within each layer.

Physical layer: In this thesis we focus on the physical layer of digital communication systems, the first layer of the OSI model. This layer directly interacts with the transmission medium. The purpose of the physical layer is to convert the information bits into a physical signal that can be transmitted over the communication medium – the modulation. This layer also performs the reverse operation and aims to retrieve the transmitted bits from the received signal – the demodulation. Communications at

[1]Readers familiar with this topic can move forward to the following section without loss of understanding.

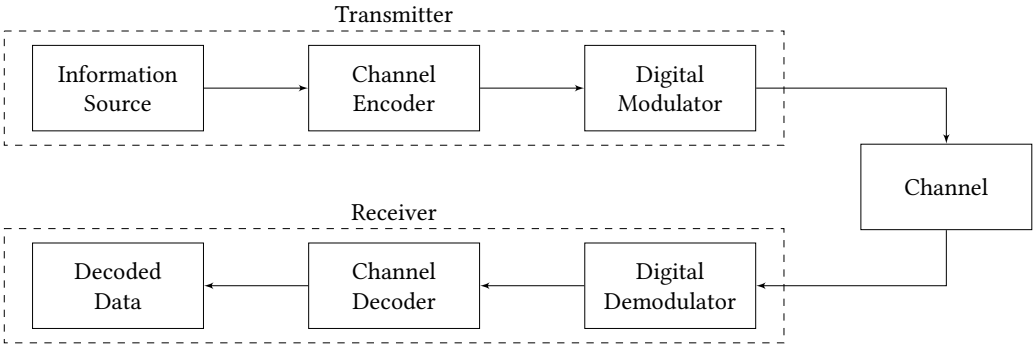

Figure 1.1 – *The transmission system model*

the physical layer level can be represented by the transmission system model depicted in Figure 1.1. It is composed of three parts: the transmitter, the channel and the receiver. We introduce in the rest of this section the different sub-systems used within the physical layer.

Modulation: At the transmitter side, the digital modulator performs the conversion from information bits to physical signals. The modulation scheme maps different groups of multiple bits to different signal points called symbols. Transmitted symbols belong to a known constellation of size M such that one symbol encodes $\log_2(M)$ bits. Constellation size M is also referred to as the modulation order. Since symbols are modulated with duration T_s, it follows that the information rate $R = \log_2(M)/T_s$ expressed in bit/s. A key performance indicator of the physical layer is the spectral efficiency defined by $\eta = R/B$ expressed in bit/s/Hz with B the system bandwidth in Hz. The higher the modulation order M, the larger the information rate R and spectral efficiency η. Further in the transmission chain, the digital symbols are converted to a continuous-time analog signal through pulse shaping. The baseband analog signal is then emitted by the Radio-Frequency (RF) front-end of the transmitter at high-frequencies, *i.e.* in the passband of the communication channel.

Channel: The physical transmission medium between the transmitter and the receiver is represented in this model by the channel. The channel alters the signal integrity with noise, distortions, nonlinearities, *etc.* Different models can be selected for the channel to reflect the different sources of impairment. In this report, we are interested in radio transmission channels based on the propagation of electromagnetic waves in free space. Some of the channels considered in this work are:

- The Additive White Gaussian Noise (AWGN) channel: a simple model that describes communications corrupted by additive thermal noise, intrinsic to any communication systems. The noise follows a normal distribution and its power spectral density is the same for all frequencies of the system bandwidth.
- The flat fading channel: a channel for which all frequency components experience the same level of fading. Fading is due to path loss over free-space propagation. The fading coefficient of the channel needs to be estimated by the communication system to then mitigate it.

Signal distortions introduced by the RF front ends at the transmitter and receiver sides are included in the channel model. The amplification of the signal and its frequency translations between baseband and passband are other sources of signal distortion, linear and nonlinear.

Demodulation: At the receiver side, the received analog signal is sampled by Analog-to-Digital Converters (ADC) to obtain digital acquisitions. The purpose of the demodulator is then to estimate the transmitted bits based on these noisy observations of the signal. Demodulation is combined with equalization techniques used to mitigate channel distortions.

Channel coding: The Forward Error Correction (FEC) scheme in communication systems is referred to as channel coding and is implemented to improve the robustness of the communication against signal distortions. As aforementioned, the received signal is subject to noise and distortions caused by the transmission over the channel. Such signal distortions may be strong enough for the demodulation scheme to make incorrect decisions, which results in bit errors in the information packet. To prevent these errors, the channel coder adds redundancy bits to the information source. Thereby, the channel decoder is able to detect and correct some of the demodulation errors.

1.2 The Sub-THz Spectrum: Motivations and Applications

1.2.1 An increasing demand for wireless connectivity

Over the last decades, an exponential growth of the data traffic has been witnessed. In particular, the main component of this traffic growth can be related to an increasing and specific demand for wireless connectivity providing efficient user-friendly data connections. With wireless links, users can access the connectivity irrespective of location. It contributes to eliminate cables and helps in reducing the complexity and cost of physical infrastructures. In addition, the different standardization procedures have enabled a world-wide deployment of wireless technologies. Each of the generations of wireless networks – either cellular networks or Wireless Local Area Networks (WLAN) – has targeted during its development a higher communication throughput. The high-speed access service of wireless networks is commonly referred to as the broadband connectivity. Though the latest generation of cellular networks, the Fifth Generation (5G), has developed new capabilities beyond broadband connectivity enabling massive machine type communications and Ultra-Reliable Low-Latency Communications (URLLC), the broadband connectivity remains the dominant and most valued segmentation of the wireless connectivity market. With regard to the increasing Internet penetration, the wireless connectivity market is expected to continue significantly its exponential growth. For this reason, future networks and wireless technologies, *e.g.* Beyond-5G, are contemplated to further enhance the broadband connectivity with higher communication data rates and increased density of access points. Overall, future wireless technologies are to continue the main path of their development towards higher data rates for more users in more places. Furthermore, higher data rates for users definitely require high-capacity backhaul to ensure the link between the core network and the radio access points.

1.2.2 Key approaches to increase the communication throughput

In this paragraph, we outline a simple analysis based on the channel capacity, more precisely on the Shannon-Hartley theorem, explaining the key approaches to increase the communication throughput. First of all, the channel capacity is defined as the maximum achievable rate of information that can be communicated at an arbitrarily low error rate. To put it differently, the channel capacity is a theoretical limit on the highest data rate, *e.g.* in bit/s, that can be sent reliably between a transmitter and a receiver. Practical channels are subject to limitations imposed by finite bandwidth and noise. The channel capacity expresses the fundamental limitations of noisy communication channels. Thereby, the channel capacity is one of the fundamental results of information theory and provides a highly valuable tool for system designers. As mentioned, we use the channel capacity in this paragraph to illustrate the different key approaches to achieve higher data rate communications. To simplify our analysis, we focus on a single-antenna and point-to-point scenario. Moreover, we consider a finite-bandwidth continuous-time channel impaired by Gaussian noise. For such channel, the Shannon-Hartley theorem on channel capacity C establishes a relation between the achievable rate R, the communication bandwidth B and the Signal-to-Noise Ratio (SNR). The SNR is defined as $\frac{P_r}{P_n}$, the ratio of the received signal power P_r and the noise power P_n. This ratio, usually expressed in dB, quantifies the quality of a communication

channel. It is directly related to the achievable information rate on the channel. Intuitively, the higher the SNR, the lower the probability of error due to noise distortion, and hence, the larger the amount of information that can be communicated over the channel. Precisely, the Shannon–Hartley theorem [1] states that

$$R < C = B \cdot \log_2 \left(1 + \frac{P_r}{N_0 B}\right), \tag{1.1}$$

where R is the information rate in bit/s, C the channel capacity in bit/s, B the system bandwidth in Hz, P_r the power of the received signal. The noise power in this equation is expressed by $P_n = N_0 B$ with N_0 denoting the spectral density of noise. It means that it is theoretically possible to transmit information at rate R up to the channel capacity limit C with an arbitrary low probability of error at the receiver. One can notice that the channel capacity is increasing with the bandwidth and with the SNR.

We now use the latter equation to demonstrate how the communication throughput can be increased in future wireless technologies. The key approaches are subdivided into two categories: approaching the channel capacity, and using channels with larger capacities. The first approach consists in improving the communication algorithms for the rate of wireless systems R to get closer to the channel capacity C. It includes the use of capacity-achieving channel coding, such as Low-Density Parity Check (LDPC) or polar codes, or advanced modulation and demodulation schemes. Nevertheless, it would be an understatement to state that such an approach is a widely investigated research topic as it has been the purpose of countless research efforts. State-of-the-art communication algorithms are already very close to the channel capacity. And though improvements are still achievable, they cannot lead to a tenfold increase of the communication throughput.

Therefore, future wireless networks will rely on a second approach to meet the forthcoming requirements on higher communication rates. This second approach considers the use of channels with larger capacities. It is worth mentioning that multi-antenna systems demonstrate larger capacities thanks to spatial multiplexing gains and thereby provide a practical method to increase the throughput. Nevertheless, the channel capacity of multi-antenna systems cannot be described with Eq. (1.1) and exceeds the scope of this first analysis. To increase the capacity C in the right side of Eq. (1.1), and hence, enable higher data rates, it is either possible to improve the SNR $\frac{P_r}{P_n}$ or to exploit a larger bandwidth B. A larger SNR allows larger throughput. With weaker noise distortion, modulations of higher order can be used, *i.e.* more bit/symbol. Conversely, a larger bandwidth allows a higher symbol rate, *i.e.* more symbol/s. Regarding the SNR, as the ratio of the received signal power over the noise power, it is immediate that the SNR increases with the transmit power and decreases with the propagation distance between the transmitter and receiver. Therefore, when it comes to improving the SNR, it is theoretically possible to increase the transmission power, still in practical systems transmission powers are regulated and limited. For this reason, it is preferable to increase the density of access points or cells to improve the SNR, which is definitely envisaged for future networks deployments. Finally, the most intuitive and efficient way to increase the communication throughput is simply by exploiting larger frequency bands. It is hence essential for future networks to take advantage of large frequency resources in order to deploy high-rate services. In this thesis, we focus on the latter method, and accordingly, we now explain why communications in the sub-THz spectrum are envisaged for future wireless technologies.

1.2.3 Building upon the frequency resource

The economic value of a frequency band can be extremely high. In general, it is directly related to the propagation conditions in that band. The more favorable the radio propagation, the more expensive the frequency resource. In addition, the wider the bandwidth allocated to the service, the higher the

achievable data rate or the more users covered. Wide frequency bands can be of higher economic interest. In short, the value of a frequency band equals the width of the band times the quality of the radio propagation in the band. For instance, the frequency bands in the sub-6 GHz are extremely expensive and highly valued for their excellent propagation conditions. By means of illustration, we can mention the cost of the newly attributed frequency bands for the 5G. There are 11 bands of 10 MHz available between 3.4 and 3.8 GHz. In France, the starting value for a 10 MHz band at the auction has been set to 70 million euros by the French agency in charge of regulating telecommunications (ARCEP) [2].

To avoid the spectrum shortage in sub-6 GHz bands and expand its available spectrum, the future generation of cellular networks 5G has started to operate at higher carrier frequencies by using of millimeter-wave (mm-Wave) bands around 30 and 40 GHz. Anyway, thanks to the evolution of semiconductor technologies, it is now possible to envisage RF communication systems at higher carrier frequencies. The so-called THz gap between RF and optical communication systems begins to narrow. Tough the propagation conditions are not particularly favorable in the sub-THz spectrum from 90 to 300 GHz, it offers an unprecedentedly large amount of unused frequency bands. This extremely large amount of frequency resources could be exploited to deploy high-rate wireless services or to cover numerous users. Initially, the radio spectrum above 90 GHz has been used by scientific services, *e.g.* radioastronomy observation, Earth exploration-satellite services, meteorology. It also offers opportunities allowing huge signal bandwidths for wireless communications. Within the range 90–200 GHz, up to 58.1 GHz bandwidth could be made available for new wireless communication services. For more details on spectrum allocation, the readers may refer to [3], which presents the outcomes of World Radiocommunication Conference (WRC) and Europe Conference of Postal and Telecommunications (CEPT). In conclusion, ***the sub-THz spectrum represents a true opportunity to achieve high data rate communications***.

The use of sub-THz frequencies should not only be contemplated to take advantage of large available bandwidths in order to continue the main path towards higher data rates of the development of communication systems. In addition, the sub-THz spectrum can also be interpreted as offering an alternative path for innovative and groundbreaking applications. Exploiting the specific features of sub-THz communications can lead to new and original use cases. For example, the quasi-null penetration in walls appears to be highly valuable for privacy applications. Moreover, the large frequency bands can also be exploited to deploy low-power systems based on a wideband regime. With a fixed transmission rate, a larger bandwidth can be used to lower the spectral efficiency and hence reduce the required transmission power.

1.2.4 Envisaged applications

As previously mentioned, sub-THz bands are considered for Beyond-5G networks to meet the requirements of emerging applications. The contemplated applications are currently being discussed and delineated. Though we will not discuss here in-depth the pragmatism nor the economic interest of the contemplated applications, they provide objectives driving the development of the sub-THz systems. The envisaged scenarios can be differentiated on several features including: the coverage range, the point-to-point or point-to-multipoint feature, the symmetry or asymmetry of the communication link, *etc.* Subsequently, we have identified three main scenarios, representative of the different flavors of contemplated applications. These three scenarios capitalize on the large sub-THz bands to deploy high-rate wireless services. They can be described as follows:

- ***High-capacity backhaul***: This scenario covers a fixed symmetric point-to-point link targeting high data rates without strong energy or complexity constraints since no user devices are involved. The envisioned ultra-dense network topology in urban areas with extreme capacity and latency require-

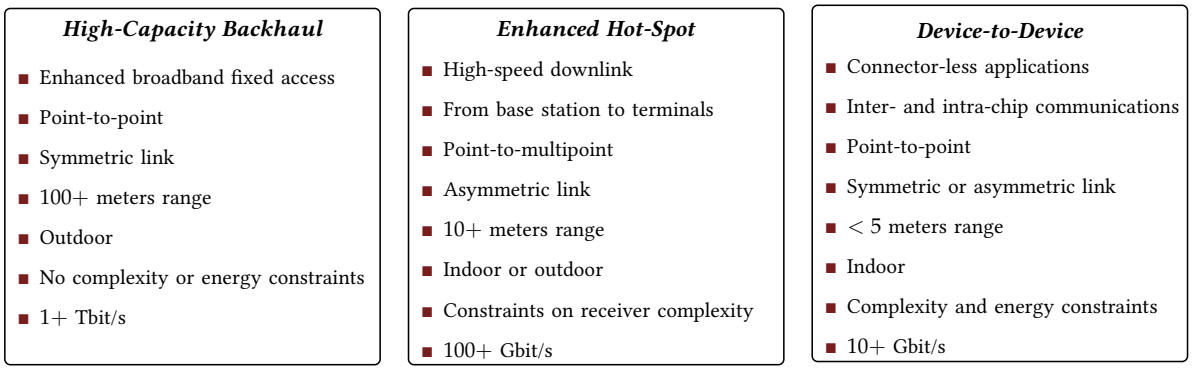

Figure 1.2 – *Main descriptive elements and performance indicators of envisaged applications*

ments makes fiber-based backhauling highly desirable but complicated due to the limited fiber network penetration. Wireless infrastructures are hence required as a flexible complement to optical fiber deployment in order to avoid any bottleneck in backhaul links. Ultra-high speed links are required since backhaul aggregates the data of numerous users. The backhaul can also provide efficient access to computing resources at the edge or in the cloud for computational or content caching. For instance, two topologies could be exploited: the backhaul link with both terminals located on high buildings or the mesh backhaul interconnecting small cells with multi-hop and redundant links.

- ***Enhanced hot-spot***: This use case refers to a high-rate downlink from a base station to several user equipments with a short coverage and strong receiver complexity constraints. By means of example, data kiosks are envisaged to serve high-speed downloads to one or several users in a short duration in crowded places such as airport gates, train stations, or shopping malls. The data offloading by using data kiosks reduces the burden of networks and the number of users connected to the network operator. The data kiosk is connected to the backbone network and can store locally large trending files such as the most downloaded movies, newspapers or software. The transmitter data kiosk has relaxed constraints since it is directly connected to a power outlet, it can also support a higher complexity with a higher cost. Conversely, user equipments have more severe constraints since they are highly limited in complexity (cost), power consumption (battery powered) and dimension that limits the overall system size and antennas position.
- ***Device-to-device communications***: In this use case, a symmetric high data rate link with energy and architecture complexity constraints is considered for Device-to-Device (D2D) communications. This scenario is also sometimes referred to as short-range communications. It includes inter-chip or intra-chip communications, wireless connectors, or connection between devices in a server farm. For instance, server farms are becoming a part of most information system infrastructures. Deployed architectures mostly use wired networks for intra- and inter-rack connections. Wired solutions require the deployment of larger number of cables, which may escalate cabling complexity problems, *e.g.* cable management, maintenance, and heat dissipation. These considerations have motivated researchers to investigate the feasibility of establishing wireless links in server farm networks. Wireless links are a relevant candidate to implement high-rate low-latency communications and hence simplify deployments of server farms.

The main descriptive elements and performance indicators of these three scenarios are provided in Figure 1.2. Further details on envisaged scenarios – data centers, autonomous vehicles, industrial automation – can be found in the deliverable [4] or in the white paper on broadband connectivity in 6G [5] – we have contributed to both.

Promises are great, still there is a long way off. Soon, we are to describe the not particularly favorable propagation conditions in sub-THz frequencies. Moreover, numerous challenges are to be addressed to implement high-rate sub-THz systems.

1.3 Requirements and Challenges

1.3.1 From link budgets to requirements

Some insight on the requirements of sub-THz systems can be obtained by evaluating some link budgets related to the contemplated applications. Link budgets establish a relation between the transmitted power and the received one, by accounting power gains and losses experienced over the communication channel. Though based on simplifications, namely a Line-of-Sight (LoS) and AWGN channel, link budgets are a highly valuable design tool to understand constraints and challenges that need to be faced. The simplistic link budgets we consider are based on Friis' transmission equation, which enables us to characterize the power of the received signal. From the received power, we can derive the SNR, essential to assess the system performance in terms of achievable spectral efficiency and error rate. Using Friis' formula, the SNR at the receiver can be evaluated by

$$\text{SNR} = \frac{P_r}{P_n} = \frac{P_t \cdot G_{\text{A}}^{\text{Tx}} \cdot G_{\text{A}}^{\text{Rx}}}{L_p \cdot P_n} \tag{1.2}$$

where P_r is the power of the received signal and P_n the power of thermal noise. In detail, P_t denotes the transmission power, G_{A}^{Tx} and G_{A}^{Rx} are the directivity gains of the transmit and receive antennas, L_p is the free-space path loss due to propagation, and P_n the power of thermal noise at the receiver. The free-space path loss $L_p = \left(\frac{4\pi f_c \cdot d}{c}\right)^2$, with f_c the carrier frequency, d the propagation distance, and c the speed of light. It means that the higher the carrier frequency f_c the larger the path loss L_p. Subsequently, sub-THz systems have to cope with strong propagation losses to achieve high-rate communications. The noise power is evaluated using the Johnson-Nyquist formula $P_n = k_B T_0 B N_f$ where k_B denotes Boltzmann's constant, T_0 is the absolute temperature, B is the system bandwidth and N_f is the noise figure of the Low Noise Amplifiers (LNA) at the receiver. Before going into details, we remind readers that the sole purpose of the link budgets presented in Figure 1.3 is to roughly delineate future requirements of sub-THz communication systems. From this perspective, we aim at highlighting technological challenges and design limitations, rather than at providing accurate system-level performance analyses. It should be noted that establishing such predictive link budgets is a complex task as it involves a wide range of different factors and forecasts. The results of our link budgets are obtained as follows. We first set some realistic system parameters with regard to envisaged applications. Then, for different modulation orders, *i.e.* different spectral efficiencies, Friis' transmission equation is used to derive the maximum path loss in order to achieve the required SNR and the targeted Bit Error Rate (BER). Thereby, we are able to evaluate the communication throughput and coverage distance.

In this paragraph, we detail how our link budgets are constructed and system parameters selected. Unconcerned readers may pass through this paragraph without repercussions on the comprehension. First of all, the considered communication systems are operating in D-Band around 145 GHz. The width of the frequency bands is chosen according to targeted data rates and pragmatic considerations. It is worth mentioning that current converters technologies limit the width of the overall bandwidth of a RF transmission chain. Accordingly, communication systems use channelization to aggregate multiple sub-bands and increase the system bandwidth. For the transmit power, our choice is set with respect to the application and usual regulations. The transmit power for the D2D scenario is set to the maximum transmit power allowed for Wi-Fi access points providing a practical comparison. For the

High-Capacity Backhaul

Carrier Frequency	f_c		145		GHz
Bandwidth	B		20		GHz
Transmit Power	P_t		40		dBm
Tx Antenna Gain	$G_{\mathrm{A}}^{\mathrm{Tx}}$		30		dBi
Rx Antenna Gain	$G_{\mathrm{A}}^{\mathrm{Rx}}$		30		dBi
Receiver Noise	P_n		-55		dBm
QAM	M	64	1024	16384	
Spectral Efficiency	η	6	10	14	bit/s/Hz
SNR	P_r/P_n	25	36	46	dB
Maximum Path Loss	L_p	126	115	105	dB
Distance	$\boldsymbol{d}$	**580**	**160**	**50**	**m**
Throughput	$\boldsymbol{R}$	**120**	**200**	**280**	**Gbit/s**

Enhanced Hot-Spot

Carrier Frequency	f_c		145		GHz
Bandwidth	B		20		GHz
Transmit Power	P_t		30		dBm
Tx Antenna Gain	$G_{\mathrm{A}}^{\mathrm{Tx}}$		30		dBi
Rx Antenna Gain	$G_{\mathrm{A}}^{\mathrm{Rx}}$		3		dBi
Receiver Noise	P_n		-55		dBm
QAM	M	16	256	1024	
Spectral Efficiency	η	4	8	10	bit/s/Hz
SNR	P_r/P_n	19	32	36	dB
Maximum Path Loss	L_p	100	87	83	dB
Distance	$\boldsymbol{d}$	**16**	**3.7**	**2.3**	**m**
Throughput	$\boldsymbol{R}$	**80**	**160**	**200**	**Gbit/s**

Device-to-Device

Carrier Frequency	f_c		145		GHz
Bandwidth	B		2		GHz
Transmit Power	P_t		10		dBm
Tx Antenna Gain	$G_{\mathrm{A}}^{\mathrm{Tx}}$		14		dBi
Rx Antenna Gain	$G_{\mathrm{A}}^{\mathrm{Rx}}$		14		dBi
Receiver Noise	P_n		-66		dBm
QAM	M	4	16	64	
Spectral Efficiency	η	2	4	6	bit/s/Hz
SNR	P_r/P_n	12	19	25	dB
Maximum Path Loss	L_p	92	85	79	dB
Distance	$\boldsymbol{d}$	**6.5**	**2.9**	**1.5**	**m**
Throughput	$\boldsymbol{R}$	**4**	**8**	**12**	**Gbit/s**

Figure 1.3 – *Link budgets for the three envisaged applications*

enhanced hot-spot, the transmit power is based on the power of common base stations of cellular networks, see the report of International Telecommunication Union (ITU) on 4G radio interface [6]. And the transmit power of the backhaul scenario refers to usual dedicated backhaul systems. Regarding the antenna gains, our assumptions are the following. For the backhaul application, we have selected highly directive antennas at the transmitter and receiver sides. For the hot-spot scenario, the transmit antenna is highly directive and includes a beam steering scheme while the receive antenna is a low-gain integrated antenna. For D2D communications, we have considered medium gain antennas with cost-efficient architectures composed of multiple elements, namely based on 10 elements of 4 dBi gain each. Thereupon, the noise power at the receiver is evaluated using the Johnson-Nyquist formula for thermal noise while considering a noise figure of 15 dB according to state-of-the-art sub-THz LNA [7]. Then, the chosen modulation is the Quadrature Amplitude Modulation (QAM), the most commonly used scheme. No channel coding is considered to simplify the analysis. The required SNR to ensure a BER below the targeted 10^{-4} is derived from well-known results of QAM performance on AWGN channels [1]. Based on Friis' formula, we are able to evaluate the maximum path loss using Eq. (1.2). Thereupon, we directly infer the maximum communication distance from the maximum path loss through the previously introduced path loss formula. Finally, the communication throughput directly results from the product of the system bandwidth and the spectral efficiency fixed by the modulation scheme. More generally, we refer interested readers for more details on antennas to [8], on amplifiers and other examples of sub-THz link budgets to [7], and on use cases definitions and requirements to [4].

We are now in a position to draw some preliminary inferences regarding requirements and design limitations of future sub-THz communication systems. The first assessment, and certainly the most straightforward one, is that the use of high carrier frequencies induces severe propagation losses over distance. Subsequently, to cover long communication ranges, highly directive antennas should be used such that these high-gain antennas can compensate the severe path losses. In addition, large transmission powers are required to cover long ranges, and hence, heavy power consumption and efficient power amplification are also needed. Altogether, we are facing the usual trade-off between communication throughput and coverage distance, yet this trade-off is emphasized by the strong path loss of high carrier frequencies of sub-THz bands. Further, an uplink transmission from an embedded terminal towards a base station appears to be extremely challenging, in the short term at least, because of required transmit powers. Besides, it is also extremely challenging to reach 1 Tbit/s data rate with a single communication link, still 100+ Gbit/s might be achievable using high-order modulation schemes. For this reason, the use of multi-antenna systems, *i.e.* Multiple-Input Multiple-Output (MIMO) schemes, is essential to increase the data rate by spatially multiplexing multiple communication streams.

Meeting future requirements using sub-THz bands is a challenging objective – at least not as direct as if large frequency bands were available in the sub-6 GHz spectrum. Notably, several challenges are directly related to the use of high carrier frequencies. For this reason, numerous of these challenges are present in mm-Wave communications as well. Accordingly, we present in the following paragraph the design limitations and technological constraints rendering difficult the realization of high-rate communications in sub-THz frequencies. Thereby, we also identify the main differences with usual sub-6 GHz communication systems.

1.3.2 Propagation and technological constraints

Propagation conditions: As aforementioned, sub-THz communications suffer from severe propagation losses due to their high carrier frequency. We can notice in Friis' transmission equation that the free-space path loss increases with the square of the carrier frequency. To compensate these severe path losses, high-gain antennas with strong directivity have to be used. Subsequently, the use of the

radio channel is highly different from usual sub-6 GHz systems. With less angular spread, the strong directivity of the antenna leads to fewer multi-path components, and hence, towards channels with a single dominant-path. More generally, the propagation conditions in high-frequency bands experience poor reflections, scattering and penetrations. These propagation characteristics entail that fewer and weaker multi-path are expected. Altogether, these considerations lead us to expect LoS channels. Recent measurements campaigns [9, 10, 11, 12] have confirmed those predictions and have shown experimentally that the radio propagation channels in sub-THz frequencies are highly dominated by the LoS component. Therefore, the channel can be considered as frequency flat and described with a single dominant path model. Radio propagation at frequencies above 90 GHz is also subject to strong attenuations from rainfall, which affect the availability of backhaul links. In addition, the vegetation foliage creates blockages in sub-THz frequencies and should be considered during backhaul deployments.

High-gain antennas: The compensation of propagation losses entails serious constraints on directivity gains of antennas and further on beam alignment as well. The research for antenna solutions achieving high gains, greater than 30 dBi, over wide frequency bands for sub-THz frequencies is still at an early stage. Examples of emerging solutions are dielectric lens antennas, or transmitarray antennas. In particular, transmitarrays provide an attractive and cost-effective solution to achieve high-gain antennas which can be fabricated using standard Printed Circuit Board (PCB) technology. For more details, we refer the readers to [8].

Oscillator phase impairments: Let us now introduce one of the main technological difficulties to implement communication systems in sub-THz bands. Digital communication systems fully rely upon RF oscillators, an indispensable element of the transmission chain. Their roles is to create stable reference signals to perform a fundamental operation: the frequency translations between baseband and passband. Unfortunately, practical RF oscillators suffer from hardware imperfections that introduce phase impairments to the communication system, namely Phase Noise (PN) and Carrier Frequency Offset (CFO). The higher the carrier frequency, the stronger the phase impairments, which means that the impact of phase impairments may be worse in systems with high carrier frequencies. For sub-6 GHz communications, the PN problem is rarely considered. Oscillators at sub-6 GHz frequencies demonstrate great reliability such that effects of PN may be negligible compared to other RF impairments. Conversely, for digital communication systems in sub-THz bands, oscillator PN represents one of the major hardware impairments [13] [14] and can considerably limit the system performance in terms of achievable data rate [15]. Though we have presented the main RF impairment for sub-THz systems it is worth mentioning some other technological difficulties including: the nonlinearities of power amplifiers, the In-phase/Quadrature (I/Q) imbalance, *etc.*

Analog-to-digital conversion: Regarding communication data rate, exploiting several GHz of frequency bands enables to achieve large throughputs, yet it also constrains severely the analog-to-digital conversion. Though sampling rates of state-of-the-art ADC technologies – *e.g.* Flash converters – reach several Gsample/s, it remains challenging for embedded terminals to perform the analog-to-digital conversion at such high sampling rates. For integrated systems, the implementation of ADC is subject to a trade-off between the power consumption, the sampling rate and the resolution – number of quantized bits and level of quantization noise. Subsequently, the analog-to-digital conversion is becoming a limiting factor to achieve high-rate sub-THz systems. It requires channelization, *i.e.* the aggregation of several sub-bands multiple RF chains. Also referred to as *channel-bonding*, channelization may lead to spectral efficiency losses resulting from the insertion of frequency guard bands between channels.

1.3.3 Main challenges for the physical layer

Prior to presenting the challenges for the physical layer, the use of sub-THz bands demonstrates some advantages that should be mentioned. Using high-gain antennas with highly directive beams, sub-THz channels are strongly dominated by the LoS path. These frequency-flat channels hence enable the use of low-complexity transceiver schemes such as single-carrier modulation with simple-tap equalization. It follows that a deviation from the widely used Orthogonal Frequency Division Multiplexing (OFDM) could be beneficial. In fact, multi-carrier modulations such as OFDM can be quite complex to implement in the context of broadband sub-THz systems – transceivers with Tbit/s digital processors still do not exist. The large Peak-to-Average Power Ratio (PAPR) and strict frequency synchronization imposed by OFDM describe extremely challenging requirements in sub-THz frequencies in regard to the strong phase impairments and large power consumptions required. The limitations of converters further prevent the analog-to-digital conversions of multi-band orthogonal signals. With regard to the required large amount of transmission power required and the poor efficiency of power amplifiers for high carrier frequencies, it is preferable to use amplifiers with low input back-offs, and hence, to exploit waveforms with low PAPR. For these reasons, single-carrier modulations for wireless communications above 90 GHz are considered as a relevant and efficient solution to achieve Tbit/s data rates.

Furthermore, it is straightforward to infer from the constraints presented above the main challenges for the development of sub-THz physical layers. The first to be mentioned is the mitigation of phase impairments issued by high-frequency oscillators. Namely, minimizing the performance degradations due to PN in coherent transceivers is an essential topic to be addressed. Moreover, phase impairments create inter-channel interference in channel-bonding systems due to the large CFO between unsynchronized oscillators. The second challenge to be tackled is to digitize large bandwidth signals with band-limited converters. Solutions based on the aggregation of multiple sub-bands, or dedicated signal processing techniques could be examined. We therefore claim that an important step towards the development of sub-THz systems is to investigate thoroughly the following problem: ***the design of high-rate wireless communications impacted by strong phase impairments and implemented with band-limited converters***. It should also be noted that the realization of spatial multiplexing, essential to achieve high data rates, in sub-THz bands is demanding. First, the strong correlation between LoS channels severely limits the potential spatial multiplexing gains. Moreover, the strong phase impairments impede the implementation of digital beamforming schemes required by MIMO systems. Before presenting the approach of research institutes and industrial companies to address these problems, we are going to introduce and appreciate some of the current solutions available in sub-THz frequencies.

1.4 Research Ambitions and Objectives

1.4.1 Existing solutions and ongoing standardizations

To begin this section, we review some of the existing solutions and on-going standardizations regarding communications in sub-THz frequencies. Multiple wireless communication links have been demonstrated in frequencies above 90 GHz. For instance, a short-range wireless link is proposed in [16] for chip-to-chip communication with low latency, high data rate, and reasonable power consumption. This transceiver is based on a fully integrated Complementary Metal–Oxide Semiconductor (CMOS) architecture operating at 260 GHz and uses On-Off Keying (OOK) to achieve a 10 Gbit/s link. In the same vein, the work in [17] proposes a fully integrated transceiver for short-range wireless communications at 300 GHz. Based on multi-level Amplitude-Shift Keying (ASK), the transceiver reaches a 20 Gbit/s throughput. Further, the advancements in CMOS technology have enabled coherent transceivers to operate in sub-THz frequencies, an important step towards spectral-efficient communications. State-

of-the art CMOS transceivers use architectures with multiple parallel RF channels, *i.e.* channel-bonding. We can mention the wireless transceiver described in [18], which implements a 56 Gbit/s link in W-band (75-110 GHz) using a 16-QAM. Eventually, it is relevant to cite [19] in which an I/Q coherent transceiver at 90 GHz is presented. Channel-bonding is implemented with 16 channels of 2 GHz bandwidth and modulation schemes up to 64-QAM in order to realize a 100 Gbit/s wireless link. The work in [19] mostly focuses on designing efficient RF technologies, while conventional algorithms are used for baseband signal processing.

With the development of multiple demonstrators for wireless communications beyond 90 GHz, standardization groups have shown a growing interest in high carrier frequency bands. The Third Generation Partnership Project (3GPP), the organization related to the standardization of mobile telecommunication protocols, has over the years included to the usual sub-6 GHz some higher carrier frequency bands. Recently, the 5G New Radio (5G-NR) has planned the exploitation of lower mm-Wave bands. The Ka-band (26.5-40 GHz) is envisaged to deploy micro-cells providing short-range high-speed data transmissions while using the standard OFDM-based physical layer. The latest release of 5G-NR has also considered some applications in V-band (40–75 GHz). Nowadays, some specifications groups of 3GPP are currently examining the use of E-band (60-90 GHz) and D-band (110-170 GHz) for future cellular networks. Furthermore, some interest groups of the Institute of Electrical and Electronics Engineers (IEEE) have examined the sub-THz spectrum as well. To be specific, the IEEE task groups referred to as 802.15.3c and 802.15.3d respectively investigate the frequency ranges 57-64 GHz and 252-325 GHz for WLAN. The 802.15.3c considers the use of the 57-64 GHz unlicensed band to support high data rate applications (at least 1 Gbit/s) such as high-speed Internet access. The task group 802.15.3d is interested in the higher sub-THz frequency range for high-rate point-to-point links. The physical layer proposed by the 802.15.3d group is based on channelized OOK or single carrier with low-order modulations combined with an LDPC code to reach data rates up to 100 Gbit/s.

1.4.2 Why is additional research required?

Current research efforts are mainly devoted to the development of efficient sub-THz technology: RF components, oscillators, power-amplifiers, high-gain and compact antennas, *etc.* Regarding the physical layer, we can notice from state-of-the-art demonstrators in sub-THz bands that conventional transceiver architectures and communication algorithms are used. Nevertheless, conventional transmission techniques cannot be transposed in a straightforward way to high carrier frequencies above 90 GHz as they do not consider the unique features of sub-THz systems. We can mention the following examples: the performance degradations in coherent systems due to oscillator PN, the difficulties to implement spatial multiplexing on strongly correlated LoS channels. For these reasons, existing wireless communication systems using sub-THz bands demonstrate limited performance and thereby leave a large room for improvement. By means of illustration, to cope with the strong RF impairments of sub-THz analog front-ends, low or medium order modulation schemes are used which cannot achieve high spectral efficiencies. We therefore claim that research activities on RF technologies for sub-THz frequencies should be complemented with investigations on the physical layer to develop dedicated baseband signal processing. In conclusion, additional research is required to design efficient physical layer algorithms and achieve high data rates wireless communications in sub-THz bands. We detail in the following paragraph the potential outcomes and value of additional research on physical layers for sub-THz communications.

1.4.3 About the research on the physical layer

We introduce in this paragraph some research topics regarding the development of the physical layer for sub-THz communication systems. We have noticed that research focuses fall into the following categories:

1. ***Optimization of communication schemes for coherent transceivers:*** One of the main challenges to deploy communication systems in sub-THz frequencies is the severe performance degradations due to the strong RF impairments of high-frequency analog front-ends. Examples of these impairments are nonlinearities, PN, I/Q imbalance, ADC impairments. Hence, limiting the performance degradations to obtain enhanced system performance with state-of-the-art RF components, is an important research topic. This can be achieved by optimizing the digital signal processing to mitigate the hardware impairments. Doing so is a well-known technique that has been successfully employed for instance to cope with power amplifier nonlinearities and could be adapted to mitigate phase impairments. Equivalently, optimized communication schemes can be used to relax implementation constraints on RF architectures, and to obtain similar or enhanced system performance with lower-quality RF components. Furthermore, it is also highly relevant to benefit from existing and mature wireless technologies such as I/Q coherent transceivers. Combining these mature technologies with optimized communication schemes is envisaged as a foremost solution to achieve high data rate communications in the sub-THz bands. One of the main research objectives is hence to increase the spectral efficiency of coherent transceivers in the presence of strong RF impairments through digital signal processing optimizations.
2. ***Design of new dedicated transceiver architectures and communication schemes:*** The previously presented design approach represents somehow a conventional and incremental development of communication systems. Conversely, the approach we discuss here is more exploratory and innovative. The development of efficient sub-THz physical layers can be extended beyond the optimization of communication schemes. The underlying principle of such an approach is to combine software optimizations – optimized digital signal processing – with initial hardware considerations of the specific features of sub-THz communications – dedicated RF architectures. Initial considerations include for instance the use of extremely wide frequency bands, and that phase information can be severely corrupted, or that propagation channels are highly dominated by a single path. With regard to hardware considerations, it is also preferable to envisage the use of RF components which are simple to implement in sub-THz frequencies rather than the commonly used ones. Accordingly, it is meaningful to rely on existing sub-THz RF technologies such as envelope detectors, 1-bit ADC, *etc.* All things considered, proposing new RF architectures dedicated to sub-THz applications with adapted communication algorithms should be contemplated as a valuable research topic.

These topics should not be interpreted as disjoint and can be jointly investigated. Besides, they highlight that while exploiting higher carrier frequencies, it is no longer possible to maintain separated the design of analog and digital domains. Therefore, we namely enter a research framework close to the ***dirty RF paradigm*** [20]. Let us describe this design paradigm with Fettweis' own words:

> In the world of "Dirty RF" we assume to design digital signal processing such that we can cope with a new level of impairments, allowing leeway in the requirements set on future RF sub-systems. [20]

Both research topics presented above point out that ***designing efficient physical layers for sub-THz systems requires a joint optimization of the analog and digital signal processing algorithms***. Let us now conclude with an analogy to the optimization of wireless communication systems in sub-6 GHz spectrum with rich multi-path environments. First, strong multi-path components have been

considered as interference that should be equalized. Later, multi-path components have been interpreted as a mean to provide spatial and diversity gains, now exploited in MIMO systems to improve significantly communication performance. We can also claim that a similar path is to be followed for the development of future communication systems in sub-THz frequencies. Dedicated communication systems and algorithms will be designed for sub-THz frequencies, and in the near future, optimized schemes will become a norm.

In this final paragraph, we present a few current research projects on sub-THz frequencies. First, this thesis research is conducted within the framework of the project BRAVE, funded by the French National Research Agency (ANR), on physical layer and waveform design for Beyond-5G systems. BRAVE is a collaborative research project started in January 2018, that aims at creating new physical-layer techniques devoted to Beyond-5G wireless communications. The partners – Siradel, Centrale-Supélec, CEA-Leti and ANFR – are designing new high-data rate and energy-efficient waveforms that operate in frequencies above 90 GHz. It is also relevant to mention the TERAPOD project, which investigates and demonstrates the feasibility of ultra high bandwidth wireless access networks operating in sub-TeraHertz bands. The project focuses on the end-to-end demonstration of sub-THz wireless links. The research project EPIC aims to develop a new generation of FEC codes. They will serve as a fundamental enabler of Beyond-5G wireless Tbit/s solutions. The UltraWave and Dream-D research projects could be cited as well. Both projects cover the technological development of analog front-ends for transceivers operating in D-Band (130-174.4 GHz). Regarding industrial companies, the vision on sub-THz communication systems is neither clear nor explicitly public. However, main research institutes such as Nokia Bell Labs and Huawei R&D Centers conduct projects on communication systems using frequency bands above 100 GHz, see for instance [21].

Synthesis

The sub-THz spectrum, with plenty of unused frequency resources, represents a real opportunity to implement high-rate communications, and thereby, to meet the requirements of future wireless networks. Contemplated applications are ambitious and promises are great. Still, the use of a new spectrum involves new technological challenges including: difficult propagation conditions, strong phase impairments, constraints on band-limited converters, *etc.* Since conventional wireless technologies cannot be straightforwardly transposed to sub-THz frequencies, additional research is conducted to design dedicated and efficient transmission techniques. The development of sub-THz transceivers lie in an uncommon design paradigm, close to the dirty RF one. In this paradigm, the design of communication schemes has to consider jointly the analog and digital domains. We have presented in this chapter the context of the research work of this thesis. By doing so, readers may better understand and appreciate our contributions to the development of the physical layer for future sub-THz communication systems. In the following chapter, we outline an overview of the thesis research: the addressed challenges, the developed approaches and our main contributions.

Chapter 2

Thesis Work on Sub-TeraHertz Physical Layer

The previous chapter has set up the scene for the design of sub-THz communication systems. The motivations and research framework have been enlightened. This chapter now outlines an overview of our research work. We first describe the problematics addressed in this thesis on the physical layer for sub-THz systems. To guide the readers throughout the whole manuscript, we also introduce here the developed approach within our research and its objectives as well. In particular, we consider that the design of the sub-THz physical layers should be driven by the technological constraints. The path from technological constraints to solutions highlights that two distinct design paradigms arise for the physical layer of sub-THz systems: spectral-efficient *vs.* low-complexity. For each paradigm, a brief introduction is given to precise how our research focuses relate to or differentiate from the literature and state-of-the-art techniques. Finally, we present briefly the main results obtained during this thesis and the organization of the manuscript.

2.1 Thesis Vision: From Technological Constraints to Solutions

2.1.1 Two distinct design paradigms for the physical layer

Despite the evolution of semiconductor technologies, additional research is required to design new physical layer algorithms and transceiver architectures to manage Radio-Frequency (RF) impairments of sub-THz systems. Therefore, we claim that a constraint-driven design of sub-THz communication systems is essential. In this paragraph, we detail a ***constraint-driven design of the physical layer*** for sub-THz systems. Figure 2.1 accordingly illustrates the path from sub-THz technological constraints to the two design paradigms for the physical layer. We have previously stated that a major challenge is to design wireless communications with strong phase impairments and band-limited converters. The phase impairments and band-limited converters represent two important technological constraints toward the realization of sub-THz systems. A fundamental solution to cope with the band-limited converters is a parallelized RF architecture. For instance, we can mention the use of channelization – *i.e.* the aggregation of several sub-bands also referred to as *channel-bonding* – or the use of correlated receivers namely projecting the received signal upon a set of analog signals. Conversely, two kinds of solution are possible to mitigate the effects of phase impairments. First, the straightforward solution is the optimization of signal processing techniques to improve robustness to Phase Noise (PN), *e.g.* the design of the constellation for PN channels [22]. This lies perfectly in the dirty RF paradigm where dedicated digital signal processing algorithms are designed to cope with impairments of the analog domain. Such optimizations may lead to complex algorithms, yet they are essential to achieve high-spectral efficiency communications since strong phase impairments limit the achievable information rate. Second, inherent robustness to phase impairments may be obtained by using an envelope detection scheme at the receiver side. It discards any phase component of the received signal such that information is transmit-

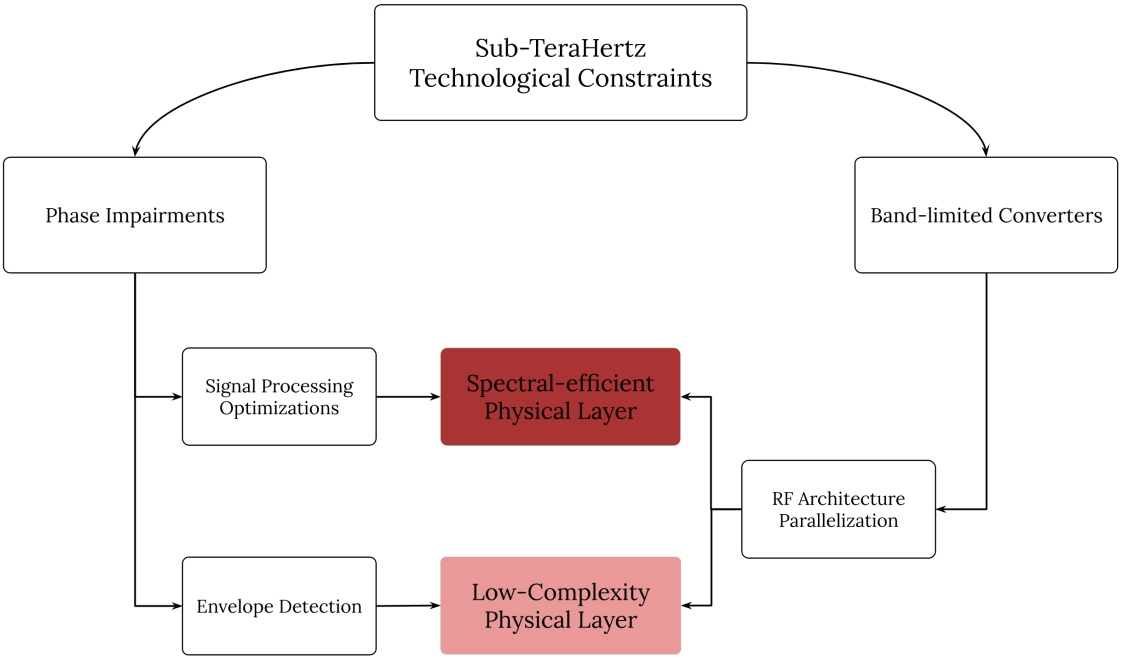

Figure 2.1 – *Illustration of the path from technological constraints to the two paradigms for the physical layer*

ted by modulating the amplitude of the sent signal. Though transceivers using envelope modulation and detection have limited spectral efficiency, they can be implemented straightforwardly even at high carrier frequency with very simple architectures. From these two kinds of solution to mitigate phase impairments, we notice that two distinct design paradigms emerge. Either the objective is to maximize the ***spectral efficiency*** of the communication system at any cost in terms of complexity or power consumption. Or the objective is a ***low-complexity*** implementation in practical systems at the detriment of using modulation schemes with low modulation orders and low spectral efficiencies. We do not claim that this analysis should define the unique comprehensive framework for the development of sub-THz systems. The aim of this illustration and analysis is to provide readers the means to rapidly understand and position our research on the design of sub-THz systems. We now describe with more details these two design paradigms in order to introduce the potential solutions for their implementation. A brief description of the two design paradigms is outlined in Table 2.1.

2.1.2 Spectral-efficient physical layer

In this paragraph, we present a concise description of the design paradigm of spectral-efficient physical layers for sub-THz communications. In the present case, the design objective is to maximize the communication throughput for a given bandwidth. Namely, the objective is to maximize the spectral efficiency expressed in bit/s/Hz. This describes somehow a conventional approach to the design of communication systems that continues the current path towards higher data rate systems. With regard to the previous chapter, this design paradigm lies in the so-called band-limited regime as targeted spectral efficiency $\eta = R/B > 1$, the limiting constraint being the finite bandwidth. To describe further this design paradigm, the contemplated applications for spectral-efficient physical layers include backhaul links, fixed wireless point-to-point links, *etc.* Put differently, this paradigm is suited to any scenarios where there are no specific constraints on the architecture complexity or on the transceiver power consumption, *i.e.* where no embedded terminals are involved. We have observed in the preceding chapter that the implementation of high spectral efficiency links is a necessary condition for

Table 2.1 – *Description of the design paradigms for the physical layer of sub-THz systems*

Design paradigm	**Spectral-efficient**	**Low-complexity**
Objective	Maximize throughput for a given band	Achieve high data rates with low-complexity
Constraint	Finite bandwidth	Architecture complexity
Regime	Band-limited $\eta > 1$	Wideband $\eta < 1$
Application	High-capacity backhaul	Enhanced hot-spot
Features	I/Q arch., high-quality RF, high-order modulations	Non-coherent arch., simple RF, pulse-based modulations

achieving Tbit/s data rates. To achieve high spectral efficiencies in sub-THz bands, transceivers require coherent In-phase/Quadrature (I/Q) architectures with high-order modulations schemes. They hence rely on high-quality RF components with strong linearity constraints and large power amplification. To introduce briefly state-of-the-art solutions, we highlight that current research projects mainly focus on channel-bonding architectures combined with digital signal processing optimizations, see [19]. Subsequently, important efforts are dedicated to the design of reliable RF components: oscillators, power amplifiers, *etc.* with the intention to realize spectral-efficient transceivers. To complete these works at the technological level, we have focused our research on the design of dedicated transmission schemes for systems impacted by strong phase impairments. State-of-the-art techniques are rather theoretical and lead to complex implementations, for instance optimized constellations for PN channels. Conversely, we intend to work at the crossroads between algorithm design and their efficient implementation in practical systems. With regard to the previous chapter, this design paradigm is related to the research objective on the optimization of communication schemes for coherent transceivers. Optimizing transmission techniques aims at: i) limiting the performance degradations due to RF impairments to obtain enhanced system performance with state-of-the-art components such as improved spectral efficiency; ii) and at relaxing RF constraints while achieving similar system performance with lower-quality components.

2.1.3 Low-complexity physical layer

For the low-complexity design paradigm, the objectives of the physical layer are considerably different. In particular, the main objective is to achieve high-rate communications with low-complexity architectures. The targeted applications for low-complexity physical layers include: short-range and device-to-device communications, or the enhanced hot-spot kiosk. In the wider sense, low-complexity sub-THz transceivers are suited to any scenarios with constrained equipment such as embedded terminals. Regarding the analysis presented in the previous chapter, the design of low-complexity physical layers is rather related to the research objective of designing new dedicated sub-THz systems. It hence represents an alternative perspective to the design of communication systems for sub-THz frequencies. The principle of this exploratory approach is to rely on existing RF technologies readily implementable in sub-THz frequencies. Moreover, this approach is based on initial considerations of the specific features of sub-THz communications: wide frequency bands, phase information corrupted, Line-of-Sight (LoS) channels, *etc.* Implementing high-rate communications with low-complexity transceivers intrinsically defines a wideband regime [23] – also referred to as the power-limited regime – in the sense that the targeted spectral efficiency $\eta = R/B \leq 1$. The limiting constraint is the complexity of the transceiver rather than the available bandwidth. Subsequently, it requires the use of simple RF architectures with low-order modulation schemes, such as On-Off Keying (OOK), and efficient analog processing of communication signals. One of our fundamental considerations for low-complexity physical layers is the use of envelope detection schemes at the receiver, or other non-coherent architectures. Envelope detection is not subject to phase impairments and can be easily implemented in sub-THz frequencies. To present some existing solutions regarding high-rate and low-complexity physical layers,

we could mention: channelized OOK transceivers using multiple sub-bands as described in [24] and proposed by the IEEE 802.15.3d interest group for Wireless Local Area Networks (WLAN) applications in sub-THz frequencies. Besides, in the context of Ultra-WideBand (UWB) communications, high-rate and low-complexity transceivers have been designed specifically for wideband regimes, see for instance [25]. These solutions are relevant to the desired objectives and can be used as inspirations for communication systems in sub-THz bands. Our research is hence directed towards the design of high-rate and non-coherent transceivers for sub-THz applications.

We have shown that considering a constraint-driven approach leads to two distinct paradigms for the design of the physical layer. Either we investigate the optimization of coherent systems to achieve high spectral efficiency, or the design of novel dedicated systems readily implementable in sub-THz frequencies. Though this design approach and the proposed paradigms can be discussed in themselves, they are the foundations of our work. We have thereby set up the framework of the thesis research and have also started to identify some research focuses. Readers are now ready to understand our contributions, and therefore, we present an overview of the thesis work.

2.2 Thesis Overview

The previous section has introduced our vision on the considered research topic: *the design of efficient physical layers for sub-THz communication systems*. We now present an overview of the thesis work and how it contributes to this topic. Figure 2.2 provides a synthetic illustration of the thesis research.

2.2.1 Scope

We define in this paragraph the scope of this thesis. First of all, this work covers the design of future sub-THz communication systems. Neither the design of RF components nor the antennas are addressed in this thesis. Our research focuses on the physical layer such that higher layers are not investigated – for instance access and network algorithms. To be more specific regarding the physical layer perspective, we investigate the design of: transceiver architectures, waveforms and modulation, and signal processing algorithms. It should be mentioned that the design of error correcting codes exceeds the scope of our research. Nevertheless, many of our results are based on numerical simulations using existing state-of-the-art channel coding schemes – *e.g.* the Low-Density Parity Check (LDPC) code of the 5G New Radio (5G-NR). For these reasons, this work overlaps multiple domains including signal processing and communication systems. Our research lies at the frontier of the analog and digital domains, and therefore, involves tools from continuous-time and discrete-time signals processing techniques. In a few words, the intention of this exploratory study is to clear the field with preliminary investigations. This work somehow prepares the groundwork within the laboratory for future research activities. Furthermore, the development of sub-THz physical layers can be tackled from numerous complementary perspectives. By way of example, we could mention the derivation of some theoretical boundaries considering RF impairments of sub-THz systems using information theory. Another example could be realistic link and system level specifications using numerical simulations. To limit the scope of our research, and not get lost along the way, it has been fundamental for us to identify a research focus and define the corresponding approach. We introduce in the following paragraph our research approach for this thesis work.

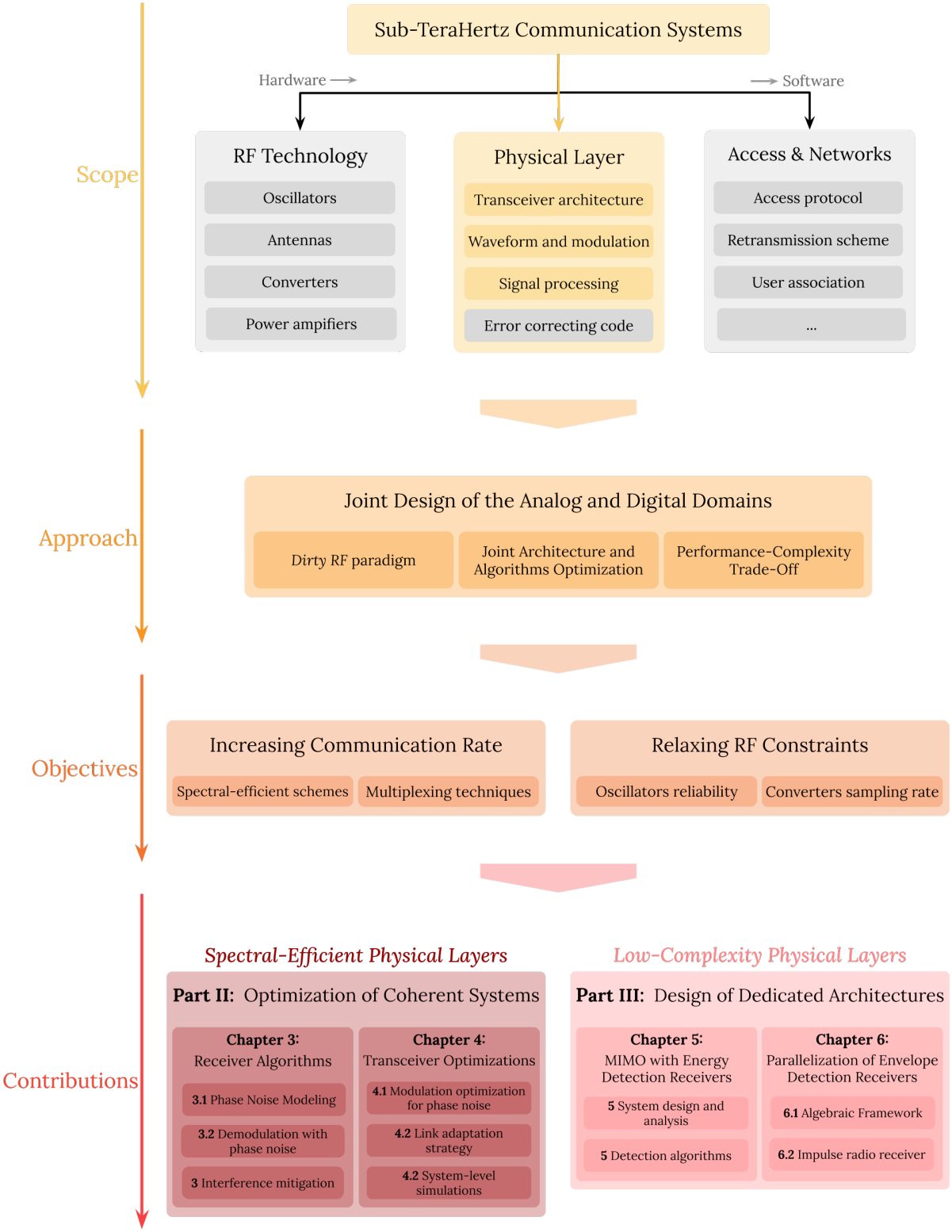

Figure 2.2 – *A synthetic overview of the thesis research*

2.2.2 Approach

Optimizing the physical layer for the specific features of sub-THz systems is a complex task. Our approach can be summarized as follows: ***a joint design of the analog and digital domains***. Let us now provide some details and clarifications to this approach. A foundation of our work is the **dirty RF paradigm** [20]. Namely, we consider the analog problems within the design of the digital signal processing. It enables new levels of RF impairments and limit performance degradations. To put it differently, we cross-correlate the optimization of the transceiver architecture and signal processing algorithms with regard to the specific features of sub-THz communications. By means of illustration, most of communication schemes have been developed for Gaussian noise, *e.g.* Quadrature Amplitude Modulation (QAM), still in the presence of strong PN it has been shown that optimizing the modulation scheme lead to valuable performance gains [22]. Nevertheless, with regard to the design of optimized signal processing algorithms, there is an inevitable trade-off between improving the system performance and maintaining a low-complexity implementation. In this work, we pay particular attention to this **performance-complexity trade-off** with a pragmatic approach. Practical implementation is one of our prime considerations. We therefore aim to propose solutions that can be implemented in standard communication systems with limited memory, latency and computational resources. Complex numerical optimizations leading to minor performance gains will be discarded for the benefit of a low-complexity implementation. Since readers have now a comprehension of the thesis scope and approach, we can present the objectives of our research while developing this approach.

2.2.3 Objectives

We have in this thesis two main objectives. Still, they should not be considered as distinct. These two objectives should rather be interpreted as two complementary ways to use the proposed solutions.

1. ***Realizing high-rate communication systems***

   - We aim at **proposing spectral-efficient communication schemes**. By means of example, we investigate in Part II the optimization of transmission schemes for PN channels with the intention to enhance the spectral efficiency of systems impaired by strong phase impairments.
   - Another objective of ours is to **design dedicated multiplexing techniques**. Conventional multiplexing schemes in either the spatial or frequency domains cannot be directly used in sub-THz bands respectively due to the strongly correlated LoS channels and oscillators instabilities. We therefore address in this thesis the adaptation of multiplexing techniques to the unique features of sub-THz systems – propagation conditions, impairments, *etc.* For instance, Chapter 5 is dedicated to realizing spatial multiplexing with strongly correlated LoS channels.

2. ***Relaxing constraints on the RF components***

   - We also intend in this work to **relax the constraints on oscillators performance**, especially in terms of PN and carrier frequency instabilities. In particular, we are interested in maintaining superior system performance with strong phase impairments.
   - A major concern in our research has been to **reduce the requirements on the sampling frequency** of Analog-to-Digital Converters (ADC). With lower requirements on sampling frequencies, the practical implementation of high-rate systems is to be simplified. From the complementary perspective, it means that the proposed solutions could be used to exploit wider bands with state-of-the-art converter technology – see for example Section 6.2.

2.3 Main Contributions and Organization

We introduce briefly in this section the manuscript organization by presenting the main contributions of the thesis. The manuscript organization reflects, mostly in a chronological way, the advances of our research. We have chosen to present our contributions in a two parts structure. These parts are inherited from the two design paradigms of sub-THz physical layers: spectral-efficient and low-complexity. The unique purpose of this structure is to articulate our contributions in the most meaningful way. To facilitate access to the individual topics, the parts and chapters are rendered as self-contained as possible. Let us now proceed to the parts and chapters description.

Part II: *Optimizations of Signal Processing for Coherent Transceivers*

In this part, we study the adaptation of existing wireless technologies, coherent I/Q transceivers, to the sub-THz spectrum. This is notably achieved through the optimization of signal processing, *i.e.* communication algorithms, to enhance system performance. In particular, our main focus in this part is on achieving high-spectral efficiency communications in the presence of strong phase impairments. A representative application for the contributions of this part is the high-capacity backhaul scenario. The following remark is fundamental to this part. The proposed solutions, designed to increase communication rates, can equally be used to relax constraints on the RF components. These two objectives are simply different perspectives of a unique approach. Most of our findings related to Part II have been published in our journal article [26].

Chapter 3: *From System Modeling to Optimized Receiver Algorithms*

The third chapter is dedicated to the optimization of receiver algorithms for strong PN channels. However, it first requires us to study the modeling of sub-THz communication systems. In particular, we focus on the selection of the oscillator PN model for large-bandwidth systems. Based on the proposed system model, we then investigate the optimum demodulation in the presence of PN. We propose a dedicated detector providing a joint complexity and performance optimization. Namely, a the decision rule for symbol detection is derived, and the probabilistic demapper for soft-decision decoding as well. The material of Chapter 3 has been partly published in four conference papers [27], [28], [29], [30]; and a journal article [26].

Chapter 4: *Transceiver Optimizations and Performance Analyses*

In Chapter 4, we extend the optimization of communication algorithms for PN channels to a transceiver perspective. First, we describe a PN robust modulation scheme: the Polar-QAM. The proposed modulation is based on a theoretical analysis on optimal constellations for PN channels and on practical implementation considerations. The Polar-QAM is designed to improve the system spectral efficiency in the presence of PN with a simple implementation. We present the performance analysis of the proposed scheme using analytical tools and numerical simulations to highlight its performance gains over conventional and state-of-the-art modulations. Second, we extend our study to system-level optimizations and performance analyses. Link adaptation strategies are presented to choose the best modulation scheme and physical layer parameters depending on the channel conditions. We further assess the performance of the proposed communication schemes using deterministic channel predictions on a realistic sub-THz scenario modeling a backhaul deployment in a city center. The content of the fourth chapter has lead to several publications including two conference papers [31], [32]; one journal article [26]; and one patent [33].

Part III: *Proposition of Dedicated Architectures*

The previous part describes a conventional and incremental approach to the development of sub-THz communication systems. In Part III, we develop a more innovative and groundbreaking approach. Our objective is to propose new transceiver architectures dedicated to communications in sub-THz frequencies. In particular, we focus on designing low-complexity transceivers based on envelope modulation and detection. In doing so, transceivers achieve an inherent robustness to phase impairments with readily-implementable RF architectures in sub-THz bands. In contrast to Part II, we do no investigate only software optimizations to mitigate RF impairments but also initial hardware considerations. The presented contributions in Part III have potential applications for the following envisaged sub-THz scenarios: enhanced hot-spot, or device-to-device communications.

Chapter 5: *MIMO systems with Energy Detection Receivers*

When considering non-coherent impulse radio transceivers, the spectral efficiency is quite limited due to the use of pulse-based modulation schemes. For this reason, the fifth chapter focuses on the study of non-coherent spatial multiplexing in sub-THz frequencies to achieve high-rate communications. Namely, we investigate the design and performance analysis of MIMO systems using energy detection receivers for future sub-THz applications. Two dedicated detection algorithms are proposed, a model-based detector and another one using neural-networks. We also present the results of a performance analysis considering an indoor wireless link in sub-THz bands using numerical simulations. The findings of this chapter have been published in part in one conference paper [34], one submitted journal article [35], and one patent [36].

Chapter 6: *Parallelization of Envelope Detection Receivers*

Using large frequency bands to achieve high-rate communications involves important constraints on ADC especially for embedded systems with low-complexity physical layers. The sixth chapter is therefore dedicated to the parallelization of the RF architecture of sub-THz receivers using envelope detection. Our objective in this chapter is to relax implementation constraints on ADC. We first focus on providing the analytical tools to develop efficient communication schemes for pulse-based transceivers. To be specific, we introduce a dedicated Hilbert space. The proposed framework describes an appropriate representation of non-negative signals for transceivers based on envelope modulation and detection. Next, we present a new receiver architecture for non-coherent sub-THz communications, entitled *RAFAE*, for Receiver based on the Analog Fourier Analysis of the Envelope. This analog-oriented receiver is designed for high-rate and pulse-based communications with relaxed constraints on ADC. The material of this chapter has lead to the publication of two conference papers [37], [38] and to the deposit of two patents [39] [40].

Part II

Optimizations of Signal Processing for Coherent Transceivers

Chapter 3

From System Modeling to Optimized Receiver Algorithms

In the previous part, we have highlighted that the sub-THz spectrum, offering large frequency resources, is an opportunity to deploy high-rate wireless services. Still, to meet the requirements of Beyond-5G networks, additional research is required to design efficient physical layer algorithms. It is essential for the development of sub-THz systems to consider the specific features of wireless communications in sub-THz frequencies, such as strong Phase Noise (PN) or Line-of-Sight (LoS) environments. A potential solution to implement sub-THz communication systems is the adaptation of existing and mature technologies, *i.e.* coherent In-phase/Quadrature (I/Q) transceivers. In this part, we develop this approach and investigate the optimization of coherent I/Q transceivers for the sub-THz spectrum. To be specific, this part is dedicated to the optimization of signal processing algorithms for sub-THz systems targeting high-spectral-efficiency communications. The purpose of designing adapted signal processing algorithms is to cope with the specific impairments of sub-THz communications and achieve high data rates. In particular, we focus in this part on the mitigation of phase impairments. With regard to the previous chapter, we consider the design paradigm of a spectral-efficient physical layer. It means that the limiting constraint of the studied transceiver is the finite bandwidth and the objective of the physical layer is to achieve high spectral efficiency. A representative application of such communication systems is high-capacity backhauling, without strong complexity or energy constraints and whose objective is large communication throughput.

In this chapter, we study the optimization of coherent receiver algorithms for strong PN channels. This task is divided into two sections. In the first section, we investigate the modeling of sub-THz communication systems. In particular, efficient modeling of Radio-Frequency (RF) impairments is essential to optimize physical layer algorithms and enhance system performance. Subsequently, we focus on the selection of the oscillator PN model. In the second section, and based on the proposed modeling, we investigate the design of optimum demodulation in the presence of strong PN. With a joint complexity and performance optimization, we propose a dedicated decision rule for symbol detection, and a probabilistic demapper for soft-decision decoding.

3.1 Modeling Sub-THz Communication Systems

Intentions: We intend in this section to determine an efficient system model for sub-THz communication systems. We consider that an efficient system model describes realistically physical processes at stake in communications – *e.g.* RF impairments or propagation –, and still remains mathematically convenient. Such model enables efficient signal processing optimizations enhancing performance with simple practical implementations. In particular, we focus on the modeling of oscillator PN since it is one of the main limiting factors in sub-THz systems [41] [14]. Phase impairments severely degrade the performance of coherent sub-THz systems and thereby significantly limit the achievable spectral

efficiency. By determining an efficient system model, we aim at providing analytical tools for sub-THz communication design and circuit specifications. We consider a spectral-efficient physical layer based on a coherent I/Q transceiver. More specifically, we study systems using single-carrier modulation with a channel-bonding architecture.

Summary: We first detail the system model describing the communication channel for the considered coherent transceiver. We use the results of recent measurement campaigns to describe the sub-THz propagation channel. Second, we present one of the main contributions of this thesis: the modeling of oscillator PN. Using numerical simulations and statistical analyses, we confront two PN models: one correlated (Wiener PN and Gaussian PN); and another uncorrelated (Gaussian PN). We then study the selection of the PN model. Given the system parameters and the spectral characterization of the oscillator, we aim to determine whether the correlated PN model or the uncorrelated one is the most efficient model. Numerical simulations results show that an uncorrelated Gaussian process is appropriate to model the impact of PN in sub-THz systems. Overall, in this first study, we provide analytical tools for sub-THz communication design and circuit specifications.

3.1.1 Channel model

As previously mentioned in Chapter 1, the radio propagation channels in sub-THz frequencies are expected to be sparse. The theoretical expectations that the LoS path provides most of the energy contribution in sub-THz propagation channels have been demonstrated by the recent measurement campaigns within sub-THz bands. The radio propagation channel has been characterized through measurements between 126 and 156 GHz in [9]. Complementary results on non-LoS components can be found in [10]. Sub-THz channels have also been characterized in [42] using deterministic ray-tracing tools. We assume subsequently in this work a LoS propagation channel model, hence considered as frequency flat.

We consider a single-carrier coherent communication system impaired by PN. The presented results can also be exploited in channel-bonding architectures. We assume that the propagation gain and phase shift of the channel are perfectly compensated at the receiver side. In addition, we assume that the receiver is synchronized in time and frequency. We therefore study the discrete-time symbol model of a complex Additive White Gaussian Noise (AWGN) channel impaired by oscillator PN. The received symbols are then expressed by

$$r[\tau] = s[\tau] \cdot e^{j\phi[\tau]} + w[\tau], \quad \tau \in \mathbb{Z} \tag{3.1}$$

where $s[\tau]$ denotes the τ-th transmitted symbol and $w[\tau]$ is a zero-mean circularly symmetric complex Gaussian variable modeling thermal noise, *i.e.* $w[\tau] \sim \mathbb{C}\mathcal{N}(0, \sigma_w^2)$. The oscillator PN to be modeled is described by $\phi[\tau]$. Transmitted symbols are modulated with duration T_s and belong to constellation $\mathcal{C}$ with modulation order M and average energy E_s. The power spectral density of thermal noise $w[\tau]$ is denoted N_0 such that $\sigma_w^2 = N_0/T_s$. The considered discrete-time symbol model in Eq. (3.1) has been further characterized in [43]. Conditions on the sampling rate and on the PN intensity of the system are given to ensure the accuracy of this model. The analysis of [43] has shown that the discrete-time symbol model provides a good representation of the physical continuous-time PN channel, still this simple model represents a worst case description.

With regard to the propagation channel, it is worth pointing out the following remarks. The model in Eq. (3.1) can be easily adapted to include the propagation gain and phase shift of a frequency-flat channel with a single dominant path, the envisaged model for sub-THz scenarios. This is achieved by integrating a complex coefficient h as follows $r = h \cdot s \cdot e^{j\phi} + w$, where h varies slowly. If the receiver

estimates and compensates the channel coefficient h with sufficient accuracy, then the channel can be described with Eq. (3.1) in a more concise way. The unique resulting difference in the system model would be the definition of the spectral density of thermal noise which should be modified from N_0 to $N_0/|h|^2$. Besides, single or multi-carrier systems communicating on multipath channels and impaired by PN have to be described differently and with more complex models, see [44]. Optimizing communication schemes for multipath channels in the presence of PN is not addressed in our research – readers may refer to [21]. This work targets sub-THz applications and hence focuses on propagation channels with a single dominant path.

Phase noise is one of the main limiting factors in sub-THz systems, hence this chapter focuses on the mitigation of this impairments using signal processing optimizations. Subsequently, we devote a significant part of this section to the modeling of oscillator PN.

3.1.2 Phase noise model

To reach 100+ Gbit/s data rates, classical coherent architectures are combined with highly spectral-efficient communication schemes. This entails numerous constraints on the design of RF components especially at the oscillator level. Indeed, high frequency oscillators severely impair sub-THz systems with PN. For a coherent system, the fundamental effect of PN is a random rotation of the constellation, which leads to:

- Detection errors resulting in performance degradation
- Spectral regrowth which may cause inter-channel interference
- In-band signal injection and out-of-band emission

It is hence essential to discuss the selection of the PN model to design dedicated transmission schemes.

A wide range of PN models have been introduced in the literature: Non-linear [45], Tikhonov [46], Wiener [47], *etc.* The selection of the PN model depends on the application. For millimeter-wave (mm-Wave) systems, the PN is usually modeled by the superposition of a correlated contribution (colored PN) and an uncorrelated one (white PN floor) [48]. However, sub-THz systems exploit even wider bandwidths and thus require to reconsider the PN model. It has been shown in [47] that performance of wide-band systems are significantly more impacted by the uncorrelated contribution of PN than the correlated one. This result prompts us to compare the efficiency of an uncorrelated Gaussian PN model to the correlated model commonly used for mm-Wave systems, *i.e.* a superposition of Wiener PN and Gaussian PN. State-of-the-art works on system performance analysis consider correlated PN models for their accurate description [47]. Conversely, research activities on communication schemes optimization use rather uncorrelated PN models for their mathematical convenience [49]. In this chapter, we compare a correlated and an uncorrelated PN models through a statistical analysis to select the most efficient model given the system parameters.

In this study, we present two PN models: one correlated (Wiener PN and Gaussian PN) and another uncorrelated (Gaussian PN). First, the accuracy of the uncorrelated Gaussian PN model is assessed with a Pearson's χ^2 goodness of fit test. We next derive the closed-form expression of the likelihood-ratio of the two models. Thereupon, an analytical condition is proposed to determine whether the correlated or the uncorrelated model should be selected given the system parameters and the spectral characterization of the oscillator. Numerical simulations are performed with a realistic PN generated according to a state-of-the-art sub-THz oscillator.

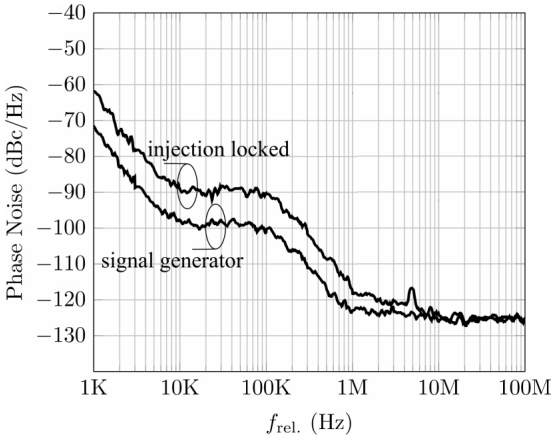

Figure 3.1 – *PSD of the considered* 200 *GHz oscillator [51].*

3.1.2.1 Oscillator Description

The modeling of the complex output v of a practical oscillator with carrier frequency f_c is given by

$$v(t) = \Big(1 + \varepsilon(t)\Big) \exp\Big(j2\pi(f_c + \zeta)t + j\phi(t)\Big), \tag{3.2}$$

where ε, ζ and ϕ denote respectively the amplitude noise, the Carrier Frequency Offset (CFO) and the PN. The amplitude noise ε is mitigated by applying a limiter on the oscillator output and is considered negligible [50]. It is also assumed that the receiver is synchronized in frequency such that the CFO term ζ is compensated. When it comes to PN, the common figure to characterize the performance of an oscillator is its single-side-band spectrum $\mathcal{L}(f)$. It is obtained throughout the following measurements

$$\mathcal{L}(f) = \frac{S_v(f_c + f)}{P_v}, \tag{3.3}$$

with S_v the Power Spectral Density (PSD) and P_v the power of the oscillator output v. Though the total power of an oscillator should ideally be concentrated in f_c and the PSD of the oscillator a pure tone, PN induces the power to be spread over frequencies around f_c. We denote S_ϕ the PSD of PN ϕ. For large f, the small angle approximation $e^{j\phi} \simeq 1 + j\phi$ leads to $S_\phi(f) \simeq \mathcal{L}(f)$. The latter equation bonds the PN ϕ and the oscillator output v. This relation enables us to calibrate the PN model on the oscillator spectral characterizations. In this work, we intend to confront several PN models on realistic observations. We therefore select a state-of-the-art 200 GHz oscillator [51], whose PSD is illustrated in Figure 3.1. The simulated PN will correspond to this oscillator by respecting the same spectral characteristics as measured in Figure 3.1. Simulation of realistic PN consists first in generating several white random PN processes. Next, each of the PN contributions is independently filtered to yield a fixed characteristic. Lastly, the different contributions are added to outcome the desired PN. Nevertheless, we refer the reader to [47] for PN simulation based on oscillator spectral characterizations and also to [52] for simulation of power law noise. It is also worth mentioning that communication systems may use separate oscillators at the transmitter and the receiver. In this case, both PN contributions must be added together.

3.1.2.2 Phase Noise Models

We now present the two studied PN models. The first one is a correlated model based on the physical modeling of the PN generation in oscillators. This model is frequently used for mm-Wave systems [48] and describes the superposition of a correlated contribution (colored PN) and an uncorrelated one (white PN floor). The second model is an uncorrelated model describing only the white PN floor. Its

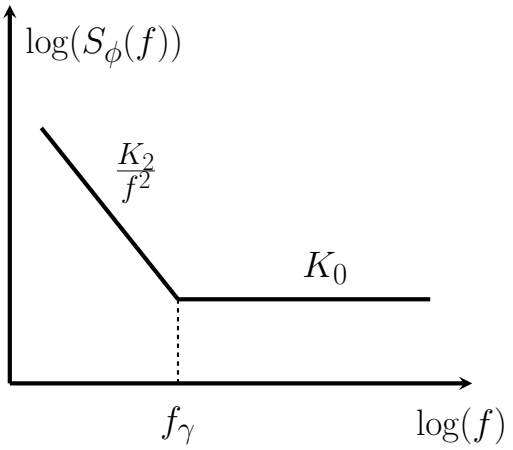

Figure 3.2 – *PSD of the considered correlated PN model.*

mathematical expression is hence simple and commonly exploited to optimize the signal processing for PN channels[22].

Correlated phase noise: The generation of PN in oscillators is due to the transformation of amplitude fluctuations into phase fluctuations. In practical systems, free-running oscillators are stabilized by means of a Phase-Locked Loop (PLL). With respect to the linear time-invariant model of the PLL, the PN generation mechanism may be modeled as an amplification and an integration of the noise sources present in the circuits [47] [50]. The integration of noise sources by the PLL gives a cumulative and correlated nature to PN. We assume that the circuitry is only subject to white noise[1]. Accordingly, the oscillator PN $\phi[\tau]$ may be modeled by the superposition of a Wiener process $\phi_W[\tau]$ (a Gaussian random-walk) and a Gaussian one $\phi_G[\tau]$ [50]. That is

$$\phi[\tau] = \phi_W[\tau] + \phi_G[\tau]. \tag{3.4}$$

The Gaussian PN $\phi_G[\tau] \sim \mathcal{N}(0, \sigma^2_{\phi_G})$ is caused by the amplification of the thermal noise in the oscillator. The Wiener PN is defined by

$$\phi_W[\tau] = \phi_W[\tau - 1] + \delta\phi_W[\tau], \tag{3.5}$$

where $\delta\phi_W[\tau] \sim \mathcal{N}(0, \sigma^2_{\phi_W})$. It expresses the integration by the PLL and hence the cumulative nature of PN. Figure 3.2 presents the PSD described by this PN composed of two characteristics. The uncorrelated Gaussian process with variance $\sigma^2_{\phi_G} = K_0/T_s$ has a flat spectrum of density K_0. The correlated Wiener PN presents a Lorentzian characteristic $(1/f^2)$ [50] with density K_2. The variance of the Wiener increment verifies $\sigma^2_{\phi_W} = 4\pi^2 K_2 T_s$ [50]. The variances $\sigma^2_{\phi_G}$ and $\sigma^2_{\phi_W}$ of the two processes are bonded by the corner frequency $f^2_\gamma = K_2/K_0$. We use hereafter the normalized corner frequency $f_\gamma \cdot T_s$ expressed as a fraction of the system bandwidth $1/T_s$. In the following, we will refer to this model as M_W for short. Based on the physical modeling of the PN generation in oscillators, this model is frequently used in the literature for its accuracy – see [47] and references therein. However, its complexity motivates the introduction of an uncorrelated Gaussian PN model.

Uncorrelated phase noise: By definition, modeling a stochastic process represents a trade-off between the accuracy of description and its complexity. Since the development of communication systems highly benefits from theoretical analyses, the low analytical complexity of a model can be preferred

[1]The influence of flicker noise is disregarded in this study.

Table 3.1 – *Spectral density K_0 (dBc/Hz) of the white PN floor.*

		Bandwith $1/T_s$		
		100 MHz	1 GHz	10 GHz
Strong PN	$\sigma^2_{\phi_G} = 10^{-1}$	−90	−100	−110
Medium PN	$\sigma^2_{\phi_G} = 10^{-2}$	−100	−110	−120
Low PN	$\sigma^2_{\phi_G} = 10^{-3}$	−110	−120	−130

over its accuracy. By means of illustration, the Gaussian PN model has already been exploited in [22] to optimize constellations for PN channels. We thus turn away from the accurate but complex M_W to consider the Gaussian PN model. Besides its mathematical convenience, the Gaussian distribution is also a relevant PN model for wide-band systems. The work in [47] has studied separately the influences of the different PN spectrum regions on communications. It has exhibited a strong dependence with the system bandwidth $1/T_s$. In particular, when considering high symbol rate systems, the oscillator noise floor – characteristic K_0 in Figure 3.2 – represents the greatest contribution to the overall PN. This result may also be appreciated by evaluating the ratio

$$\gamma = \frac{\sigma^2_{\phi_W}}{\sigma^2_{\phi_G}} = 4\pi^2 f_\gamma^2 T_s^2. \tag{3.6}$$

For wide-band systems, $f_\gamma \ll 1/T_s$ leads to $\sigma^2_{\phi_W} \ll \sigma^2_{\phi_G}$. It follows that the Wiener PN becomes negligible compared to the Gaussian PN. For these reasons, it is worth considering a Gaussian PN model denoted M_G. The oscillator PN $\phi[\tau]$ is described by a truncated Gaussian distribution,

$$\phi[\tau] \sim \mathcal{N}(0, \sigma^2_{\phi_G}). \tag{3.7}$$

As the phase is naturally bounded by $(-\pi, \pi]$, the Gaussian distribution must be truncated. The probability density function is normalized[2] by $\lambda = (F_{\mathcal{N}}(\pi) - F_{\mathcal{N}}(-\pi))^{-1}$ to ensure that $\int_{-\pi}^{\pi} p(\phi)d\phi = 1$, where F denotes the cumulative distribution function. Returning to oscillator characterization, Table 3.1 presents some values of spectral density K_0 of the white PN floor for different variances $\sigma^2_{\phi_G}$ and system bandwidth $1/T_s$. The presented spectral densities can be related to practical oscillators with Figure 3.1. Still, Figure 3.1 presents a state-of-the-art oscillator such that worse PN performance may be expected in practice. The following work evaluates the efficiency of M_G to model PN observations. It is clear from Eq. (3.6) that the accuracy of M_G is function of the normalized corner frequency $f_\gamma \cdot T_s$.

3.1.2.3 Accuracy of the Gaussian model

We have previously introduced two PN models: M_W, correlated with a complex and accurate description of PN; and M_G, uncorrelated with a simple mathematical expression. We first evaluate the accuracy of M_G, the Gaussian distribution, to model PN observations. Then, we compare the likelihood of the correlated M_W and uncorrelated M_G models in order to select the most efficient one given the system bandwidth and the oscillator spectral characterization.

To assess the accuracy of M_G, we perform a Pearson's χ^2 goodness of fit test on simulated PN. By doing so, we intend to determine the systems parameters, communication bandwidth and oscillator spectral characteristics, for which M_G models accurately the PN observations. The simulated PN samples are generated either according to M_W, considered as an accurate and realistic PN model, or to the oscillator described in Figure 3.1. First, the goodness of fit test is described, and then, the simulations results are presented.

[2]It is worth mentioning that most demodulation algorithms are not subject to a normalization of the likelihood function and hence a factor multiplication does not increase the complexity.

Pearson's χ^2 goodness of fit test: The aim of this paragraph is to establish whether an observed PN frequency distribution differs from a truncated Gaussian distribution. In other words, we operate normality tests on simulated PN. Let $\phi = \{\phi[\tau]\}_{1\leq\tau\leq N}$ denote the observed values of random PN and N the number of symbols within a communication frame. Two different communication frames hence represent two independent realizations of PN. The null hypothesis can now be described as

$$H_0 : \ M_G \text{ is consistent with the observations } \phi. \tag{3.8}$$

To test this hypothesis, a *Neyman-Pearson approach* is a reasonable choice. This approach is designed for binary detection problem with a given significance α [53]. The hypothesis testing δ takes the following form

$$\delta(\phi) = \begin{cases} \text{accept } H_0, & \text{if } S(\phi) < \lambda_c, \\ \text{reject } H_0, & \text{otherwise,} \end{cases} \tag{3.9}$$

where S is the test statistic of observed samples ϕ compared to a decision threshold λ_c which maximizes the probability of detection. The significance is the probability of rejecting the null hypothesis when it is true, *i.e.* $\alpha = P\left(S(\phi) > \lambda_c | \, H_0\right)$. Further, we exploit the common Pearson's χ^2 goodness of fit to test the observations against the null hypothesis H_0. In this case, the value of the statistic S is

$$S(\phi) = N \sum_{k=1}^{K} \frac{(\frac{O_k(\phi)}{N} - p_k)^2}{p_k}, \tag{3.10}$$

where O_k is the number of observations $\phi[\tau] \in I_k$, while K denotes the number of intervals I_k partitioning $(-\pi, \pi]$ and $p_k = Pr(\phi[\tau] \in I_k)$. To determine the goodness of fit we compare the value of $S(\phi)$ to a χ^2_{K-1} distribution with $K-1$ degrees of freedom. The variance is estimated from observations, the mean is known to be null. The critical value is given by $\lambda_c = F^{-1}_{\chi^2_{K-1}}(1-\alpha)$, where α is the given significance.

Simulations results: We first perform the χ^2 test on PN samples generated according to M_W, with significance $\alpha = 0.1$. Figure 3.3a illustrates the frequency of accepting H_0 as a function of the normalized corner frequency $f_\gamma \cdot T_s$. This confirms the aforementioned intuition in Eq. (3.6) that M_G is accurate when $f_\gamma \ll 1/T_s$. The value 0.9 of the frequency of accepting H_0 is consistent with the significance $\alpha = 0.1$. It must be pointed out that N, the length of the studied sequence, has a great influence on the selection of the model. For long sequences, the impact of the PN correlation is significant and cannot be neglected. Second, we test H_0 against realistic PN samples simulated according to the oscillator described in Figure 3.1. The frequency of choosing $\delta(\phi) = H_0$ is presented in Figure 3.3b as a function of the system bandwidth $1/T_s$. Properties observed in Figure 3.3b and the resulting conclusions are similar to the ones of Figure 3.3a. We have confirmed with the Pearson's χ^2 goodness of fit test that the uncorrelated Gaussian PN model M_G is accurate if the corner frequency remains small compared to the system bandwidth. However, we have not yet derived an analytical expression of the dependence between the accuracy of M_G and the system features N and $f_\gamma \cdot T_s$. This is carried out in the following paragraph.

3.1.2.4 Model Selection

We have previously witnessed the limitations of the Neyman-Pearson approach. The properties of M_G have been highlighted, still they have not been expressed analytically. To do so, we compare the efficiency of M_W and M_G to model some PN observations $\phi = \{\phi[\tau]\}_{1\leq\tau\leq N}$ in terms of likelihood. We recall that N denotes the number of symbols within a frame and that different frames represent independent realizations of PN.

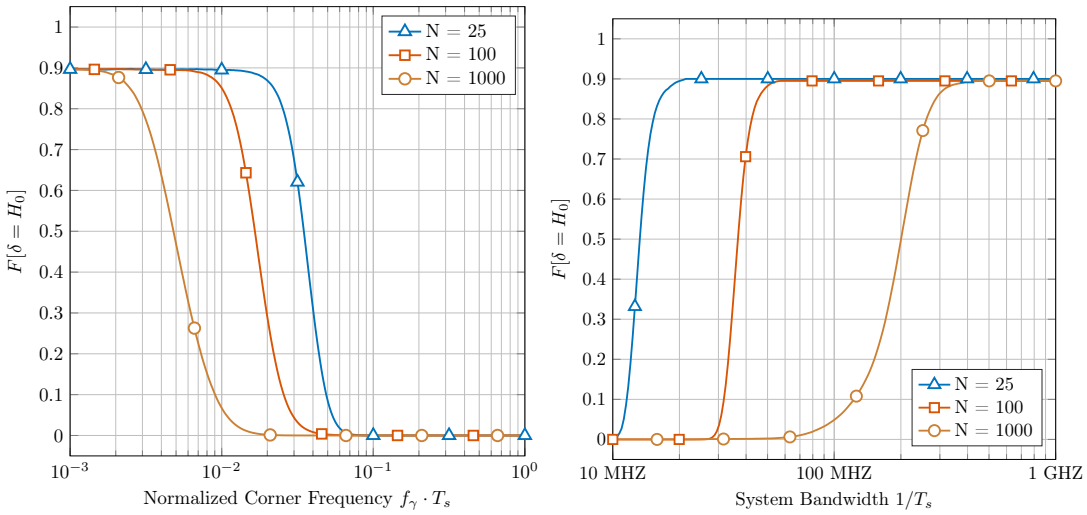

(A) *Correlated PN simulated* (B) *Realistic PN simulated*

Figure 3.3 – *Frequency of accepting the Gaussian model H_0 with a χ^2 goodness of fit test for simulated PN*

Log-likelihood ratio: Given the oscillator PSD, the comparison between M_G and M_W can be achieved by evaluating the Log-Likelihood Ratios (LLR) of the models for observations ϕ. The LLR is expressed by

$$\Lambda_{G/W} = \ln\left(\frac{p(\phi|M_G)}{p(\phi|M_W)}\right), \tag{3.11}$$

and is denoted Λ for brevity. While the sign of Λ infers the model to select (M_G if $\Lambda \geq 0$, M_W otherwise), its absolute value quantifies the reliability of this decision. So, a small $|\Lambda|$ leads to the conclusion that M_G and M_W are equally likely. Conversely, a high value of $|\Lambda|$ indicates that the observations are particularly in favor of one model over the other. To derive the expression of Λ, we must express the joint distributions $p(\phi|M_G)$ and $p(\phi|M_W)$. Regarding M_G, $\phi[\tau]$ are independent and identically distributed. It is hence straightforward from Eq. (3.7) that

$$p(\phi|M_G) = \left(2\pi\sigma^2_{\phi_G}\right)^{-\frac{N}{2}} \cdot \exp\left(-\sum_{\tau=1}^{N}\frac{\phi[\tau]^2}{2\sigma^2_{\phi_G}}\right). \tag{3.12}$$

As for M_W, PN is correlated and we must start by applying the conditional chain rule. We have

$$p(\phi|M_W) = \prod_{\tau=1}^{N} p\left(\phi[\tau]|M_W, \phi[\tau-1], \cdots, \phi[1]\right) = \prod_{\tau=1}^{N} p(\phi[\tau]|M_W, \phi[\tau-1]). \tag{3.13}$$

The latter equality holds as M_W is a Markov chain of order 1. To evaluate the factors in the previous equation, we next define $\Delta\phi[\tau] = \phi[\tau] - \phi[\tau-1]$ which yields

$$\begin{aligned} p(\phi[\tau]|M_W, \phi[\tau-1]) &\sim \mathcal{N}\left(\phi[\tau-1], \sigma^2_{\phi_G}(2+\gamma)\right), \\ &= p(\Delta\phi[\tau]|M_W) \sim \mathcal{N}\left(0, \sigma^2_{\phi_G}(2+\gamma)\right), \end{aligned} \tag{3.14}$$

where $\gamma = \sigma^2_{\phi_W}/\sigma^2_{\phi_G}$ as defined in Eq. (3.6). Substituting Eq. (3.14) into (3.13), we have

$$p(\phi|M_W) = \left(2\pi\sigma^2_{\phi_G}(2+\gamma)\right)^{-\frac{N}{2}} \cdot \exp\left(-\sum_{\tau=1}^{N}\frac{\Delta\phi[\tau]^2}{2\sigma^2_{\phi_G}(2+\gamma)}\right). \tag{3.15}$$

Since $p(\phi|M_G)$ and $p(\phi|M_W)$ have been derived, we are now in a position to express the LLR Λ. At last, we obtain the closed-form expression of the LLR:

$$\Lambda = \frac{N}{2}\ln(2+\gamma) + \sum_{\tau=1}^{N} \frac{\Delta\phi[\tau]^2}{2\sigma_{\phi_G}^2(2+\gamma)} - \sum_{\tau=1}^{N} \frac{\phi[\tau]^2}{2\sigma_{\phi_G}^2}, \tag{3.16}$$

which completes our derivations.

Simulation results with correlated phase noise: Let us now consider that the PN observations are generated by a M_W process and study the expected value $E[\Lambda]$. Given the system features N and $f_\gamma \cdot T_s$, the expected value of the LLR yields the selected model in average. Since M_W is considered as an accurate and realistic PN model, studying the expected value of the LLR enables us to characterize analytically the observed properties in Figure 3.3a and 3.3b. When $\phi[\tau]$ are generated according to M_W, we have in Eq. (3.16)

$$\sum_{\tau=1}^{N} \frac{\Delta\phi[\tau]^2}{\sigma_{\phi_G}^2(2+\gamma)} \sim \chi_N^2, \text{ with } E\left[\chi_N^2\right] = N. \tag{3.17}$$

Then, the second sum in Eq. (3.16) has for expected value

$$\begin{aligned} E\left[\sum_{\tau=1}^{N}\phi[\tau]^2\right] &= \sum_{\tau=1}^{N} E\left[(\phi_W[\tau]+\phi_G[\tau])^2\right], \\ &= \sum_{\tau=1}^{N} E\left[\phi_W[\tau]^2\right] + E\left[2\phi_W[\tau]\cdot\phi_G[\tau]\right] + E\left[\phi_G[\tau]^2\right], \\ &= \sigma_{\phi_G}^2 \cdot \sum_{\tau=1}^{N}(k\cdot\gamma+1) = \sigma_{\phi_G}^2\left(\frac{N(N+1)}{2}\gamma + N\right). \end{aligned} \tag{3.18}$$

When the PN observations ϕ are generated by a M_W process, it follows that the expected value of the LLR is given by

$$E[\Lambda] = \frac{N}{2}\left(\ln(2+\gamma) - \gamma\cdot\frac{N+1}{2}\right). \tag{3.19}$$

Several remarks must be mentioned with regard to this expression. First, $E[\Lambda] \propto -\gamma\cdot N$ confirms the simulation results that the longer the sequence, the lower the normalized corner frequency must be to ensure that M_G remains an accurate model. Furthermore, we are now able to give a condition on N and $f_\gamma \cdot T_s$ for the correlated PN to be negligible. By evaluating the inequality $E[\Lambda] \geq 0$, we claim that the PN is appropriately modeled by M_G if

$$N \cdot f_\gamma^2 \cdot T_s^2 \leq \frac{\ln(2)}{2\pi^2}. \tag{3.20}$$

Regarding communication design, the condition in Eq. (3.20) may either be exploited to specify the normalized corner frequency $f_\gamma \cdot T_s$ or to set the length N of the frame[3]. Second, even when the PN is generated with M_W, if γ small, then the value of Λ can be greater than zero. The LLR actually penalizes the complexity of M_W in comparison to M_G. This illustrates the principle of the Occam's razor: if both M_G and M_W accurately model the observations, then the simplest model should be favored. Eventually, Figure 3.4a presents the mean LLR value for different frame lengths with M_W simulated PN. Figure 3.4a and condition in Eq. (3.20) may be exploited to select the best PN model – M_G if $E[\Lambda] \geq 0$, M_W otherwise – with regard to system features N and $f_\gamma \cdot T_s$.

[3]We recall here that the frame length N is related to the estimation scheme. Every N symbols, the phase shift of the channel is estimated and compensated.

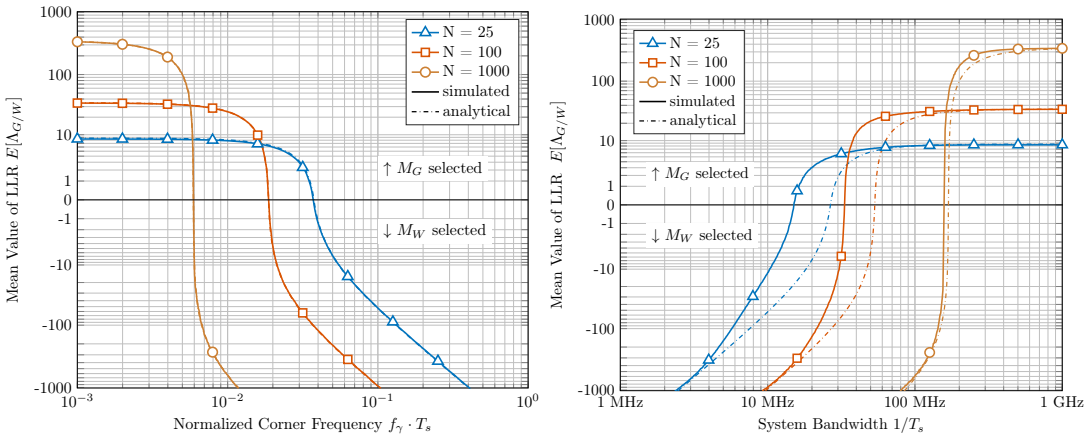

(A) *Correlated PN simulated* (B) *Realistic PN simulated*

Figure 3.4 – *Mean value of LLR $\Lambda_{G/W}$ on simulated PN*

Simulation results with realistic PN: In this paragraph, the simulation results are presented for a realistic PN corresponding to the sub-THz oscillator described in the Figure 3.1. The Figure 3.4b shows the mean value of the LLR as a function of the system bandwidth $1/T_s$ for several frame lengths N. The analytical curves correspond to the expected value of the LLR if the PN samples where generated according to M_W with characteristics K_0 and K_2 measured on Figure 3.1. We can deduce from these results that the condition given in Eq. (3.20) does ensure that an uncorrelated PN model is valid. Nevertheless, it can be observed that this analytical condition is slightly conservative in view of the results obtained by simulation. This may be explained by the fact that the correlated PN of the oscillator close to the carrier frequency is not as strong as the one described by a Lorentzian characteristic. In other words, M_W models a stronger correlated PN contribution than the one measured in practice. Furthermore, considering that the contemplated bandwidths of sub-THz systems will be of the order of the GHz [14], we can conclude from these results that an uncorrelated Gaussian model is appropriate to describe the PN in sub-THz communications.

3.1.3 Conclusion on modeling sub-THz systems

First, we have introduced the system model for sub-THz communication systems. The propagation channel has been described by a LoS model according to the results of recent measurement campaigns, which is a common model in current research on sub-THz communication systems. We have also addressed in this section the problem of PN modeling for sub-THz communications. We have compared two PN models: one correlated, accurate but complex, and another uncorrelated, analytically simpler. Numerical simulations have been performed considering realistic PN corresponding to a state-of-the-art 200 GHz oscillator. We have demonstrated that the uncorrelated Gaussian PN model is accurate when the oscillator corner frequency remains small compared to the system bandwidth. We have also proposed an analytical condition to select the best PN model between correlated or uncorrelated given the system parameters. Overall, our results have shown that an uncorrelated Gaussian process is an appropriate PN model for sub-THz communication systems. In addition, they provide theoretical support to several research studies using uncorrelated PN models to optimize transmission techniques for PN channels.

The presented analysis can be used for PN modeling but also for the specification of communication systems. The proposed analytical condition is useful to specify the required oscillator features, or the frame structure to ensure that the correlated PN remains negligible. By means of example, an

application of the proposed PN model selection is outlined in our paper [28]. The presented application illustrates that our method for PN model selection can be used to adapt the modulation scheme with regards to the oscillator PN performance. Namely, it is proposed to select between a coherent or a differential modulation scheme in order to maximize the system performance. Though the contributions of this chapter are presented within the context of sub-THz communications, they remain relevant to any communication channel impaired by oscillator PN such as satellite communications or next generation of mm-Wave communications, for instance considered in 5G. The main application of our contributions on PN modeling is the optimization of signal processing algorithms for strong PN channels. The Gaussian PN model with a simple analytical description allows in-depth theoretical analyses. Subsequently, the next section capitalizes on the Gaussian PN model to derive the optimum demodulation in the presence of PN.

3.2 Optimum Demodulation in the Presence of Phase Noise

Intentions: The aim of this section is to improve the spectral efficiency of coherent sub-THz communication systems. More specifically, we intend to enhance the demodulation in the presence of PN. Improving the demodulation performance enables systems impaired by PN to communicate with more spectral-efficient transmission schemes. We consider in this section a single-carrier system communicating on a frequency-flat channel corrupted by Gaussian oscillator PN. The considered channel is described by

$$r = s \cdot e^{j\phi} + w, \tag{3.21}$$

with $s \in \mathcal{C}$, $w \sim \mathbb{C}\mathcal{N}(0, \sigma_w^2)$ and $\phi \sim \mathcal{N}(0, \sigma_\phi^2)$. Hereafter, this channel is referred to as the Gaussian PN channel. Since the channel is not time-dependent, the time index τ is discarded for brevity. In the following, we adopt the polar representation and use subscripts ρ and θ to respectively denote the amplitude and phase of a symbol.

Related works: The poor performance of high frequency oscillators plagues sub-THz systems with strong random PN. It severely degrades the communication performance and limits the achievable information rate. Nevertheless, receiver algorithms can be adapted to PN channels. An appropriate decision rule for data detection is to improve the demodulation performance. This has motivated extensive work on the design of optimum receivers for systems impacted by PN, a research topic studied for decades. For each PN model, a corresponding optimum receiver has to be derived. Several optimum receivers for the common PN models are listed in [54]. When it comes to the Gaussian PN channel, the state-of-the-art detection scheme is presented in [54]. This detector is based on the approximate of the Maximum Likelihood (ML) decision rule and is optimum at high Signal-to-Noise Ratio (SNR). The symbol detection in this case relies on a joint amplitude-phase decision rule. However, detectors of the literature present complex definitions making the practical implementation difficult, in particular when soft-decision decoding is considered. Current communication systems are combined with soft-decision decoding known to improve significantly the demodulation performance. Still, the computability of probabilistic bit values, namely LLR, has rarely been studied in the literature and should be a prime consideration in this problem. In this section, our research mainly pursues the work of [54] in order to achieve a joint optimization of system performance and implementation complexity.

Summary: We address in this section the design of the optimum demodulation scheme for the Gaussian Phase Noise (GPN) channel. We exploit a high SNR and strong PN assumption to characterize the likelihood function of the GPN channel, and further, to propose an optimized detector. Our approach is based on a joint performance and implementation complexity optimization. First, we introduce the

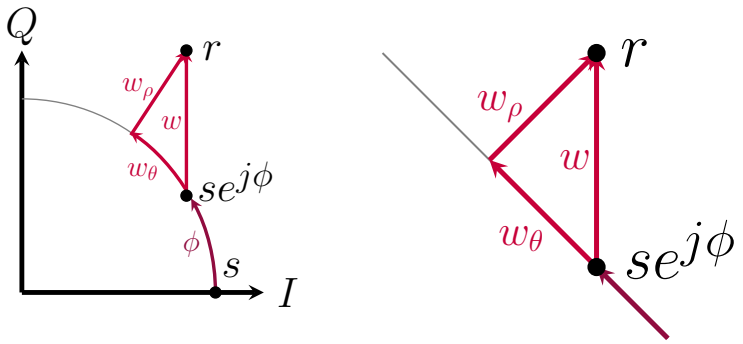

(A) *Exact description* (B) *High SNR approximation*

Figure 3.5 – *Illustration of the received symbol expression*

polar metric, a low-complexity detection scheme minimizing the error probability. The proposed detector achieves, with a simpler implementation, the optimum detection performance of the state-of-the-art detector described in [54]. We also propose a low-complexity implementation of the soft-output demapper using the polar metric for soft-decision channel decoding. Our simulation results demonstrate that using the proposed polar metric leads to important performance gains and significant complexity reductions of the receiver implementation. Second, we show in this section that representing signals upon an appropriate metric space allows the design of efficient transmission schemes. We provide an original mathematical framework to design PN robust algorithms based on a signal decomposition in polar coordinates. The introduced framework enables us to highlight the similarity between the complex Gaussian channel in the I/Q plane and the GPN channel represented in the amplitude-phase domain.

3.2.1 Decision rule for symbol detection

Derivation of the polar metric: Regarding symbol-by-symbol detection, the Symbol Error Probability (SEP) is minimized by the ML decision criterion [1] for equiprobable and independent symbols. The optimum detection decision rule is expressed upon $p(r|s)$ the channel likelihood function. With the considered channel in Eq. (6.25), it is appropriate to write the likelihood function as follows

$$p(r|s) = p(r_\rho, r_\theta | s_\rho, s_\theta), \tag{3.22}$$

and further to express (r_ρ, r_θ) from (s_ρ, s_θ). We denote the shifted noise $w \cdot e^{-j(s_\theta+\phi)}$ by w'. Since the complex noise is circularly symmetric, w and w' are identically distributed. It follows that the amplitude of the received symbol is given by

$$\begin{aligned} r_\rho &= \left| (s_\rho + w') \cdot e^{j(s_\theta+\phi)} \right|, \\ &= \sqrt{\left(s_\rho + \mathrm{Re}\left(w'\right)\right)^2 + \mathrm{Im}\left(w'\right)^2}, \\ &\simeq s_\rho + \mathrm{Re}\left(w'\right), \end{aligned} \tag{3.23}$$

and the phase by

$$\begin{aligned} r_\theta &= \arg\left((s_\rho + w') \cdot e^{j(s_\theta+\phi)} \right), \\ &= s_\theta + \phi + \arctan\left(\frac{\mathrm{Im}\left(w'\right)}{s_\rho + \mathrm{Re}\left(w'\right)} \right), \\ &\simeq s_\theta + \phi + \frac{\mathrm{Im}\left(w'\right)}{s_\rho}. \end{aligned} \tag{3.24}$$

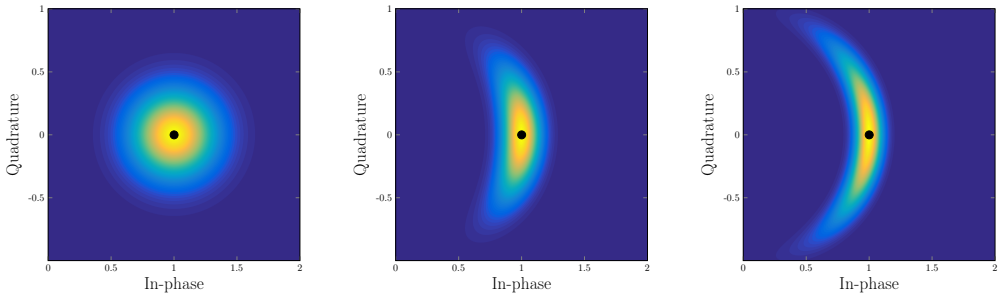

(a) *Low SNR, no PN* (b) *Medium SNR, medium PN* (c) *High SNR, strong PN*

Figure 3.6 – *Illustrations of channel likelihood functions with* $s = 1$

These approximations are illustrated in Figure 3.5. The two latter equations consider the transmission of non-zero symbols. If a zero symbol is sent, the channel in Eq. (6.25) is only corrupted by Gaussian noise. The first-order approximations in Eq. (3.23) and (3.24) are tight at high SNR. Since high data rate applications are targeted in this work, it is reasonable to assume a high SNR in order to allow the use of high-order modulation schemes. Accordingly, we further pursue under a high SNR assumption. It is then straightforward from the channel and PN models that

$$\begin{aligned}(r_\rho - s_\rho) &\sim \mathcal{N}(0, \sigma_w^2),\\ (r_\theta - s_\theta) &\sim \mathcal{N}(0, \sigma_\phi^2 + \sigma_w^2/s_\rho^2).\end{aligned} \tag{3.25}$$

We conclude that the channel likelihood function can be expressed as a bivariate Gaussian distribution:

$$p(r|s) = \frac{\exp\left(-\frac{1}{2}\left(\frac{(r_\rho - s_\rho)^2}{\sigma_w^2} + \frac{(r_\theta - s_\theta)^2}{\sigma_\phi^2 + \sigma_w^2/s_\rho^2}\right)\right)}{2\pi\sqrt{\sigma_w^2(\sigma_\phi^2 + \sigma_w^2/s_\rho^2)}}. \tag{3.26}$$

Figure 3.6 illustrates the channel likelihood functions for different SNR and PN levels. The sent symbol in Figure 3.6 is $s = 1$. Deriving the ML decision rule using this expression of the channel likelihood, we obtain the *ML premetric*. This decision rule was originally derived in [54] and is given by

$$\hat{s} = \underset{s \in \mathcal{C}}{\arg\min} \frac{(r_\rho - s_\rho)^2}{\sigma_w^2} + \frac{(r_\theta - s_\theta)^2}{\sigma_\phi^2 + \sigma_w^2/s_\rho^2} + \log\left(\sigma_\phi^2 + \frac{\sigma_w^2}{s_\rho^2}\right). \tag{3.27}$$

It has been shown in [54] that using the ML premetric leads to important performance gains in comparison to standard receivers based on the Euclidean distance – optimum for the complex AWGN channel. Due to its non-constant logarithmic term $\log\left(\sigma_\phi^2 + \frac{\sigma_w^2}{s_\rho^2}\right)$, this decision rule might be complex to evaluate in practical systems. Further, this decision rule is entitled the ML premetric since it does not define a metric – neither symmetric nor sub-additive – and only a premetric. In this study, we are interested in strong PN scenarios. Using the strong PN and high SNR assumption, we have $\sigma_\phi^2 + \sigma_w^2/s_\rho^2 \simeq \sigma_\phi^2 + \sigma_w^2/E_s$, which is a tight approximation. Thereupon, we propose the *polar metric* detector. Its decision rule is given by

$$\hat{s} = \underset{s \in \mathcal{C}}{\arg\min}\, d_\gamma(r, s)^2, \tag{3.28}$$

where d_γ is the *polar metric* defined by

$$d_\gamma(r, s)^2 = (r_\rho - s_\rho)^2 + \frac{(r_\theta - s_\theta)^2}{\gamma^2}, \tag{3.29}$$

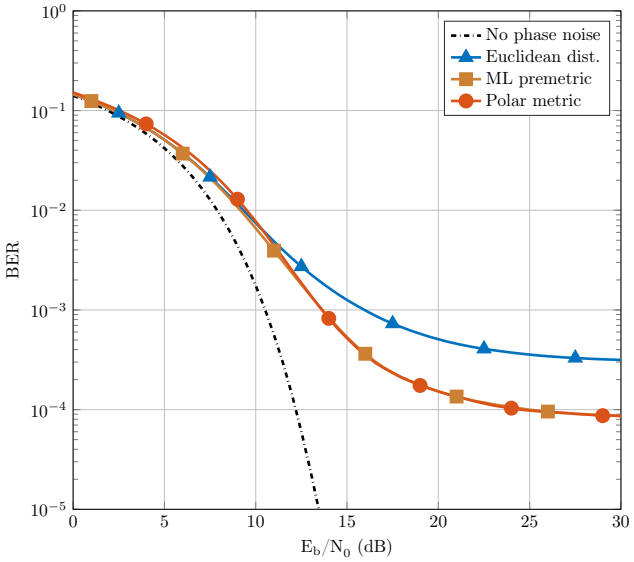

Figure 3.7 – *Performance of the different decision rules for an uncoded* 16*-QAM with PN variance* $\sigma_\phi^2 = 10^{-2}$

and $\gamma^2 = \sigma_\phi^2/\sigma_w^2 + 1/E_s$. The proposed detection criterion is the minimization of the distance related to the polar metric. The detected symbol is then the closest constellation symbol to the received one. The demodulation therefore consists in a nearest neighbor search. It should be noted that this decision rule is a joint amplitude-phase detector. The polar metric is a weighted combination of the amplitude and phase of the received symbols. The detector adapts its decision rule to thermal and PN variances. When PN gets stronger, the detection relies more and more on the amplitude of received symbols rather than on the phase.

Numerical simulations, demodulation of uncoded QAM: We depict in Figure 3.7 the BER performance of an uncoded 16-Quadrature Amplitude Modulation (QAM) with detection based either on the Euclidean distance, or on the ML premetric, or on the polar metric. Simulation results demonstrate that exploiting a joint amplitude-phase detector rather than a Euclidean one yields valuable detection performance gains. In particular, the error floor caused by PN is significantly lowered by using an appropriate detection criterion. These simulations also demonstrate that performance achieved by the polar metric, with a simpler expression, are identical to the ML premetric one at high SNR.

One of the advantages of using the polar metric rather than the ML premetric is that the evaluation of distances to perform the detection is simpler to implement on practical systems. We will demonstrate in the following the benefits of the polar metric over the ML premetric. In the case of structured constellations, the polar metric greatly simplifies the implementation of the receiver. With the polar metric, the symbol detection can be simplified as threshold comparisons and the evaluation of soft-bit values can be efficiently approximated with piecewise linear functions. These receiver complexity reductions are not possible with the ML premetric due to its non-constant logarithmic terms in the decision rule. In addition, the map d_γ verifies the algebraic properties of a metric. Subsequently, we pursue the analysis within the scope of complete metric spaces.

3.2.2 Algebraic Framework

We present here an original theoretical framework related to the polar metric. This framework enables us to draw a parallel between the GPN channel and the complex AWGN one. In particular, the proposed framework provides the analytical tools to design PN robust communication schemes, which

will be used in the following chapter to optimize the signal constellation. It also gives tools to evaluate many literature proposals related to modulation design for PN channels.

Lemma 1. *Let the complex number s be represented by its polar coordinates $(s_\rho, s_\theta) \in \mathbb{P} = [0, \infty) \times [-\pi, \pi]$. Then the space $\mathbb{P}^N$ - of sequences $\boldsymbol{s} = \{(s_\rho[\tau], s_\theta[\tau])\}_{1 \leq \tau \leq N}$ of N numbers in $\mathbb{P}$ - is a complete metric space when equipped with the metric $d_\gamma : \mathbb{P}^N \times \mathbb{P}^N \mapsto \mathbb{R}^+$ defined by*

$$d_\gamma(\boldsymbol{x}, \boldsymbol{y})^2 = \sum_{\tau=1}^{N} \left((x_\rho[\tau] - y_\rho[\tau])^2 + \frac{(x_\theta[\tau] - y_\theta[\tau])^2}{\gamma^2} \right), \tag{3.30}$$

with $\gamma^2 \in \mathbb{R}_*^+$ for every $\boldsymbol{x}, \boldsymbol{y}$ vectors of $\mathbb{P}^N$.

Proof. It is sufficient to demonstrate that $\mathbb{P}^N$ is a closed subset of the complete metric space $(\mathbb{R}^{2N}, d_\gamma)$. First, it is clear that the map d_γ is a weighted Euclidean distance in $\mathbb{R}^{2N}$. It follows immediately that $(\mathbb{R}^{2N}, d_\gamma)$ is a complete metric space. Ultimately, the metric space $(\mathbb{P}^N, d_\gamma)$ is complete as $\mathbb{P}^N$ is clearly a closed subset of $\mathbb{R}^{2N}$. □

In the following, p^2 denotes the metric space $(\mathbb{P}^N, d_\gamma)$. It results from Lemma 1 that p^2 is a complete metric space and therefore provides a valuable framework to design efficient algorithms for the GPN channel. For instance, the symbol detection based on nearest neighbor search in Eq. (3.29) can be efficiently implemented within p^2 using projections or sphere decoding. Furthermore, it should be noticed that a strong similarity exists between the GPN channel represented in the amplitude-phase domain and the complex AWGN channel in the I/Q plane. This property can be highlighted by approximating, according to Eq. (3.25), the system model at high SNR as follows

$$(r_\rho, r_\theta) \simeq (s_\rho + w_\rho, s_\theta + w_\theta), \tag{3.31}$$

where w_ρ and w_θ follow Gaussian distributions. The radial noise w_ρ models the impact of thermal noise on the amplitude. By Eq. (3.25), we have $w_\rho \sim \mathcal{N}(0, \sigma_w^2)$. The angular noise w_θ models the contributions of both the PN and the thermal noise on the phase. In Eq. (3.25), the angular noise is given by $w_\theta \sim \mathcal{N}(0, \sigma_\phi^2 + \sigma_w^2/s_\rho^2)$. It should be recalled that the variance of the angular noise w_θ is function of (i) the amplitude of the sent symbol s_ρ (ii) the thermal noise variance σ_w^2 and (iii) the PN variance σ_ϕ^2. For the GPN channel, the noise on the amplitude and the noise on the phase are Gaussian and independently distributed. This property can also be observed on a complex AWGN channel in the I/Q plane where the noise on the real part and the noise on the imaginary part are as well Gaussian and independently distributed. Accordingly, the space p^2 is entitled by analogy to the commonly used discrete signal space ℓ^2, the space of square-summable complex-valued sequences equipped with the Euclidean inner product.

Figure 3.8 depicts the Voronoi regions – *i.e.* the ML decision regions – related to the Euclidean distance and the polar metric for a 16-QAM. It illustrates the joint amplitude-phase feature of the polar metric detector. We recall here that the polar metric detector adapts its decision regions to the thermal and phase noise variances. Furthermore, it should be emphasized that the polar metric in the amplitude-phase domain is defined as a weighted Euclidean distance as illustrated on Figure 3.8.(c). Altogether, the latter property along with Lemma 1 highlight the strong similarity between Gaussian PN and complex AWGN channels which will be used further to optimize the modulation scheme.

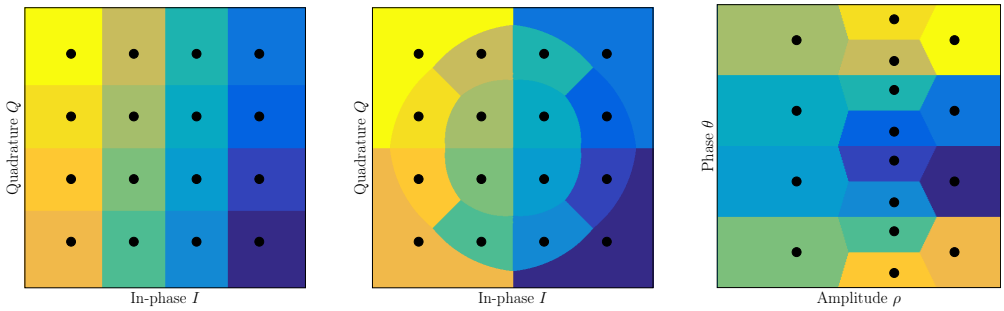

(A) *Euclidean distance in* ℓ^2 (B) *Polar metric in* ℓ^2 (C) *Polar metric in* p^2

Figure 3.8 – 16-*QAM Voronoi regions*

3.2.3 Probabilistic Demapper

It is of practical interest to consider the integration of a Forward Error Correction (FEC) scheme in order to achieve channel coding gains. Channel coding is usually combined with soft-decision decoding known to significantly improve the performance of channel decoders. We therefore propose in this paragraph to study the probabilistic demapper based upon the polar metric.

LLR expression: In practical communication systems, computing the exact values of the bit LLRs may be too complex. Therefore, close approximations of the bit LLRs are evaluated to be computed efficiently. We consider a Bit-Interleaved Coded Modulation (BICM) architecture. Let the symbol s map the binary word $\boldsymbol{b} = (b_1, ..., b_{\log_2(M)})$. Regarding the detection of bit b_i, the decision $\hat{b}_i$ minimizing the error probability is derived from the ML criterion [53]. We have

$$\hat{b}_i(r) = \begin{cases} 1, & \text{if } L_i(r) > 0 \\ 0, & \text{otherwise} \end{cases}, \tag{3.32}$$

where the LLR L_i of the bit b_i is given by

$$L_i(r) = \log\left(\frac{p(b_i = 1|r)}{p(b_i = 0|r)}\right). \tag{3.33}$$

The sign of L_i is used to infer the detection decision while its absolute value $|L_i|$ quantifies the reliability of this decision. Since transmitted symbols are equiprobable, we can express with Bayes' rule the LLR as

$$L_i(r) = \log\left(\frac{\sum_{s_1 \in \mathcal{C}_1^i} p(r|s_1)}{\sum_{s_0 \in \mathcal{C}_0^i} p(r|s_0)}\right). \tag{3.34}$$

We adopt the notation $\mathcal{C}_\beta^i$ to describe the subset of the constellation symbols such that $b_i = \beta$. To simplify the computation of soft bit values, we derive sub-optimal LLRs expressions using the *log-sum* approximation: $\log(\sum_k x_k) \simeq \max_k \log(x_k)$. This approximation is tight at high SNR and is commonly used in practical communication systems for conventional modulation schemes such as QAM [55]. It has been shown in [55] and in [56] that the log-sum approximation does not lead to any significant performance loss, even at low SNR. Subsequently, we obtain

$$L_i(r) \simeq \max_{s_1 \in \mathcal{C}_1^i} \log\left(p(r|s_1)\right) - \max_{s_0 \in \mathcal{C}_0^i} \log\left(p(r|s_0)\right). \tag{3.35}$$

The channel decoding algorithms implemented in practical systems are not impacted by a normalization factor, for instance the *min-sum* decoder for Low-Density Parity Check (LDPC) codes. For this reason,

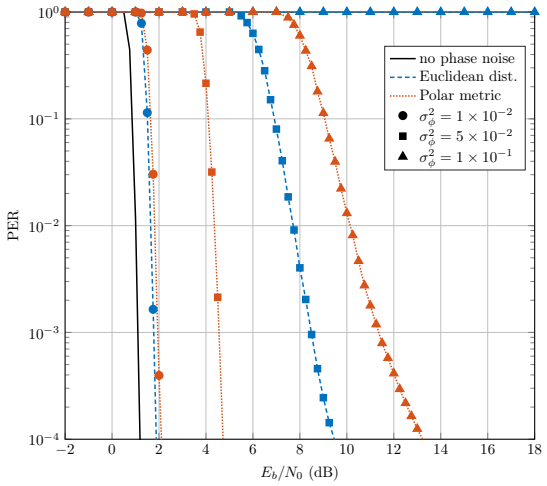

Figure 3.9 – *Performance of a LDPC coded* 16*-QAM with LLR based on the Euclidean distance or on the polar metric for different PN variances* σ_ϕ^2

the approximations of the LLRs can be expressed upon the polar metric introduced in Eq. (3.29) by

$$L_i(r) \simeq \min_{s_0 \in \mathcal{C}_0^i} d_\gamma(r, s_0)^2 - \min_{s_1 \in \mathcal{C}_1^i} d_\gamma(r, s_1)^2. \tag{3.36}$$

The proposed bit LLR values in the latter expression can be easily evaluated. The computation of bit LLR values relies on the polar metric d_γ, and therefore, requires only the evaluation of few weighted Euclidean distances within p^2. In comparison, if the LLR computation is based on Eq. (3.34), the receiver is required to evaluate logarithmic terms as well as multiple sums of Gaussian functions of the received symbol. It should be further highlighted that such complexity reductions are not possible with the ML premetric as this decision rule implies several non-constant logarithmic terms. For this reason, the new soft-output demapper proposed in Eq. (3.36) allows significant complexity reductions of the receiver in comparison to state-of-the-art detectors [54]. It is worth mentioning that the expression in Eq. (3.36) of the bit LLRs remains valid if the propagation channel is considered by integrating a complex coefficient h to Eq. (3.1). The unique difference is that the variance of the thermal noise should be adapted.

Numerical simulations, demodulation of LDPC-coded QAM: Let us now evaluate the demodulation performance of coded systems over the GPN channel. The implemented FEC scheme is a LDPC code respecting the 5G New Radio (5G-NR) specifications [57] with an input packet size of 1500 bytes, a coding rate of 0.8 and a *min-sum* decoder. LDPC codes demonstrate excellent performance with highly parallelizable decoder architectures. Therefore, they are considered as a foremost solution for error-correcting codes in high-rate communication systems. Figure 3.9 presents the Packet Error Rate (PER) performance of a coded 16-QAM for different values of PN variance and demodulation schemes. Simulated PER have been obtained by Monte-Carlo simulations. Results show that important demodulation performance gains are achieved by the polar metric in comparison to the Euclidean detector. For low values of SNR and PN variance, the Euclidean detector performs slightly better than the polar metric (< 0.1 dB). This minor performance loss results from the assumptions of a high SNR, in Eq. (3.23) and (3.24), and a strong PN used to derive the polar metric decision rule. When the PN variance gets stronger, the performance gain of the polar detector in comparison to the Euclidean one becomes significant – *e.g.* > 4 dB for $\sigma_\phi^2 = 5 \times 10^{-2}$. For strong PN variances, the PER of the receiver using the Euclidean distance is 1 for any SNR as the iterative decoder never converges. In contrast, the receiver based on polar metric demonstrates the waterfall feature of LDPC codes and can achieve low error rate communications. The presented PN variances can be related to their corresponding oscillator noise floor spectral densities K_0 using Table 3.1. Though more complex to compute, the demodulation algorithm based on

ML premetric demonstrates identical performance to the one using polar metric one, and hence, is not presented. The proposed demodulation scheme has been assessed for QAM, yet remains valid for any modulation scheme. Ultimately, these results highlight that the proposed demodulation scheme based on the polar metric achieves important performance gains on the GPN channel with valuable complexity reductions of the receiver. Altogether, the results of numerical simulations are an illustration of the performance maximization through channel information capitalization. It is worth mentioning that using channel statistics to properly represent the signal and optimize the communication algorithms is a widely used technique.

3.2.4 Channel Estimation

The previous subsection has shown that knowledge of the channel statistics may be used to improve the performance of the receiver. Therefore, estimations of thermal and PN variances: σ_w^2, σ_ϕ^2 are required. The PN variance σ_ϕ^2 results from the combination of two PN processes issued by the transmitter and the receiver oscillators, hence is not inherent to the receiver only.

Derivation of estimators: Estimation of σ_w^2 and σ_ϕ^2 may be realized by inserting N_p pilot symbols and evaluating the appropriate estimators. The pilot symbols denoted $\boldsymbol{s} = (s[1], s[2], ..., s[N_p])$ are known from the receiver and possibly distributed. The joint likelihood function of the N_p received pilot symbols $\boldsymbol{r} = (r[1], ..., r[N_p])$ is given by

$$p_{N_p}(\boldsymbol{r}|\ \boldsymbol{s}, \sigma_w^2, \sigma_\phi^2) = \prod_{\tau=1}^{N_p} p(r[\tau]|s[\tau], \sigma_w^2, \sigma_\phi^2). \tag{3.37}$$

It should be mentioned that here $\tau \in \{1, \ldots, N_p\}$ is the index of pilots symbols and may refer to non-consecutive received symbols. In the following, we set pilot symbols to have a constant amplitude $\sqrt{E_s}$. The average symbol energy E_s is considered perfectly known as it can be estimated blindly through all sent symbols. The ML estimators of σ_w^2 and σ_ϕ^2 are defined by

$$\hat{\sigma}_w^2 = \underset{\sigma_w^2}{\arg\max}\ p_{N_p}(\boldsymbol{r}|\ \boldsymbol{s}), \ \text{ and } \ \hat{\sigma}_\phi^2 = \underset{\sigma_\phi^2}{\arg\max}\ p_{N_p}(\boldsymbol{r}|\ \boldsymbol{s}). \tag{3.38}$$

To derive these estimators, we first use the definition of the channel likelihood function in Eq. (3.26). We then use Fermat's theorem on stationary points, the function derivative is null at a local extremum, to evaluate the maximum of the likelihood function. It follows that

$$\begin{aligned} \hat{\sigma}_w^2 &= \frac{1}{N_p} \sum_{\tau=1}^{N_p} (r_\rho[\tau] - \sqrt{E_s})^2, \\ \hat{\sigma}_\phi^2 &= \frac{1}{N_p} \sum_{\tau=1}^{N_p} (r_\theta[\tau] - s_\theta[\tau])^2 - \frac{\hat{\sigma}_w^2}{E_s}. \end{aligned} \tag{3.39}$$

We express these estimators as $\chi^2_{N_p}$ distributions to evaluate their biases and dispersions. That is

$$\begin{cases} \mathrm{E}\left[\hat{\sigma}_w^2\right] = \sigma_w^2, \\ \mathrm{V}\left[\hat{\sigma}_w^2\right] = \frac{2\sigma_w^4}{N_p}, \end{cases} \quad \begin{cases} \mathrm{E}\left[\hat{\sigma}_\phi^2\right] = \sigma_\phi^2, \\ \mathrm{V}\left[\hat{\sigma}_\phi^2\right] = \frac{2(\sigma_\phi^2 + \sigma_w^2/E_s)^2}{N_p} + \frac{2\sigma_w^4}{N_p E_s}. \end{cases} \tag{3.40}$$

It is clear that these estimators are unbiased. In addition, it is of practical interest to compare the proposed estimators to their Cramer-Rao Lower Bounds (CRLB) [58] since the regularity conditions

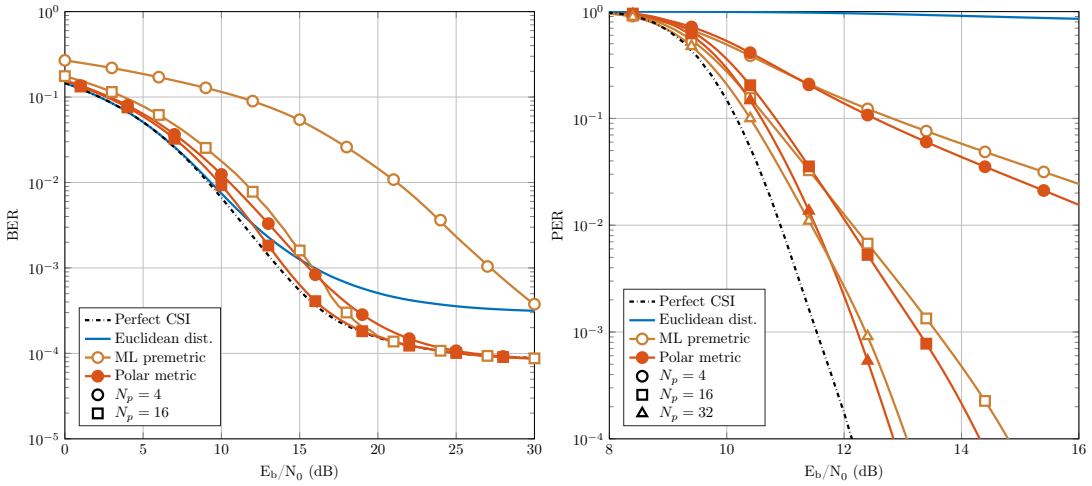

(A) *Uncoded with PN variance* $\sigma_\phi^2 = 10^{-2}$ (B) *LDPC coded with PN variance* $\sigma_\phi^2 = 10^{-1}$

Figure 3.10 – *Performance degradation due to estimation errors for a* 16*-QAM with different number of pilot samples*

are satisfied by the likelihood function in Eq. (3.26). The corresponding CRLBs are given by

$$\mathrm{V}\left[\hat{\sigma}_w^2\right] \geq \frac{2\sigma_w^4}{N_p}, \quad \mathrm{V}\left[\hat{\sigma}_\phi^2\right] \geq \frac{2(\sigma_\phi^2 + \sigma_w^2/E_s)^2}{N_p}. \tag{3.41}$$

It is shown that the estimator of thermal noise variance achieves the CRLB. The estimator of the PN variance is tight to the CRLB but does not achieve it. Nevertheless, it is possible to demonstrate that the proposed estimators present the smallest mean square error among any unbiased estimators. It is immediate from Eq. (3.37), that the joint probability density function p_{N_p} belongs to the exponential family. Therefore, statistic $S = (\sum_\tau (r_\rho[\tau] - \sqrt{E_s})^2, \sum_\tau (r_\theta[\tau] - s_\theta[\tau])^2)$ is complete and sufficient for parameter $(\sigma_w^2, \sigma_\phi^2)$. We can conclude from the Lehman-Scheffé theorem that the proposed unbiased estimators $(\hat{\sigma}_w^2, \hat{\sigma}_\phi^2)$ defined upon S are the unique minimum-variance unbiased estimators of σ_w^2 and σ_ϕ^2. It should be mentioned that these estimators use amplitude and phase information, and can be described in p^2.

The effect of a propagation channel with a single dominant path could be modeled by integrating a complex coefficient h to Eq. (3.1). Nonetheless, the estimation of the channel coefficient required for equalization is not carried out here. The necessary framework has been proposed such that the estimation of the channel complex coefficient is straightforward to derive.

Performance degradation due to estimation errors: Though we have been able to evaluate the performance of the estimators, definitions of the ML premetric and the polar metric are subject to estimation errors. The performance degradation due to such estimation errors has to be quantified to specify the required number of pilots. Therefore, Figure 3.10a and 3.10b present respectively the performance of an uncoded and a LDPC coded 16-QAM for different number of pilots symbols. The reference is the system performance with perfect channel knowledge, *i.e.* perfect Channel-State Information (CSI). We may remark that the polar metric is more resilient than the ML premetric to estimation errors for hard symbol detection, and also in the case of soft decision decoding.

3.2.5 Conclusion on demodulation in the presence of phase noise

In this section, we have addressed the problem of the optimum demodulation scheme in the presence of Gaussian PN. We have proposed the polar metric, a joint amplitude-phase detector. This decision rule has been derived as a symbol detection scheme minimizing the error probability. We have also proposed a low-complexity implementation of the soft-output demapper using the polar metric for probabilistic channel decoding. In contrast to state-of-the-art detectors, the proposed soft-output demapper allows a simple evaluation of soft bit values. Our results show that significant demodulation performance gains are achieved for coded and uncoded systems by using the polar metric in comparison to standard detectors. In brief, the polar metric detector provides a valuable solution optimizing jointly the system performance and the implementation complexity. We have also proposed a framework to properly represent signals upon the GPN channel. It has been highlighted that the GPN channel in the amplitude-phase domain present similar properties to the complex AWGN channel in the I/Q plane.

3.3 Synthesis and Discussions

Conclusion: In this chapter, we have been interested in adapting I/Q coherent transceiver to the specific features and impairments of the sub-THz spectrum. Our attention has been in particular focused on the strong phase impairments issued by high carrier frequency oscillators. In the first section, we have shown that an uncorrelated Gaussian process is an appropriate PN model for sub-THz communication systems. We have also justified that considering a propagation channel with a single-dominant path is an appropriate channel model for sub-THz communication systems. Once the system model characterized, it has been shown in the second section that using a dedicated demodulation algorithm, based on a joint amplitude-phase detector, leads to significant demodulation performance gains in the presence of PN. In contrast to state-of-the-art detectors, the proposed soft-output demapper allows a simple practical implementation with optimum demodulation performance. The content of this chapter has lead to several publications including three conference papers: [27], [28], [30]; and a journal article: [26]. Interested readers may refers to these publications for further details, see citations below.

Contribution on CFO mitigation: We briefly summarize in this paragraph an additional contribution of ours on the optimization of receiver algorithms for future sub-THz systems. Our work has been presented in [30] and has not been developed in this chapter. It addresses the mitigation of independent CFO in channel-bonding architectures. The strong oscillator instabilities does not only impair sub-THz systems with PN but also with large CFO. Future sub-THz systems are contemplated to use channel-bonding architectures to maximize the communication throughput. This type of architecture aggregates several channels with multiple RF chains in order to benefit from the large frequency bands available in the sub-THz spectrum. To cope with the oscillator instabilities, frequency guards bands are usually inserted between channels which results in a spectral efficiency loss. This performance loss motivates us to investigate the mitigation of CFO in a channel-bonding scenario. In [30], we study the analog parallelization of multiple channels. Each of them is corrupted by an independent and randomly distributed CFO. We show that these independent CFOs lead to inter-carrier interference and severely affect the communication performance. In contrast to state-of-the-art approaches, we do not consider the mitigation of this impairment by the estimation and compensation of CFO. In paper [30], we propose and compare digital signal processing algorithms to jointly demodulate the multiple carriers in the presence of strong independents CFOs. Such algorithms are widely used in the domain of digital-subscriber line systems in order to mitigate cross-talk [59]. We adapt in this work theses techniques to a sub-THz channel-bonding scenario. As expected significant performance gains are demonstrated when a joint linear receiver algorithm is considered. It enables to demodulate jointly multiple channels

in the presence of strong CFOs without compensating them. The proposed detection algorithm hence allows relaxing the constraints on oscillators stability without system performance losses.

Perspectives: We have presented in this chapter the main receiver algorithm schemes to realize robust communications impaired by PN. However, many receiver algorithms regarding practical communications are yet to be addressed, *e.g.* the estimation of the channel complex coefficient. In particular, the synchronization between the transmitter and the receiver in the presence of strong PN is challenging. Time and frequency synchronization errors lead respectively to inter-symbols interference and CFO. Synchronization errors need to be compensated in order to limit the resulting performance degradation. For this reason, dedicated synchronization techniques should be designed for systems impaired by strong PN. This topic is of important practical interest and remains to be investigated. Additionally, further perspectives to this study are detailed in the next chapter.

Applications and limitations: This paragraph aims to delineate the potential applications and limitations of our contributions. In doing so, we hope that readers may better appreciate the value of our research work. Our results on PN modeling can be used for system performance analysis or communication schemes optimization. Equivalently they can also be used for system specification in order to determine the required oscillator performance or frame structure. Furthermore, the proposed demodulation scheme provides a readily implementable solution to adapt coherent transceiver to PN channels. Simply modifying the demodulation, either the symbol detection or the LLR evaluation, contributes to alleviating the technological limitations due to oscillator PN and realizing high-rate sub-THz communications. Though the main considered application has been high-capacity back-hauling, the proposed schemes can be used for any coherent transceiver targeting a spectral efficient physical layer. This study is presented within the context of sub-THz communication, yet these results remain valid for any frequency bands. They are particularly relevant for scenarios in which oscillator PN is a major impairment such as satellite communications or next generation of millimeter-wave communication. It should be reminded that the scope of this research covers single-carrier communication systems with frequency-flat channels. Our results are also relevant to system using channel-bonding architectures. However, and as aforementioned, either the use of multi-carrier modulation or multi-path propagation channels requires a different system modeling, and hence, different signal processing optimizations to cope with PN. Besides, our results are subject to some limitations regarding the considered system model. In this work, the impact of PN has been described with a discrete-time symbol model. As previously discussed, this model is efficient yet remains simplistic. We have also considered a single-dominant path channel model. Nevertheless, and though other paths present weak energy contributions, they might cause some interference slightly lowering the SNR. In addition, high SNR and strong PN conditions have been considered to ease analytical derivations, which could lead to approximation errors. Implications of the related approximation errors have been characterized. It has been shown that these errors lead either to none or to minor performance losses at low SNR and low PN. Eventually, we emphasize the great value of experimental validations regarding algorithms design. Experimental validations could assess the performance gains of the proposed schemes but could also demonstrate the impact of other RF impairments such as I/Q imbalance or amplifier nonlinearities. Such experimental validations are envisaged in the research team and should be conducted in the near future.

In this chapter, we have notably shown that using dedicated receiver algorithms enables spectral-efficient communications in the presence of PN. The next chapter continues in the same vein. It investigates under a transceiver perspective the optimization of communication algorithms for strong PN channels. In other words, the following chapter studies optimizations at the transmitter and receiver sides including: the modulation scheme and the link adaptation strategy. Moreover, one objective of

the next chapter is to evaluate the performance gains achieved by the proposed solutions in a realistic sub-THz scenario.

First-authored contributions

[27] S. Bicaïs, J.-B. Doré, and J.-L. Gonzalez Jimenez, "On the Optimum Demodulation in the Presence of Gaussian Phase Noise," in *2018 International Conference on Telecommunications (ICT)*, June 2018

[28] S. Bicaïs and J.-B. Doré, "Phase Noise Model Selection for Sub-THz Communications," in *2019 IEEE Global Communication Conference (GLOBECOM)*, December 2019

[30] S. Bicaïs and J.-B. Doré, "Mitigation of Carrier Frequency Offset in a Sub-THz Channel Bonding Scenario," in *2019 IEEE 30th International Symposium on Personal, Indoor and Mobile Radio Communications (PIMRC Workshops)*, 2019, pp. 1–6

[26] S. Bicaïs and J.-B. Doré, "Design of Digital Communications for Strong Phase Noise Channels," *IEEE Open Journal of Vehicular Technology*, vol. 1, pp. 227–243, 2020

Chapter 4

Transceiver Optimizations and Performance Analyses

This part is dedicated to the adaptation of coherent In-phase/Quadrature (I/Q) transceivers, a mature technology for wireless communications, to the sub-THz spectrum. And more precisely, we focus on signal processing optimizations to cope with the strong phase impairments of high-frequency oscillators. The previous chapter has investigated the design of receiver algorithms for Phase Noise (PN) channels. Thereby, it has unveiled valuable information on the Gaussian PN channel. To determine the optimum receiver, we have previously considered conventional modulation schemes, such as Quadrature Amplitude Modulation (QAM), which are not particularly suited to strong PN channels. Optimizing the transmission schemes also at the transmitter side gives an additional degree of freedom which enables us to further improve the system performance. For this reason, this chapter pursues the study of the previous one. It extends the optimization of transmission algorithms for PN channels to both the transmitter and receiver sides. We lie in the design paradigm of spectral-efficient physical layers for sub-THz communications. Our investigations aim to maximize the communication throughput given a fixed bandwidth without strong complexity or energy constraints. High-capacity backhaul in the sub-THz bands is the most representative envisaged application of the considered scenario.

This chapter deals with the optimization of communication algorithms from a transceiver perspective for strong PN channels. In the first half of this chapter, we propose the Polar-QAM, a PN robust modulation scheme. Based upon a theoretical analysis, the proposed modulation scheme is designed to enhance communication performance on strong PN channels with a simple practical implementation. The performance analysis of the proposed modulation is pursued analytically and numerically to demonstrate the performance gains over conventional and state-of-the-art modulations. In the second half of this chapter, our focus is on system-level optimizations and performance analyses. We present link adaptation strategies to select the modulation scheme and physical layer parameters with regard to the channel conditions. The performance of the proposed modulation and demodulation schemes are further assessed in a realistic sub-THz scenario using ray-tracing channel predictions.

4.1 Polar-QAM: a Phase Noise Robust Modulation Scheme

Intentions: We intend in this work to increase the spectral efficiency of communications impaired by strong PN. In particular, we focus on designing a modulation scheme providing significant performance gains while maintaining a simple implementation in practical systems – with limited computational resources, memory, power consumption *etc.*

Working hypotheses: Let us now recall the framework introduced in the previous chapter. We consider a coherent transceiver whose objective is to maximize the spectral efficiency. More specifically, we study a single-carrier modulation impacted by Gaussian PN. The communication channel is described

as follows. Received symbols are expressed by $r = s \cdot e^{j\phi} + w$ where s is the sent symbols and belong to constellation $\mathcal{C}$, ϕ is the oscillator PN and w models an Additive White Gaussian Noise (AWGN). Furthermore, we use in this chapter the polar metric detector, *i.e.* the joint amplitude-phase detector proposed in the previous chapter and optimized for demodulation in the presence of Gaussian PN. We also represent signals in the amplitude-phase domain. As shown in the previous chapter, the Gaussian PN channel in the amplitude-phase domain present similar properties to the complex AWGN channel represented in the I/Q plane.

Related works: Designing optimized modulation schemes is a widely investigated problem. Notably, choosing M points in a two-dimensional space such that a target function is optimized. In particular, there exists an extensive amount of literature on constellation optimization for PN channels. The following articles are representative of prior work. Research on constellation optimization for PN has begun fifty years ago with Foschini in [46] where signal points are selected among a lattice with a heuristic search to minimize the Symbol Error Probability (SEP) for Tikhonov PN. More recent works have exploited powerful numerical optimization algorithms such as simulated annealing [60] or gradient-search [22] to maximize the mutual information or minimize the SEP. The work in [45] optimizes Amplitude-Phase-Shift Keying (APSK) constellations with a simplex algorithm to minimize the SEP for nonlinear PN. A state-of-the-art solution on constellation optimization for Gaussian PN is proposed in [15]: The *spiral constellation* based on a semi-analytical description, *i.e.* the modulation points are defined with a closed-form expression upon an optimized modulation shape parameter. Nevertheless, most of the constellations proposed in the literature are efficient but local solutions. These schemes are optimized for a specific Signal-to-Noise Ratio (SNR) and PN variance, and thus, do not describe a comprehensive solution. Furthermore, existing solutions are often unstructured which leads to difficult practical implementation with complex binary labeling and demodulation, including the computation of Log-Likelihood Ratios (LLR). In contrast to prior work, we investigate in this work a joint optimization of communication performance and complexity of implementation on practical systems.

Summary: This first section is dedicated to the optimization of the modulation scheme for strong PN channels. An analytical approach is conducted to demonstrate how optimal constellations can be built to maximize performance on the Gaussian Phase Noise (GPN) channel. Motivated by this theoretical analysis, we propose the polar quadrature amplitude modulation (PQAM or Polar-QAM), a PN robust modulation scheme based on a structured APSK. The constellation and the binary labeling of the Polar-QAM are jointly designed to improve the system performance on PN channels while maintaining a low-complexity implementation. In particular, it enables to implement the symbol detection with a simple threshold comparison, and the soft-output demapper with piecewise linear functions. The proposed modulation scheme is compared to conventional and state-of-the-art solutions taking into account different performance metrics. The performance of the Polar-QAM is assessed analytically and numerically considering state-of-the-art channel codes. Our results highlight that the Polar-QAM significantly enhances performance in terms of achievable data rate with valuable complexity reductions of the transceiver.

4.1.1 Optimum constellation for the Gaussian phase noise channel

Optimum constellation from sphere packing: Let us investigate the problem of finding the constellation, *i.e.* the set of signal points in the complex plane, that minimizes the SEP for a given channel. The number of points is fixed to M and the constellation average energy is constrained to E_s. For a transmitted symbol s, the SEP $Pr(E|s)$ may be defined upon its complementary event, the probability of correct detection, as follows

$$Pr(E|s) = 1 - Pr(\hat{s} = s|s). \tag{4.1}$$

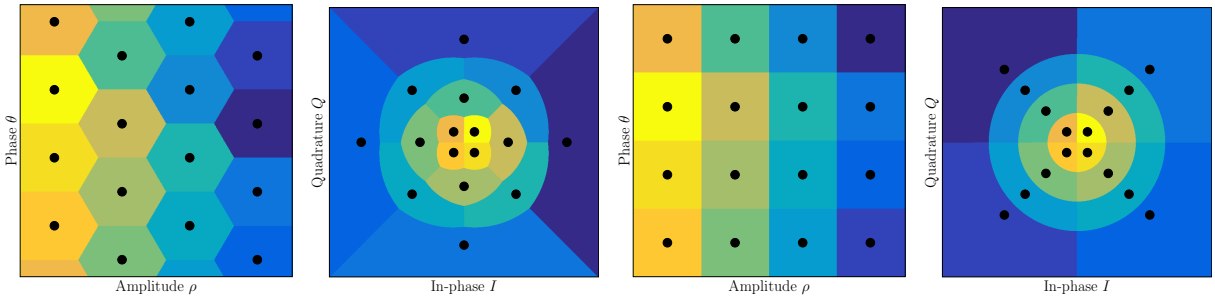

(A) *Hexagonal polar-lattice in* p^2 (B) *Hexagonal polar-lattice in* ℓ^2 (C) *Rectangular polar-lattice in* p^2 (D) *Rectangular polar-lattice in* ℓ^2

Figure 4.1 – *Voronoi regions for the polar metric of polar-lattice based constellations with* 16 *signal points*

With regard to a detection rule defined upon the ML criterion, the probability of correct detection is equal to the integral of the likelihood function over the Voronoi region of the symbol. That is

$$Pr(\hat{s} = s|s) = \int_{\mathcal{V}_s} p(r|s)dr, \tag{4.2}$$

where $\mathcal{V}_s$ is the Voronoi region of symbol s and $p(r|s)$ is the channel likelihood function. It follows that the larger the areas of the Voronoi regions, the smaller the error probability. This result is valid for any channel, yet let us consider the GPN channel. We are hence looking for the constellation that maximizes the areas of Voronoi regions defined by the polar metric. By way of illustration, it is clear on Figure 3.8 that the QAM constellation does not maximize the areas of the Voronoi regions for the polar metric and is thus not optimal for the GPN channel. As previously stated, the proposed constellation in the literature lead to difficult implementations due to their lack of structure. We therefore investigate constellations defined upon lattices in the amplitude-phase plane. Since the ML detector in Eq. (3.28) describes a joint amplitude-phase detector, we study the optimal lattice-based constellation problem within p^2. It results that the noise distribution is circular[1] in p^2 for high SNR and strong PN scenarios. The modulation order and the average energy of the constellation being fixed, the problem of finding the lattice that maximizes the areas of the Voronoi regions can be regarded as finding the densest sphere packing in a two dimensional space. The well-known result of this problem gives that the highest density in the plane is achieved by the hexagonal lattice [61]. Subsequently, a constellation based upon a hexagonal structure is to maximize the areas of the Voronoi Regions [62], and thus, minimizes the SEP. Nevertheless, we consider hereafter the use of a rectangular polar-lattice to define a modulation scheme with the intention to ease the demapping implementation. For the purposes of illustration, Figure 4.1 presents the I/Q and amplitude-phase representations of the hexagonal and rectangular polar-lattice based constellations. Figure 4.1 depicts the Voronoi regions, for the polar metric, of the constellations based on polar-lattice. We will show in the following paragraph that though a hexagonal lattice performs better in terms of error probability than a rectangular one, the performance gain is small and the complexity increase is significant. Therefore, the proposed Polar-QAM scheme relies on a rectangular polar-lattice.

We have previously highlighted the similarity between the GPN channel and the complex AWGN one. Thanks to the analytical framework described in this section, it follows that the derivation of the optimum lattice-based constellation for the GPN channel in the polar domain is highly similar to the one for the complex AWGN channel in the I/Q plane – see [1]. Likewise, the optimal constellation for the complex AWGN channel relies on a hexagonal lattice in the I/Q plane and is referred to as the hexagonal-QAM (HQAM). Though the HQAM demonstrates a performance gain in comparison to the

[1]The noise is distribution is actually ellipsoidal in the amplitude-phase domain, yet is circular in p^2 with the axis scaling γ.

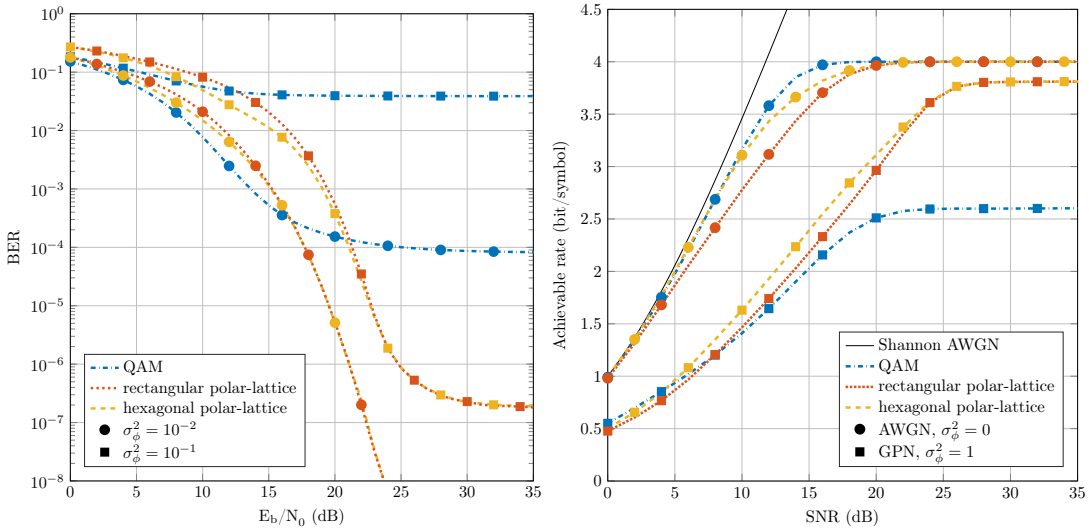

(A) *BER* (B) *Achievable rate*

Figure 4.2 – *Performance of different constellations with $M = 16$ on the GPN channel*

QAM using a rectangular lattice [63], the rectangular QAM remains the most exploited modulation scheme for its simple implementation.

Performance of constellations based on polar-lattices: We discuss here the results of numerical simulation concerning the BER performance of the different constellations based on polar-lattices. The implemented symbol detection rule is the polar metric. The BER performance for different PN variances of the QAM and the polar-lattice based solutions are outlined in Figure 4.2a with $M = 16$. First, we can remark that the optimized constellations are sub-optimal at low SNR. The previous analysis on the design of PN robust constellations is correct under a high SNR assumption. In the low SNR regime, the channel is dominated by thermal noise, even in the presence of strong PN, and in this case, conventional modulation schemes should be preferred. However, it is shown that the constellation of the QAM reaches an error floor due to PN which can be high for strong PN scenarios. Conversely, constellation based on polar-lattice achieve significant performance gains and enable low error rate communications on strong PN channels. These results exhibit the performance gain of hexagonal lattice over the rectangular one, but at the detriment of a complexity increase of the demodulation algorithm.

The performance analysis can be improved by studying the achievable Information Rate (IR) related to the constellations. Figure 4.2b compares the achievable rates of the different constellations for AWGN and GPN channels[2]. The presented achievable IR have been obtained through Monte-Carlo simulations as described in [66]. Given a channel and a constellation, the achievable rate is evaluated by computing numerically the mutual information of the transmitted and received symbols. Our results demonstrate that the achievable rate of the QAM scheme is severely limited by PN. Therefore, we conclude that the optimization of the modulation scheme is essential to target high-rate communications on the GPN channel. For this purpose, constellations based on polar-lattices are a relevant solution to achieve enhanced performance with simple practical implementation.

[2]The theoretical upper bound for the achievable IR on the GPN channel is not presented but can be evaluated. Nevertheless, it requires complex numerical evaluations and an extremely high-SNR assumption. Interested readers may refer to [64] or [65] and references therein.

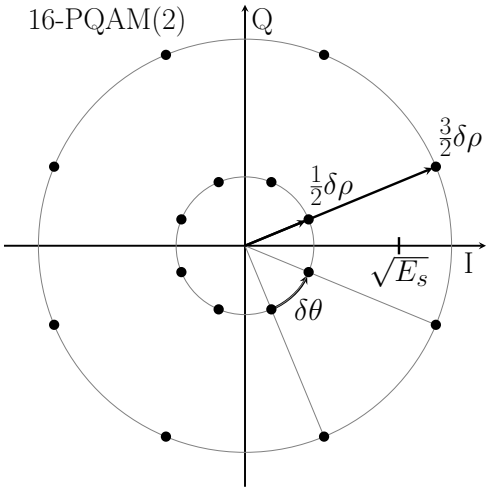

Figure 4.3 – *Illustration of a* 16*-PQAM(*2*) in the complex plane*

In contrast to constellations obtained through numerical optimization [22], modulation schemes defined upon polar-lattices present an analytical expression of signal points expression. It hence results in a plain signal generation at the transmitter. Furthermore, the binary labeling regarding Bit-Interleaved Coded Modulation (BICM) architectures is trivial. In this case, the binary labeling in the polar domain is identical to the labeling in the I/Q plane of a QAM for a rectangular lattice and respectively to a HQAM for a hexagonal lattice. The difference in implementation between the use of a hexagonal and a rectangular lattice to define the constellation is the following. It has been shown previously that the symbol detection is defined as a nearest neighbor search. As a result, this detection for a rectangular polar-lattice relies on simple threshold comparisons in the polar domain. This simple demodulation algorithm can be observed on Figure 4.1c. In addition, the bit LLR values related to a rectangular lattice and necessary to channel decoding can be approximated as piecewise linear functions in the amplitude-phase domain. These two complexity reductions at the receiver are enabled only with the use of a rectangular polar-lattice and not a hexagonal one. In conclusion, a constellation based on a hexagonal polar-lattice, in comparison to a rectangular one, leads to relatively small performance gains – see Figure 4.2a and 4.2b – yet at the detriment of a more complex receiver. Therefore, we propose a modulation scheme based on a rectangular polar-lattice: the Polar-QAM.

It is interesting to mention that state-of-the-art approaches [22] [15] [67] on PN channels shape the constellations toward hexagonal and rectangular polar-lattices. For instance, the representation of the circular-QAM proposed in [67] in the amplitude-phase domain is close to a hexagonal lattice. Further, it has been shown in [67] that the circular-QAM realizes, in comparison to a conventional QAM, performance gains on PN channels. Similarly, it is worth studying the Gray-APSK proposed in [68] to provide a shaping gain for satellite communications. Signal points of the Gray-APSK represented in the amplitude-phase domain nearly describe a rectangular lattice, the amplitudes of signal points are non-linearly distributed though. Thanks to the presented analysis, we can conclude that such modulation scheme should provide valuable performance gains on PN channels. Eventually, the following remark should be pointed out. We have presented here a theoretical analysis based on the signal decomposition in the amplitude-phase domain to optimize the modulation scheme for the GPN channel. This original analysis provides a valuable theoretical framework to design PN robust communication schemes but also to evaluate many of the literature proposals.

4.1.2 Definition of the proposed Polar-QAM

Polar-QAM constellation: The proposed Polar-QAM is defined by the constellation $\mathcal{C}$ illustrated in Figure 4.3. With $m, n \in \mathbb{N}$ and $m \geq n$, the constellation $\mathcal{C}$ is a set of $M = 2^m$ complex points placed on $\Gamma = 2^n \in \{1, 2, 4, \ldots, M\}$ concentric circles, *i.e.* amplitude levels. The average energy of the constellation is denoted E_s. Each of the Γ circles contains M/Γ signal points. Correspondingly, the *minimum angular distance* $\delta\theta$ between two symbols is

$$\delta\theta = \frac{2\pi\Gamma}{M}. \tag{4.3}$$

The phase shift θ_p of the p-th symbol on a circle is described by $\theta_p = \frac{\delta\theta}{2}(2p-1)$. Likewise, the amplitude ρ_q of the q-th circle ρ_q is defined by $\rho_q = \frac{\delta_\rho}{2}(2q-1)$ where $\delta\rho$ is the *minimal radial distance*. It results from this definition of the amplitudes of signal points and from the average symbol energy E_s that the minimal radial distance $\delta\rho$ is given by

$$\frac{\delta\rho}{\sqrt{E_s}} = \sqrt{\frac{12}{4\Gamma^2 - 1}}. \tag{4.4}$$

Then, any PQAM constellation can be entirely defined by two parameters M and Γ respectively the modulation order and shape. Therefore, we use the notation M-PQAM(Γ) to described the constellation

$$\mathcal{C} = \left\{ \frac{\delta\rho}{2}(2q-1) \cdot \exp\left(j \cdot \frac{\delta\theta}{2}(2p-1) \right) \mid 1 \leq q \leq \Gamma, 1 \leq p \leq M/\Gamma \right\}. \tag{4.5}$$

One may remark that some particular cases of the PQAM fall into known modulations: a M-PQAM($M/2$) describes an amplitude-shift keying while a M-PQAM(1) is a Phase-Shift Keying (PSK). The PQAM is a structured definition of an APSK constellation. For the demodulation of the PQAM on the GPN channel, it is relevant to use the proposed detection scheme based on the polar metric. When this demodulation scheme is used, the symbol detection for the PQAM can be implemented with a simple threshold detection in the amplitude-phase domain.

Polar-QAM binary labeling: Nonetheless, the PQAM is not only defined by its constellation but also by its binary labeling. For a given channel, optimizing the symbol mapping in order to minimize the Bit Error Rate (BER) is not trivial and induces a high complexity – *cf.* binary switching algorithm [69]. Thanks to the regular structure of the PQAM, an efficient binary labeling can be proposed in order to achieve robustness and simple demodulation. In a 2^m-ary modulation system, every m bits form a binary word $\boldsymbol{b} \in \{0,1\}^m$. This binary word is modulated by a symbol $s \in \mathcal{C}$ under a mapping rule called constellation labeling μ,

$$\mu : \{0,1\}^m \to \mathcal{C}. \tag{4.6}$$

To minimize the bit error probability, the mapping rule must implement a Gray code. Namely, a Gray code mapping consists in labeling the M points with binary words of length $m = \log_2(M)$ such that the Hamming distance between two nearest points is equal to 1. Subsequently, incorrectly estimating a symbol by one of its nearest neighbors leads to a single bit error. In the case of a M-PQAM(Γ), any binary words $\boldsymbol{b} \in \{0,1\}^{\log_2(M)}$ mapped to a symbol s can be expressed as

$$\boldsymbol{b} = (b_1^\rho, ..., b_{\log_2(\Gamma)}^\rho, b_{\log_2(\Gamma)+1}^\theta, ..., b_{\log_2(M)}^\theta), \tag{4.7}$$

where $\log_2(\Gamma)$ bits are encoded by the amplitude level s_ρ of s, and $\log_2(M/\Gamma)$ bits are encoded by the phase s_θ of s. Therefore, the mapping rule μ may be subdivided into two uni-dimensional rules μ_ρ and μ_θ:

$$\begin{aligned} \mu_\rho &: \{0,1\}^{\log_2(\Gamma)} \to s_\rho, \\ \mu_\theta &: \{0,1\}^{\log_2(M/\Gamma)} \to s_\theta. \end{aligned} \tag{4.8}$$

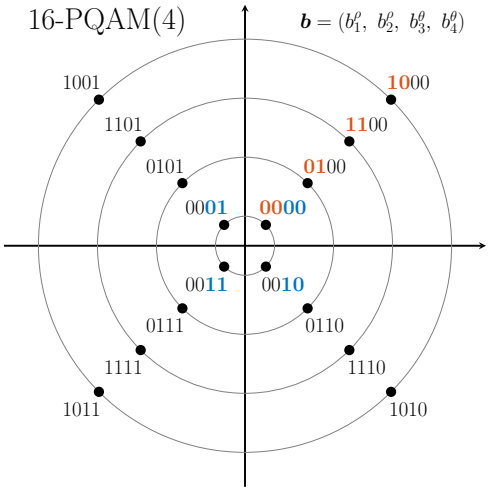

Figure 4.4 – *Binary labeling of a* 16*-PQAM(*4*)*

Uni-dimensional mapping of signal points respecting a Gray code is straightforward and a well-known result. It is worth mentioning that the PQAM constellation has been designed to achieve such efficient binary labeling. Figure 4.4 depicts the binary labeling for a 16-PQAM(4). Conversely, optimized constellations of the literature present no particular structure and lead to complex labeling and poor performance in terms of BER. Besides, the binary labeling of the Polar-QAM allows low-complexity evaluation of the bit LLR. When the PQAM is used with the proposed soft-output demapper based on the polar metric, the soft-bit values can be efficiently approximated with piecewise linear functions. The piecewise linear approximations of the LLR of the $\log_2(\Gamma)$ bits related to the amplitude level present similar expressions to the ones of a QAM constellation, see [70]. While for the $\log_2(M/\Gamma)$ bits encoded on the phase, approximations are similar to a PSK [71]. The evaluation of the bit LLRs based on piecewise linear functions is an important complexity reduction of the receiver. This complexity reduction highlights the benefits of using the PQAM and the proposed demodulation scheme over state-of-the-art solutions, based on numerically optimized constellations. It also emphasizes the relevance of jointly optimizing the modulation and demodulation schemes.

4.1.3 Performance analysis of the Polar-QAM

4.1.3.1 Performance analysis

Bit-error-rate: We use the definition of the PQAM and the expression of the likelihood function to derive the closed-form expression of the SEP. We can approximate the detection error probability $Pr(E)$ by

$$\begin{aligned} Pr(E) &= \frac{1}{M}\sum_{s\in\mathcal{C}} Pr(\hat{s}\neq s|s) = \frac{1}{M}\sum_{s\in\mathcal{C}}\left(1-Pr(\hat{s}=s|s)\right), \\ &\simeq \frac{1}{M}\sum_{s\in\mathcal{C}}\left(1-p\left(-\frac{\delta\rho}{2}<(s_\rho-r_\rho)<\frac{\delta\rho}{2}\right)\cdot p\left(-\frac{\delta\theta}{2}<(s_\theta-r_\theta)<\frac{\delta\theta}{2}\right)\right), \\ &\simeq 2Q\left(\frac{\delta\rho}{2\sigma_n}\right)+2Q\left(\frac{\delta\theta}{2\sqrt{\sigma_\phi^2+\sigma_n^2/E_s}}\right). \end{aligned} \tag{4.9}$$

The latter approximation holds for high SNR and corresponds to the widely used assumption that errors occur on the nearest neighbors of the sent symbol. To simplify the closed form expression in Eq. (4.9), it is assumed that the average detection errors on the phase of symbols occur for an amplitude of $\sqrt{E_s}$

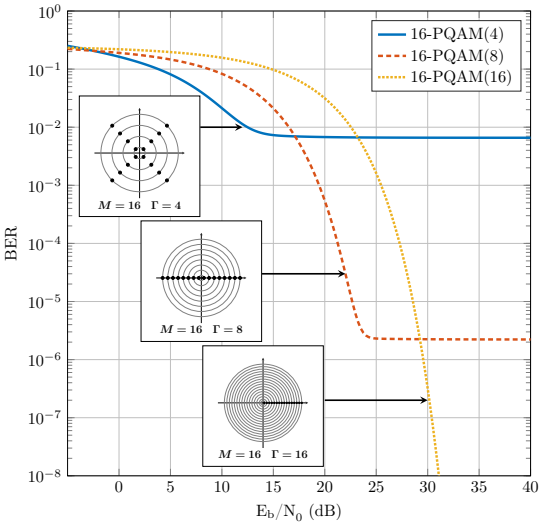

Figure 4.5 – *Analytical BER of a 16-PQAM(Γ) for different modulation shapes* $\Gamma \in \{4, 8, 16\}$ *with* $\sigma_\phi^2 = 1.25 \times 10^{-1}$

which is slightly optimistic. Since the binary labeling implements a Gray code mapping and under the nearest neighbors error assumption, the bit error probability P_{be} may be derived from the symbol detection error probability as

$$P_{be} = \frac{Pr(E)}{\log_2(M)}. \tag{4.10}$$

Let us replace $\delta\rho$ and $\delta\theta$ by their definitions in Eq. (4.3) and (4.4) to express the BER as a function of E_b/N_0, σ_ϕ^2, M and Γ. Hereafter, it is assumed that $T_s = 1$ which results in no loss of generality. The average bit energy $E_b = E_s/\log_2(M)$ and the noise power spectral density $N_0 = 2\sigma_w^2$. Eventually, the BER of a M-PQAM(Γ) can be approximated by the following closed-formed expression

$$P_{be} \simeq \frac{2}{\log_2(M)} \left(Q\left(\sqrt{\frac{6 \cdot \log_2(M) \cdot E_b/N_0}{4\Gamma^2 - 1}} \right) + Q\left(\frac{\pi\Gamma}{M\sqrt{\sigma_\phi^2 + \frac{1}{E_b/N_0} \frac{1}{2 \cdot \log_2(M)}}} \right) \right). \tag{4.11}$$

In the BER expression, the two terms in the addition should be interpreted differently. The first term expresses the probability of misestimating the amplitude level of the received symbol whereas the second term corresponds to mistestimating the phase. Figure 4.5 outlines the analytical BER performance of a 16-PQAM(Γ) for $\Gamma \in \{4, 8, 16\}$ and their respective constellations. As depicted in Figure 4.5, the BER reaches an error floor when E_b/N_0 tends to infinity. This error floor is caused by PN and can be evaluated by

$$\lim_{E_b/N_0 \to \infty} P_{be} = \frac{2}{\log_2(M)} Q\left(\frac{\pi\Gamma}{M\sigma_\phi} \right). \tag{4.12}$$

It is shown in Figure 4.5 and in Eq. (4.12) that the smaller Γ, the higher the error floor. For a PN channel, the error floor of a constellation is caused by several signal points using the same amplitude level and can be lowered by increasing the minimum angular distance. In brief, a large number of amplitude levels Γ entails a low error floor, yet attained at a higher E_b/N_0.

Peak-to-average power ratio: With regard to the Radio-Frequency (RF) power-amplifiers, directly related to the energy consumption of transmitters, the Peak-to-Average Power Ratio (PAPR) is a key performance indicator for any communication system. In the context of the Polar-QAM, the PAPR is

Table 4.1 – *PAPR of the Polar-QAM constellation for different parameter* Γ

Number of amplitude levels Γ	1	2	4	8	16	32
M-PQAM(Γ) PAPR (dB)	0	2.55	3.68	4.23	4.50	4.64

Table 4.2 – *PAPR of the QAM constellation for different modulation order* M

Modulation order M	4	16	64	256
M-QAM PAPR (dB)	0	2.55	3.68	4.23

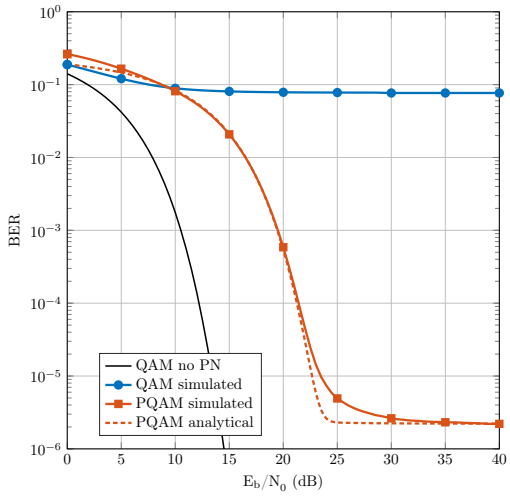

Figure 4.6 – 16-*QAM and* 16-*PQAM*(8) *performance with PN variance* $\sigma_\phi^2 = 1.25 \times 10^{-1}$

given by

$$\frac{\max\limits_{s\in\mathcal{C}} |s|^2}{E_s} = 3 \cdot \frac{2\Gamma - 1}{2\Gamma + 1}. \tag{4.13}$$

It can be noticed that the PAPR is a strictly increasing function of the number of amplitude levels Γ and is not function of the modulation order M. In addition, the PAPR of the Polar-QAM is upper-bounded by 4.77 dB. Table 4.1 and 4.2 present the value of the PAPR for the Polar-QAM and QAM constellations with different configurations. As previously mentioned increasing Γ does improve the PN robustness at the detriment of a higher PAPR. Finally, the closed-form expressions of the BER and the PAPR of the Polar-QAM provide new and valuable results for the specification and analysis of future systems. The theoretical analysis of such important performance metrics is not possible for the numerically optimized constellations of [22] or the state-of-the-art modulation proposed in [15]. This further motivates the use of a structured constellation.

Numerical simulations results: The results of numerical simulations for uncoded systems are presented in Figure 4.6. The BER performance of the QAM and PQAM are compared for $M = 16$ and $\sigma_\phi^2 = 1.25 \times 10^{-1}$. The demodulation with the polar metric detector is implemented. Results demonstrate the performance gain achieved by the PQAM constellation over a conventional QAM on a strong GPN channel. The QAM constellation presents a high error floor which results from the low angular distance between its signal points. Nonetheless, it is worth mentioning that this performance gain is achieved to the detriment of the PAPR. A 16-QAM presents a PAPR of 2.55 dB while the 16-PQAM(8) exhibits a 4.23 dB PAPR. It is also illustrated that the analytical expression of the BER for a PQAM is

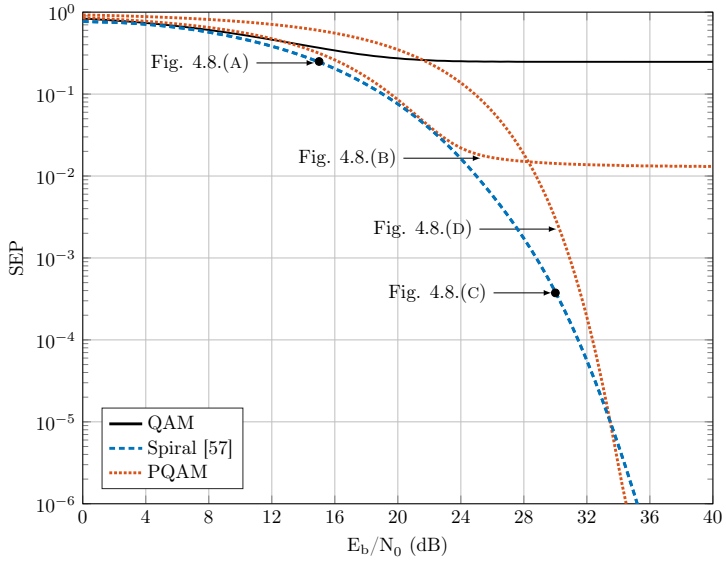

Figure 4.7 – *Comparison of PQAM to the spiral constellation [15] with* $M = 64$ *and* $\sigma_\phi^2 = 10^{-1}$

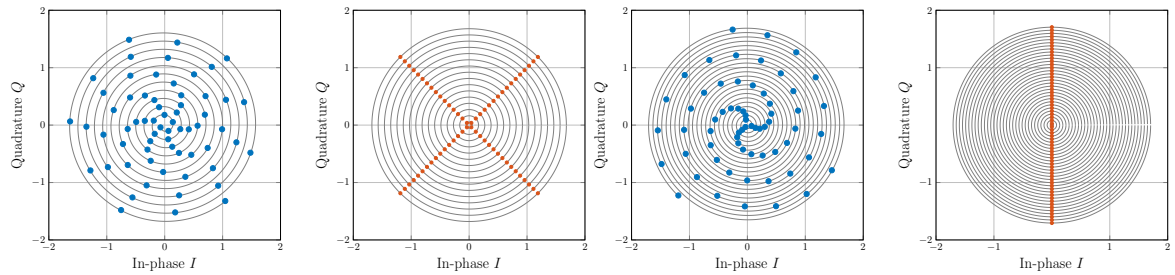

(A) *Spiral,* $E_b/N_0 = 15$ *dB* (B) 64-*PQAM*(16) (C) *Spiral,* $E_b/N_0 = 30$ *dB* (D) 64-*PQAM*(32)

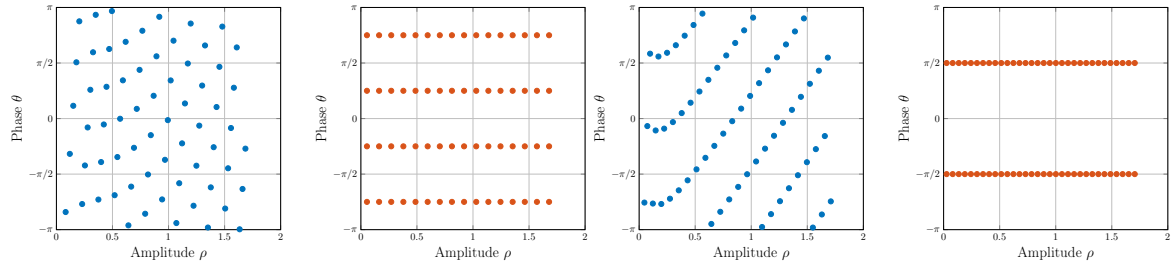

(E) *Spiral,* $E_b/N_0 = 15$ *dB* (F) 64-*PQAM*(16) (G) *Spiral,* $E_b/N_0 = 30$ *dB* (H) 64-*PQAM*(32)

Figure 4.8 – *Spiral and PQAM constellations in* ℓ^2 *(first row) and in* p^2 *(second row)*

tight to the simulation results. Nevertheless, the optimistic consideration made in Eq. (4.9) is to explain the slight difference between the analytical expression and the simulation results.

4.1.3.2 Comparative studies

State-of-the art-constellation: The definition of the Polar-QAM is close to the one of the Gray-APSK, proposed in [68] to provide a shaping gain for satellite communications and not to achieve PN robustness. Both modulation schemes use structured APSK and two independent Gray mapping on the phase and on the amplitude, and hence, demonstrate similar performance. The difference between these constellations is that the amplitudes of Gray-APSK signal points are nonlinear. We have proposed the Polar-QAM and derived its analytical and numerical performance analysis in the context of PN chan-

nels. For this reason, we compare in this paragraph the performance of the proposed solution to the one of the state-of-the-art solution proposed in [15] on constellation optimization for the GPN channel: the *spiral* constellation. Nonetheless, interested readers may refer to [15] which evaluates the performance of the Gray-APSK. Figure 4.7 compares the SEP performance of the PQAM and the spiral constellation for $M = 64$ and $\sigma_\phi^2 = 10^{-1}$ demodulated with a polar metric receiver. It is shown that the spiral constellation demonstrates a performance gain in comparison to the PQAM at the expense of a transceiver complexity increase. The spiral constellation presents a semi-analytical description: the modulation points are defined with a closed-form expression upon an optimized modulation shape parameter $f_s \in \mathbb{R}_{\geq 0}$. For each SNR, the spiral constellation requires the optimization of the parameter f_s through important Monte-Carlo simulations to maximize the achievable information rate of the modulation. Conversely to this, the modulation shape parameter Γ of the Polar-QAM belongs to a small finite set; and therefore, adapting the modulation scheme to the channel is straightforward. Though a simple and efficient symbol detection rule is proposed in [15], the binary labeling of the spiral constellation entails a complex LLR evaluation which cannot be efficiently approximated. Figure 4.7 precisely illustrates the benefits of the proposed solution: near-optimal performance are achieved with a simple implementation. By way of illustration, Figure 4.8 presents the Polar-QAM and spiral constellations in the I/Q plane and in the amplitude-phase domain. It can be observed on Figure 4.8e that the definition of the spiral constellation is actually closed to a hexagonal polar-lattice in the amplitude-phase domain. The Polar-QAM and the spiral constellations demonstrate similar PAPR values. For the spiral constellation optimized for $E_b/N_0 = 30$ dB the PAPR is 4.66 dB while the PAPR of the 64-PQAM(32) is 4.64 dB.

Complexity of implementation: It is clear that numerically optimized constellations, and more generally speaking generalized APSK modulations, are difficult to demodulate due to the complex nature of the Voronoi regions. Conversely, using the proposed Polar-QAM and polar metric detector, the symbol detection can be implemented with a simple Cartesian-to-polar transform followed by an independent component processing with threshold detection. Considering a soft-decision decoding, with a probabilistic demapper, the Polar-QAM is even more beneficial. On one hand, non-structured constellations leads to multi-dimensional processing involving all signal points. This leads to a wide literature to reduce decoder complexity, see [72] or [73]. On the other hand, with the Polar-QAM, the commonly used log-sum approximation – *e.g.* widely considered for QAM demapping – can be implemented after the Cartesian-to-polar transform. In addition, the binary labeling and structure of the Polar-QAM enables efficient approximations of the bit LLR values with piecewise linear functions, similar to the ones presented in [70] and in [71], and therefore leads to a significant complexity reduction of the decoder. This is an important benefit of using the PQAM and the polar metric. In comparison to state-of-the-art techniques, it offers significant complexity reductions of the transceiver.

4.1.4 Conclusion on modulation for phase noise channels

We have studied the optimization of the modulation scheme for the GPN channel. A mathematical framework, based on a signal decomposition in polar coordinates, has been presented to design robust constellations and also to evaluate state-of-the-art solutions. It has been shown that a constellation defined upon a lattice in the amplitude-phase domain is robust to PN and leads to a low-complexity implementation. Thereupon, we have proposed the Polar-QAM scheme. We have compared the proposed modulation to conventional and state-of-the-art solutions on different performance metrics such as the PAPR, the BER. Our results highlight the important performance gains realized by the Polar-QAM in comparison to conventional schemes. In contrast to state-of-the-art optimized constellations, the advantage of the proposed solution is that near-optimal performance is achieved with significant complexity reductions of the transceiver. Altogether, we have shown that the transmission schemes optimized

for PN channels have the following properties. Optimized schemes expressed in the amplitude-phase domain are highly similar to the commonly used ones for the complex AWGN channel represented in the I/Q plane. This property has been highlighted for multiple transmission techniques including modulation, estimation and detection.

In this section, our results have highlighted that the proposed modulation scheme leads to valuable performance gains in the presence of PN. Nevertheless, an important task remains to be addressed: selecting the physical layer parameters with regard to the channel conditions. By means of illustration, the modulation order and the constellation shape should be chosen according to the thermal and PN variances in order to maximize the system performance. The next section tackles this problem and outlines link adaptation strategies. Furthermore, the following section also investigates a second untreated topic of significant practical interest: the comparison between the proposed communication schemes and the conventional ones in a realistic sub-THz scenario. Hence, results of system-level simulations are presented considering a high-capacity backhaul in a city downtown and the integration of a state-of-the-art channel coding scheme.

4.2 System-Level Optimizations and Performance Analyses

The purpose of this second section is to extend the previous study with more practical considerations. Our main objective is to provide a more comprehensive performance assessment of the proposed schemes by considering their application in sub-THz bands. This section investigates system-level optimizations and performance analyses. We first present a new link adaptation technique particularly adapted to the wide spectrum covered by envisaged sub-THz applications. Implemented to maximize the spectral efficiency, commonly used link adaptation strategies adapt the modulation order and the coding rate to the SNR. In contrast, we propose to adapt the modulation order and the modulation shape as well as the coding rate to the SNR and PN variance. Thanks to the regular structure of the Polar-QAM, the proposed modulation scheme can be easily adapted to the SNR and PN variances, and hence, provides a general solution to various channel conditions. Next, the integration of a state-of-the-art channel coding scheme is considered and the achievable information rate is assessed. Finally, the results of system-level simulations are presented considering a high-capacity backhaul scenario in a North-American city downtown. Recent works on communication design for PN channels limit their performance analysis to the common performance indicators: mutual information, Symbol Error Rate (SER), achievable information rate, *etc.* Thanks to our collaboration with Siradel, and their expertise on deterministic channel predictions, we have been able to extend the performance analysis to more realistic simulations. These simulations are based on ray-tracing channel predictions using accurate LiDAR point cloud and a realistic link budget. Overall, it is shown that the communication throughput is severely limited by PN when using conventional modulation schemes over sub-THz channels. Conversely, the proposed solutions can achieve high spectral efficiency communications even in the presence of strong PN.

4.2.1 Link adaptation

In order to maximize the spectral efficiency, practical communication systems implement adaptive modulation schemes. Namely, the modulation order is set with regard to the quality of the channel. In particular, a link adaptation scheme is highly valuable for sub-THz communications. Regarding contemplated applications for terrestrial, a base station is to address several users' equipment with different qualities, and thus, different SNR and PN levels. Moreover, for channel-bonding systems, the aggregated spectrum may be wide enough to exhibit significant differences between oscillators performance in higher and lower frequencies. In the case of the Polar-QAM, we propose a new link

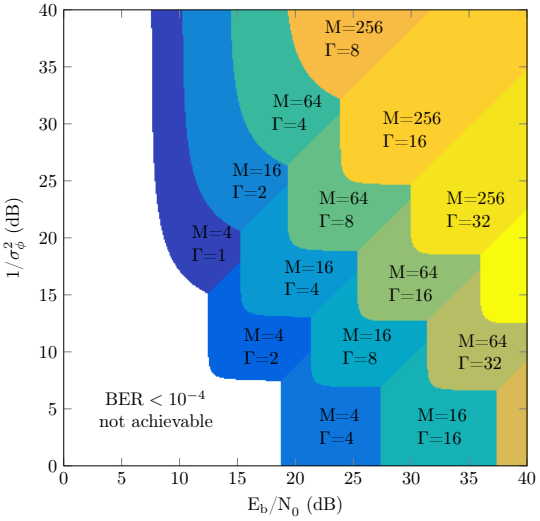

Figure 4.9 – *PQAM parameters M and Γ with the highest spectral efficiency such that BER$< 10^{-4}$*

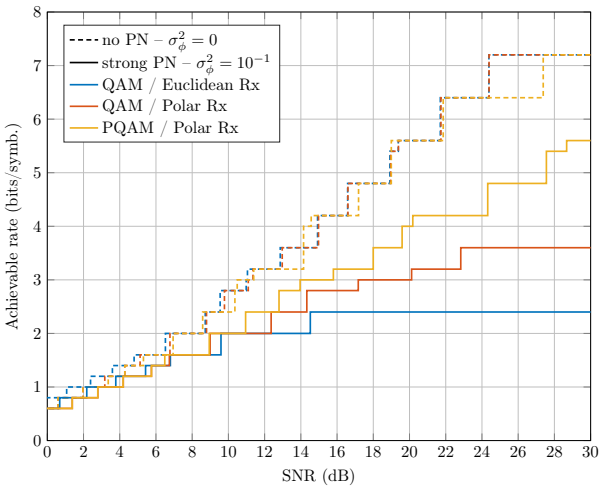

Figure 4.10 – *Highest achievable rate given the SNR, the PN level and the modulation/demodulation strategy*

adaptation strategy which is developed beyond adjusting the modulation order M of conventional techniques, by also adapting the modulation shape with parameter Γ. In particular, the introduced theoretical analysis of the performance of the Polar-QAM is valuable for the link adaptation. We can use the analytical expression of the BER in Eq. (4.11) to determine the best set of parameters (M, Γ) to achieve the highest spectral efficiency while maintaining the BER below a fixed threshold. Figure 4.9 presents the PQAM parameters M and Γ for a given PN variance σ_ϕ^2 and E_b/N_0 such that the spectral efficiency is maximized and the BER remains inferior to 10^{-4}. This link adaptation strategy requires a channel estimation scheme which has been previously introduced in Sec. 3.2.4. It should be emphasized that the Polar-QAM enables a simple link adaption strategy. In contrast to state-of-the-art solutions, the modulation order and shape parameters (M, Γ) belong to small finite sets, and therefore, adapting the modulation scheme to the channel conditions is straightforward.

4.2.2 Physical layer performance assessment

Figure 4.10 presents the results of numerical simulation for coded systems. It outlines the achievable rate in bit/symbol for $\sigma_\phi^2 = 10^{-1}$ and a Low-Density Parity Check (LDPC) code. Three modulation/demodulation schemes are considered: QAM with Euclidean detector, QAM with polar detector

Table 4.3 – *Simulation parameters*

Carrier Frequency	f_c	150 GHz
Channel bandwidth	B	1 GHz
Allocated bandwidth	B	0.8 GHz
Thermal noise	N_0	-174 dBm
Noise figure	N_f	10 dB
Transmit power	P_t	30 dBm
Tx/Rx antenna gain	g_0	25 dBi
Implementation loss	L	2 dB

and PQAM with polar detector. The FEC scheme is based on the 5G New Radio (5G-NR) LDPC and is implemented with an input packet size of 1500 bytes and a coding rate ranging from 0.3 to 0.9. The communication performance has been characterized to determine the best set of parameters: coding rate, modulation order M and modulation shape Γ given the SNR, the PN variance. A PER of 10^{-2} is targeted for numerical evaluations. This quality of service gives reliable transmission with low throughput penalty when automatic repeat request scheme is implemented. It avoids the design of low error floor and reliable FEC scheme. This level of PER is widely considered in modern wireless communication standards [57]. The PN variance $\sigma_\phi^2 = 10^{-1}$ rad^2 corresponds to an oscillator spectral density K_0 of -100 dB for a bandwidth of 1 GHz. These simulation results clearly highlight the benefits of using optimized modulation and demodulation schemes to implement high-rate communication systems impaired by PN. In the low SNR regime or without PN, the optimized schemes exhibit minor performance losses on the achievable rate. These losses result from the high-SNR and strong PN assumptions made to derive the polar metric and to construct the PQAM. These results confirm that at low SNR, and even with strong PN, conventional modulation schemes such as QAM should be used. Furthermore, it should be mentioned that the probabilistic bit values derived for the PQAM upon the polar metric decision rule present non-uniform protections. With regard to the SNR and PN variance, the bits mapped on the phase and on the amplitude experience different levels of protection. A joint optimization of the modulation and the channel coding (*e.g.* similar to multi-level coding techniques) could exploit the latter property to further enhance the demodulation performance and increase the achievable rate.

4.2.3 System-level numerical simulations

In this paragraph, the performance of the proposed PN robust schemes, the polar receiver and the P-QAM, are further assessed through system-level simulations in a sub-THz scenario. These numerical evaluations assume a city center environment (from the San José, USA, 3D model) while targeting a high capacity mesh backhaul. The system performance is characterized for an outdoor mesh backhaul application, which could be exploited to feed an ultra-broadband mobile access network or fixed wireless access network. The sub-THz devices are supposed to be installed on lampposts, located along the streets at 8 meters above the ground, in order to transport the data streams from a fiber point of presence to dense local high-speed access points that either provide mobile or fixed wireless access typically at a lower frequency. The antennas of the sub-THz devices are considered with 6° beamwidth, 25 dBi maximum gain. The antenna beam is supposed to be perfectly aligned on the dominant propagation path, which is either the direct Line-of-Sight (LoS) path, a reflected path, or an attenuated path. Other transmission parameters are given in Table 4.3. Additional justifications regarding the selection of these system parameters and references to state-of-the-art systems can be found in Chapter 1. The propagation paths and losses are predicted from the ray-tracing tool. The throughput

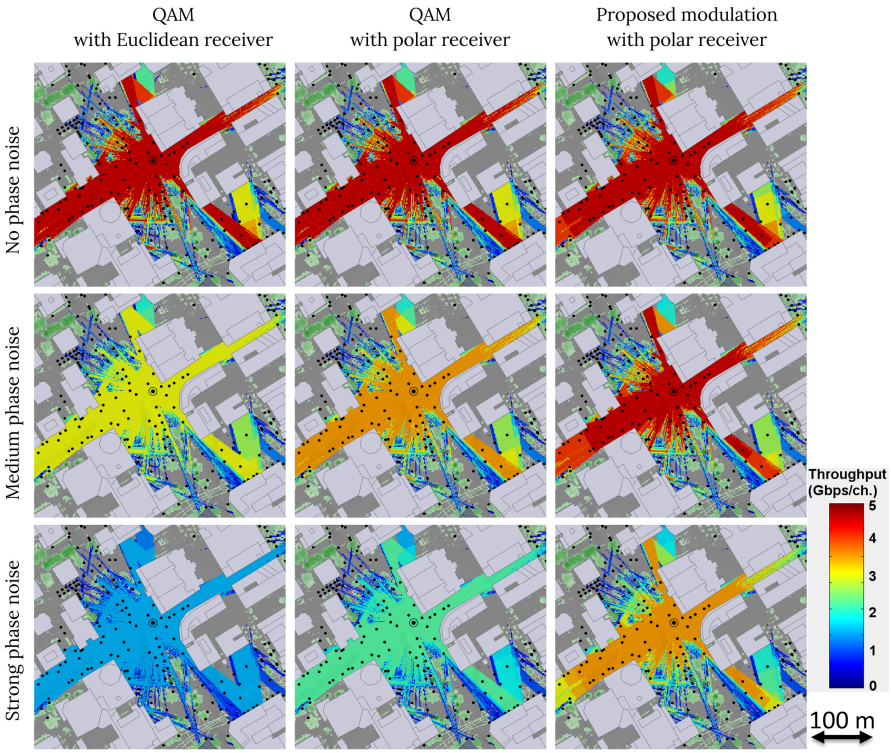

Figure 4.11 – *Throughput heat maps for a city center when impaired by PN*

of each calculated link is obtained from the estimated SNR which is mapped to the spectral efficiency of the considered modulation scheme using the previous performance assessment in Sec. 4.2.2. In other words, the throughput evaluation relies on precomputed direct correspondences (*i.e.* a lookup table) between the channel conditions (*i.e.* SNR and PN variance) and the physical layer parameters (*i.e.* modulation scheme, coding rate, and resulting spectral efficiency). It should be noticed that the throughput is estimated for a channel of 1 GHz bandwidth. Thereupon, a channel-bonding scheme could increase the aggregated throughput and allow to benefit from the large spectrum available in the sub-THz bands. The choice of a channelization of 1 GHz is motivated by the current technology of analog-to-digital converters [74].

The heat maps in Figure 4.11 illustrates how the lamppost-to-lamppost link performs depending on the distance, the propagation condition, the PN level and the selected modulation scheme. The illustrated environment may be characterized as a square in the middle of a dense urban center with medium tree density. The peak throughput per channel is computed between two aligned sub-THz devices; the first one at the center of the figure; the second one at any pixel of the map. Note that the real lamppost locations, where this second device could precisely be positioned, are shown by black dots. The connectivity is strongly affected by building and foliage obstructions, while LoS propagation and strong clear reflections leads to the best performance. These throughput heat maps demonstrate that optimizing the modulation and demodulation schemes for PN channels results in significant performance gains for future sub-THz systems. These numerical simulations have been carried out with the collaboration of Siradel, also a member of the ANR project BRAVE. Precisely, Yoann Corre and Grégory Gougeaon from Siradel have been in charge of the deterministic channel predictions using ray-tracing and LiDAR point cloud. Thereupon, we have mapped the estimated SNR to the corresponding spectral efficiency using the proposed communication schemes and the presented link budget.

4.2.4 Beyond memoryless phase noise

The phase shift induced by the propagation channel must be estimated and then corrected. Generally speaking, pilot-based estimation schemes are considered and lead to a spectral efficiency loss. Moreover, the oscillator at the receiver may not be synchronized to the carrier frequency of the transmitter resulting in a Carrier Frequency Offset (CFO). If the CFO is not perfectly estimated and compensated, then a residual frequency synchronization error corrupts received symbols with a cumulative phase error. This phase error is increasing between reference pilots and phase corrections, and thus, can be modeled as cumulative PN. Besides, it has been stated in the previous chapter that oscillator PN also demonstrates a cumulative nature. For these reasons, the cumulative PN in certain systems might not be negligible or not perfectly compensated using reference signals. These impairments affecting practical systems lead to performance degradation and motivate the use of a differential modulation. It should be mentioned that the use of differential M-QAM with $M > 4$ is not simple and remains challenging to design. In contrast to conventional solutions or state-of-the-art constellations, the proposed modulation scheme has the advantage of being straightforwardly compatible with a differential scheme. We denote DPQAM the Differential implementation of the PQAM. The information encoded upon the amplitude of symbols remains identical whereas the phase information is encoded in the relative phase difference between two symbols. Subsequently, the DPQAM is not subject to the initial phase shift of the channel. We propose the DPQAM to provide a high-order modulation scheme with an improved robustness to the cumulative PN and residual CFO. The performance analysis of the DPQAM has been pursued but are not presented in this manuscript. Nevertheless, one may refer to our previous work [31] which assessed analytically and numerically the performance degradation due to cumulative PN for phase modulated signals. In addition, we have proposed in [31] a link adaptation technique to select the most robust modulation between a coherent or different scheme in the presence of cumulative PN.

4.3 Synthesis and Discussions

Conclusion: In this chapter, we have investigated the optimization of transmission algorithms for strong PN channels. In the first section, we have proposed the Polar-QAM, a PN robust modulation scheme with simple practical implementation. Lattices in the amplitude-phase domain can be used to define structured constellations with enhanced performance on PN channels. Moreover, structured constellations, in contrast to numerically optimized ones, achieve near-optimal performance with significant complexity reductions of the transceiver. In the second section, we have assessed the performance gains of the proposed modulation and demodulation schemes using deterministic ray-tracing in a backhaul scenario. It has been notably pointed out that the communication throughput when using conventional transmission techniques is severely limited by PN. Conversely, our proposals achieve high information rates even in the presence of strong PN. The material of this chapter has been partly published in two conference papers [31], [32]; one journal article [26]; and one patent [33], see full citations below. In addition, the proposed optimized schemes have also been exploited to assess the performance of another sub-THz application: an indoor mesh backhaul in D-band. This study has been led by Siradel and its results have been published in [75]

Perspectives: Regarding the modulation scheme for strong PN channels further performance enhancement are possible. The use of hexagonal polar-lattice or Gaussian constellation shaping (either probabilistic or geometric) could improve the communication performance. Still, such performance gains are to be realized at the detriment of a complexity increase of the transceiver implementation. Besides, channel coding schemes could be further optimized for strong PN channels. It has been remarked that information sent on the amplitude and on the phase of symbols experience different levels of protec-

tion. Subsequently, techniques similar to multi-level coding can be implemented to achieve additional performance gains. The work in [76] could be easily adapted to our propositions since it investigates multi-level coding for regular APSK. We have shown that modulation and demodulation schemes for strong PN channels exploit the polar coordinates of transmitted symbols. For this reason, transceivers with a polar RF architecture are relevant for strong PN channels and could be studied for application in sub-THz bands. Polar transceivers send the amplitude and phase signals as independent streams. We use here the term polar transceiver to refer to the combination of a polar transmitter and a polar receiver. Polar transmitters are a well-known implementation [77], whereas polar receivers are less common [78]. Eventually, any findings related to algorithm design should be confronted to experimental validations. Upcoming research projects on sub-THz communication systems are oriented in this direction, which would provide valuable complementary results.

Applications and limitations: As mentioned multiple times, coherent transceivers using sub-THz bands are contemplated for high-capacity backhauling applications. The research presented in this chapter has been conducted with regard to this scenario. Our findings contribute to the development of spectral-efficient physical layers for sub-THz communications. More generally, our contributions can be used for any PN limited communications system. For instance, the next generation of mobile networks (5G) envisages the exploitation of millimeter-wave (mm-Wave) frequency bands, known to be impacted by PN. Optical communication systems are also severely impaired by PN. Still, the scope of our contributions is limited to single-carrier modulation and channel-bonding systems in LoS environments. It does not include multi-path channels with rich environment nor multi-carrier modulation. Readers interested in signal processing optimization for multi-carrier modulation impaired by PN may refer to [21]. In addition, it should be recalled that the discrete-time symbol model used in this chapter is simplistic. This model to be accurate requires up-sampling at the receiver. Otherwise, a SNR penalty loss might be observed. Although it is mentioned that a large power amplification is required, the effects of amplifier nonlinearities has not been considered in this study. The power-amplifier nonlinearities and other RF impairments (*e.g.* I/Q imbalance) can affect the system performance which could be assessed in further studies.

First-authored contributions

[33] S. Bicaïs, J.-B. Doré, and J. L. Gonzalez Jimenez, "Digital High-Order Modulation Scheme Robust to Phase Noise," Patent, Mar. 2019

[26] S. Bicaïs and J.-B. Doré, "Design of Digital Communications for Strong Phase Noise Channels," *IEEE Open Journal of Vehicular Technology*, vol. 1, pp. 227–243, 2020

[31] S. Bicaïs, J.-B. Doré, and J.-L. Gonzalez Jimenez, "Adaptive PSK Modulation Scheme in the Presence of Phase Noise," in *2018 Signal Processing Advances in Wireless Communications (SPAWC)*, June 2018

[32] S. Bicaïs, J.-B. Doré, G. Gougeon, and Y. Corre, "Optimized Single Carrier Transceiver for Future Sub-TeraHertz Applications," in *2020 45th International Conference on Acoustics, Speech, and Signal Processing (ICASSP)*, Barcelona, Spain, May 2020

4.4 Towards Dedicated Architectures

The main contribution of this part of the manuscript is to propose a comprehensive optimization of the communication schemes for strong PN channels. We have investigated and cross-correlated the

design of multiple communication schemes including the constellation, the binary labeling, the symbol detection, the soft-output demapper, and the link adaptation strategy. To the best of our knowledge, such extensive optimization has not been addressed in the literature. Moreover, many works on communication design for PN channels are either based on i) complex numerical optimizations; or on ii) semi-analytical approaches – optimizing a reduced set of parameters. These approaches lead to complex practical implementations. In contrast, our work is supported by an original theoretical framework, based on the signal decomposition in the amplitude-phase domain. It provides analytical tools to design PN robust communications. Efficient PN modeling and appropriate signal representation have been the two cornerstones of our research. It has been demonstrated that the optimum transmission schemes for the GPN channel represented in the amplitude-phase domain are highly similar to the commonly used ones for the complex AWGN channel in the I/Q plane: *e.g.* the modulation, the demodulation, and the estimation of channel parameters. Our propositions have been compared to conventional and state-of-the-art techniques on key performance indicators and on a realistic sub-THz scenario. The results of numerical simulations show that optimized schemes system performance can greatly enhance system performance even in the presence of strong phase impairments. Poor performances of high-frequency oscillators, causing strong phase impairments, can be considered as no longer a critical and limiting factor. Overall, we have illustrated that using dedicated communication algorithms enables to implement spectral-efficient communications with relaxed constraints on the RF architecture. Our findings contribute to the development of spectral-efficient physical layers for future sub-THz wireless communication systems.

We have shown in this part of the manuscript that coherent I/Q transceivers can achieve high communication throughput in sub-THz bands. To further increase the spectral efficiency, spatial multiplexing could be used with Multiple-Input Multiple-Output (MIMO) systems. Still, usual MIMO techniques (precoding, beamforming, detection) suffer from the strong phase impairments and LoS environments of sub-THz communications. The design of new and adapted spatial multiplexing techniques is a relevant topic to investigate for the development of spectral-efficient physical layers in sub-THz bands. As mentioned in the Prologue of this manuscript, some of the envisaged sub-THz applications have strong complexity and energy constraints and necessitate low-complexity physical layers. Coherent I/Q transceivers are an efficient method to realize high-rate communications, yet require complex optimizations and high-quality RF components. And more generally, coherent I/Q transceivers are more suited to spectral-efficient applications in sub-THz bands rather than the low-complexity ones. To develop low-complexity communication systems in sub-THz bands, we investigate in the next part the design of dedicated architectures for sub-THz applications.

No longer targeting spectral efficiency, our objective is from now on the development of low-complexity physical layers readily implementable in sub-THz frequencies. To put it differently, we are not anymore interested in adapting an existing technology with software optimizations to the sub-THz bands. Rather, we study the use of dedicated systems with intrinsic hardware considerations of the specific sub-THz characteristics. Therefore the following part is dedicated to our investigations and proposals on the design of dedicated architectures for sub-TeraHertz communications. In the previous study, signal processing optimizations have been designed to mitigate the impact of oscillator phase impairments. Conversely, in the following, we consider transceivers using envelope modulation and detection, inherently robust to phase impairments. More specifically, two major challenges related to non-coherent sub-THz transceivers are addressed in the next part: increasing the communication throughput with spatial multiplexing, and relaxing the implementation constraints on analog-to-digital converters in wideband transceivers.

Part III

Propositions of Dedicated Architectures

Chapter 5

MIMO Systems with Energy Detection Receivers

In the previous part, we have studied the optimization of coherent transceivers to realize spectral-efficient communications in sub-THz bands. Our findings lie in the dirty Radio-Frequency (RF) paradigm in the sense that digital signal processing techniques have been proposed to mitigate RF impairments of sub-THz systems. It has been notably shown that efficient signal processing techniques, at transmitter side and receiver side, is performed using polar coordinates. This observation motivates the use of new transceiver architectures such as polar RF transceivers, but also highlights that In-phase/Quadrature (I/Q) coherent transceivers may not be particularly suited to sub-THz applications. The main drawback of coherent architectures in sub-THz bands is that they require some high-quality RF components: stable oscillators, high sampling rate converters, and large power amplification. Therefore, I/Q transceivers cannot be considered as a cost-efficient solution and is difficult to implement in embedded systems such as users' equipments. This is not particularly problematic for high-capacity backhaul applications in sub-THz bands, yet it is an important issue for the envisaged device-to-device communications or the enhanced hot-spot scenario. For these reasons, in this part, our design paradigm changes from a spectral-efficient to a low-complexity physical layer. The considered communication systems are no longer characterized by their band-limited regime but rather by a wideband regime in which the main constraint is the complexity of the receiver. In the following, we investigate the mitigation of specific sub-THz impairments not only through software optimizations (optimized digital signal processing) but also with initial hardware considerations (dedicated RF architectures). Subsequently, we consider non-coherent receiver architectures for their inherent robustness to Phase Noise (PN) and their simple implementation, even at high carrier frequencies. The first communication systems implemented in sub-THz frequencies used non-coherent transmission schemes, in particular impulse radio and envelope detectors, *e.g.* [16]. Since then, numerous demonstrators have been developed for sub-THz communications using envelope detection because it can be easily implemented at high carrier frequencies, and in the end, is a well-mastered technology. The use of high-rate impulse radio appears to be relevant for contemplated sub-THz applications in which complexity is limited. Nevertheless, there is a significant gap between the throughput achieved by current pulse-based demonstrators and the theoretical capacity [64] [79] of non-coherent channels, and hence, still room for improvement.

The spectral efficiency is quite limited when pulse-based modulation schemes are used. Then, we can mention two possible solutions to achieve high-rate communications with non-coherent transceivers: ***i) using extremely large bandwidths***. In that case, embedded converters are subject to severe constraints and the analog-to-digital conversion limits the width of the aggregated band. One way to alleviate the constraints on converters is the use of sub-band channelization (channel-bonding). This type of architecture requires the challenging implementation of efficient filter-bank with energy splitter and bandpass filters [24]. This solution has been selected by the IEEE 802.15.3d interest group for high-rate Wireless Local Area Networks (WLAN) in sub-THz frequencies. As a complement or an alternative to channel-bonding, we investigate in Chapter 6 the parallelization of non-coherent sub-THz

receiver in order to relax the implementation constraints on converters; ***ii) spatial multiplexing***. When the objective is to increase the communication throughput, it is straightforward to consider the use of Multiple-Input Multiple-Output (MIMO) systems to benefit from spatial multiplexing. Spatial multiplexing consists in making multiple signal streams orthogonal to each other by spatially separating them. Using multiple antennas at the transmitter and receiver sides, the throughput of MIMO systems can be increased using a fixed band. Nevertheless, spatial multiplexing gains can be severely limited in sub-THz bands by the spatial correlation between the system channels. With propagation channels being largely dominated by the Line-of-Sight (LoS) component and transceivers using directive antennas, the channels of a MIMO system in sub-THz frequencies can be strongly interfering.

This chapter is entirely dedicated to the study of non-coherent spatial multiplexing in sub-THz frequencies. We present the design and performance analysis of MIMO systems using energy detection receivers for future sub-THz applications. This chapter begins with a brief summary of our contributions. We then outline the system model and derive the distribution of received symbols. Thereupon, the design of the detection algorithm is addressed and the two proposed detectors are presented. The performance analysis is next carried out through numerical simulations modeling an indoor wireless link in sub-THz bands.

5.1 Introduction

Intentions: In this chapter, our purpose is to design high-rate non-coherent sub-THz systems by using spatial multiplexing. We consider a pulse-based single-carrier communication system using envelope modulation at the transmitter and envelope detection at the receiver. The envelope of the received signal is extracted with an energy detector by integrating the square of the received signal over a symbol duration. Subsequently, the spectrum of the communication signals is described with a double sideband representation.

Related works: Let us now briefly review some of the existing work and literature related to our objective. Transceivers based on energy detection have been extensively studied for systems with a single transmit antenna and multiple receive antennas, see [80] and references therein. Nevertheless, these works have been conducted for reliability purposes and not for multiplexing. With regard to our objective, the work in [81] and [82] is particularly relevant. It studies MIMO systems with amplitude detection receivers and has shown that they can exploit spatial multiplexing to increase their spectral efficiency. Our study in this chapter pursues the work of [82] by evaluating and analyzing the system performance in a sub-THz scenario. In [82], the channel is built from independent and identically distributed Gaussian entries modeling a rich multipath environment. In contrast to [82], we assume that each spatial stream is transmitted with a directive antenna on a LoS channel. Subsequently, the channels are strongly correlated, and moreover, the resulting interference is nonlinear due to the energy detection at the receiver. Since we study a nonlinear MIMO channel, conventional techniques cannot be used. The strong and nonlinear interference between channels represents a significant challenge to implement spatial multiplexing with non-coherent transceivers in sub-THz frequencies. In the rest of this chapter, we are interested in achieving this objective.

Summary: The contributions of this chapter are the following. First, we derive the model for MIMO systems using energy detection receivers in sub-THz bands. Second, the design of the receiver detection algorithm is investigated. We derive the joint Maximum Likelihood (ML) detector corresponding to the studied nonlinear MIMO channel using a Gaussian approximation. In addition, we propose an original and efficient detector based on neural networks, which does not need any knowledge or assumption

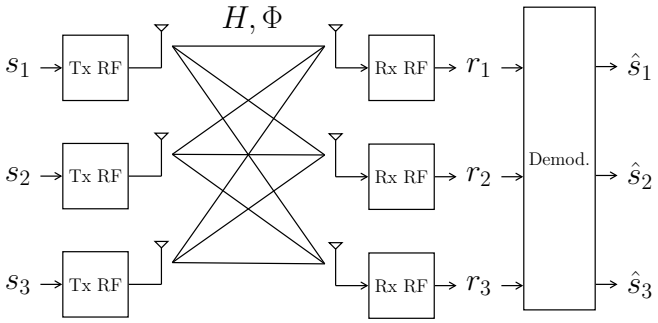

Figure 5.1 – *Block diagram of a* 3×3 *MIMO transceiver*

of the channel. We also detail the differences between state-of-the-art detection methods and the two proposed detectors. Third, the system performance is evaluated through numerical simulations. We introduce a realistic scenario modeling a fixed indoor wireless link in the D-band at 145 GHz. The integration of a channel coding scheme is considered, and more specifically, the use of a short-packet Bose–Chaudhuri–Hocquenghem (BCH) code to ensure a low-complexity decoder. Our results show that low-error rate communications can be achieved with strong spatial interference between channels using the proposed demodulation algorithms. The main contribution of this work is to demonstrate that spatial multiplexing with non-coherent sub-THz transceivers can be realized on strongly correlated LoS channels.

5.2 System Model

We consider in this chapter a MIMO communication system as illustrated in Figure 5.1 with N_t transmit antennas and N_r receive antennas and $N_t \leq N_r$. The propagation channel is described by two $N_r \times N_t$ matrices: $H = (h_{k,n})$ and $\Phi = (\varphi_{k,n})$ where $h_{k,n}^2$ and $\varphi_{k,n}$ denote respectively the propagation gain and phase shift of the channel for signals transmitted on the n-th Tx RF chain and received on the k-th Rx RF chain. To refer to this channel, we adopt hereafter the symbolic notation $n \to k$. In addition, it is of interest to express the propagation gain for channel $n \to k$ as $h_{k,n}^2 = g_{k,n}^{\text{Tx}} \cdot l_{k,n} \cdot g_{k,n}^{\text{Rx}}$ to highlight the influence of the antennas directivity gains $g_{k,n}^{\text{Tx}}$, $g_{k,n}^{\text{Rx}}$ and the path loss $l_{k,n}$. Let the column vectors $\boldsymbol{s} = (s_1 \ \dots \ s_{N_t})^\intercal$ and $\boldsymbol{r} = (r_1 \ \dots \ r_{N_r})^\intercal$ denote the sent and received symbols. The transceiver uses envelope modulation at the transmitter and energy detection at the receiver.

Transmitter RF chain: The transmitter implements envelope modulation and the architecture of one of its RF chains is depicted in Figure 5.2. Using envelope modulation allows a simple implementation and an efficient use of power amplifiers [77]. In the present context, a wideband regime with envelope transmission schemes, OOK appears to be a simple and efficient modulation scheme considering a non-coherent demodulation – see flash-signaling in [23]. On the n-th RF chain, we write $s_n(t) \in \mathbb{R}_{\geq 0}$ the modulating signal which results from a rectangular pulse-shaping Π. Using OOK, the modulating signal is given by

$$s_n(t) = \sum_{\tau \in \mathbb{Z}} s_n[\tau] \cdot \frac{\Pi\left(\frac{t}{T_s} - \tau - \frac{1}{2}\right)}{\sqrt{T_s}}, \quad t \in \mathbb{R}, \tag{5.1}$$

where $s_n[\tau]$ is the τ-th modulated symbol from constellation $\mathcal{C} = \{0, \sqrt{2}\}$ and T_s is the symbol duration. We have $\int_{\tau T_s}^{\tau T_s + T_s} |s_n(t)|^2 dt = s_n[\tau]^2$. The transmitted signal $x_n(t)$ at carrier frequency f_c on the n-th RF chain is expressed by

$$x_n(t) = s_n(t) \cdot \sqrt{2} \cos(2\pi f_c t + \phi(t)), \tag{5.2}$$

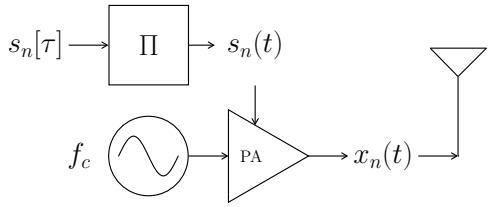

Figure 5.2 – *Block diagram of one Tx RF chain*

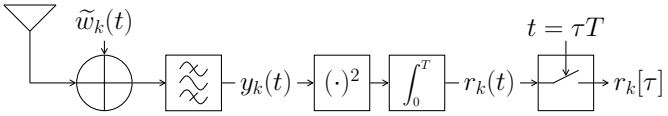

Figure 5.3 – *Block diagram of one Rx RF chain*

where $\phi(t)$ is a stochastic process modeling a strong oscillator PN. The transmitter uses a single oscillator reference, common to all RF chains, hence the PN process $\phi(t)$ is unique.

Propagation channel: The recent measurement campaigns [9] [11] have shown that sub-THz propagation channels are largely dominated by a single path, often the LoS direct path, which provides most of the energy contribution. It is due to the stronger channel sparsity at those frequencies and to the usage of highly directive antennas. Accordingly, we assume in this work a static LoS channel model.

Receiver RF chain: We detail here the receiver RF chains whose architecture is depicted in Figure 5.3. The input of the k-th chain is the double sideband signal $y_k(t)$ band-limited with bandwidth $B \geq 2/T$ and centered around carrier frequency f_c. The band-pass filter prevents the spectral folding of noise resulting from envelop detection. This signal is given by

$$y_k(t) = \sum_{n=1}^{N_t} h_{k,n} s_n(t) \cdot \sqrt{2} \cos\left(2\pi f_c t + \varphi_{k,n} + \phi(t)\right) + w_k(t), \tag{5.3}$$

where $w_k(t)$ is a band-limited continuous Gaussian process with spectral density N_0 modeling thermal noise. For further derivations, it is interesting to express the thermal noise using the baseband quadrature signals $w_{k,c}(t)$ and $w_{k,s}(t)$. It follows that

$$w_k(t) = w_{k,c}(t) \cdot \sqrt{2} \cos(2\pi f_c t) - w_{k,s}(t) \cdot \sqrt{2} \sin(2\pi f_c t), \tag{5.4}$$

where $w_{k,c}(t)$ and $w_{k,s}(t)$ are band-limited continuous Gaussian process with spectral density $N_0/2$. The channel phase shift $\varphi_{k,n} = d_{k,n} \cdot 2\pi f_c / c$, with $d_{k,n}$ the propagation distance and c the speed of light. The frequency down-conversion of the signal to baseband is achieved without impact of PN by squaring signal $y_k(t)$ and low-pass filtering it. That is

$$r_k(t) = \int_t^{t+T_s} y_k(u)^2 du, \tag{5.5}$$

with $f_c \gg 1/T_s$. For interested readers, more details are provided on frequency translation from passband to baseband using a self-mixer and a low-pass filter in Chapter 6, Section 6.1.1. For the k-th Rx RF chain, the τ-th received symbol $r_k[\tau] = r_k(\tau T_s)$ is obtained after integration and sampling. This is

expressed by

$$\begin{aligned} r_k[\tau] = &\sum_{n=1}^{N_t}\sum_{m=1}^{N_t} h_{k,n}s_n[\tau]\cdot h_{k,m}s_m[\tau]\cos(\varphi_{k,n}-\varphi_{k,m}) \\ &+2\int_{\tau T_s}^{\tau T_s+T_s} w_{k,c}(t)\cdot\sum_{n=1}^{N_t} h_{k,n}s_n(t)\cos\left(\varphi_{k,n}+\phi(t)\right)dt \\ &+2\int_{\tau T_s}^{\tau T_s+T_s} w_{k,s}(t)\cdot\sum_{n=1}^{N_t} h_{k,n}s_n(t)\sin\left(\varphi_{k,n}+\phi(t)\right)dt \\ &+\int_{\tau T_s}^{\tau T_s+T_s} w_{k,c}(t)^2+w_{k,s}(t)^2dt. \end{aligned} \tag{5.6}$$

Regarding this equation, the first line represents the energy of the received signals of the different Tx RF chains whereas the following lines express the contribution of thermal noise in the received symbols. Accordingly, we denote the energy of received signals

$$E_k[\tau] = \sum_{n=1}^{N_t}\sum_{m=1}^{N_t} h_{k,n}s_n[\tau]h_{k,m}s_m[\tau]\cos(\varphi_{k,n}-\varphi_{k,m}). \tag{5.7}$$

It should be noted that E_k expresses the nonlinear interference between the different channels of the system. To design the receiver detection algorithm it is necessary to express the probability distributions of received symbols $r_k[\tau]$. It is hence required to derive the distributions of the integrals in Eq. (5.6). Appendix A details the derivations of the distributions of received symbols. These derivations are based on the dimensionality theorem [1]. Finally, denoting $2M = \lfloor 2BT_s \rfloor + 1$ the time-bandwidth concentration of received signals, the received symbols can be expressed by

$$r_k[\tau] = E_k[\tau] + \sqrt{2E_k[\tau]}\cdot w_k[\tau] + z_k[\tau], \tag{5.8}$$

where $w_k[\tau] \sim \mathcal{N}(0,\sigma_w^2)$ is a zero-mean Gaussian variable with variance $\sigma_w^2 = N_0B/2M$ and $z_k[\tau] \sim \sigma_w^2/2\cdot\chi_{4M}^2$ is a chi-square distributed variable with $4M$ degrees of freedom. Furthermore, Eq. (5.8) defines the nonlinear MIMO channel of the considered transceiver. In the following section, we investigate the design of the detection algorithm related to this channel. From now on, the time index τ is disregarded for brevity.

5.3 Detection Algorithm Design

In this section, we present three detection algorithms for the studied nonlinear MIMO channel described in Eq. (5.8). The first detection algorithm to be presented is the optimal detection method used to demodulate an OOK based on the received energy. The second one is the proposed detection algorithm based on an analytical criterion and derived from the ML decision rule. Finally, the third detector to be described is the proposed demodulation based on neural networks.

5.3.1 Threshold detector (TD)

We present in this paragraph the commonly used *threshold detector* abbreviated by *TD*. When using a single-antenna transceiver, this criterion is known to be optimal for the detection of an OOK with an energy detection receiver, *i.e.* minimizing the error probability [83]. This decision rule is defined upon a threshold comparison. The detected symbol $\hat{s}_k$ at the receiver is expressed by

$$\hat{s}_k = \begin{cases} 0, & \text{if } r_k < \lambda_{\text{opt}}, \\ \sqrt{2}, & \text{otherwise.} \end{cases} \tag{5.9}$$

where λ_{opt} is the optimal threshold, function of $h_{k,k}^2$. This detector only requires the estimation of propagation gains $h_{k,k}^2$. The expression of λ_{opt} and its evaluation in practical systems are presented in [83]. Estimating symbol $\hat{s}_k$ on the k-th Rx RF chain, this detection criterion demodulates symbols from the different spatial streams independently, even if they are interfering. Using the TD in multiple-antennas systems implies the modeling of the spatial interference between channels as noise. On the one hand, if the spatial interference is negligible, this decision rule provides an efficient and low-complexity demodulation scheme. On the other hand, in the case of strongly correlated channels, this detector might not be able to estimate sent symbols. In this case, a joint demodulation of the received symbols over all antennas should be used. We propose in the following paragraph a joint demodulation algorithm which exploits spatial interference between channels as information to demodulate symbols on strongly correlated channels.

5.3.2 Maximum likelihood detector with Gaussian approximation (MLD-GA)

Position to state-of-the-art techniques: Well-known for linear MIMO channels, the ML detector jointly demodulates the received symbols of the different RF chains. This detector uses spatial interference as information to demodulate symbols in strongly correlated LoS channels. It is important to point out the following remark. Unlike linear MIMO channels, the spatial interference between channels expressed in Eq. (5.7) is nonlinear due to the squaring of received signals such that traditional detectors cannot be used. Therefore, we derive here the ML detector corresponding to the nonlinear MIMO channel described in Eq. (5.8) using a Gaussian approximation approach. The proposed detector is further abbreviated by *Maximum Likelihood Detector with a Gaussian Assumption (MLD-GA)*. It should be mentioned that [82] also addresses the demodulation for a nonlinear MIMO system. In [82], the demodulation is based on amplitude detection of complex symbols resulting from a coherent receiver with a local oscillator. It follows that the demodulation proposed in [82] may be sensitive to phase impairments since the output of the matched-filter is subject to a penalty in Signal-to-Noise Ratio (SNR) resulting from PN [84]. Conversely, we consider envelop extraction using energy detectors robust to PN. For this reason, the detector described in [82] cannot be used for the studied transceiver and differs from the proposed MLD-GA.

Derivation of the MLD-GA decision rule: For independent and equiprobable symbols, the ML decision rule is optimum, *i.e.* minimizes the error probability. This detection criterion is defined upon the channel likelihood and detected symbols $\hat{\boldsymbol{s}}$ are given by

$$\hat{\boldsymbol{s}} = \underset{\boldsymbol{s}\in\mathcal{C}^{N_t}}{\arg\max}\, p(\boldsymbol{r}|\boldsymbol{s}, H, \Phi). \tag{5.10}$$

With regard to the superposition of χ^2 and Gaussian distributions in Eq. (5.8), the detection criterion resulting from the channel likelihood would be too complex to be evaluated in practical systems. To derive a decision rule with a simple practical implementation, we approximate the contribution of the χ^2 distributed noise – precisely z_k in Eq. (5.8) – by its expected value. Received symbol r_k is then modeled with a Gaussian distribution

$$r_k \sim \mathcal{N}(\mu_k, \sigma_k^2), \tag{5.11}$$

where the mean and variance are given by

$$\mu_k = E_k + 2M \cdot \sigma_w^2, \quad \text{and} \quad \sigma_k^2 = 2E_k \cdot \sigma_w^2 + \varepsilon. \tag{5.12}$$

Though the noise contribution is approximated as Gaussian, the interference between channels remains nonlinear as expressed by E_k in Eq. (5.7). The term ε is introduced to prevent discontinuity[1] in the

[1]Empirical results have shown that setting $\varepsilon = \sigma_w^2$ is an efficient choice to minimize the BER.

detection criterion. Then, the joint probability density function is given by

$$p(\boldsymbol{r}|\boldsymbol{s}, H, \Phi) = \prod_{k=1}^{N_r} \frac{1}{\sqrt{2\pi\sigma_k^2}} \exp\left(-\frac{|r_k - \mu_k|^2}{2\sigma_k^2}\right). \tag{5.13}$$

Finally, the detection decision rule can be written as

$$\hat{\boldsymbol{s}} = \underset{\boldsymbol{s}\in\mathcal{C}^{N_t}}{\arg\min} \sum_{k=1}^{N_r} \frac{|r_k - \mu_k(\boldsymbol{s})|^2}{\sigma_k(\boldsymbol{s})^2} + \ln\left(\sigma_k(\boldsymbol{s})^2\right). \tag{5.14}$$

This expression fully describes the proposed MLD-GA. The minimization space $\mathcal{C}^{N_t}$ increases exponentially with the number of antennas N_t. Since OOK is used, the modulation order remains small, $|\mathcal{C}| = 2$, and the complexity of the MLD-GA algorithm is not an issue. It must be emphasized that the MLD-GA requires the estimation of H and Φ. The implementation of such estimation algorithm is not presented here. In the following, we assume perfect knowledge of the channel at the receiver. Basic and simplistic estimation schemes are straightforward to design. For instance, the estimation of channel parameters can be realized by using some reference pilots and transmitting all $|\mathcal{C}|^{N_t}$ possible MIMO symbols. Still, we highlight the large room for improvement. The number of transmitted pilots can be largely reduced by switching different pairs of antennas, *i.e.* optimized selection of sent symbols. In addition, a Bayesian estimation algorithm could capitalize on the prior knowledge of the antenna radiation pattern to provide channel knowledge.

5.3.3 Neural Networks based Detector (NND)

We now propose to use a novel and original *Neural-Networks based Detector (NND)* in order to estimate sent symbols. The motivation of using neural networks is twofold. First, as discussed previously, the considered system communicates through a nonlinear MIMO channel and neural networks are efficient to solve multi-variables nonlinear problems. Moreover, in the case of the MLD-GA algorithm, the impact of noise on received symbols is assumed to follow a Gaussian distribution, assumption we do not make using the NND. In addition, the NND does not need the explicit knowledge propagation matrices H and Φ to estimate symbols as it learns the channel features during the training phase.

Position to state-of-the-art techniques: This paragraph briefly reviews some of the state-of-the-art relating to the use of neural networks within communication systems, and more specifically, for detection purposes. First, [85] provides a general overview of the use of neural networks for detection in communication systems and also for linear MIMO systems. Moreover, in [86], the use of deep neural network detection is investigated for linear MIMO systems with knowledge of the propagation matrices. Nevertheless, no mention is made on the use of neural networks for nonlinear MIMO systems. Similarly to the proposed NND, the combination of neural networks with energy detectors is addressed in [87]. Still, in [87] neural networks serve a different purpose and aim to detect the unused portions of the spectrum in order communicate in an opportunistic way, *i.e.* spectrum sensing applications. To the best of authors' knowledge, the proposed neural network based demodulation for MIMO systems with energy detection receivers is original and has not been addressed in the literature.

Architecture of the NND: The architecture of the NND is illustrated in Figure 5.4. It is worth noticing that the NND uses one neural network by transmit antenna. Each of the N_t neural networks estimates a single transmitted symbol. The proposed architecture of the n-th neural network is depicted in Figure 5.5 for the detection of symbol s_n. This neural network uses fully connected hidden layers, each one composed of N_n neurons using rectified linear unit (ReLU) as activation function. The number of

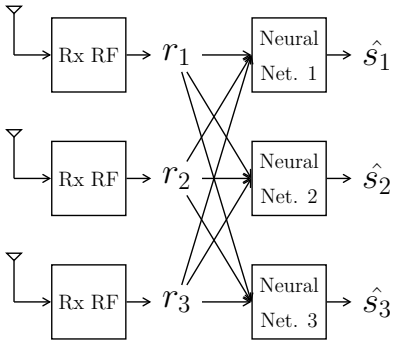

Figure 5.4 – *Receiver using the NND with* $N_t = N_r = 3$

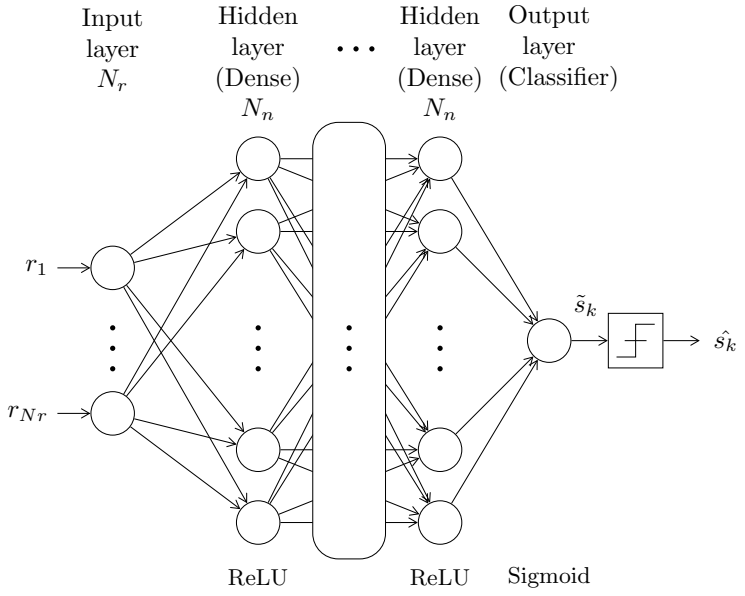

Figure 5.5 – *Architecture of the n-th neural network of the NND*

hidden layers N_{hl} is function[2] of the number of transmit antennas N_t. The input layer has N_r units, each one representing a received symbol r_k. Finally, a prediction $\widetilde{s}_k$ – homologous to the probability $Pr(s_n = 0|\boldsymbol{r})$ – is produced at the output layer with a sigmoid unit. Thus, we build a multi layer perceptron classifier in order to estimate the transmitted symbols s_n. It should be mentioned that this architecture is replicated N_t times. Besides, it is worth mentioning that optimizing jointly the N_t neural networks is more complex, and we have not observed any performance improvement with respect to the parallel optimization. Therefore, we consider the parallel optimization of the neural networks in this work. Eventually, the use of the NND is relevant for high-rate applications requiring parallel processing since sent symbols are estimated independently.

Training of the NND: The training of the NND is realized by transmitting some reference symbols known by the receiver. The set of weights is optimized during the training phase to maximize the detection performance of the NND. Each neural network, one by transmit antenna, is trained independently using an *Adam* optimizer and its own loss function J_n. Since OOK is exploited, it is pertinent to use a

[2]It shall be mentioned that the choice of these parameters is empirical, still we have noticed some relations between the NND parameters and the system parameters such as $N_{hl} \simeq N_t/2$ and $N_n \simeq N_t^2$

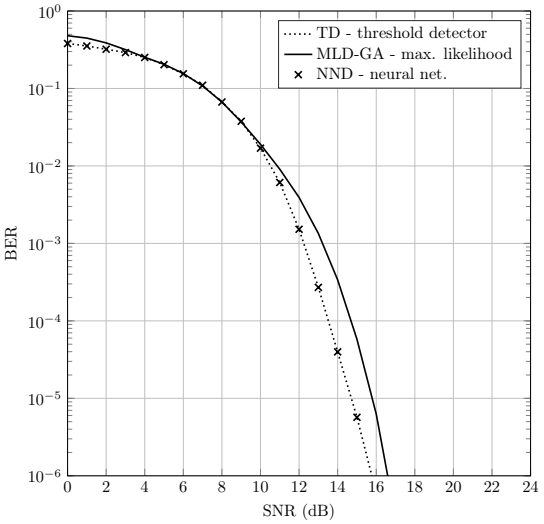

Figure 5.6 – *Detection performance without spatial interference*

binary cross-entropy loss function described by

$$J_n = -\frac{1}{B_s}\sum_{\tau=1}^{B_s}\left[\frac{s_n[\tau]}{\sqrt{2}}\ln\left(\widetilde{s}_n[\tau]\right) + \left(1-\frac{s_n[\tau]}{\sqrt{2}}\right)\ln\left(1-\widetilde{s}_n[\tau]\right)\right], \tag{5.15}$$

where B_s stands for the batch size. In addition, it could be noted that the fixed property of the wireless link in the targeted application is particularly suited to machine learning. A detailed description of the NND implementation parameters is outlined in the following section presenting the results of numerical simulations.

5.4 Performance Analysis

In this section, we present the results of numerical simulations, conducted to assess the performance of MIMO systems using energy detectors in sub-THz bands. This task is addressed in two steps. First, we present a simplified performance analysis based on an analytical model, namely the sectored antenna model. Second, we consider the real radiation pattern of transmit and receive antennas and also the integration of a channel coding scheme. Thereby, the performance analysis is enhanced thanks to the system-level perspective and more realistic modeling. In the light of simulation results, we finally discuss and compare the implementation of the proposed detection algorithms.

5.4.1 Simplified simulations based on an analytical model

5.4.1.1 Systems without spatial interference

To evaluate the performance of the detectors, we first investigate MIMO systems without spatial interference. The channels are perfectly spatially multiplexed, *i.e.* H is diagonal. To implement the TD decision rule in practical systems, the threshold λ_{opt} has to be evaluated efficiently. Therefore, we use the expression of λ_{opt} proposed in [83] using a polynomial approximation. Figure 5.6 presents the results of numerical simulations for systems using OOK with $N_t = N_r$ and no spatial interference. The communication performance is expressed in terms of Bit Error Rate (BER) as a function of the SNR defined by $h_{k,k}^2/\sigma_w^2$. We can remark that the TD and the NND present a performance gain in comparison to the MLD-GA decision rule. This performance loss of the MLD-GA results from the Gaussian

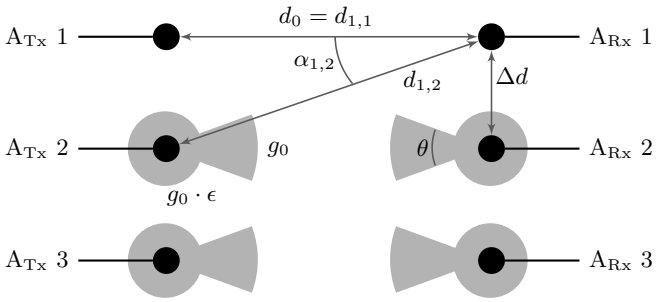

Figure 5.7 – *Disposition of the antennas in the scenario*

approximation of the noise distribution. Furthermore, for transceivers without spatial interference, it can be shown that the NND achieves the optimal detection performance given by the TD.

5.4.1.2 Scenario description: a fixed indoor link in the D-band

We introduce here a realistic sub-THz scenario. The targeted application is a fixed indoor wireless link in the D-band. Table 5.1 outlines the main simulation parameters for this scenario. The considered system uses a Uniform Linear Arrays (ULA) of antennas with $N_t = N_r = N$. The disposition of the antennas is depicted in Figure 5.7. The specification of the antenna is extracted from [8] which describes the design of a high-gain antenna for the D-band based on transmit-arrays. We evaluate the propagation gain $h_{k,n}^2/\sigma_w^2$ for channel $n \to k$ using the link budget given by the Friis' transmission equation. Denoting $P_{A_{Tx}}$ the transmit power by antenna, $G_{k,n}$ the antennas gain, and $d_{k,n}$ the propagation distance, the link budget is given by

$$\frac{h_{k,n}^2}{\sigma_w^2} = P_{A_{Tx}} G_{k,n} \left(\frac{c}{4\pi f_c d_{k,n}}\right)^2 \left(\frac{N_0 B}{2M} N_f\right)^{-1}. \tag{5.16}$$

We have $G_{k,n} = g_{k,n}^{Tx} \cdot g_{k,n}^{Rx}$ the product of the Tx and Rx antennas directivity gains for channel $n \to k$. We assume the commonly used ***sectored antenna model*** illustrated in Figure 5.7. The antenna directivity gain is then defined by

$$g(\alpha) = \begin{cases} g_0, & \text{if } |\alpha| < \frac{\theta}{2}, \\ g_0 \cdot \epsilon, & \text{otherwise,} \end{cases} \tag{5.17}$$

upon the beam width θ, the beam offset angle to the main lobe α, the side lobe level ϵ ($0 < \epsilon \ll 1$) and the antenna gain g_0. The considered scenario is symmetric and the beam of the k-th transmit antenna is aligned with the k-th receive one. This leads to $g_{k,n}^{Tx} = g_{k,n}^{Rx} = g(\alpha_{k,n})$ with $\alpha_{k,n}$ the beam offset angle for

Table 5.1 – *Simulation parameters*

Carrier Frequency	f_c	145 GHz
Symbol rate	$1/T_s$	1 GHz
Bandwidth	B	2 GHz
Thermal noise	N_0	-174 dBm
Noise figure	N_f	10 dB
Antenna gain	g_0	32 dBi
Beam width	θ	3
Side lobe level	ϵ	-20 dB
Distance Tx-Rx	d_0	10 m

channel $n \rightarrow k$. Eventually, the channel matrix H may be evaluated using Eq. (5.16) and Table 5.1. The maximum propagation gain $h_{k,k}^2$ is achieved for any channel $k \rightarrow k$. For a transmit power by antenna $P_{\mathrm{A_{Tx}}} = -30$ dBm, we have

$$\mathrm{SNR} = \frac{h_{k,k}^2}{\sigma_w^2} \simeq 16.23 \text{ dB}. \tag{5.18}$$

With $k' \neq k$, the interference terms (off-diagonal elements) in matrix H are approximately

$$\frac{h_{k,k'}^2}{h_{k,k}^2} \simeq \begin{cases} -0.01 \text{ dB}, & \text{if } |\alpha_{k,k'}| < \frac{\theta}{2}, \\ -40.02 \text{ dB}, & \text{otherwise.} \end{cases} \tag{5.19}$$

When $\Delta d \ll d_0$ the differences in path loss between channels are close to zero. Subsequently, the channels are either strongly interfering or almost not. The level of interference between two channels, either strong 0 dB or very low -40 dB, only results from the angle $\alpha_{k,k'}$. If the inter-antenna distance Δd is sufficiently large,

$$\Delta d \geq d^* = d_0 \tan\left(\frac{\theta}{2}\right), \tag{5.20}$$

the spatial streams are almost perfectly multiplexed. The interference between channels in this case results from side lobes of the antennas and is very low (< -40 dB). This corresponds closely to an ideal case and the system performance for any N equals the one described in Figure 5.6 without interference. Since $d^* \simeq 26$ cm, the latter condition implies that the width ℓ of the array of antennas may be significantly large for practical implementation. The width of the ULA $\ell = d_{\mathrm{A}} + (N-1)\Delta d$, where $d_{\mathrm{A}} = 5$ cm is the width of the antenna itself [8]. By way of illustration, for $N = 8$ we have $\ell > 1.8$ m. To reduce the width of the transceiver, we now consider a smaller inter-antenna distance such that multiple spatial streams interfere strongly. The inter-antenna distance is characterized by the following condition

$$d^* \frac{2}{\kappa - 1} \; > \; \Delta d \; \geq \; d^* \frac{2}{\kappa + 1}, \tag{5.21}$$

where $\kappa \in \{3,5,\ldots,2N-1\}$. In this case, the main lobe of one transmit antenna beam enlightens multiple receive antennas, namely up to κ. To put it differently, κ denotes the maximum number of transmitted symbols strongly interfering on a receive antenna. Hence, the larger the value of κ, the stronger the spatial interference between channels. By means of illustration, the channel gain matrix H for $N = 4$ and $\kappa = 3$ could be accurately approximated[3] as follows

$$H \simeq h_{1,1} \cdot \begin{bmatrix} 1 & 1 & \rho & \rho \\ 1 & 1 & 1 & \rho \\ \rho & 1 & 1 & 1 \\ \rho & \rho & 1 & 1 \end{bmatrix}, \tag{5.22}$$

where ρ models the residual interference due to side lobes of the antennas with $\rho^2 = -40$ dB. There are κ diagonals of H whose elements are equal to 1 which corresponds to the maximum number of interfering symbols on a receive antenna. We use hereafter $\kappa = 1$ to denote the multiplexed case corresponding to Eq. (5.20). Eventually, parameter κ enables us to quantify the level of spatial interference.

5.4.1.3 Systems with strong spatial interference

Let us now evaluate the influence of the spatial interference on the system performance using parameter κ. In these simulations, the propagation gain and phase shift matrices are not approximated and are exactly computed from the scenario description and simulation parameters.

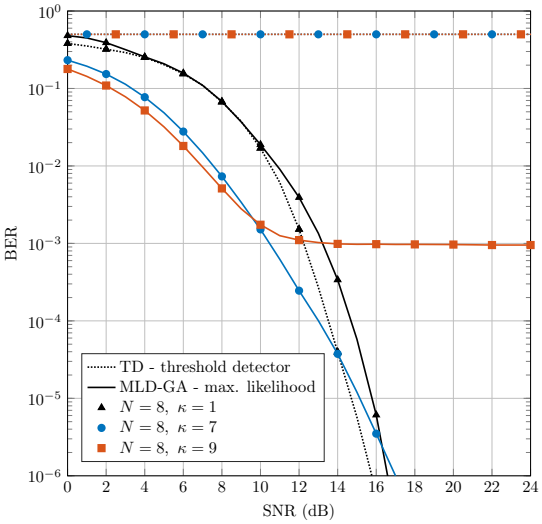

Figure 5.8 – *Influence of the level of spatial interference (parameter κ) on the system performance*

Table 5.2 – *NND parameters*

	1×1 **MIMO**	4×4 **MIMO**	8×8 **MIMO**
Hidden layers (HL)	1	2	4
Neurons/HL	8	16	64
Batch size	32	32	256
Epochs	50	150	150
Optimizer	Adam		
Learning rate	0.001		
Loss function	Binary cross-entropy Eq. (5.15)		
Activation	ReLU and Sigmoid		

MLD-GA *vs.* TD: The results of numerical simulations comparing the detection performance of the MLD-GA and the TD are depicted in Figure 5.8. The BER performance is assessed for $N = 8$ and different values of κ. First, it must be emphasized that the MLD-GA is essential to communicate on strongly correlated channels. As expected in the presence of spatial interference, *i.e.* for $\kappa > 1$, the TD cannot demodulate sent symbols and presents a BER of $1/2$. Simulation results also show that in the moderate SNR regime transceivers with large values of κ, *i.e.* strong spatial interference, may demonstrate lower BER than the multiplexed case $\kappa = 1$. Subsequently, setting κ large is interesting to achieve low error rate communications while reducing the width of the transceiver. Nevertheless, we can remark that if the spatial interference is too strong, *e.g.* $k = 9$ in Figure 5.8, the BER reaches an error floor. The properties exhibited for $N = 8$ in Figure 5.8 also hold for different values of N.

MLD-GA *vs.* NND: This paragraph presents the communication performance of the NND and the MLD-GA algorithms on strongly correlated LoS channels. Table 5.2 presents the parameters of the NND architecture for the different system configurations. Here the tuning of the NND parameters is empirical, yet we have observed that increasing the number of antennas requires to increase the number of hidden layers and neurons. The results of numerical simulations are depicted in Figure 5.9. The BER performance is assessed for $N = 4$ and $N = 8$ and different values of κ, *i.e.* different levels of spatial

[3]Since the differences in path loss is less than 0.02 dB, the adjacent channels interference and the residual side lobes interference can be respectively approximated to 1 and a constant ρ.

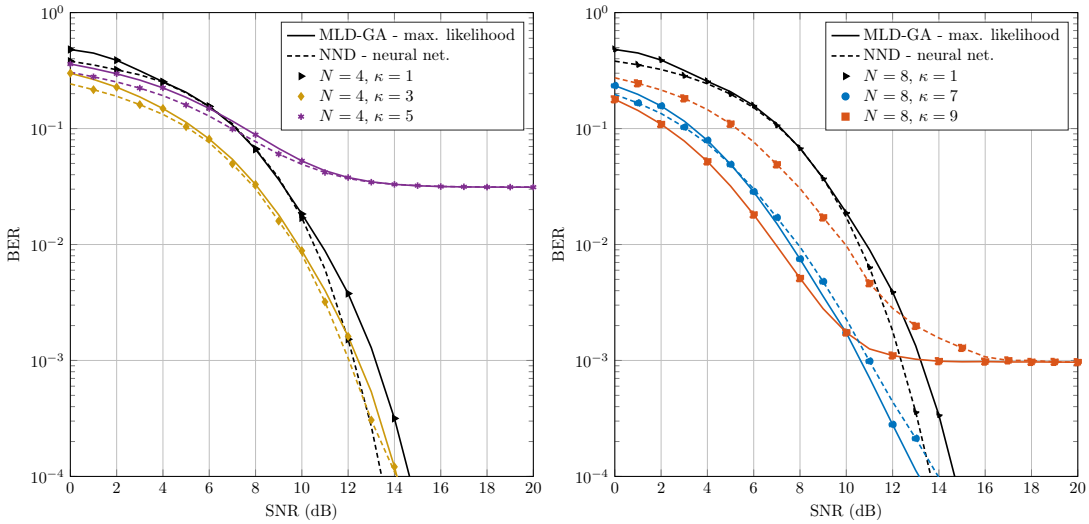

(A) $N = 4$ (B) $N = 8$

Figure 5.9 – *BER performance of the MLD-GA and the NND*

interference. First, we can notice that, for $\kappa = 1$ with any number of antennas N, the performance equals the one without interference previously described in Figure 5.6. Second, for $N = 4$ with spatial interference, it can be observed that the MLD-GA and the NND present similar detection performance. Though, the NND demonstrates slight performance gains. Nonetheless, it should be noted that if the spatial interference is too strong, *e.g.* $\kappa = 5$ for $N = 4$ or $\kappa = 9$ for $N = 8$, the BER reaches an error floor. Third, for $N = 8$, we notice that the system performance of the NND is close to the one of the MLD-GA if the spatial interference is not too strong. With strong interference, $\kappa = 9$ and $N = 8$, using the NND leads to a significant performance loss.

5.4.1.4 *Discussions*

We conclude this first analysis of the system performance by discussing some properties of the transceiver. Similarly to linear MIMO systems, the considered system benefits from the spatial diversity. A symbol transmitted on one transmit-antenna may be received on several receive antennas. This property thus improves the robustness to thermal noise. It justifies the performance gains achieved by systems with strong interference in the moderate SNR regime in comparison to the multiplexed case, for instance shown in Figure 5.8. In addition to diversity, the studied system is also subject to ambiguity. Since the communication channel is a nonlinear MIMO channel, different transmitted MIMO symbols $\boldsymbol{s}$ may lead to similar received observations $\boldsymbol{r}$. For this reason, the BER of system configurations with strong spatial interference reaches an error floor, see for instance Figure 5.9. Subsequently, we claim that the level of spatial interference, and hence the inter-antenna spacing Δd, is directly related to a trade-off between diversity and ambiguity. Eventually, our results show that low-error rate communications can be achieved with strong spatial interference between channels. Still, the detection algorithm must use jointly the different received symbols to demodulate transmitted symbols, similarly to the NND or the MLD-GA. Our results demonstrate that spatial multiplexing with non-coherent sub-THz transceivers can be realized on strongly correlated LoS channels. MIMO systems with energy detection receivers hence offer a valuable solution to achieve high-rate communications in sub-THz frequencies. Since the analysis is carried out with some approximations, in particular on the antenna model, the exactitude of the conclusions could be questioned. Nevertheless, the next section proposes to improve the performance analysis by considering and discussing some practical implementation issues and specifically by assessing the system performance with the real radiation pattern of the antenna.

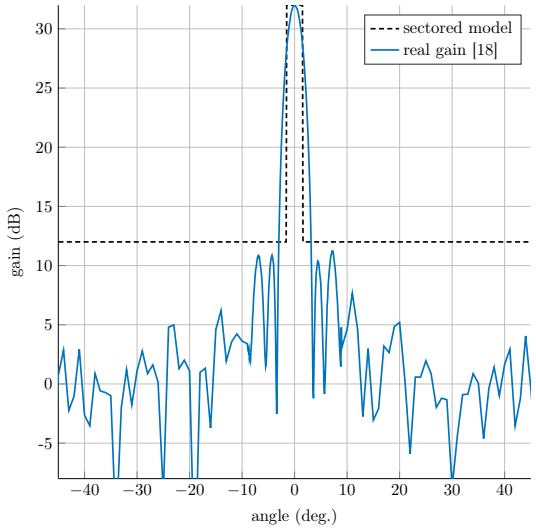

Figure 5.10 – *Antenna gain measured in [8]*

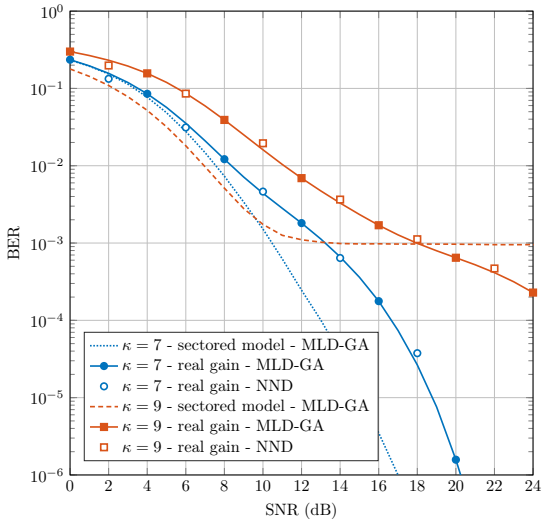

Figure 5.11 – *BER for $N = 8$ with the real antenna gain*

5.4.2 System-level simulations based on measurements

We have previously shown that low-complexity low-power transceivers using MIMO systems with energy detection receivers can be implemented within sub-THz frequencies. Nonetheless, the presented performance analysis could be improved by further considering some practical implementation issues. To do so, we first evaluate the system performance with the real radiation pattern of the antenna as measured in [8]. Second, we consider the integration of a Forward Error Correction (FEC) scheme as channel coding. Third, the practical implementation of the proposed detection schemes are discussed.

5.4.2.1 Performance with the real antenna radiation pattern

Previously, we have based the performance analysis upon the commonly used sectored antenna model. The sectored model is relevant for its simple analytic expression. However, the accuracy of the analysis can be improved by considering the real antenna gain pattern measured and published in [8]. Figure 5.10 depicts the real antenna gain pattern and the sectored model. The assessment of communication performance with the real antenna gain, in comparison to the sectored model, is presented in Figure 5.11 for $N = 8$ using the MLD-GA and the NND. It can be observed that the BER performance of system configurations with strong interference is deteriorated when the real antenna gain is considered. Nevertheless, and conversely to the sectored model, no error floor is observed with the real antenna pattern, see the configuration $N = 8$, $\kappa = 9$. In addition, it should be emphasized that the MLD-GA and the NND demonstrate similar demodulation performance when considering the real antenna gain. We conclude from these results that the sectored antenna gain model is an efficient but optimistic model to describe practical systems. In the following, any further performance analysis is based on the real radiation pattern of the antenna gain.

5.4.2.2 Integration of channel coding

It is interesting to consider the integration of a FEC scheme to achieve channel coding gain and low error rates. However, implementing the FEC, and in particular its decoder, may entail a significant complexity and power consumption. To achieve a low-complexity low-power transceiver, we propose here to use a BCH code. The considered FEC scheme is a BCH code with a packet size of 63 bits, a coding rate ranging from 0.4 to 1 and a decoder based on hard decisions. It should be mentioned that the key features of this code are a low-complexity implementation and a low-power consumption –

interested readers may refer to [88]. In addition, with regard to the short packet size, this code has a low-latency decoder. These features appear to be highly relevant for the scenario investigated in this study. The considered transceiver architecture with the integration of channel coding is presented in Figure 5.12. Multiple FEC schemes are used and the coding rate can be adapted to the channel quality of the receive antenna. The channel presents significant differences in terms of quality depending on the receive antenna. Receive antennas in the middle of the ULA are subject to stronger interference than the ones on the extremities. For this reason, adapting the coding rate to the receive antenna enables us to capitalize on the latter property to further enhance the demodulation performance. The system architecture in Figure 5.12 is particularly interesting as it also maintains a high degree of parallelism. Conversely, using a unique FEC is not an efficient solution to define a parallel implementation and to optimize the coding rate to the transmit-receive antennas.

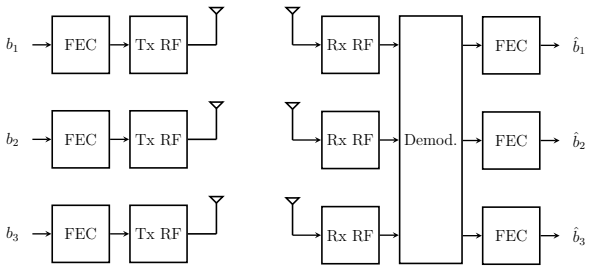

Figure 5.12 – *System architecture integrating a FEC scheme*

Figure 5.13 presents the achievable rates as function of E_b/N_0B for systems with a BCH code such that the BER is below 10^{-6}. The BCH code is implemented with a coding rate ranging from 0.4 to 1 and a channel decoder based on the hard decisions produced by the MLD-GA. Numerical results have been obtained through the Monte-Carlo simulations with the real antenna gain pattern. First, it should be remarked that integrating a FEC scheme enables to achieve valuable channel coding gains. Second, it can be remarked that the adaption of the coding rate to the antenna leads to performance gains in comparison to setting a fixed coding rate for all antennas. In particular, we can see that for $N = 4$ and $N = 6$ the performance gains are larger than 2 dB.

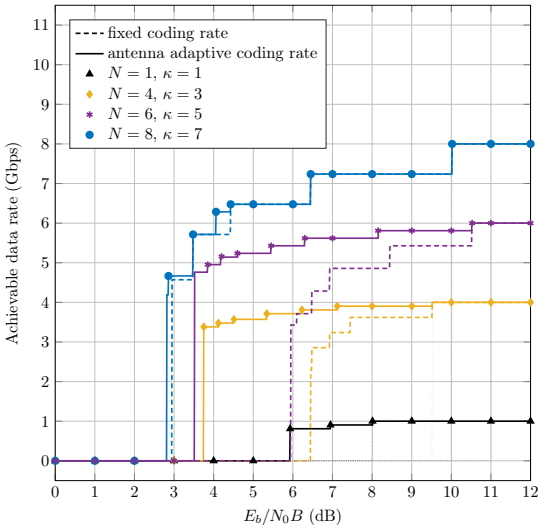

Figure 5.13 – *Achievable data rate with a BCH code and the real antenna gain*

Table 5.3 – *Simulation parameters and results*

Carrier Frequency	f_c	145 GHz			
Symbol rate	$1/T_s$	1 GHz			
Bandwidth	B	2 GHz			
Distance Tx-Rx	d_0	10 m			
Antenna gain	g_0	32 dBi			
Number of antennas	N	1	4	6	8
Throughput	$\frac{N}{T} \cdot 0.9$	0.9 Gbps	3.6 Gbps	5.4 Gbps	7.2 Gbps
Power by antenna	$P_{\mathrm{A_{Tx}}}$	−31.8 dBm	−31.2 dBm	−30.4 dBm	−32.3 dBm
Transceiver width	ℓ	5 cm	44 cm	50 cm	55 cm
Inter-antenna dist.	Δd	∅	13 cm	9 cm	7 cm

To present the results of Figure 5.13 differently, we propose in Table 5.3 a synthesis of the system performance and parameters for different number of antennas. For all system configurations, the bandwidth is $B = 2$ GHz, the distance Tx-Rx is $d_0 = 10$ m, and the coding rate of the BCH is 0.9. Though the system performance is evaluated with the MLD-GA, similar results are expected using a demodulation based on the NND. Further, a channel bonding scheme, aggregating several sub-bands, could increase the throughput and allow to benefit from the large spectrum available in sub-THz bands. It can be concluded that MIMO systems using energy detection receivers may achieve high-rate communications in sub-THz bands with low-power and low-complexity RF architectures. Performance of coded systems could be further improved by considering longer packet length, soft-decision channel decoding, or capacity-achieving codes – *e.g.* a polar code – yet at the detriment of a complexity increase. It is worth mentioning that we have implemented a state-of-the-art polar code with soft-decisions channel decoding, results are presented in our paper [34].

5.4.3 Comparison of the proposed detection algorithms

This section outlines a quick overview of the practical aspect of MLD-GA and NND techniques to understand the benefits and drawbacks of each technique.

Channel estimation: The first difference between the MLD-GA and NND is the following. To perform its decision rules, the MLD-GA algorithm requires an explicit knowledge of H, σ_w^2 and Φ, and hence, also the design of a channel estimation algorithm. In contrast, the NND is able to learn the channel features, and implicitly the channel matrices, during the training phase in order to demodulate symbols. The transmission of reference symbols is required for both detection algorithms which results in a spectral efficiency loss.

Algorithm complexity: It is delicate to compare the complexity of MLD-GA and NND algorithms since they lie in different paradigms. The MLD-GA algorithm is a common detection method. Though the complexity of the MLD-GA is $O(|\mathcal{C}|^N)$ and increases exponentially with the number of antennas, the decision rule only requires the evaluation of simple weighted Euclidean distances. Moreover, the complexity of the MLD-GA depends on the order of the modulation scheme. Using an OOK with $|\mathcal{C}| = 2$, the resulting complexity is $O(2^N)$ which is reasonable for practical implementation. The implementation of the MLD-GA in practical systems would likely use a common digital signal processor. In contrast, the complexity of the NND depends on the size of the used neural networks. It means that increasing the number of layers would drastically increase the complexity. Thereby, in our case,

increasing the number of antennas will also increase the complexity of the NND. The complexity of both training and inference stages should be differentiated. Indeed, the training stage involves many data and consuming resources whereas the inference stage could be quite simple. Pre-training or offline training can be envisaged to reduce the cost and the complexity of the receivers. Besides, the implementation of neural networks is currently a largely investigated research topic. Thus, implementing neural networks on dedicated hardware such as GPU, FPGA and ASIC can significantly decrease computation time regarding the chosen neural network architecture – readers may refer to [89] and [90].

Transceiver RF nonlinearities: Eventually, it is interesting to mention that RF components of the transceiver might present additional nonlinearities, *e.g.* quantization, RF power amplifier. In particular, envelope detectors based on diodes may present non-ideal square law response such that $X_{\text{out}} \propto X_{\text{in}}^{\alpha}$ with $\alpha < 2$ [91]. It is expected that the NND might learn these channel nonlinearities and still demodulates symbol efficiently. The MLD-GA does not consider any other nonlinearities, such that it might be sensitive to these impairments and might require additional modeling. Nevertheless, it is of practical interest to characterize the detector robustness to imperfect RF components.

5.5 Synthesis and Discussions

Conclusion: Regarding the development of sub-THz communication systems, state-of-the-art approaches mostly rely on coherent transceivers with high-order modulation schemes and high-quality RF components to achieve spectral-efficient communication links [19]. Conversely, we have studied in this chapter non-coherent spatial multiplexing in sub-THz frequencies to achieve high data rate with low-complexity transceivers. More precisely, in this chapter, we have investigated the design of MIMO systems with energy detection receivers for future applications in sub-THz bands. The main challenge to be faced in these systems is the strong and nonlinear interference between the correlated LoS channels. First, the system model has been characterized Next, we have proposed two original detection algorithms: i) the MLD-GA, derived from the ML decision rule for the studied nonlinear MIMO channel using a Gaussian approximation; ii) and the NND, a demodulation based on the use of neural networks. Later, a realistic scenario modeling an indoor wireless link has been considered to assess the communications performance. Simulation results have proved that low error rate communications can be achieved on strongly correlated LoS channels using the proposed detection schemes. The two proposed detectors present similar demodulation performance, yet their implementations in practical systems are significantly different. Moreover, we have shown that integrating a low-complexity channel coding scheme leads to valuable performance gains in terms of achievable data rate while maintaining a simple practical implementation. In conclusion, the main contribution of this chapter is to demonstrate that spatial multiplexing with non-coherent sub-THz transceivers can be realized on strongly correlated LoS channels. The spectral efficiency of non-coherent communication systems using sub-THz bands can be efficiently increased using MIMO systems and energy detection receivers with low-complexity and low-power RF architectures. The material of this chapter has been partly published in one conference paper [34]; one submitted journal article [35]; and has lead to the deposit of one patent [36], see citations below. The authors would like to thank Valentin Savin and Alexis Falempin, from CEA-Leti, for their significant contributions. Valentin Savin has offered a precious help with regard to the integration of channel-coding and careful readings of the related publications. Alexis Falempin has carried out numerical simulations regarding the performance analysis of the NND. Moreover, the authors would like to express their gratitude to Francesco Manzillo and Antonio Clemente, from CEA Leti, who have provided valuable information on antennas contributing to the relevance of this work.

Perspectives: We now outline some meaningful perspectives to the research in this chapter. In doing so, we hope that readers will better appreciate the scope of our contributions and the remaining topics to be addressed. First, we have assumed in this chapter perfect channel knowledge for the model-based detection algorithm, the MLD-GA. Therefore, it must be mentioned that efficient channel estimation schemes need to be designed. Though basic and simplistic estimation schemes are straightforward to design, we highlight the large room for improvement. Notably, a Bayesian estimation algorithm could capitalize on the prior knowledge of the antenna radiation pattern to provide channel knowledge. In addition to the design of estimation schemes, it is of practical interest to quantify the performance degradations due to estimation errors. Second, when it comes to practical implementation, the robustness of the proposed detection algorithms to additional RF nonlinearities should be characterized, *e.g.* non-ideal square law response of the envelope detectors [91]. Third, we find worthwhile to mention one of our on-going research study. We are currently investigating the design of a probabilistic demapper using neural networks. In the case of the MLD-GA, the probabilistic demapper is straightforward to compute. Soft-channel decoding using the probabilistic outputs of the MLD-GA has been implemented and presented in [34]. Conversely, in this chapter, the channel decoding scheme is based on the hard decisions generated by the MLD-GA. It is clear that using the NND with soft-decisions channel decoding is to provide further performance enhancements and should be a prime investigation.

Applications and limitations: It is worth discussing the potential applications and limitations of the presented results. Our findings contribute to the development of future sub-THz applications with low-complexity physical layers, and in particular, of short-range wireless links targeting high data rates. And our contributions are expressly relevant in the light of the current wireless networks context where an extreme densification of access points is envisaged. Besides, it is worth mentioning that the presented techniques and results are relevant to applications beyond sub-THz communications such as Visible Light Communications (VLC) or optical systems. VLC systems commonly implement intensity modulation and direct detection. Subsequently, the nonlinear interference between channels in these systems is also a major challenge to implement spatial multiplexing [92]. The proposed detectors, and especially the neural network based demodulation, could be easily adapted to VLC systems in order to achieve spatial multiplexing. It is a well known result that machine learning methodologies are efficient to solve nonlinear and multi-variable problems. It has been used in this chapter to mitigate nonlinear interference and thereby has unveiled new possible applications for future physical layers. Nevertheless, some limitations regarding the contributions of this chapter should be mentioned. In this chapter, the sub-THz scenario has considered a fixed wireless link with perfect antenna alignments. The fixed property is extremely useful for machine learning and channel estimation. However, they remain somehow idealistic assumptions. Misalignments between transmit and receive antennas would lead to a lower received power and to a stronger interference between channels, and hence, to some performance deteriorations. And though this does not question the value of our contributions, the resulting requirements on beam alignment are challenging. We have also observed that the inter-channel interference is a limiting factor to communicate over a long range with MIMO systems in sub-THz bands. When the communication range increases, either the inter-antenna separation has to scale with the distance or the beamwidth of the antennas has to narrow in order to limit the inter-channels interference. The strong requirements on antenna directivity and beam alignment are a topical problematic. It is common to numerous future wireless systems such millimeter-wave (mm-Wave) communications and is directly related to the use of higher carrier frequencies.

Coherent LoS MIMO: We could not conclude this chapter without referring to the research activities on the development of MIMO systems in LoS environments with coherent transceivers. This field of research has gained interest with regard to the future deployment of spectral-efficient links in the mm-Wave bands. This research topic should be related to our work in this chapter. Though the design

paradigms are considerably different since we target low-complexity implementations, some design issues are shared. Using coherent or non-coherent transceivers, in both cases the use of ULA of antennas is considered and geometric approaches are developed. Moreover, the system performance is directly linked to the antenna separation in any cases. In LoS environments with sparse channels, multiplexing and detecting several signal streams with MIMO systems is challenging due to the correlation among channels. To cope with the spatial correlation of the channels in coherent systems, the work in [93] propose to include a precoding scheme in the transmission chain whereas the work in [94] investigates the optimization of the antennas separation. These techniques improve the system performance of coherent MIMO systems in LoS environments by maximizing spatial degrees of freedom and channel capacity. Subsequently, it is legitimate to ask the following question: Is it possible to implement LoS MIMO with coherent transceivers in sub-THz bands? Such communication systems rather belong to the paradigm of spectral-efficient sub-THz physical layers with complex RF architecture and transmission techniques, and not to the low-complexity paradigm. And with regards to the previous chapters of Part II, phase impairments entail severe consequences on the design of coherent LoS MIMO systems. Oscillator instabilities render difficult the implementation of beamforming but also of precoding and detection. For these reasons, the design of coherent LoS MIMO systems in sub-THz frequencies could be relevant to further increase the spectral efficiency, still numerous design problematics are yet to be addressed in addition to state-of-the-art techniques and existing literature.

Increasing the communication throughput is one of the main challenges of using non-coherent transceivers in sub-THz bands. In this chapter, we have shown that spatial multiplexing is an efficient method to implement large communication throughputs with low-complexity sub-THz systems. In the next chapter, we pursue a different approach to achieve high-rate sub-THz communications with low-complexity transceivers. This approach relies on the use of large bandwidth transceivers in sub-THz bands with non-coherent receivers. Still, the demodulation of large-bandwidth signals implies strong constraints on the analog-to-digital conversion. To relax the constraints on converters, we investigate in the next chapter the parallelization of the RF architecture of non-coherent receivers.

First-authored contributions

[36] S. Bicaïs, J.-B. Doré, and A. Falempin, "Neural Networks Based Demodulation for MIMO systems using Energy Detection Receivers," Patent, Jun. 2020

[35] S. Bicaïs, A. Falempin, J.-B. Doré, and V. Savin, "Design and Analysis of MIMO Systems using Energy Detectors for Sub-THz Applications," *IEEE Transactions on Wireless Communications*, Submitted

[34] S. Bicaïs, J.-B. Doré, and V. Savin, "Design of MIMO Systems Using Energy Detectors for Sub-TeraHertz Applications," in *2020 IEEE 31st International Symposium on Personal, Indoor and Mobile Radio Communications (PIMRC)*, 2020, pp. 1–6

Chapter 6

Parallelization of Envelope Detection Receivers

Our intention in this part of the manuscript is to propose high-rate and cost-efficient transceiver architectures for sub-TeraHertz communications. Subsequently, we study non-coherent transceivers with low spectral efficiency. In the previous chapter, we have studied the design of Multiple-Input Multiple-Output (MIMO) systems based on energy detection receivers. Not subject to phase impairments, these systems enable to benefit from spatial multiplexing and can achieve high-rate communications in sub-THz frequencies. In this chapter, our objective remains the same, still a different approach is investigated. The approach developed in this chapter exploits more original signal processing techniques. The sub-THz spectrum offers unprecedentedly large bands. We hence consider the use of these large bandwidths to achieve high data rates communications with non-coherent transceivers. It involves important constraints on Analog-to-Digital Converters (ADC) especially in the case of embedded systems with low-complexity physical layers. The implementation of converters in embedded systems is subject to a trade-off between sampling frequency, power consumption and quantization resolution. The width of the aggregated frequency bands is restricted by the sampling rates of current converters technologies. The communication throughput is then limited by the analog-to-digital conversion. This chapter deals with this trade-off between system performance and architecture constraints. To illustrate the design paradigm of this chapter, the enhanced hot-spot, delivering high-rate download from a base station to user terminals in a short-range, is representative of the considered scenario.

The objective of this chapter is to investigate the parallelization of the Radio-Frequency (RF) architecture of sub-THz receivers using envelope detection. In doing so, we propose valuable techniques to relax the constraints on ADC. Similarly to the previous chapter, we consider a single-carrier communication systems with a double sideband spectrum using envelope modulation at the transmitter and envelope detection at the receiver. Within the chapter, we first focus on the representation of non-negative signals – for transceivers based on envelope modulation and detection. The definition of an appropriate Hilbert space is examined. Our goal is to provide the analytical tools to design efficient transmission techniques for envelope modulation schemes. Later, a new receiver architecture for non-coherent sub-THz systems is proposed and analyzed: the *RAFAE* scheme. This acronym stands for Receiver based on the Analog Fourier Analysis of the Envelope. The proposed architecture is designed for pulse-based communications and targets high-rate applications. This analog-oriented receiver allows the use of sampling rates lower than the symbol rate, and hereby, relaxes constraints on ADC.

6.1 An Algebraic Framework for Envelope Modulation

The objective of this chapter is to relax constraints on the analog-to-digital conversion for non-coherent sub-THz receivers. In particular, we attempt in this section to reduce the ADC sampling rates

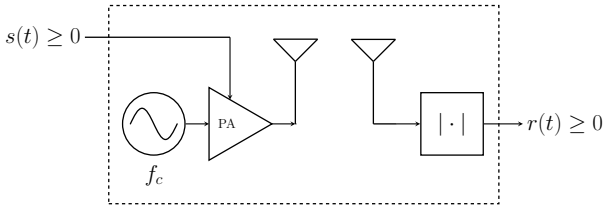

Figure 6.1 – *Frequency translations performed with envelope modulation and detection*

with the use of multiplexing techniques. To do so, our approach is to provide the analytical tools to design transmission methods based on envelope modulation and demodulation. We consider amplitude modulation at the transmitter and envelope detection at the receiver – either implemented with a diode, or by combining a self-mixer and a low-pass filter. This type of architecture are used in a wide range of applications: pulse-based Ultra-WideBand (UWB) systems, Visible Light Communications (VLC), optical systems, *etc.* For such transceiver architectures, the potential multiplexing techniques include: sub-bands frequency channelization or time division multiplexing. Nevertheless, not all multiplexing schemes can be used with the considered architecture, *e.g.* Orthogonal Frequency Division Multiplexing (OFDM) or Code Division Multiplexing (CDM). Indeed, we study here the transmission of signals modulated in amplitude whose values are real and non-negative. Generally, signal-spaces $\mathcal{L}^2$ and ℓ^2 are used to represent communication signals. The Hilbert space $\mathcal{L}^2$ (resp. ℓ^2) denotes the set of square-integrable real or complex valued functions, *i.e.* continuous-time signals, (resp. the set of square-summable sequences, discrete-time signals) equipped with the usual inner product $\langle \cdot, \cdot \rangle_2$. They provide powerful analytical tools for real and complex valued signals and have lead to the design of numerous efficient transmission schemes. Nonetheless, these spaces are not particularly well-suited to non-negative signals and yield a limited analytic description. We claim that a dedicated theoretical framework would provide the analytical tools to design new multiplexing schemes and evaluate existing ones. This motivates us to introduce an appropriate Hilbert space to represent non-negative real-valued signals. It enables us to redefine fundamental properties and operators for non-negative signals: orthogonality, projection, *etc.* Then, we present an application of the proposed framework. It is demonstrated that constraints on embedded ADC may be relaxed with the use of orthogonal non-negative waveforms. Altogether, our results show that the introduced framework provides efficient tools to design multiplexing schemes adapted to non-coherent sub-THz systems.

6.1.1 System Model

Transmitter: Sub-THz systems based on coherent receivers suffer from severe phase impairments issued by oscillators [41]. To perform a frequency translation from passband to baseband without impact of phase impairments, using envelope detection at the receiver is a relevant solution. In addition, envelope modulation at the transmitter allows an efficient use of power amplifiers [77]. We consider here a communication system based on envelope modulation and detection as depicted in Figure 6.1. At the transmitter, the band-limited modulating signal is denoted $s(t)$ and lies in $\mathbb{R}_{\geq 0} = \{s(t) \in \mathbb{R},\ s(t) \geq 0\}$. The transmitted signal at carrier frequency f_c is then expressed by

$$x(t) = s(t) \cdot \sqrt{2}\cos(2\pi f_c t + \phi(t)), \tag{6.1}$$

where $\phi(t)$ represents the oscillator Phase Noise (PN). Further, we consider a digital modulation such that the modulating signal is defined by

$$s(t) = \sum_{\tau \in \mathbb{Z}} s[\tau] \cdot \frac{\Pi\left(\frac{t}{T_s} - \tau - \frac{1}{2}\right)}{\sqrt{T_s}},\ t \in \mathbb{R}, \tag{6.2}$$

where $s[\tau] \in \mathbb{R}_{\geq 0}$ is the τ-th modulated symbol with duration T_s and belongs to the constellation $\mathcal{C}$, and $\Pi(t)$ is the rectangular pulse shaping function.

Channel: Recent measurement campaigns [9] have shown that the Line-of-Sight (LoS) component prevails in sub-THz channels. Accordingly, we consider a frequency-flat channel, further assumed to be equalized. Subsequently, we study a waveform corrupted by Additive White Gaussian Noise (AWGN). The received signal is given by

$$y(t) = x(t) + w(t), \tag{6.3}$$

where $w(t)$ is a zero-mean real Gaussian process with spectral density $2\sigma_w^2$. The noise $w(t)$ is filtered at the input of the envelope detector and is hence band-limited. Hereafter, we will refer to Eq. (6.3) as the Non-Negative Channel (NNC).

Receiver: The down frequency translation from passband to baseband is realized at the receiver by an envelope detector. Typically, envelope detectors rely on an self-mixer combined with a low-pass filter. First, multiplying the signal by itself yields

$$x(t)^2 = s(t)^2 \cdot \left[1 + \cos(4\pi f_c t + 2\phi(t))\right]. \tag{6.4}$$

Then, it is sufficient to filer images at $2f_c$ and take the square root in order to recover the signal of interest $s(t)$. The details on the implementation of envelope detectors exceed the scope of our work though. It is hence assumed that the detector perfectly demodulates the envelope $r(t)$ of the received signal $y(t)$. Hereafter, the received symbols $r[\tau] \in \mathbb{R}_{\geq 0}$ are obtained by integrating and sampling as follows

$$r[\tau] = \int_{\tau T_s}^{\tau T_s + T_s} r(t)dt. \tag{6.5}$$

We further consider that the receiver evaluates symbol estimates using a Maximum Likelihood (ML) detection criterion. The estimated symbols are hence expressed by

$$\hat{s}[\tau] = \arg\max_{s \in \mathcal{C}} p(r[\tau]|s), \tag{6.6}$$

where p denotes the channel likelihood function.

6.1.2 Definition of the non-negative Hilbert space

6.1.2.1 Motivations

Hilbert spaces provide an efficient framework for the development of communication systems. Linear signal analysis, processing and reconstruction are entirely developed upon the properties of Hilbert spaces. For instance, optimal filtering exploits the concept of orthogonality, meanwhile the projection theorem is used in any approximation problem. Nonetheless, conventional algebraic structures are primarily designed for real-valued signals and are not well-suited to envelope modulation. By means of example, it is difficult for a set of non-negative signals to be orthogonal with the usual inner product of real functions $\langle \cdot, \cdot \rangle_2$. A common set of orthogonal signals with non-negative values is the set of pulse slots disjoint in time. This set is exploited as an orthogonal modulation in the Pulse-Position Modulation (PPM), or as a multiplexing scheme in Time Division Multiple Access (TDMA). We intend in this work to define an algebraic framework that could enable the design of new envelope modulation schemes adapted to sub-THz communications. To do so, non-negative waveforms, whose values lie in $\mathbb{R}_{\geq 0}$, are represented within a Hilbert space. This space is denoted H_ρ for continuous waveforms and h_ρ for discrete signals. Moreover, we also desire to exploit the signal processing techniques developed

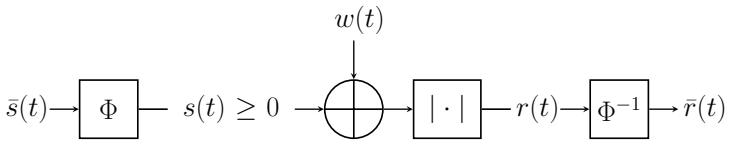

Figure 6.2 – *Illustration of the non-negative channel*

for real-valued signals. Therefore, the Hilbert space H_ρ (resp. h_ρ) is defined by *transport of structure* of the signal-space $\mathcal{L}^2$ (resp. ℓ^2 in the discrete case). The transport of structure $\Phi : \mathcal{L}^2 \to H_\rho$ relies on a bicontinuous function Φ in order to bond real-valued waveforms to non-negative ones. The use of map Φ in the NNC is depicted in Figure 6.2. Here and subsequently, we write $\mathcal{L}^2$ the Hilbert space $\big(\mathcal{L}^2([0,T_s]), \langle\cdot,\cdot\rangle_2\big)$, the vector space of square-integrable functions with domain $[0,T_s]$ equipped with the usual inner product of real functions, *i.e.* $\langle f,g\rangle_2 = \int_0^{T_s} f(t)g(t)^* dt$. Similarly, ℓ^2 denotes the Hilbert space of square-summable sequences. We first present the transport of structure of Hilbert spaces and then detail the definition of H_ρ. I would like to thank Pr. Grégory Berhuy from the Mathematics Department of the Fourier Institute, of Université Grenoble Alpes for his collaboration on the elaboration of the following paragraphs.

6.1.2.2 Transport of structure and Hilbert spaces

From vector space V_1 to V_2: We first consider two sets S_1, S_2 and a homeomorphism $\Phi : S_1 \to S_2$. Further, the set S_1 equipped with vector addition $+$ and scalar multiplication $\times$ over the field F defines a vector space $V_1 = (S_1, +, \times)$. We next study $V_2 = (S_2, \oplus, \otimes)$ the set S_2 equipped with the vector addition $\oplus$ and the scalar multiplication $\otimes$ over field F defined as follows. Set $u_1, v_1 \in V_1$ and $\lambda \in F$. We denote $u_2 = \Phi(u_1), v_2 = \Phi(v_1) \in V_2$, then the vector addition and the scalar multiplication are respectively defined by

$$u_2 \oplus v_2 = \Phi(u_1 + v_1), \tag{6.7}$$

$$\lambda \otimes u_2 = \Phi(\lambda \times u_1). \tag{6.8}$$

Proposition 1: *$V_2 = (S_2, \oplus, \otimes)$ is a vector space over the field F.*

Proof. Proposition 1 is easily proven by showing that V_2 satisfies the eight axioms of a vector space. □

From Hilbert space H_1 to H_2: Let the inner product $\langle\cdot,\cdot\rangle_1 : V_1 \times V_1 \to F$ such that $H_1 = (V_1, \langle\cdot,\cdot\rangle_1)$ is a Hilbert space. Subsequently, the set S_1 is a complete metric space when equipped with the distance induced from the inner product $d_1(u_1, v_1) = \sqrt{\langle u_1 - v_1, u_1 - v_1\rangle_1}$. We next evaluate $H_2 = (V_2, \langle\cdot,\cdot\rangle_2)$, where the map $\langle\cdot,\cdot\rangle_2 : V_2 \times V_2 \to F$ is defined by

$$\langle u_2, v_2\rangle_2 = \langle \Phi^{-1}(u_2), \Phi^{-1}(v_2)\rangle_1 = \langle u_1, v_1\rangle_1. \tag{6.9}$$

Proposition 2: *$H_2 = (V_2, \langle\cdot,\cdot\rangle_2)$ is an inner product space.*

Proof. Proposition 2 is easily proven by showing that H_2 satisfies the three axioms of an inner product space. □

It follows that H_2 defines a norm $\|\cdot\|_2$ and a metric $d_2(\cdot,\cdot)$ upon its inner product expressed by:

$$\|u_2\|_2 = \sqrt{\langle u_2, u_2\rangle_2}, \tag{6.10}$$

$$d_2(u_2, v_2) = \sqrt{\langle u_2 \oplus \neg v_2, u_2 \oplus \neg v_2\rangle_2}, \tag{6.11}$$

where $\neg v_2$ stands for the opposite of vector v_2, *i.e.* $\neg v_2 = \Phi(-v_1)$.

Proposition 3: *$H_2 = (V_2, \langle\cdot,\cdot\rangle_2)$ is a Hilbert space.*

Proof. To prove that $H_2 = (V_2, \langle\cdot,\cdot\rangle_2)$ is a Hilbert space, it is sufficient to show that (S_2, d_2) is a complete metric space since $(V_2, \langle\cdot,\cdot\rangle_2)$ is already proved to be an inner product space. To do so, we exploit the property that (S_2, d_2) and (S_1, d_1) are isometric. Isometry preserves completeness – more precisely, uniformly continuous function maps Cauchy sequences into Cauchy sequences – and (S_1, d_1) is known to be complete. It follows immediately that (S_2, d_2) is a complete metric space. □

Properties of transport of structure: The introduced definition of H_2 upon H_1 is referred to as a transport of structure whose properties are listed below.

Theorem 1: *Let the transport of structure $\Phi : H_1 \to H_2$, then the following properties are sastified:*

1. *Φ is surjective and preserves the inner product.*
2. *Φ is surjective and isometric.*
3. *Φ maps an orthonormal basis for H_1 into an orthonormal basis for H_2.*

Proof. We first recall that H_2 is defined such that Φ is surjective and preserves the inner product. Therefore, property 1. is satisfied and the other properties follow directly. This theorem may also be demonstrated from the observation that $\Phi : H_1 \to H_2$ is a bounded linear operator by definition of H_2. For a deeper discussion of operators on Hilbert spaces, we refer the reader to [95]. □

6.1.2.3 Definition of the envelope Hilbert space H_ρ

We will now use the previously described results on transport of structure of Hilbert spaces to define an algebraic framework for envelope modulation. As aforementioned, we also desire to rely on conventional Hilbert space $\mathcal{L}^2$. Subsequently, we define

$$\begin{aligned} \Phi : \mathcal{L}^2 &\to H_\rho, \\ : \bar{s}(t) &\mapsto s(t), \end{aligned} \tag{6.12}$$

where $\bar{s}(t)$ is a real-valued waveform. To ensure the soundness of envelope modulation, Φ is subject to the following constraint: the image of $\bar{s}(t)$ must be non-negative *i.e.* $\Phi : \bar{s}(t) \mapsto s(t) \in \mathbb{R}_{\geq 0}$. As an illustration, a DC offset may be sufficient to map a real-valued waveform onto the non-negative real space. This could also be achieved with different maps such as the exp function for instance. The Hilbert space $H_\rho = (V_\rho, \langle\cdot,\cdot\rangle_\rho)$ is defined by vector space V_ρ and inner product $\langle\cdot,\cdot\rangle_\rho$. The vector space V_ρ denotes the set $\Phi(\mathcal{L}^2([0, T_s]))$ equipped with vector addition $\oplus$ and scalar multiplication $\otimes$ over the field $\mathbb{R}$ defined by Eq. (6.7) and (6.8). Furthermore, the inner product $\langle\cdot,\cdot\rangle_\rho$ on vector space V_ρ is defined from Φ and the usual inner product of real functions $\langle\cdot,\cdot\rangle_2$ by Eq. (6.9). It is worth mentioning that Hilbert space H_ρ can be extended to higher dimensions by Cartesian product. It is sufficient to define vector space operations component-wise and to set the inner product as the sum of the inner products associated to the different components. As represented in Figure 6.2, the NNC may also be expressed by

$$\bar{r}(t) = \Phi^{-1}\left(\left|\Phi\big(\bar{s}(t)\big) + w(t)\right|\right), \tag{6.13}$$

where $\bar{s}(t)$ and $\bar{r}(t)$ are real-valued signals. In a similar manner to the definition of H_ρ upon $\mathcal{L}^2$ for continuous waveforms, the envelope Hilbert space h_ρ for discrete signals is defined upon ℓ^2.

6.1.2.4 Orthonormal sequences in H_ρ

Orthonormal sequences play an important role in communication systems to design orthogonal modulation or multiplexing schemes. We here introduce them in the context of H_ρ. A set $\boldsymbol{\psi} = \{\boldsymbol{\psi_n}\}_{1 \leq n \leq N}$

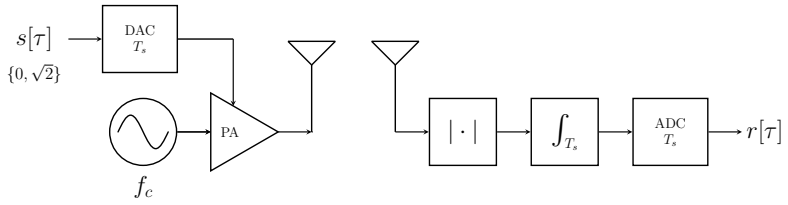

Figure 6.3 – *Illustration of a serial OOK transceiver*

of N vectors in H_ρ is orthonormal if it satisfies $\forall n_1, n_2$, $\langle \boldsymbol{\psi_{n_1}}, \boldsymbol{\psi_{n_2}} \rangle_\rho = \delta_{n_1 n_2}$. Then, the *synthesis operator* refers to the linear isomorphism from $\mathbb{R}^N$ onto H_ρ defined by

$$\varphi : \boldsymbol{\lambda} \mapsto \boldsymbol{u} = \lambda_1 \otimes \boldsymbol{\psi_1} \oplus \cdots \oplus \lambda_N \otimes \boldsymbol{\psi_N}, \tag{6.14}$$

where $\boldsymbol{u} \in H_\rho$ and $\boldsymbol{\lambda} = (\lambda_1, \cdots, \lambda_N) \in \mathbb{R}^N$. We may also use the notation $\boldsymbol{u} = (\boldsymbol{\lambda})_{\boldsymbol{\psi}}$ to define a vector $\boldsymbol{u}$ by its coordinates $\boldsymbol{\lambda}$ relatively to $\boldsymbol{\psi}$. Conversely, given a vector $\boldsymbol{u} \in H_\rho$ the *analysis operator* is the inverse map $\varphi^{-1} : H_\rho \to \mathbb{R}^N$ that evaluates coordinates $\boldsymbol{\lambda}$ of $\boldsymbol{u}$ with regards to basis $\boldsymbol{\psi}$. By orthonormality of $\boldsymbol{\psi}$, we have

$$\lambda_n = \langle \boldsymbol{u}, \boldsymbol{\psi_n} \rangle_\rho. \tag{6.15}$$

Theorem 1 gives that a sequence $\boldsymbol{\psi}$ is orthonormal in H_ρ if and only if the sequence $\bar{\boldsymbol{\psi}} = \Phi^{-1}(\boldsymbol{\psi})$ is orthonormal in $\mathcal{L}^2$. Accordingly, any orthonormal sequence in $\mathcal{L}^2$ can be exploited upon envelope modulation with an appropriate map Φ. In addition to the aforementioned example on PPM, this result entails that new orthogonal modulations or multiplexing schemes can be designed with non-negative waveforms. By means of illustration, it is interesting to mention the DC-biased OFDM, a multiplexing scheme frequently used in VLC systems. Using the proposed framework, this multiplexing scheme can directly described with $\bar{\boldsymbol{\psi}}$ the Fourier basis and Φ a DC offset. Besides, the introduced framework can be used to develop novel and more efficient solutions.

6.1.3 Applications of the proposed framework

The objective of this section is to give the reader some application examples. In particular, it aims to illustrate that the proposed framework enables the design of efficient envelope modulation schemes adapted to sub-THz communications. Subsequently, the focus is neither on thorough performance evaluation of the described system nor on details of implementation. One of the contemplated applications for the sub-THz communications is the enhanced hot-spot scenario, also called kiosk. A short-range hot-spot supplies users with a high-rate downlink, refer to Chapter 1 for more details. Receiver architectures must remain simple in order to be embedded into users' terminals. Even if low complexity schemes are implemented, *e.g.* On-Off Keying (OOK), it is difficult for embedded ADC to sample several GHz of band. Our objective is therefore to relax the constraints on ADC. We show that the sampling rate of ADC can be made twice slower by multiplexing transmitted symbols on two orthogonal non-negative waveforms.

For the purpose of comparison, we first describe a pulse-based transceiver with a serial architecture as represented in Figure 6.3. The considered modulation scheme is OOK. Symbols $s_\tau \in \{0, \sqrt{2}\}$ are transmitted using a rectangular pulse shaping. As illustrated in Figure 6.3, the received symbols $\hat{r}[\tau]$ are obtained by integrating signal $r(t)$ and sampling every τT_s instants. In this case, the sampling rate $1/T_s$ of the ADC is equal to the symbol rate. Then the receiver estimates transmitted symbols $s[\tau]$ with the ML decision rule.

Conversely, we now present an architecture where the receiver is parallelized and the ADC sampling rate is half the symbol rate. The sampling rate reduction is achieved by considering the modulation and demodulation of sequences of two symbols. The informative symbols $\bar{\boldsymbol{s}} = (\bar{s}[2\tau], \bar{s}[2\tau+1]) \in \{0, \sqrt{2}\}^2$

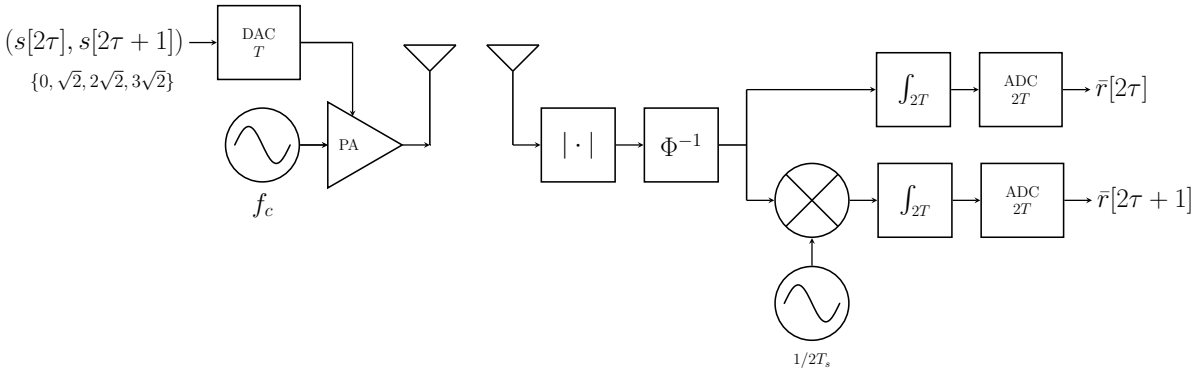

Figure 6.4 – *Illustration of a parallel OOK transceiver, with a serial transmitter and a parallel transceiver*

are mapped onto an orthogonal sequence $\boldsymbol{\psi}$ composed of vectors $\boldsymbol{\psi}_1, \boldsymbol{\psi}_2 \in h^2_\rho$. Then the transmitted symbols $\boldsymbol{s} = (s[2\tau], s[2\tau+1])$ are defined by

$$\boldsymbol{s} = (\bar{\boldsymbol{s}})_{\boldsymbol{\psi}}. \tag{6.16}$$

By way of illustration, we consider $\boldsymbol{\psi}$ to be the image of Hadamard code $\bar{\psi} = \{(1,1),(1,-1)\}$ by map $\Phi(u) = u + \sqrt{2}$, a simple DC offset. At the transmitter, mapping from $\bar{\boldsymbol{s}}$ to $\boldsymbol{s}$ is achieved by the synthesis operator introduced in Eq. (6.14)

$$\begin{aligned} \boldsymbol{s} &= \bar{s}[2\tau] \otimes \boldsymbol{\psi_1} \oplus \bar{s}[2\tau+1] \otimes \boldsymbol{\psi_2}, \\ &= \Phi\big(\bar{s}[2\tau] + \bar{s}[2\tau+1], \bar{s}[2\tau] - \bar{s}[2\tau+1]\big). \end{aligned} \tag{6.17}$$

The transmitter keeps a serial architecture, yet it no longer sends symbols belonging to $\{0, \sqrt{2}\}$ but $s[\tau] \in \{0, \sqrt{2}, 2\sqrt{2}, 3\sqrt{2}\}$. Incidentally, the transmitter complexity is not an issue in the considered scenario as it is implemented within a base station. It is in general easier to realize Digital-to-Analog Converters (DAC) with high sampling rates than ADC. At the receiver side, received symbols may be obtained from the received sequence $\boldsymbol{r} = (r[2\tau], r[2\tau+1])$ by the analysis operator defined in Eq. (6.15)

$$\bar{r}[2\tau] = \langle \boldsymbol{r}, \boldsymbol{\psi_1} \rangle_\rho, \quad \text{and} \quad \bar{r}[2\tau+1] = \langle \boldsymbol{r}, \boldsymbol{\psi_2} \rangle_\rho. \tag{6.18}$$

Nonetheless, these projections on $\boldsymbol{\psi}$ may also be realized within the analog domain since a Hadamard code may actually be regarded as the discrete Fourier transform on the two-element additive group $\mathbb{Z}/(2)$. This requires first to evaluate $\bar{r}(t) = \Phi^{-1}(r(t))$ and second to project $\bar{r}(t)$ onto two signals, one constant and the other oscillating with frequency $1/2T_s$. As depicted in Figure 6.4, these projections are expressed by

$$\bar{r}[2\tau] = \int_{2\tau T_s}^{2\tau T_s + 2T_s} \bar{r}(t) dt, \tag{6.19}$$

$$\bar{r}[2\tau+1] = \int_{2\tau T_s}^{2\tau T_s + 2T_s} \bar{r}(t) \cdot \frac{\pi}{2} \sin\left(\frac{2\pi t}{2T_s}\right) dt. \tag{6.20}$$

In the latter equations, it should be highlighted that the sampling rate is $1/2T_s$, half the symbol rate. The receiver finally obtains symbol estimates from these projections by using the ML decision rule, *i.e.*

$$\hat{\bar{s}}[2\tau] = \arg\max_{\bar{s} \in \mathcal{C}} p\big(\bar{r}[2\tau] | \bar{s}\big), \quad \text{and} \quad \hat{\bar{s}}[2\tau+1] = \arg\max_{\bar{s} \in \mathcal{C}} p\big(\bar{r}[2\tau+1] | \bar{s}\big). \tag{6.21}$$

This achieves the desired objective. For a fixed symbol rate, the receiver demodulates the symbols based on ADC whose sampling rates are twice slower. Furthermore, this can be easily extended to N

orthogonal non-negative waveforms, and thus, to systems with N times slower ADC. Still, it is straightforward to show that the presented multiplexing scheme entails a performance loss in Signal-to-Noise Ratio (SNR) due to the DC offset in Φ. Precisely, to achieve a Bit Error Rate (BER) of 10^{-6}, the use of the parallelized transceiver induces a performance loss of $\simeq 4.77$ dB in SNR in comparison to the serial transceiver. Though such performance loss may be considered significant, this scheme is unoptimized and could be improved. Other choices of map Φ can be more efficient. We have presented it in order to illustrate the potential applications of the introduced framework to sub-THz communications. Furthermore, another direct application of the proposed framework is presented in our paper [37] where an In-phase/Quadrature (I/Q) signal is transmitted using envelope modulation and detection to achieve PN robustness at the detriment of a performance loss in SNR.

6.1.4 Conclusion on the algebraic framework

We have proposed in this section an algebraic framework for envelope modulation. Non-negative real waveforms have been represented within appropriate Hilbert spaces H_ρ and h_ρ. These spaces are defined by transport of structure of usual signal-spaces $\mathcal{L}^2$ and ℓ^2 which enables to exploit existing schemes developed for real-valued waveforms upon envelope modulation. It is further shown that the introduced framework may be used to design efficient transmission schemes for non-coherent sub-THz communications. By way of illustration, we have demonstrated that the constraints on embedded ADC may be relaxed with the use of orthogonal non-negative waveforms. More or less directly, the research findings presented in this section have lead to the deposit of one patent [39]. In this patent, the proposed transceiver architecture enables a coherent demodulation using a combination of two envelope detectors at the receiver and a DC offset at the transmitter, and thereby, alleviates the impact of phase impairments.

This work has been conducted while targeting sub-THz applications with low-complexity physical layers *e.g.* the enhanced hot-spot. Nevertheless, our findings are relevant to multiple non-coherent communication systems, and in particular, systems based on the transmission of amplitude, energy or intensity signals. We could mention optical systems, UWB radio, or even VLC. For instance, it can be remarked that the DC-biased OFDM, a commonly used multiplexing scheme in VLC, can be easily expressed using the proposed framework.

We remind here that this contribution remains an introductory work proposing an analytical framework. It should hence be followed by some investigations on the design of non-coherent multiplexing schemes for sub-THz systems, and as well, by the evaluation of potential solutions. In addition, the proposed framework could also be extended. As remarked in the previous chapter, polar RF transceivers – transmitting the amplitude and phase of signals as independent streams – are a relevant architecture for sub-THz communications. To fully describe polar RF transceivers, the proposed framework, for amplitude-only signals, could be complemented by an analytical description of phase-only signals.

Further, it is worth comparing this amplitude-only framework H_ρ to the analytical framework p^2 previously introduced. In Part II, the analytical framework p^2, a metric space describing signals in the amplitude-phase domain, has been proposed for the purpose of detection and estimation. For this purpose, measuring distances is fundamental, thus we have focused on complete metric spaces. Conversely, the intention in this chapter is to provide orthogonal sequences for multiplexing. With regard to this objective, the definition of an inner-product space, and further, of a Hilbert space is essential. In summary, we have proposed two distinct analytical frameworks for two distinct purposes. It highlights that appropriate signal representation is one of the foundations of our research.

We have shown in this section that converters sampling frequencies of non-coherent sub-THz receivers can be reduced by using multiplexing techniques. In the next section, we also investigate the relaxation of converters constraints. Nevertheless, we develop another perspective of analog parallelization of RF architectures. Namely, we propose a receiver architecture that partitions the signal processing related to demodulation between analog and digital domains in order to lower the requirements on the analog-to-digital conversion.

6.2 RAFAE: A receiver architecture for high-rate impulse radio with reduced sampling rates

Intentions: In this section, we are interested in relaxing the constraints on embedded converters of non-coherent sub-THz receivers. We thus propose a new receiver for sub-THz applications entitled *RAFAE* based on an analog parallelization of the RF architecture. Namely, ***RAFAE stands for Receiver based on the Analog Fourier Analysis of the Envelope***. Similarly to the previous section, we study a non-coherent single-carrier communication system using a pulse-based modulation with a double sideband spectrum. Prior to the description of the proposed receiver architecture, we introduce some of the related works and literature.

Related works: The proposed receiver is directly inspired by the one described in [96] and [25] where an estimation of a pulse delay is obtained by projecting the received signal onto double quadrature signals. The method in [96] has been designed for UWB localization. We also exploit the idea of using projections of the received signal in the analog domain. We adapt this principle to digital communication applications in sub-THz bands. The proposed architecture enables to demodulate jointly multiple consecutive symbols, and hence, to lower the sampling frequency of converters. In brief, we use a non-coherent multi-symbol detection to reduce the ADC sampling rates while achieving PN robustness. And more generally, it is worth noting that the proposed receiver architecture lie in the framework of correlator receivers, see for instance [97].

Summary: The content of this section is organized as follows. First, we introduce the system model and describe in details the proposed receiver. Thereupon, we address the design of the detection algorithm based on the ML decision rule. Second, we use the proposed scheme to design a PPM receiver with relaxed constraints on ADC. A detailed performance analysis is presented. Numerical simulations results show that near-optimal performance can be achieved with low-complexity RF architecture. Our results highlight that the proposed receiver provides, in comparison to conventional impulse radio receiver, additional degrees of freedom to adjust the trade-off between system performance and architecture complexity.

6.2.1 Principle of the proposed architecture

The proposed receiver relies on the two following key points:

1. The proposed receiver performs a ***waveform-to-vector conversion***: Within the receiver, the square of the received signal is projected onto the Fourier basis using multiple parallel branches in the analog domain before being sampled. The parallel projections are obtained by correlating the square of the received signal to a set of quadrature signals oscillating with different frequencies. The received coordinates are then used in the digital domain to estimate transmitted symbols.
2. We consider a ***multi-symbol detection***, based on the ML decision rule, which demodulates jointly multiple consecutive symbols. Then, the integration time of the analog projections can be

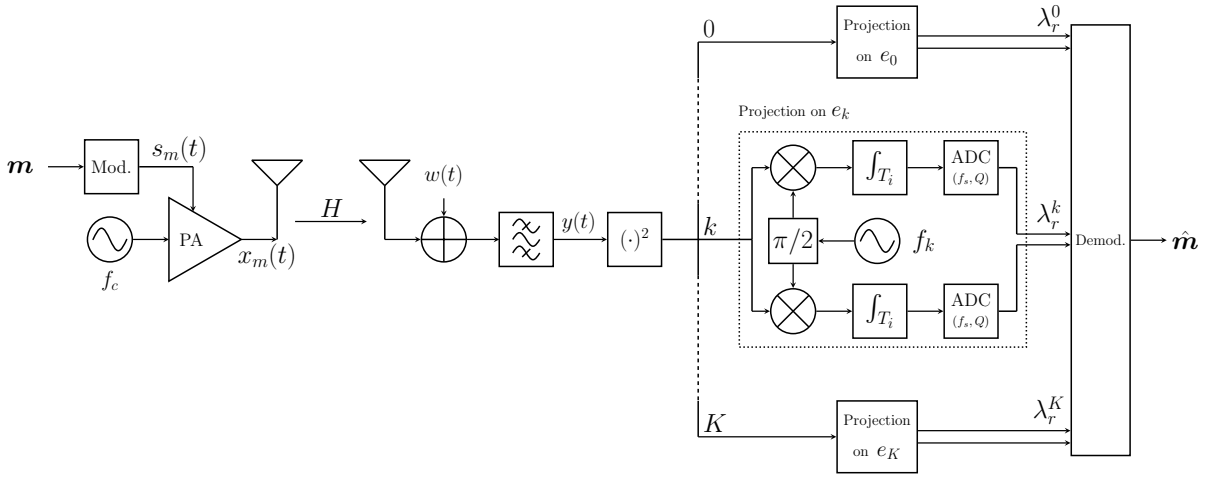

Figure 6.5 – *Block diagram of the transceiver using the proposed receiver architecture*

set to multiple symbol durations which enables to set the sampling rate lower than the symbol rate.

6.2.1.1 System description

Transmitter: The transmitter is based on envelope modulation and the architecture of its RF chain is depicted in Figure 6.5. Using envelope modulation allows a low-complexity implementation and an efficient use of power amplifiers [77]. We denote M the modulation order. Let the informative symbol $m \in [\![1, M]\!]$ be modulated by transmitting signal $s_m(t) \in \mathbb{R}_{\geq 0}$ with duration T_s. We write $s_m(t)$ the modulating signal and $x_m(t)$ the transmitted signal at carrier frequency f_c expressed by

$$x_m(t) = s_m(t) \cdot \sqrt{2}\cos(2\pi f_c t + \phi(t)), \tag{6.22}$$

where $\phi(t)$ is a stochastic process modeling the oscillator PN. This analytical representation enables us to describe pulse-based modulation schemes such as OOK, PPM, *etc.* In the following, we consider a sequence of $L \geq 1$ consecutive symbols such that we adopt the notation $\boldsymbol{m} = (m_1, \ldots, m_L) \in [\![1, M]\!]^L$.

Channel: The recent measurement campaigns have confirmed the theoretical expectations that the LoS path provides most of the energy contribution in sub-THz propagation channels. Accordingly, we assume in this work a static LoS channel model and denote H the propagation gain. At the input of the receiver RF chain, we have the double sideband signal $y(t)$ and band-limited with bandwidth $B \geq 2/T$ centered around carrier frequency f_c. The band-pass filter is required to prevent the spectral folding of noise, see Eq. (6.4). The received signal is expressed by

$$y(t) = \sqrt{H} \cdot x_m(t) + w(t), \tag{6.23}$$

where $w(t)$ is a band-limited continuous Gaussian process with spectral density N_0 modeling thermal noise in the receiver.

Receiver: The receiver performs a waveform-to-vector conversion which is illustrated in Figure 6.5 and can be described as follows. The received signal $y(t)$ is squared, then parallelized to be correlated to a set of quadrature signals oscillating at different frequencies and finally is sampled by the converters. The projection signal of each branch is composed of in-phase and quadrature components related to each other by the Hilbert transform. For this reason, we use hereafter the complex representation to

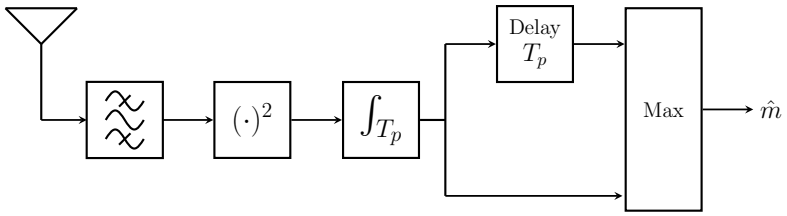

Figure 6.6 – *Architecture of a conventional* 2*-PPM receiver*

describe the projection and the received coordinates. The real part (resp. imaginary part) corresponds to the in-phase component (resp. quadrature component). Accordingly, the square of the received signal $y(t)^2$ is projected in the analog domain onto the Fourier basis $\boldsymbol{e} = \{e_k(t)\}_{0\leq k\leq K}$. The observed coordinate λ_r^k on the k-th branch, $k \in [\![0, K]\!]$, is obtained after integration and sampling as follows

$$\lambda_r^k = \int_0^{T_i} y^2(t) \cdot e_k(t)^* dt, \tag{6.24}$$

where $e_k(t) = \exp\left(j2\pi\frac{k}{T_i}t + j\theta_k\right)$ with $\theta_k \in [-\pi, \pi)$ a phase offset[1]. The digital demodulation relies on the observed vector $\boldsymbol{\lambda}_r = (\lambda_r^0, \cdots, \lambda_r^K) \in \mathbb{C}^{K+1}$. Regarding Eq. (6.24), it is worth mentioning that the integration time may be larger than the symbol duration, *i.e.* $T_i = L \cdot T_s \geq T_s$. In this case, consecutive symbols are jointly demodulated and the sampling rate of the converters $f_s = 1/T_i$ is reduced. It can be easily shown that the system can be described as a $K+1$ dimensional complex channel by

$$\boldsymbol{\lambda}_r = H \cdot \boldsymbol{\lambda}_m + \boldsymbol{\lambda}_w, \tag{6.25}$$

where $\boldsymbol{\lambda}_m$ denotes the transmitted point of $\mathbb{C}^{K+1}$ modulating symbol $\boldsymbol{m}$ and $\boldsymbol{\lambda}_w$ models the impact of noise. We refer to the set of all possible transmitted points $\boldsymbol{\lambda}_m$ as constellation $\mathcal{C} \subset \mathbb{C}^{K+1}$ known or estimated by the receiver with $|\mathcal{C}| = M^L$. In the following section, our purpose is to design the detection algorithm to estimate the sent symbol $\boldsymbol{m}$ from vector $\boldsymbol{\lambda}_r$. To do so, we derive the probability distribution of observations $\boldsymbol{\lambda}_r$ by expressing analytically $\boldsymbol{\lambda}_m$ and $\boldsymbol{\lambda}_w$. Nonetheless, let us first present a practical example to gain more insight on the transceiver operation and its advantages.

Practical example, demodulation of a 2-PPM: In this paragraph, we study the demodulation of a 2-PPM using the proposed receiver architecture. We illustrate here without further analytical analysis the receiver principle, properties and advantages. The two possible transmitted signals with $m \in [\![1, 2]\!]$, depicted in Figure 6.7, are expressed by

$$s_m(t) = \frac{\prod\left(\frac{t}{T_p} - m + \frac{1}{2}\right)}{\sqrt{T_p}}, \tag{6.26}$$

where T_p denotes the pulse duration such that $T_p = T_s/M$ and $\Pi(t)$ is the unit pulse – or also referred to as the rectangular function. With regard to the architecture of conventional PPM receivers [1], the energy of the received signals is measured over all possible pulse positions. Then, the position with the maximum energy is used to estimate the transmitted symbol m. In this case, the sampling rate of converters is $1/T_p = 2/T_s$. The architecture of a conventional 2-PPM receivers is depicted in Figure 6.6.

Conversely, the proposed architecture allows to set the integration time as the duration of multiple pulses. In this example, we consider an integration time equal to a symbol duration, *i.e.* $T_i = T_s = 2 \cdot T_p$.

[1]It is worth mentioning that the frequencies of projection signals k/T_i are small – of the order of the GHz – in comparison to the carrier frequency f_c. Accordingly, we can assume that the projection signals are not corrupted by phase impairments.

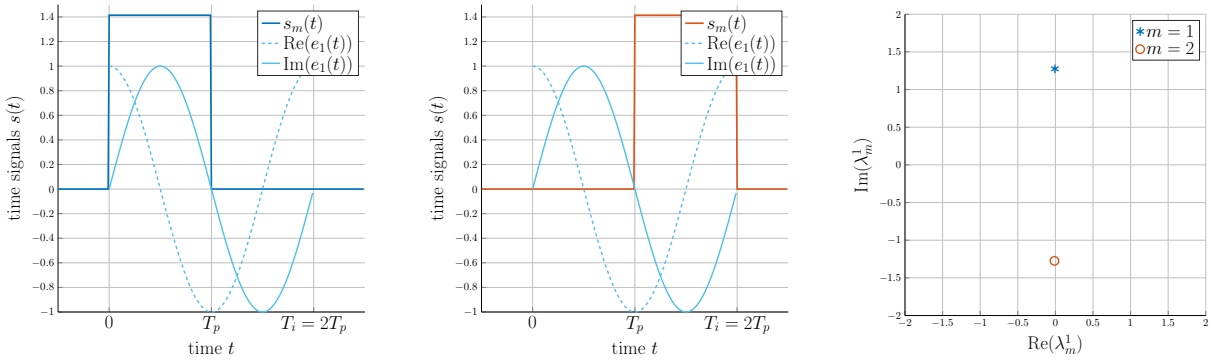

(A) *signals in time for* $m = 1$ (B) *signals in time for* $m = 2$ (C) λ^1_m *in the complex plane*

Figure 6.7 – *Projection onto* e_1 *of possible transmitted signals for a* 2*-PPM*

This allows to reduce by a factor 2 the sampling rate of converters, *i.e.* $f_s = 1/2T_p = 1/T_s$. Regarding the proposed architecture, Figure 6.7a and 6.7b illustrate the projection of the two possible transmitted signals onto signal e_1. Figure 6.7c depicts the possible noiseless observations λ^1_m in the digital domain, *i.e.* the constellation $\mathcal{C}$ in the complex plane. It can be remarked that the two different codewords lead to two different projections λ^1_m, which is used to differentiate the transmitted symbols from one another. This illustrates the fundamental principle of the proposed receiver architecture.

Further, one can notice on Figure 6.7c that only the imaginary part of λ^1_m is necessary to differentiate the two codewords. Then if the projection signals $\boldsymbol{e}$ are synchronized – $\forall k,\ \theta_k = 0$ – to the transmitter pulse rate, half of the projections can be dismissed – the real parts. In this case, the number of required ADC can be divided by two. Nevertheless,using quadrature signals enables to demodulate the transmitted symbols without synchronization of the receiver. When $\theta_k \neq 0$, both projections $\lambda^1_{m=1}$ and $\lambda^1_{m=2}$ are subject to the same phase offset. The real and imaginary parts are in this case useful to differentiate the two codewords. Thereby, we have illustrated one of the fundamental trade-offs of the RAFAE architecture: increasing the number of converters enables to relax the synchronization constraints, whereas having a strict synchronization enables to reduce the number of ADC. Eventually, this example is not sufficient to present some performance results since the demodulation algorithm is yet to be designed with regard to the probability distributions of received vectors.

6.2.1.2 *Detection algorithm design*

Closed-form expression of received vector λ_r**:** We have shown previously that the channel of the considered transceiver can be expressed as

$$\boldsymbol{\lambda}_r = H \cdot \boldsymbol{\lambda}_m + \boldsymbol{\lambda}_w. \tag{6.27}$$

However, this does not yield the probability distribution of received observations such that we are not yet in a position to design the receiver detection algorithm. To do so, we study the distribution of the noise term $\boldsymbol{\lambda}_w$ and derive the closed-form expression of the transmitted point $\boldsymbol{\lambda}_m$. By Eq. (6.24), the received observation on branch k is given by

$$\lambda^k_r = \int_0^{T_i} \left(\sqrt{H} \cdot x_m(t) + w(t)\right)^2 \cdot e_k(t)^* dt, \tag{6.28}$$

$$= H \int_0^{T_i} x_m(t)^2 \cdot e_k(t)^* dt + 2\sqrt{H} \int_0^{T_i} x_m(t) w(t) \cdot e_k(t)^* dt + \int_0^{T_i} w(t)^2 \cdot e_k(t)^* dt, \tag{6.29}$$

$$= H \cdot \lambda^k_m + 2\sqrt{H} \cdot \lambda^k_{xw} + \lambda^k_{ww}. \tag{6.30}$$

In contrast to Eq. (6.25), we can see that the noise term λ_w^k can be decomposed as a sum of two noise components: λ_{xw}^k a mixed signal-noise contribution and λ_{ww}^k a squared noise contribution. The expressions of λ_m^k, λ_{ww}^k and λ_{xw}^k are derived in Appendix B and their distributions analyzed. The analytical developments are based on the following principle. We express signals $x_m(t)$ and $w(t)$ using Fourier series decomposition and the dimensionality theorem. It is then straightforward to express the projection of these signals onto a particular Fourier signal.

Distribution of received vectors: The main result of Appendix B is that the channel can be described, for $k \neq 0$, by

$$\lambda_r^k = H \cdot \lambda_m^k + 2\sqrt{H \cdot E_m^k} \cdot w_k + \sqrt{2(2N+1-k)} \cdot z_k, \tag{6.31}$$

where w_k and z_k are complex normally circular-symmetric distributed variables with variances N_0/T_i and $(N_0/T_i)^2$, *i.e.* $w_k \sim \mathbb{C}\mathcal{N}(0, N_0/T_i)$ and $z_k \sim \mathbb{C}\mathcal{N}(0, N_0^2/T_i^2)$. The term E_m^k represents the contribution of the modulating signal in the mixed signal-noise projection λ_{xw}^k and is defined as follows

$$E_m^k = \sum_{n=-N+k}^{N} \left| S_m\left(\frac{n}{T_i}\right) \right|^2 \cdot \frac{1}{T_i}, \tag{6.32}$$

with $S_m(f)$ the Fourier transform of signal $s_m(t)$. For the first branch , *i.e.* $k = 0$, the expression of the projection is slightly different since it is purely real. It follows from Appendix B that

$$\lambda_r^0 = H \cdot \lambda_m^0 + 2\sqrt{H \cdot 2E_m^0} \cdot w_0 + \sqrt{4(4N+2)} \cdot z_0 + 2(4N+2)\frac{N_0}{T_i}, \tag{6.33}$$

where w_0 and z_0 are Gaussian distributed with zero-mean and variances N_0/T_i and $(N_0/T_i)^2$, *i.e.* $w_0 \sim \mathcal{N}(0, N_0/T_i)$ and $z_k \sim \mathcal{N}(0, N_0^2/T_i^2)$. It is worth noting that subscripts m are used in order to denote the dependence of the possible codewords on the channel. Regarding the channel model introduced in Eq. (6.31) and (6.33), it should mentioned that the contribution of the square-noise term λ_{ww}^k is efficiently modeled as Gaussian, though it is χ^2 distributed. The degree of freedom of the χ^2 distribution is large and its variance is small in comparison to the one of the mixed signal-noise term λ_{xw}. For these reasons, the Gaussian assumption is an accurate approximation which enables to considerably simplify the detection algorithm. In the following, we define the SNR as $\frac{H \cdot \sigma_s^2}{N_0/T_s}$ where σ_s^2 is the average energy of sent signals. In other words, the SNR is the ratio of the received signal energy over the noise energy integrated during a symbol duration. Altogether, the communication channel of vector $\boldsymbol{\lambda}_r$ follows a $(K+1)$-dimensional complex circularly-symmetric Gaussian channel. To illustrate this, Figure 6.8 illustrates the simulated and modeled distributions of received coordinates for different values of k. One can observe that the approximation of a Gaussian distribution is an efficient modeling close to the observations.

Detection decision rule: We have previously concluded that the channel may be efficiently modeled as a multi-dimensional complex Gaussian channel. We are now interested in this paragraph in designing the detection algorithm related to the proposed received architecture. The demodulation is realized in the digital domain and relies on the received complex vector $\boldsymbol{\lambda}_r$. It is known [53] that for independent and equiprobable symbols the ML decision rule is the optimum detection criterion, *i.e.* minimizing the Symbol Error Rate (SER). In the present case, the ML decision rule is defined upon the channel likelihood function and detected symbols $\hat{\boldsymbol{m}}$ are expressed by

$$\hat{\boldsymbol{m}} = \underset{\boldsymbol{m} \in [\![1,M]\!]^L}{\arg\max}\ p(\boldsymbol{\lambda}_r | \boldsymbol{m}, H). \tag{6.34}$$

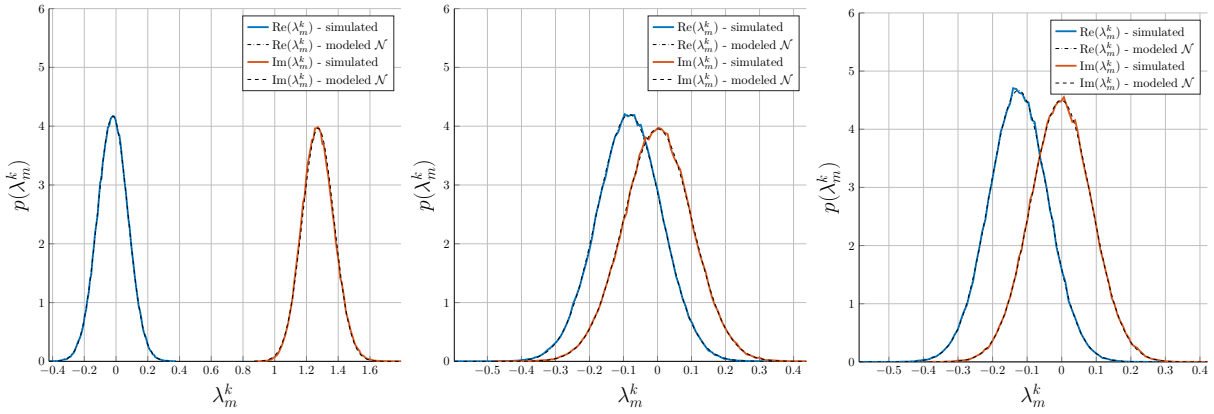

(A) $k = 1$ (B) $k = 2$ (C) $k = 6$

Figure 6.8 – *Probability distribution of* $\boldsymbol{\lambda}$

The channel is described as a $(K+1)$-dimensional complex Gaussian channel, *i.e.* $\boldsymbol{\lambda}_r \sim \mathbb{C}\mathcal{N}(\boldsymbol{\mu}, \boldsymbol{\sigma}^2)$. With regard to Eq. (6.31), the channel likelihood function is expressed as

$$p(\boldsymbol{\lambda}_r|\boldsymbol{m}, H) = \prod_{k=1}^{K}(2\pi\sigma_k^2)^{-1} \cdot \exp\left(-\frac{\left\|\lambda_r^k - \mu_k\right\|_2^2}{2\sigma_k^2}\right) \times (2\pi\sigma_0^2)^{-\frac{1}{2}} \cdot \exp\left(-\frac{(\lambda_r^0 - \mu_0)^2}{2\sigma_0^2}\right) \tag{6.35}$$

where $\|\cdot\|_2$ stands for the complex Euclidean distance – for $k = 0$ the real Euclidean distance is used. The expression of $\boldsymbol{\mu}$ and $\boldsymbol{\sigma^2}$ can be directly derived from Eq. (6.31). The ML decision rule can thus be written as

$$\hat{\boldsymbol{m}} = \underset{\boldsymbol{m}\in[\![1,M]\!]^L}{\arg\min} \frac{\left|\lambda_r^0 - \mu_0(\boldsymbol{m})\right|^2}{\sigma_0^2(\boldsymbol{m})} + \ln\sigma_0^2(\boldsymbol{m}) + \sum_{k=1}^{K}\frac{\left\|\lambda_r^k - \mu_k(\boldsymbol{m})\right\|_2^2}{\sigma_k^2(\boldsymbol{m})} + 2\cdot\ln\sigma_k^2(\boldsymbol{m}). \tag{6.36}$$

This expression fully describes the detection algorithm required to implement the digital demodulation related to the proposed receiver. Further, $(\boldsymbol{\mu}, \boldsymbol{\sigma^2})$ is a sufficient statistic of the joint probability density function described by the channel likelihood function. Hence its knowledge is essential to implement the decision rule. Two options are possible to evaluate this sufficient statistic: either it can be easily estimated with some reference pilots; or it can also be derived from the sent signal using the expressions of λ_m^k and E_m^k given in Appendix B and the estimation of the channel gain H and noise density N_0.

The ML decision rule outlined in Eq. (6.36) describes a comprehensive detection algorithm. Nevertheless, the detection algorithm can be simplified by exploiting the properties of the modulation scheme. By means of example, let us consider PPM. Then the energy of modulated signals is the same for all transmitted symbol $\boldsymbol{m}$. As a result, the 0-th coordinate λ_m^0 does not convey any information on $\boldsymbol{m}$ and can be dismissed. In addition, it also results that $\forall \boldsymbol{m},\ E_m^k = E_1^k \Rightarrow \sigma_k^2(\boldsymbol{m}) = \sigma_k^2(1)$. Subsequently, the ML decision rule simplifies to

$$\hat{\boldsymbol{m}} = \underset{\boldsymbol{m}\in[\![1,M]\!]^L}{\arg\min} \sum_{k=1}^{K}\frac{\left\|\lambda_r^k - H\cdot\lambda_m^k\right\|_2^2}{2N+1-k}. \tag{6.37}$$

In this case, it is much more intuitive to interpret the detection criterion since it is the minimization of a weighted Euclidean distance in a K-dimensional complex space, *i.e.* a Mahalanobis distance. Furthermore, the detection algorithm is implemented as a nearest neighbor search with regard to constellation $\mathcal{C}$.

6.2.2 Performance analysis and discussions

It is time to present and analyze the results of numerical simulations regarding the proposed architecture. In particular, we focus on designing an original and efficient PPM receiver. Regarding the RAFAE architecture, we highlight the implementation trade-off between the number of converters K, their sampling frequency f_s and their quantization order Q.

6.2.2.1 PPM for sub-THz communications

Let us first outline the reasons that motivate the use of PPM for sub-THz communications and then use the proposed architecture to design a parallel receiver. Sub-THz systems are critically impacted by PN [14]. For this reason, coherent communications are severely degraded and non-coherent schemes appear to be highly valuable. Furthermore, achieving high-rate communications over wireless links in the sub-THz spectrum demands a tremendous amount of power[14]. With regard to the wideband power-limited regime, using an orthogonal modulation is appropriate since it maximizes the spectral efficiency per unit of energy, *i.e.* bit/s/Hz/J [23]. Therefore, PPM is a relevant scheme choice for sub-THz communications. It enables a non-coherent demodulation robust to PN while maximizing the spectral efficiency per unit of energy. It should also be mentioned that PPM yields low-complexity RF architectures which is consistent with requirements of the envisaged complexity constrained applications. Now let us illustrate how constraints on the analog-to-digital conversion may be relaxed using the RAFAE architecture.

6.2.2.2 Numerical simulations:

We present in this paragraph the numerical simulations results regarding the performance of the proposed architecture. For different system configurations, the BER performance of the proposed receiver is compared to a conventional receiver architecture, as described in the practical example of Sec. 6.2.1.1. The simulated BER results have been obtained through Monte-Carlo simulations and are presented as function of the SNR defined by $\frac{H \cdot \sigma_s^2}{N_0/T_s}$ where σ_s^2 is the average energy of the sent signal – *i.e.* the SNR is the ratio of the received signal energy over the noise energy integrated over a symbol duration. We do not present here simulation results concerning the influence of the modulation order and the system bandwidth. The influence of these parameters are well-known results and thus are not detailed. As any orthogonal modulation, the larger the modulation order M the lower the required SNR to achieve a fixed BER. It is important to mention that using the proposed architecture the sampling rate reduction is at least $1/M$ for a M-PPM in comparison to a conventional receiver. The integration time $T_i \geq T_s = MT_p$ which leads to $f_s = 1/MT_p$ for the proposed PPM receiver, whereas for a conventional receiver the sampling rate is $1/T_p$. Therefore, with a large modulation order M, the sampling rate is significantly reduced, yet the demodulation performance is more sensitive to noise and implementation trade-offs. As for the receiver bandpass filter, using a wider bandwidth B leads to a greater amount of noise integrated in the projections and hence to some performance deteriorations.

Influence of the number of converters: We study here the influence of the number of parallel branches K on the communication performance. The degree of parallelization represented by K is directly mapped to the number of ADCs used by the receiver which is $2K$. Figure 6.9a depicts the simulated BER as function of K for two modulation order $M = 2, 4$. It should be mentioned that the more converters are used (the larger K), the closer is the performance of the proposed receiver to the optimal one achieved by the conventional receiver. This property outlines an implementation trade-off of the RAFAE architecture between the number of converters and the communication performance. In addition, we highlight that the larger the modulation order M, the larger the performance loss induced by using fewer converters (a lower K).

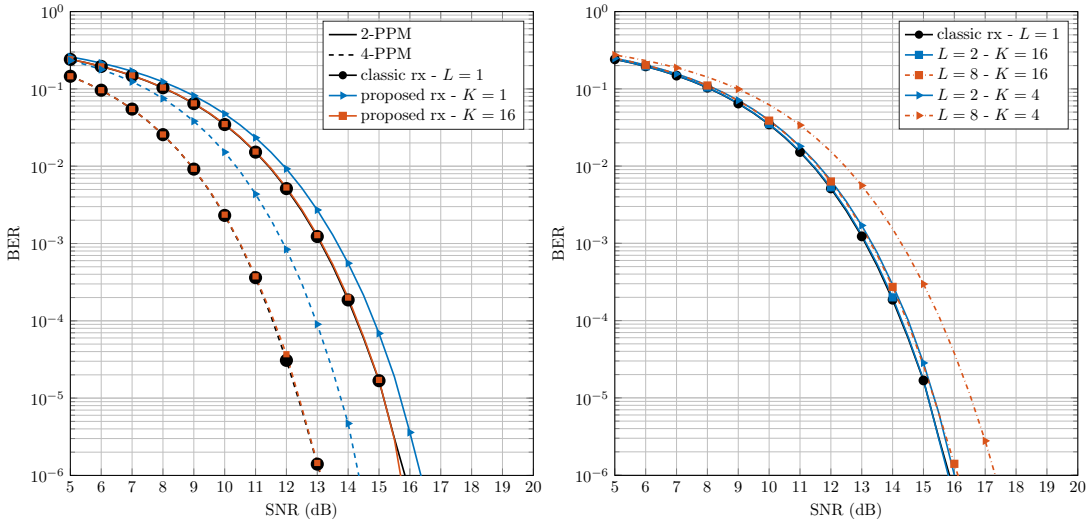

(A) *Influence of parallelization K* (B) *Influence of integration time L for a 2-PPM*

Figure 6.9 – *BER performance of the proposed PPM receiver*

Influence of the sampling rate: In this paragraph, we study the trade-off between the sampling rate reduction and the communication performance. We consider here a receiver in which several consecutive symbols are jointly demodulated, *i.e.* $L \geq 1$. Accordingly, we set the integration time $T_i = L \cdot T_s$. In this case, the sampling rate f_s is divided by a factor $1/ML$ in comparison to a conventional receiver architecture. We evaluate the impact of increasing the length of the sequence L on communication performance. Figure 6.9b outlines the simulated BER as function of the SNR for a 2-PPM with different lengths L and degree of parallelization K. We remark on these results that the lower the sampling rate (the larger L), the more converters (the larger K) are required to achieved a fixed BER performance. This may be explained by the fact that when L increases, the number of possible codewords M^L increases as well. Subsequently, the more parallel branches (the more converters) are required to differentiate the codewords.

Influence of the quantization order: Up to now, we have not considered the impact of quantization operated by the ADCs to supply the digital domain. The performance assessment of the detection algorithm has considered a perfect quantization. With the intention to better characterize the implementation of the the proposed architecture, we now introduced the quantization function in the ADCs. Further, evaluating its impact on the detection performance is to unveil the trade-off between the quantization order and the communication performance. Let us express the converters sampling and quantizing operations as follows. We define the continuous-time signal at the input of the k-th converter by

$$r_k(t) = \int_t^{t+T_i} y^2(u) \cdot e_k(u)^* du. \tag{6.38}$$

Considering a uniform quantization, the discrete-time outputs of the converters can be expressed by

$$\lambda_r^k[\tau] = \Delta \cdot \left\lfloor \frac{r_k(\tau \cdot T_i)}{\Delta} + \frac{1}{2} \right\rfloor, \ \tau \in \mathbb{Z}, \tag{6.39}$$

where Δ denotes the step size. The quality of the quantization is then defined by the quantization order Q, a power of two $Q = 2^q$, $q \in \mathbb{N}$. The quantization order Q denotes the number of thresholds implemented in each converter. Put it in a different way, coordinates λ_r^k are all quantified on q bits and the representation space is subdivided into $2^q - 1$ segments of size Δ. Figure 6.10 presents the simulated

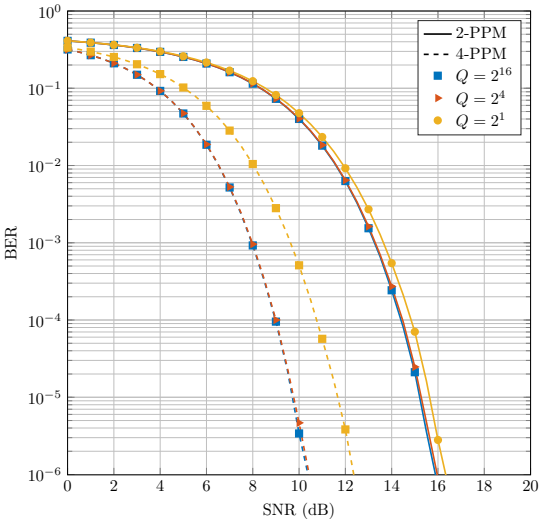

Figure 6.10 – *BER performance of the proposed PPM receiver for different quantization order Q*

BER as function of the quantization order Q for different configurations. These results highlight the fact that the larger the quantization order, the closer the performance to the optimal. Moreover, using converters with low-quantization order (low Q), the performance loss is larger when the numbers of codewords to differentiate is great (large M or large L).

6.2.3 Implementation trade-offs

Previously, the numerical simulations and the performance analysis have pointed out three implementation trade-offs to the design of a PPM receiver with the proposed architecture. These implementation trades-offs are:

(i) The higher the converter sampling rate, the better the communication performance.

(ii) The larger the number of converters, the better the communication performance.

(iii) The larger the quantization order, the better the communication performance.

Accordingly, if one of the three parameters f_s, K, Q is lowered, then it follows that the communication performance is to be deteriorated. Nonetheless, it is interesting to interpret these trade-offs as an equilibrium of the system parameters. Figure 6.11 illustrates the equilibrium between the number of converters K, their sampling rate f_s and their quantization order Q. The interpretation may be the following. If one of the three parameter is lowered, for implementation purposes, then the other parameters should be increased in order to achieve a fixed BER. For instance, if the converter sampling rate is reduced to relax the implementation constraints, then it may be possible to increase the number of converters to still achieve a similar communication performance.

To illustrate these implementation trade-offs and equilibrium, we compare the communication performance of two systems with different constraints. A numerical application regarding an implementation in the D-band is outlined in Table 6.1. Two system configurations are compared. The first system has constraints on the number of converters $2K$ and their quantization order Q. The second system has constraints on the sampling rate f_s and on the quantization order Q. The implementation loss ΔSNR is the difference in SNR between the system performance and the optimal receiver to achieve a BER of 10^{-6}. It is shown that constraining both the number of converters K and the quantization order Q leads to minor performance loss, $\Delta\text{SNR} \leq 0.25$ dB. Nonetheless, constraining the sampling rate f_s entails a larger performance deterioration. Indeed, increasing L and jointly demodulating multiple symbols, in

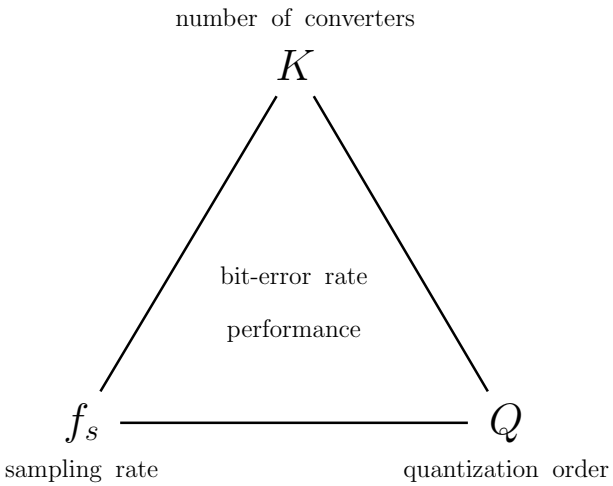

Figure 6.11 – *Illustration of the equilibrium between system parameters*

order to reduce the sampling rate, leads to an exponential increase of the number of possible codewords $\boldsymbol{m}$. Subsequently, differentiating the numerous different codewords is more sensitive to noise and to the constraints on quantization and parallelization.

Table 6.1 – *Example of applications in D-band*

Carrier frequency	f_c	145 GHz	
Bandwidth	B	2 GHz	
Modulation order	M	2-PPM	
Bit rate	$1/T_s$	500 Mbit/s	
Projection signals freq.	f_k	$k \cdot 500$ MHz	
System configuration		System 1	System 2
Constraint n°1		few converters	low sampling rate
Constraint n°2		low quantization	medium quantization
ADCs sampling rate	f_s	500 MHz	**125 MHz**
Number of ADCs	$2K$	**2**	8
Quantization order	Q	$\mathbf{2^1}$	$\mathbf{2^3}$
Implementation loss	ΔSNR	**0.25 dB**	**2 dB**

We conclude this discussion on implementation by presenting the type of converter suited to envisaged applications. The targeted high-rate applications, and high sampling frequencies, lead us to consider the use of *Flash* converters for the implementation of RAFAE receivers. The flash, also known as direct-conversion, converters are the best candidate for extremely high sampling frequency with low quantization order, and therefore, are well suited to the considered applications. In addition, this kind of converters presents a low-complexity architecture, namely it uses a simple linear voltage ladder. For this type of ADCs, the power consumption is proportional to the number of thresholds within the receiver, *i.e.* $2K \cdot Q$. Put differently, the power consumption increases exponentially with the number of quantization bits and linearly with the number of converters, *i.e.* $2K \cdot 2^q$. This property yields a key criterion to determine implementation parameters.

6.2.4 Conclusion on the proposed receiver RAFAE

To conclude this section, this work presents an efficient analog-oriented receiver, entitled RAFAE, relaxing implementation constraints for sub-THz applications. The proposed architecture, in contrast to conventional impulse radio receivers, partitions the signal processing related to the demodulation between analog and digital domains. The use of a non-coherent detection yields an inherent robustness to phase impairments. In addition, combining an analog projection with a multi-symbol detection allows lowering the ADC sampling rates. Numerical simulation results show that near-optimal performance can be achieved with largely reduced sampling frequencies. The performance analysis has highlighted the trade-off between the number of converters, their sampling rate and their quantization resolution. Altogether, the proposed receiver scheme enables to realize a joint optimization of system performance and architecture complexity. We have proposed the RAFAE architecture with the intention to lower the sampling frequency of ADCs given a fixed bandwidth and symbol rate. Equivalently, the RAFAE scheme can also be used to aggregate wider bandwidths with a given converter technology, and hence increase the possible data rate.

Our findings contribute to the design of high-rate impulse radio in sub-THz bands. We propose a low-complexity receiver that is relevant to multiple envisaged applications such as device-to-device communications, or enhanced hot-spot. Some of the potential perspectives to this work are the following. It is interesting to consider and study different basis for projection, *e.g.* the Walsh-Hadamard basis, wavelet decomposition, *etc.* In addition, the proposed framework can be used to realize the demodulation of other pulse-based modulation schemes such as a Pulse-Amplitude Modulation (PAM) which could increase the spectral efficiency. Finally, it is also meaningful to investigate the integration of channel-coding scheme, known to improve significantly system performance. In particular, the design of a probabilistic demapper in order to implement soft-channel decoding should be addressed. Furthermore, the proposed architecture can be combined with channel bonding similarly to [83]. In this case, the transceiver aggregates several sub-bands with multiple RF chains which could increase the communication throughput and allows to benefit from the large spectrum available in the sub-THz bands.

6.3 Synthesis and Discussions

Conclusion: To the implement high-rate and low-complexity transceivers in sub-THz bands, existing solutions use impulse radio combined with channel-bonding. For example, readers may refer to the specifications of the IEEE 802.15.3d group. Channel-bonding is commonly used to alleviate constraints on converters when aggregating large frequency bands. In this chapter, we have investigated the parallelization of envelope detection receivers. In doing so, we have intended to provide alternatives or complementary solutions to channel-bonding. Our objective has been to relax constraints on converters. In the first half of this chapter, we have introduced Hilbert spaces to represent non-negative signals. The proposed framework provides valuable analytical tools to design multiplexing schemes adapted to non-coherent sub-THz systems. In the second half, we have proposed an efficient analog-oriented receiver, entitled RAFAE. The purpose of proposed receiver is to relax implementation constraints on ADC for high-rate impulse radio in sub-THz bands. The main advantages of the RAFAE scheme are its PN robustness and its demodulation using low converter sampling rates. The material of this chapter has been partly published in two conference papers [37], [38]; and two patents [39] [40].

Perspectives: Regarding non-coherent multiplexing schemes, the proposed framework could be further characterized by the comparison of different potential maps and orthogonal sequences. Furthermore, the use of non-surjective map has led to promising results for non-coherent multiplexing [98]. Re-

garding the RAFAE scheme, it is worth investigating the use of other pulse-based modulation schemes such as Pulse-Width Modulation (PWM) or PAM. We also find relevant to mention one of our on-going studies. We are currently investigating the design of an OOK receiver using the RAFAE architecture with a Walsh-Hadamard projection basis. In addition, efficient hardware implementations of analog signal projection have been designed for compressed sensing applications and could be used within the proposed receiver, *e.g.* projection on the Walsh-Hadamard basis, or wavelet decomposition, see [99] and references therein. In this chapter, our goal has been to relax converters constraints by lowering sampling rates. However, this goal can also be achieved by using fast converters with low quantization order. By means of example, the design of transmission schemes based on 1-bit converters is an ongoing research topic that is highly relevant to future sub-THz communication systems.

Applications and limitations: We have by our research aimed to contribute to the development of low-complexity physical layers for sub-TeraHertz communication systems. Contemplated applications in sub-THz bands requiring low-complexity physical layers include device-to-device communications and enhanced hot-spot. Our findings can be used as intended to reduce the sampling rates of converters for a given throughput. Equivalently, they can be used to increase the aggregated bandwidth for a given converter technologies. We have proposed valuable solutions for envisaged sub-THz applications and in particular device-to-device communications and the enhanced hot-spot scenario. However, our results are relevant to every applications involving high-rate communication systems based on envelope modulation and detection. By means of illustration, we can mention VLC, or optical systems. Several aspects of our work limits the scope of these contributions. First, it should be remarked that envelope detectors may present non-ideal square-law response. Such impairment can result in performance degradations and require supplementary modeling. Second, Inter-Symbol Interference (ISI) has not been considered in this work. With regard to the studied architectures, ISI can be caused by a band-limited channel, or additional nonlinearities. To prevent ISI, it may be necessary to introduce some guard time between symbols leading to a spectral efficiency loss.

First-authored contributions

[39] S. Bicaïs, J.-B. Doré, and B. Miscopein, "Coherent Quadratic Receiver with Low Intermediate Frequency," Patent, Jan. 2020

[40] S. Bicaïs and Doré, "Analog and Parallel Receiver Architecture for the Demodulation of Large-Bandwidth Signals," Patent, Mar. 2020

[37] S. Bicaïs and J. Doré, "An Algebraic Framework for Digital Envelope Modulation," in *2019 27th European Signal Processing Conference (EUSIPCO)*, 2019, pp. 1–5

[38] S. Bicaïs and J.-B. Doré, "Espaces de Hilbert pour les Modulations Numériques d'Enveloppe," in *XXVIIème Colloque francophone de traitement du signal et des images-GRETSI 2019*, Lille, France, Aug. 2019

6.4 Dedicated Architectures: Retrospective and Opening

The previous part has presented incremental research works optimizing a mature technology to the constraints of the sub-THz spectrum in order to realize spectral-efficient communications. Ongoing standardizations and main research projects also propose contributions in this direction. Conversely, we have in this part investigated the design of low-complexity physical layers readily implementable

in sub-THz frequencies. We have claimed that one of the stepping-stones on the path toward cost-efficient implementations is the use of envelope detectors for their simple hardware implementation and robustness against phase impairments. We have hence studied the design of dedicated communication systems using non-coherent and high-rate architectures.

Transceivers using envelope modulation schemes have limited spectral efficiency, especially if the Peak-to-Average Power Ratio (PAPR) is constrained at the transmitter. Subsequently, to achieve high-rate communications with non-coherent transceivers, we have investigated two potential solutions:
i) using extremely large bandwidths. In this case, the analog-to-digital conversion is highly constrained. State-of-the-art approaches consider the use of sub-band channelization (channel-bonding) based on filter banks to relax constraints on converters, see for instance the specifications of the IEEE 802.15.3d interest group. In Chapter 6, our objective has been to alleviate the constraints on the analog-to-digital conversion. And to do so, we have studied the design of analog signal processing techniques such as projecting the received signal in the analog domain. Subsequently, we have proposed an efficient analog-oriented receiver, entitled RAFAE, relaxing implementation constraints on ADC for high-rate impulse radio in sub-THz bands;
ii) spatial multiplexing. The correlation between LoS propagation channels in sub-THz bands can limit the spatial multiplexing gains. In Chapter 5, our results have demonstrated that spatial multiplexing can be implemented in sub-THz bands with low-complexity and low-power architectures using MIMO systems and energy detection receivers. It has been shown that low-error rate communications can be achieved using the proposed detection algorithms even in the presence of strong spatial correlation between channels.

Conversely to the previous part, the contributions of Chapter 5 and 6 are not directly related to some existing solutions or to state-of-the-art techniques. These contributions propose novel and original communication systems, inspired from less common transceiver architectures, originally designed for different applications in the sub-6 GHz spectrum [82] [25]. Altogether, the findings of Part III offer valuable solutions to implement low-complexity physical layers for high-rate sub-THz communications, a still wide open research topic. And regarding this area of research, few promising solutions are currently under investigation. In particular, we would like to mention the work in [100]. The latter work uses spatial multiplexing to implement index modulation and provide low-power high-rate wireless links. Such investigations should be continued towards the development of low-power transceivers for sub-THz frequencies, which remains an uncommon research topic relevant to envisaged device-to-device communications. Eventually, the following remark should be pointed out. While the previous part has investigated a conventional approach on the design of RF communication systems, this part has developed a considerably different perspective closer to the development of optical systems [101]. We have studied transceivers using envelope modulation at the transmitter and envelope detection at the receiver. Within this framework, we have highlighted that multiple design problematics are shared with the development of optical communication systems. By means of example, we could mention the mitigation of nonlinear interference between channels, the design of non-coherent multiplexing schemes, or the use of frequency-flat channels with large bandwidth.

It is now time to take a step back and draw some concluding words on the presented contributions, and more generally, on those of this Ph.D. The next chapter summarizes the preceding ones and ends by sketching some open questions. Our main contributions are to be recalled and our findings discussed in a wider context. In a sense, the following chapter proposes to look back on our research and ahead on its future.

Part IV

Epilogue

Chapter 7

Conclusion and Perspectives

Future wireless networks are contemplated to provide higher communication data rates for more users in more places. To achieve this objective, the use of wide frequency bands is considered as a foremost solution. Still, the usual frequency bands in the sub-6 GHz spectrum are extremely limited and expensive. To aggregate larger bandwidths, the fifth-generation of mobile networks has already planned to operate in millimeter-wave (mm-Wave) bands. In this search for frequency resources, the sub-THz spectrum, from 90 to 300 GHz, offers large available bands. The sub-THz spectrum hence represents a valuable opportunity to deploy high data rate wireless services. Thanks to the evolution of semi-conductor technologies, it is now possible to envisage Radio-Frequency (RF) communications in the sub-THz spectrum. It is expected that wireless communications in the large sub-THz bands will play an important role in Beyond-5G networks. Still, conventional transmission techniques cannot be straightforwardly used since they do not consider the specific features of communications in sub-THz frequencies. The use of a new spectrum entails different technological constraints and challenges including: the strong phase impairments issued by high-frequency oscillators; the high sampling rates required by the analog-to-digital conversion; the difficult propagation conditions; and the challenging design of high-gain antennas. To achieve high-rate communications in sub-THz bands, additional research is required to design efficient physical layer algorithms. It has been highlighted that two distinct design paradigms arise for the physical layer of sub-THz systems: spectral-efficient vs. low-complexity. Current research projects mainly focus on spectral-efficient systems combining coherent transceivers with channel-bonding. In this case, the main objective is to realize a large communication throughput without strong constraints on the transceiver complexity or power consumption. One of the envisaged applications for spectral-efficient systems in sub-THz bands is high-capacity backhauling. Nevertheless, the development of cost-efficient communication systems, with energy or complexity constraints, in sub-THz frequencies is also investigated. Accordingly, the use of spatial multiplexing or impulse radio transceivers is considered to implement high-rate communications with limited transceiver complexity. Contemplated applications for low-complexity systems using sub-THz frequencies include device-to-device communications, and enhanced hot-spots.

7.1 Summary of Thesis Research

The research conducted in this thesis was oriented towards the development of efficient physical layers for future sub-THz communication systems. We have intended to answer the following research question: How can transceiver architectures and algorithms be designed to cope with the specific constraints of sub-THz communications? Our approach has consisted in designing jointly the analog and digital domains. In other words, we have investigated joint optimizations of the RF architecture and the digital signal processing. Our results have shown that using transmission techniques specifically designed for sub-THz frequencies allows both increasing the communication throughput and relaxing

the constraints on the RF components. In particular, we have proposed in Part II signal processing optimizations for coherent transceivers targeting a spectral-efficient physical layer. We have also designed in Part III dedicated communication systems using non-coherent and high-rate architectures to implement low-complexity physical layers in sub-THz frequencies. It should be mentioned that the development of sub-THz systems lies in the gap between RF and optical communication systems, and somehow narrows this gap. We have notably observed in Parts II and III that sub-THz systems share some design problematics with both RF and optical systems. To conclude this manuscript, we summarize our main contributions from theoretical tools to algorithm design and architecture proposals:

- **Phase noise modeling for large bandwidth transceivers:** We have addressed in Chapter 3 the problem of Phase Noise (PN) modeling for sub-THz communications. State-of-the-art works on system performance analysis consider correlated PN models for their accurate description [47]. Conversely, research activities on communication schemes optimization use rather uncorrelated PN models for their mathematical convenience [54]. We have compared through a statistical analysis two PN models: one correlated, accurate but complex, and another uncorrelated, analytically simpler. Our objective has been to select the most efficient PN model given the system parameters. Numerical simulations have been performed considering realistic PN corresponding to a state-of-the-art 200 GHz oscillator. First, the accuracy of the uncorrelated Gaussian PN model has been assessed with a Pearson's χ^2 goodness of fit test. We have demonstrated that the uncorrelated Gaussian PN model is accurate when the oscillator corner frequency remains small compared to the system bandwidth. We have next derived the closed-form expression of the likelihood-ratio of the two models. Thereupon, we have proposed an analytical condition to determine whether the correlated or the uncorrelated model should be selected given the system parameters and the spectral characterization of the oscillator. Overall, our results have shown that an uncorrelated Gaussian process is an appropriate PN model for sub-THz communication systems, and more generally for large-bandwidth systems. In addition, they provide theoretical support to several research studies using uncorrelated PN models to optimize transmission techniques for PN channels. The presented analysis can be used for PN modeling but also for the specification of communication systems. The proposed analytical condition is useful to specify the required oscillator features, or the length of the frame structure to ensure that the correlated PN remains negligible.

- **Optimization of transmission schemes for strong phase noise channels:** The strong phase impairments of high-frequency oscillators is one of the limiting factor for sub-THz systems. In Part II, we have presented a comprehensive optimization of the communication schemes for strong PN channels. Namely, phase impairments limit the achievable information rate. We have investigated the design of multiple communication schemes including the modulation, the demodulation and the link adaptation strategy. Many works of the literature on communication design for PN channels are either based on i) complex numerical optimizations; or on ii) semi-analytical approaches – optimizing a reduced set of parameters. These approaches lead to complex practical implementations. In contrast, we have focused on the trade-off between enhanced system performance and simple practical implementation. Besides, our research is supported by an original theoretical framework, based on the signal decomposition in the amplitude-phase domain. This framework provides the analytical tools to design PN robust communications. It has been demonstrated that the Gaussian Phase Noise (GPN) channel represented in the amplitude-phase domain demonstrates similar properties to the ones of the complex AWGN channel in the In-phase/Quadrature (I/Q) plane. First, we have designed an optimized demodulation scheme for PN channels, the polar metric detector. We have presented both the decision rule for symbol detection and the probabilistic demapper for soft-decision channel decoding. Our results have shown that significant performance gains are achieved for coded and uncoded systems by using the polar metric in comparison to standard detectors. And in contrast to state-of-the-art detectors, the proposed demodulation presents a lower complexity of

implementation. Second, we have proposed the Polar-QAM, a PN robust modulation scheme with a simple practical implementation. It has been highlighted that lattices in the amplitude-phase domain can be used to define structured constellations with enhanced performance on PN channels. Moreover, structured constellations, in contrast to numerically optimized ones, achieve near-optimal performance with significant complexity reductions of the transceiver. Our propositions have been compared to conventional and state-of-the-art techniques on key performance indicators. In particular, we have assessed the performance of the proposed modulation and demodulation schemes using deterministic ray-tracing in a sub-THz backhaul scenario. It has been observed that the communication throughput when using conventional transmission techniques is severely limited by PN. Conversely, our results have shown that using optimized transmission algorithms enables to achieve spectral-efficient communications even in the presence of strong PN.

- **Design and performance analysis of MIMO systems using energy detectors:** State-of-the-art sub-THz communication systems mainly use coherent transceivers with high order modulation schemes and high-quality RF components to realize high-rate communications [19]. In contrast, we have investigated in Chapter 5 the use of non-coherent spatial multiplexing in sub-THz frequencies. Our objective has been to achieve high-rate communications with low-complexity transceivers. To be specific, we have studied the design of Multiple-Input Multiple-Output (MIMO) systems using energy detectors for applications in sub-THz bands. The implementation of non-coherent spatial multiplexing in sub-THz frequencies is challenging due to the strong and nonlinear interference between the correlated Line-of-Sight (LoS) channels. Conventional detection techniques cannot be used for the studied nonlinear MIMO channel. Hence we have proposed two original detection algorithms: an analytical detector derived from the Maximum Likelihood (ML) criterion with a Gaussian approximation; and another detector using neural networks for binary classification. Numerical simulations have been performed to assess the communication performance considering a wireless link in D-band at 145 GHz. Our results have shown that spatial multiplexing with non-coherent sub-THz transceivers can be realized on strongly correlated LoS channels using the proposed detection schemes. In addition, we have considered the integration of a channel coding scheme which provides valuable performance gains in terms of achievable data rate. In summary, the communication throughput of non-coherent sub-THz transceivers can be efficiently increased using MIMO systems and energy detection receivers with low-complexity and low-power RF architectures.
- **A novel receiver for high-rate impulse radio with reduced sampling rate:** To implement high-rate and low-complexity transceivers in sub-THz bands, existing solutions use impulse radio combined with channel-bonding (see the specifications of the IEEE 802.15.3d group). Channel-bonding is commonly used to alleviate the strong constraints on converters when aggregating large frequency bands [19]. In Chapter 6, our objective has been to design complementary solutions to channel-bonding in order to relax constraints on converters. In particular, we have proposed an efficient analog-oriented receiver for high-rate impulse radio in sub-THz bands, named RAFAE. The acronym RAFAE stands for Receiver based on the Analog Fourier Analysis of the Envelope. In contrast to conventional impulse radio receivers, the RAFAE architecture partitions the signal processing related to the demodulation between analog and digital domains. The proposed receiver is based on a non-coherent detection, which provides robustness to phase impairments. In addition, the RAFAE scheme combines an analog projection with a multi-symbol detection which allows lowering the Analog-to-Digital Converters (ADC) sampling rates. The performance analysis has been carried out through numerical simulations considering the demodulation of Pulse-Position Modulation (PPM). The simulation results have shown that near-optimal performance can be achieved with largely reduced sampling frequencies. In particular, an implementation trade-off has been highlighted between the number of converters, their sampling rate and their quantization resolution. Altogether, the proposed receiver scheme enables to realize a joint optimization of system performance and architecture

complexity. The main advantages of the RAFAE scheme are its PN robustness and its demodulation using converters with low sampling rate. We have proposed the RAFAE scheme with the intention to lower the sampling frequency of ADCs given fixed symbol rate and bandwidth. Equivalently, the RAFAE architecture can also be used to aggregate wider bandwidths with a given converter technology, and hence increase the possible data rate.

7.2 Applications of Thesis Findings

In this section, we present some of the potential applications of our findings. In doing so, we aim to clarify the scope of our research and thereby highlight its value. The large bands available in the sub-THz spectrum provide the necessary frequency resources to deploy high data rate communications. Wireless communication systems using sub-THz bands are hence contemplated to meet the requirements of future wireless networks. In this paragraph, we briefly review how our research contributes to the development of efficient physical layers for sub-THz systems. It should also be mentioned that our contributions are expressly relevant with regard to the extreme densification of access points envisaged in the future.

- **Spectral-efficient sub-THz physical layers:** To avoid any bottleneck in the backhaul, high-speed wireless links are considered in future wireless networks as a complement to optical fiber. One of the envisaged applications for sub-THz communication systems is high-capacity backhauling. For this application, the unique objective is to maximize the spectral efficiency, with no strong constraints on the transceiver complexity or power consumption. Our research, particularly in Part II, has been conducted in the light of this scenario. Our findings and analyses contribute to the development of spectral-efficient physical layers for sub-THz communications. We have notably focused on alleviating the impact of strong PN on coherent transceivers, one of the main limiting factors for sub-THz systems. We have proposed optimized transmission schemes for PN channels that enable to double the information rate in comparison to conventional techniques. Thereby, we have provided valuable solutions to increase the communication throughput of future sub-THz communication systems.

- **Low-complexity sub-THz physical layers:** Sub-THz communication systems are also contemplated to deploy short-range and high-rate wireless links. We can mention as examples applications in device-to-device communications or enhanced hot-spots. These use cases involve embedded terminals and hence constraints in terms of transceiver complexity. In this case, the main objective is to achieve high-rate communications with limited transceiver complexity. Our findings, specifically those of Part III, describe efficient transmission techniques for low-complexity physical layers targeting high-rate communications in sub-THz frequencies. In particular, we have considered non-coherent receivers for their simple implementation in sub-THz frequencies and robustness to phase impairments. Two challenges related to high-rate and non-coherent transceivers have been addressed: increasing the communication throughput with spatial multiplexing; and relaxing the constraints on analog-to-digital conversion. In brief, we have proposed dedicated architectures to achieve high-rate communications in sub-THz bands with limited transceiver complexity.

- **Other applications:** As mentioned multiple times, some design problematics of sub-THz systems are shared with other communication systems. For this reason, our research could demonstrate applications beyond sub-THz communications. We now outline a few applications in which our contributions could be used. Contributions of Part II are relevant to any PN limited communication system, *e.g.* mm-Wave communications, optical systems or satellite communications. The findings of Chapter 5, the proposed detectors and performance analyses, could be useful to any case of non-coherent spatial multiplexing. For instance, non-coherent spatial multiplexing using Visible Light Communications (VLC) is envisaged to deploy low-complexity and high-rate wireless links in smart

offices. Furthermore, the communication throughput in wideband systems can be limited by the current converter technology. Accordingly, the proposed transceiver architectures outlined in Chapter 6 are particularly relevant to any application involving high-rate communication systems based on envelope modulation and detection, *e.g.* optical systems.

7.3 Discussions

It should be reminded that the presented findings are subject to some limitations. These limitations are discussed in details at the end of each chapter. In this section, we briefly summarize the main limitations. They can be categorized in two groups: simplistic system modeling and ideal assumptions. First, let us discuss the limitations induced by the considered simplistic system model. The impact of phase noise has been described with a discrete-time symbol model, an efficient yet simplistic model. We have also considered a single-dominant path channel model, neglecting other paths with weak energy contributions and the potential resulting minor interference. The power-amplifier nonlinearities and other RF impairments, *e.g.* I/Q imbalance, quantization, can affect the system performance which could be assessed in further studies. Second, to simplify our developments, some ideal assumptions have been considered. We have assumed perfect channel knowledge and perfect channel compensation, still some performance deteriorations can be expected in practical systems with implemented estimation schemes. In addition to that, high Signal-to-Noise Ratio (SNR) and strong PN conditions have been considered to ease analytical derivations. Implications of the related approximation errors have been characterized and lead either to none or to minor performance losses at low SNR and low PN.

In this work, we have studied non-Gaussian channels. In particular, we have focused on the GPN channel and on non-coherent channels for single- and multiple-antenna systems. With regard to these channels, our work certainly lacks the introduction and examination of theoretical bounds on achievable information rates. It is not necessary to recall the great value of theoretical bounds providing precious tools for channel characterizations and specifications of future systems. Regarding the considered channels, some information theory studies exist. For phase noise channels, we refer interested readers to [64] and [65], for single-antenna and non-coherent systems to [64], and for multiple-antenna and non-coherent systems to [81]. The analysis of these theoretical bounds could significantly contribute to the research on sub-THz communication systems. Nevertheless, to provide accurate and reliable results, it requires a rigorous approach with extensive well-reasoned developments and hence significant time to be devoted. The analysis of theoretical bounds has not been an objective of this thesis work since our focus has been set on system optimizations for sub-THz communications.

The future of sub-THz communication systems is strongly related to the level of maturity of wireless technologies, from the RF components to the signal processing and the resource management. Proposed architectures dedicated to sub-THz applications, such as non-coherent MIMO systems or the RAFAE architecture, still require significant development before practical products can be deployed. Conversely, coherent transceivers with optimized transmission techniques rely on mature wireless concept and know-how. For these reasons, we are to expect in the short-term that the forthcoming communication systems in sub-THz frequencies will be based on coherent I/Q transceivers, *e.g.* [19]. Nevertheless, in the long-term, the development of dedicated wireless systems is to be envisaged and could provide valuable performance gains on specific sub-THz applications.

Last, we discuss the on-going standardization of sub-THz wireless systems. Despite the challenges highlighted in this manuscript, the IEEE 802.15.3d interest group has proposed a simplistic wireless technology, This technology is not fully optimized for envisaged applications and is based on conser-

vative assumptions, still technological choices are pertinent. We currently witness a trend to apply well-known communication techniques to new problematics. In the context of mm-Wave communications, numerous efforts are deployed to use an Orthogonal Frequency Division Multiplexing (OFDM) structure for the waveform. Then, the waveform parameters are adapted to fulfill the specific requirements of mm-Wave: inter-carrier-spacing, precoding for Peak-to-Average Power Ratio (PAPR) or for phase noise robustness, *etc.* see for instance [21]. Overall, two approaches can be discerned: start from a clean-sheet and design dedicated systems; or optimize settings of OFDM-based solutions. Eventually, it is worth pointing out that interoperability, intellectual property and commercial issues do have an influence on the selection of wireless technologies for future sub-THz communications.

7.4 Perspectives

Immediate perspectives

We first outline a few potential perspectives that are directly related to our contributions. Further research should be conducted in order to get closer to practical implementation. Such research topics may sometimes be perceived as less valuable since they represent incremental rather than original approaches. Nevertheless, addressing these topics is essential for practical implementations of future communication systems.

- **Channel estimation and synchronization algorithms:** We have often assumed in our work perfect channel knowledge or synchronized receivers. These assumptions are mathematically convenient, still efficient algorithms remain to be designed. This topic is of important practical interest and should be investigated. Though basic estimation and synchronization schemes are straightforward to design, we highlight the large room for improvement. By means of example, the synchronization between the transmitter and the receiver in the presence of strong PN is challenging. Time and frequency synchronization errors need to be compensated in order to limit the resulting performance degradation. Similarly, efficient channel estimation schemes need to be designed. Either in the presence of PN or with non-coherent receivers, estimates of the propagation channel gain and phase shift are required to implement the demodulation algorithms. In particular, we highlight that a channel estimation scheme for MIMO systems with energy detection receivers should be a prime investigation, see Chapter 5.
- **Experimental validations:** We have dedicated a significant part of our research to the design of communications algorithms and transceiver architectures. Developing proof of concepts and demonstrators would enable to test the proposed solutions and confront them to practical issues. By means of example, it could show the impact or not of other RF impairments such as power-amplifier nonlinearities, or I/Q imbalance. Experimental validation is one of the most relevant next steps for the development of future sub-THz communication systems. Fortunately, several research projects are envisaged on this topic such that experimental validations should be conducted in the near future. Still, it should be mentioned that developing demonstrators in sub-THz frequencies represents important costs and hence requires large investments.
- **Joint coding and modulation design:** It has been noticed in Chapters 4 and 5 that joint coding and modulation design could be beneficial. In Chapter 4, considering the Polar-QAM, we have remarked that information bits sent on the amplitude and on the phase of symbols experience different levels of protection. In Chapter 5, studying non-coherent spatial multiplexing, we have observed that the protection of information bits depends on the transmit and receive antennas. Subsequently, techniques similar to multi-level coding can be implemented to achieve additional performance gains. In our research, we have been dealing with non-Gaussian channels. Though channel decoders do not

require any assumption on the channel, the construction of coding schemes commonly consider a Gaussian channel. For instance, the construction of Low-Density Parity Check (LDPC) or polar codes through density evolution usually assumes a Gaussian channel. In addition to the optimization of the probabilistic demapper as in Chapters 3 and 5, it could be interesting to construct channel coding schemes dedicated to the studied non-Gaussian channels.

Novel perspectives

Let us now present some alternative research topics. Conversely to the previous paragraph, the following research directions are not oriented towards practical implementation. Rather, the perspectives outlined below present some new research subjects that could be relevant to future sub-THz communication systems.

- **Polar transceiver RF architectures:** In Part II, we have shown that efficient signal processing techniques for PN channels rely on polar coordinates. Conversely to I/Q transceivers, transmitting real and imaginary parts of symbols, polar transceivers communicate the amplitude and phase of signals as independent streams. For these reasons, it is interesting to envisage the use of a polar RF transceiver architecture, combining a polar transmitter [77] and a polar receiver [78]. Future research on sub-THz communications could evaluate polar transceiver architectures. It requires first to investigate again the system modeling, and next to address the design of communication schemes and carry out performance analyses.
- **One-bit communication systems:** One of the main objective for future wireless networks is to achieve larger communication throughput. With regard to this objective, we have remarked throughout this manuscript that the analog-to-digital conversion at the receiver can be a limiting factor in state-of-the-art sub-THz communication systems. High-speed converters with high-resolution (*e.g.* 8-12 bits) have significant cost and also present large power consumption. Therefore, they are not suited to envisaged sub-THz applications with embedded receivers – enhanced hot-spot, device-to-device communications. It follows that transceivers using low-resolution ADC are relevant candidates for sub-THz communications. In particular, one-bit converters have valuable characteristics in terms of cost and power efficiency. For these reasons, it is worth investigating the use of one-bit quantization systems for sub-THz communications. Regarding one-bit communication systems, there already exists some literature, see [102] [103]. Capitalizing on the existing literature, transceiver design and performance analysis in the context of sub-THz frequencies remain to be addressed.
- **Beamforming and beam alignment in the presence phase impairments:** To cope with the severe propagation losses, sub-THz systems have to use high-gain antennas. Strong requirements on antenna directivity and beam alignment directly follow. In addition to the development of antenna technology, achieving these requirements on beamforming and beam alignment is a current research problematic. Sub-THz and mm-Wave communication systems share these problematics which are directly related to the use of higher carrier frequencies. Moreover, the strong phase impairments make difficult the use of conventional beamforming techniques, *e.g.* digital beamforming. The design of adapted beamforming and beam-alignment techniques could be highly valuable for future sub-THz systems. It is also worth investigating joint communication and beam-alignment strategies for user-tracking in sub-THz frequencies.

Part V

Appendices

Appendix A

Distribution of Received Symbols over the Non-Linear MIMO Channel

We derive in this appendix the probability distribution of received symbols for MIMO systems with energy detection receivers. This appendix complements the system model described in Chapter 5. Let us first recall the following result from Chapter 5. The received symbols are expressed by

$$\begin{aligned} r_k[\tau] = & \sum_{n=1}^{N_t}\sum_{m=1}^{N_t} h_{k,n}s_n[\tau]\cdot h_{k,m}s_m[\tau]\cos(\varphi_{k,n}-\varphi_{k,m}) \\ & + 2\int_{\tau T_s}^{\tau T_s+T_s} w_{k,c}(t)\cdot\sum_{n=1}^{N_t} h_{k,n}s_n(t)\cos\left(\varphi_{k,n}+\phi(t)\right)dt \\ & + 2\int_{\tau T_s}^{\tau T_s+T_s} w_{k,s}(t)\cdot\sum_{n=1}^{N_t} h_{k,n}s_n(t)\sin\left(\varphi_{k,n}+\phi(t)\right)dt \\ & + \int_{\tau T_s}^{\tau T_s+T_s} w_{k,c}(t)^2 + w_{k,s}(t)^2 dt. \end{aligned} \tag{A.1}$$

where $w_{k,c}(t)$ and $w_{k,s}(t)$ are band-limited continuous Gaussian process with spectral density $N_0/2$. The energy of received signals is denoted as follows

$$E_k[\tau] = \sum_{n=1}^{N_t}\sum_{m=1}^{N_t} h_{k,n}s_n[\tau]h_{k,m}s_m[\tau]\cos(\varphi_{k,n}-\varphi_{k,m}). \tag{A.2}$$

This appendix intends to evaluate the distributions of the three integrals in Eq. (A.1). In Chapter 5, these integrals are modeled in Eq. (5.8), the studied nonlinear MIMO channel, by the terms $w_k[\tau]$ and $z_k[\tau]$ defined by

$$\begin{aligned} \sqrt{2E_k[\tau]}\cdot w_k[\tau] &= 2\int_{\tau T_s}^{\tau T_s+T_s} w_{k,c}(t)S_{k,c}(t) + w_{k,s}(t)S_{k,s}(t)dt, \\ z_k[\tau] &= \int_{\tau T_s}^{\tau T_s+T_s} w_{k,c}(t)^2 + w_{k,s}(t)^2 dt. \end{aligned} \tag{A.3}$$

It should be mentioned that in Eq. (5.8) $w_k[\tau]$ and $z_k[\tau]$ respectively denote the mixed signal-noise contribution and the squared noise contribution in the channel.

Let us now proceed to the analytical developments and derive the distributions of received symbols in Eq. (A.1). We use the following notations

$$\begin{aligned} S_{k,c}(t) &= \sum_{n=1}^{N_t} h_{k,n} s_n(t) \cos\left(\varphi_{k,n} + \phi(t)\right), \\ S_{k,s}(t) &= \sum_{n=1}^{N_t} h_{k,n} s_n(t) \sin\left(\varphi_{k,n} + \phi(t)\right). \end{aligned} \tag{A.4}$$

Under a strong oscillator phase noise assumption, we obtain

$$\int_{\tau T_s}^{\tau T_s + T_s} S_{k,c}(t)^2 dt = \int_{\tau T_s}^{\tau T_s + T_s} S_{k,s}(t)^2 dt = \frac{E_k[\tau]}{2}. \tag{A.5}$$

The strong oscillator phase noise assumption corresponds to $\int_{T_s} \cos\left(\phi(t)\right)^2 dt = \frac{T_s}{2} + o(1)$. This assumption is verified for a fast varying phase noise (strong phase impairments). Nevertheless, if not the case, nothing but the variance of the mixed signal-noise term $w_k[\tau]$ is different, which has no further impact on the design of the detection algorithm. For this reason, this assumption results in no loss of generality. Signals $S_{k,c}(t)$, $S_{k,s}(t)$, $w_{k,c}(t)$ and $w_{k,s}(t)$ are real band-limited and finite energy signals. With an observation of duration T_s and a bandwidth B, these signals lie in a signal space of dimension $2M = \lfloor 2BT_s \rfloor + 1$, see [104]. The latter property is also referred to as the dimensionality theorem [1]. Hence these signals can be decomposed onto an orthonormal basis $\boldsymbol{\psi} = \{\psi_i\}_{1 \leq i \leq 2M}$ as follows

$$\begin{aligned} S_{k,c}(t) &= \sum_{i=1}^{2M} S_{k,c}^i \cdot \psi_i(t), & S_{k,s}(t) &= \sum_{i=1}^{2M} S_{k,s}^i \cdot \psi_i(t), \\ w_{k,c}(t) &= \sum_{i=1}^{2M} w_{k,c}^i \cdot \psi_i(t), & w_{k,s}(t) &= \sum_{i=1}^{2M} w_{k,s}^i \cdot \psi_i(t). \end{aligned} \tag{A.6}$$

This decomposition enables us to derive the probability distribution of received symbols. It is easily shown that the scalar coefficients of the decomposition verify

$$\begin{aligned} \sum_{i=1}^{2M} \left(S_{k,c}^i\right)^2 &= \sum_{i=1}^{2M} \left(S_{k,s}^i\right)^2 = \frac{E_k[\tau]}{2}, \\ \mathrm{E}\left[\sum_{i=1}^{2M} |w_{k,c}^i|^2\right] &= \mathrm{E}\left[\sum_{i=1}^{2M} |w_{k,s}^i|^2\right] = \frac{N_0 B}{2}, \end{aligned} \tag{A.7}$$

where $\mathrm{E}[\cdot]$ is the expectation operator. Coefficients $w_{k,c}^i$ and $w_{k,s}^i$ are thus zero-mean Gaussian variables with variance $\sigma_w^2/2$. Let us recall that $\sigma_w^2 = N_0 B/2M$. By definition of basis $\boldsymbol{\psi}$, $\int_T \psi_i(t)\psi_j(t)dt = \delta_{ij}$. We are now in a position to express the distributions of the integrals in Eq. (A.1). First, for the mixed signal-noise contribution, the decomposition of the signals on basis $\boldsymbol{\psi}$ leads us to

$$\begin{aligned} \int_{\tau T_s}^{\tau T_s + T_s} w_{k,c}(t) S_{k,c}(t) dt &= \sum_{i=1}^{2M} \sum_{j=1}^{2M} w_{k,c}^i S_{k,c}^j \int_{\tau T_s}^{\tau T_s + T_s} \psi_i(t)\psi_j(t) dt \\ &= \sum_{i=1}^{2M} w_{k,c}^i S_{k,c}^i \sim \mathcal{N}\left(0, \frac{E_k[\tau]}{2}\frac{\sigma_w^2}{2}\right). \end{aligned} \tag{A.8}$$

Using similar derivations to evaluate $\int_T w_{k,s}(t) S_{k,s}(t) dt$, we obtain

$$\int_{\tau T_s}^{\tau T_s + T_s} w_{k,c}(t) S_{k,c}(t) + w_{k,s}(t) S_{k,s}(t) dt \sim \mathcal{N}\left(0, \frac{E_k[\tau]}{2} \cdot \sigma_w^2\right) \tag{A.9}$$

Second, for the squared noise contribution, we can express the integral as follows

$$\begin{aligned}\int_{\tau T_s}^{\tau T_s+T_s} w_{k,c}(t)^2 dt &= \sum_{i=1}^{2M}\sum_{j=1}^{2M} w_{k,c}^i w_{k,c}^j \int_{\tau T_s}^{\tau T_s+T_s} \psi_i(t)\psi_j(t)dt \\ &= \sum_{i=1}^{2M} (w_{k,c}^i)^2 \sim \frac{\sigma_w^2}{2}\cdot\chi_{2M}^2. \end{aligned} \tag{A.10}$$

With an identical reasoning on $\int_T w_{k,s}(t)^2 dt$, it finally appears that

$$\int_{\tau T_s}^{\tau T_s+T_s} w_{k,c}(t)^2 + w_{k,s}(t)^2 dt \sim \frac{\sigma_w^2}{2}\cdot\chi_{4M}^2 \tag{A.11}$$

In summary, the received symbols can be expressed by

$$r_k[\tau] = E_k[\tau] + \sqrt{2E_k[\tau]}\cdot w_k[\tau] + z_k[\tau], \tag{A.12}$$

where $w_k[\tau] \sim \mathcal{N}(0,\sigma_w^2)$ and $z_k[\tau] \sim \frac{\sigma_w^2}{2}\cdot\chi_{4M}^2$.

Appendix B

Channel Model for the RAFAE Architecture

This appendix comes in complement to Chapter 6. Namely, it provides detailed derivations of the channel model when considering transceivers using the proposed RAFAE architecture. The acronyme RAFAE stands for Receiver based on the Analog Fourier Analysis of the Envelope. In this appendix, we derive the closed-form expression and probability distributions of received symbols. Expressing the distribution of received symbols is a necessary step to design the detection algorithm. We remind readers that the received observation on branch k is given by

$$\lambda_r^k = H \cdot \lambda_m^k + 2\sqrt{H} \cdot \lambda_{xw}^k + \lambda_{ww}^k. \tag{B.1}$$

where H is the propagation gain. The projection λ_m^k represents the projection of the transmitted symbol m on branch k. In addition, the noise components λ_{xw}^k and λ_{ww}^k respectively denote the mixed signal-noise contribution and the squared noise contribution of the channel. These three projections are defined by

$$\lambda_m^k = \int_0^{T_i} x_m(t)^2 \cdot e_k(t)^* dt, \tag{B.2}$$

$$\lambda_{xw}^k = \int_0^{T_i} x_m(t) w(t) \cdot e_k(t)^* dt, \tag{B.3}$$

$$\lambda_{ww}^k = \int_0^{T_i} w(t)^2 \cdot e_k(t)^* dt. \tag{B.4}$$

The rest of the appendix is organized as follows. We derive the expressions of first λ_m^k, then λ_{ww}^k and finally λ_{xw}^k. The appendix is concluded by the expression of the channel model.

Expression of the squared signal projection λ_m^k: We represent signals $x_m(t)$ and $s_m(t)$ using finite Fourier series to derive λ_m^k. With a Fourier series decomposition, the projection of these signals onto a particular frequency is straightforward to evaluate. As shown by the work of Gabor in [105], any band-limited signal of finite duration can be represented by a finite superposition of elementary functions. Let $s(t)$ be a complex finite-energy signal with bandwidth B and T_i be the duration of observation. We consider in this appendix complex signals – conversely to Appendix A – with regard to the projection on the in-phase and quadrature components. It follows from [104] and the dimensionality theorem [1] that the signal $s(t)$ can be represented exactly by a Fourier series of $2N = 2\lfloor BT_i \rfloor + 1$ complex terms. We refer to $2N$ as the time-bandwidth concentration and write the Fourier orthonormal basis $\boldsymbol{e} = \left\{ e_n(t) = \exp\left(j2\pi \frac{n}{T_i} t\right), n \in [\![-N, N]\!], t \in (0, T_i) \right\}$. Hence, we have

$$s_m(t) = \sum_{n=-N}^{N} S_m^n \cdot e_n(t), \text{ with } S_m^n = \frac{1}{T_i} S_m\left(\frac{n}{T_i}\right), \tag{B.5}$$

where S_m^n is the n-th Fourier coefficient and $S_m(f)$ is the Fourier transform of signal $s_m(t)$.
The expression of $x_m(t) = s_m(t) \cdot \sqrt{2}\cos(2\pi f_c + \phi(t))$ with Fourier series follows directly as

$$x_m(t) = \sum_{n=-N}^{N} \frac{S_m^n}{\sqrt{2}} \exp\left(j2\pi\left(f_c + \frac{n}{T_i}\right)t + j\phi(t)\right) + \frac{S_m^{n\,*}}{\sqrt{2}} \exp\left(j2\pi\left(f_c + \frac{n}{T_i}\right)t + j\phi(t)\right)^*. \tag{B.6}$$

We are now able to express $x_m(t)^2$ as

$$\begin{aligned} x_m(t)^2 = &\sum_{n=-N}^{N}\sum_{n'=-N}^{N} \frac{S_m^n S_m^{n'}}{2} \exp\left(j2\pi\left(2f_c + \frac{n+n'}{T_i}\right)t + j2\phi(t)\right) + \frac{S_m^{n\,*} S_m^{n'\,*}}{2} \exp\left(j2\pi\left(2f_c + \frac{n+n'}{T_i}\right)t + j2\phi(t)\right)^* \\ &+ \sum_{n=-N}^{N}\sum_{n'=-N}^{N} \frac{S_m^n S_m^{n'\,*}}{2} \exp\left(j2\pi\frac{n-n'}{T_i}t\right) + \frac{S_m^{n\,*} S_m^{n'}}{2} \exp\left(j2\pi\frac{n-n'}{T_i}t\right)^*. \end{aligned} \tag{B.7}$$

It should be remarked that the first line in the latter equation represents the image of signal $s_m(t)^2$ at frequency $2f_c$ and the second line denotes the signal of interest $s_m(t)^2$ in baseband. The down-conversion from passband to baseband is realized without impact of the phase impairments from the oscillator. It can be easily shown that the two terms of the second line sum up to same amount. Thereupon, to express the coordinate λ_m^k it suffices to evaluate the projection of signal $x_m(t)^2$ onto $e_k(t)$. It is clear that the projection of the image at $2f_c$ onto the frequency $\frac{k}{T_i}$ is null. By definition of basis $\boldsymbol{e}$, we have $\int_0^{T_i} e_i(t) \cdot e_j(t)^* dt = \delta_{i,j} \cdot T_i$. Finally, the observation λ_m^k is expressed by

$$\begin{aligned} \lambda_m^k &= \int_0^{T_i} x_m(t)^2 \cdot e_k(t)^* dt, \\ &= \sum_{n=-N}^{N}\sum_{n'=-N}^{N} S_m^n S_m^{n'\,*} \cdot \int_0^{T_i} e_{n-n'}(t) \cdot e_k(t)^* dt, \\ &= \sum_{n=-N}^{N}\sum_{n'=-N}^{N} S_m^n S_m^{n'\,*} \cdot \delta_{n-n',k} T_i, \\ &= \sum_{n=-N+k}^{N} S_m\left(\frac{n}{T_i}\right) S_m\left(\frac{n-k}{T_i}\right)^* \frac{1}{T_i}. \end{aligned} \tag{B.8}$$

This closed-form expression of the squared signal projection achieves the objective of the paragraph. This expression can be used to evaluate the possible noiseless observations λ_m^k of the different codewords and hence to determine the constellation $\mathcal{C}$.

Expression and distribution of squared noise projection λ_{ww}^k: We proceed with a similar reasoning to evaluate $\lambda_{ww}^k = \int_0^{T_i} w(t)^2 \cdot e_k(t)^* dt$. The Fourier transform of the noise signal $w(t)$ is denoted $W(f)$ and the Fourier coefficients $W_n = W(f_c + \frac{n}{T_i}) \cdot \frac{1}{T_i}$. We express $w(t)$ as a sum of Fourier series,

$$w(t) = \sum_{n=-N}^{N} W_n \exp\left(j2\pi\left(f_c + \frac{n}{T_i}\right)t\right) + W_n^* \exp\left(j2\pi\left(f_c + \frac{n}{T_i}\right)t\right)^*. \tag{B.9}$$

The expression of $w(t)^2$ follows easily. Evaluating the projection of $w(t)^2$ onto $e_k(t)$, we have

$$\begin{aligned} \lambda_{ww}^k &= \int_0^{T_i} w(t)^2 \cdot e_k(t)^* dt, \\ &= 2\sum_{n=-N+k}^{N} W\left(f_c + \frac{n}{T_i}\right) W\left(f_c + \frac{n-k}{T_i}\right)^* \cdot \frac{1}{T_i}. \end{aligned} \tag{B.10}$$

We now intend to characterize the probability distribution of the squared noise projection in Eq. (B.10). First, it should be remarked that if $k \neq 0$ then W_n and W_{n-k}^* are uncorrelated and circularly-symmetric complex Gaussian variables with variance N_0, *i.e.* $W_n \sim \mathbb{C}\mathcal{N}(0, N_0)$. To express the distribution of the products, we use $XY = \frac{1}{4}(X+Y)^2 - \frac{1}{4}(X-Y)^2$. Let X and Y be complex normally distributed, we obtain $XY \sim \frac{1}{4}\chi_2^2 + \frac{j}{4}\chi_2^2 - \frac{1}{4}\chi_2^2 - \frac{j}{4}\chi_2^2$. It follows that

$$\begin{aligned}\lambda_{ww}^k &\sim \frac{2}{T_i}\sum_{n=-N+k}^{N}\frac{N_0}{4}\left(\chi_2^2 + j\chi_2^2 - \chi_2^2 - j\chi_2^2\right), \\ &\sim \frac{N_0}{2T_i}\left(\chi_{2(2N+1-k)}^2 + j\chi_{2(2N+1-k)}^2 - \chi_{2(2N+1-k)}^2 - j\chi_{2(2N+1-k)}^2\right).\end{aligned} \tag{B.11}$$

It is rather difficult to express the distribution of the difference of two $\chi_{2(2N+1-k)}^2$ distributions. Still, these distributions can be efficiently approximated as Gaussian ones if the degree of freedom is large enough, *i.e.* $k \ll 2N$. To design an implementable detection algorithm, we use this approximation which yields

$$\begin{aligned}\lambda_{ww}^k &\simeq \frac{N_0}{2T_i}\left(\mathbb{C}\mathcal{N}\Big(2(2N+1-k), 4(2N+1-k)\Big) - \mathbb{C}\mathcal{N}\Big(2(2N+1-k), 4(2N+1-k)\Big)\right), \\ &\sim \sqrt{2(2N+1-k)}\cdot\mathbb{C}\mathcal{N}\left(0, \left(\frac{N_0}{T_i}\right)^2\right).\end{aligned} \tag{B.12}$$

Eventually, the squared noise projection is approximately complex circularly-symmetric Gaussian distributed. Its variance is the product of N_0^2/T_i^2, the square of the energy of the integrated noise, and $2(2N+1-k)$, related to the time-bandwidth concentration of noise. Nevertheless, this expression does not holds for the projection on the 0-th branch since signal $e_0(t) = 1$ is purely real. For $k = 0$, W_n and W_{n-k}^* are correlated and $W_n \cdot W_{n-k}^* = |W_n|^2$. We evaluate the distribution of λ_{ww}^0 as follows

$$\begin{aligned}\lambda_{ww}^0 &= \frac{2}{T_i}\sum_{n=-N}^{N}\left|W\left(f_c + \frac{n}{T_i}\right)\right|^2, \\ &\sim \frac{2N_0}{T_i}\chi_{4N+2}^2, \\ &\simeq \sqrt{4(4N+2)}\cdot\mathcal{N}\left(0, \left(\frac{N_0}{T_i}\right)^2\right) + 2(4N+2)\cdot\frac{N_0}{T_i}.\end{aligned} \tag{B.13}$$

As previously, we use a Gaussian approximation to describe the χ^2 distribution in order to obtain an implementable detection algorithm The distribution of the squared noise projection on the 0-th branch cannot be associated to the distributions on other branches as it belongs to the real line and not the complex plane.

Expression and distribution of mixed signal-noise projection λ_{xw}^k: In this paragraph, we express and evaluate the distribution of $\lambda_{xw}^k = \int_0^{T_i} x_m(t)w(t)\cdot e_k(t)^* dt$. Combining the decompositions of $x_m(t)$ and $w(t)$ into Fourier series, we have

$$\begin{aligned}x_m(t)\cdot w(t) = &\sum_{n=-N}^{N}\sum_{n'=-N}^{N} S_m^n W_{n'}\exp\left(j2\pi\left(2f_c + \frac{n+n'}{T_i}\right)t + j2\phi(t)\right) + {S_m^n}^* W_{n'}^*\exp\left(j2\pi\left(2f_c + \frac{n+n'}{T_i}\right)t + j2\phi(t)\right)^* \\ &+ \sum_{n=-N}^{N}\sum_{n'=-N}^{N} S_m^n W_{n'}^*\exp\left(j2\pi\frac{n-n'}{T_i}t + j\phi(t)\right) + {S_m^n}^* W_{n'}\exp\left(j2\pi\frac{n-n'}{T_i}t + j\phi(t)\right)^*.\end{aligned} \tag{B.14}$$

This leads us to

$$\begin{aligned}\lambda_{xw}^{k} &= \int_{0}^{T_i} x_m(t) w(t) \cdot e_k(t)^* dt, \\ &= \frac{e^{-j\phi_0}}{\sqrt{2}T_i} \sum_{n=-N+k}^{N} S_m\left(\frac{n}{T_i}\right) W\left(f_c + \frac{n-k}{T_i}\right)^* + S_m\left(\frac{n-k}{T_i}\right)^* W\left(f_c + \frac{n}{T_i}\right). \end{aligned} \tag{B.15}$$

where $\phi_0 \sim \mathcal{U}[-\pi, \pi)$ denotes the oscillator phase noise. To obtain this expression, we have considered that the phase noise process has small variations over T_i, *i.e.* $\phi(t) \simeq \phi_0 \sim \mathcal{U}[-\pi, \pi)$. This assumption represents a worst case scenario. If the phase noise is fast varying over T_i, it can be easily shown that nothing but the variance of the mixed signal-noise projection is different – it is lowered. The impact of fast varying phase noise does not modify the distribution of the mixed signal-noise projection. Subsequently, the detection algorithm remains the same and this assumption results in no loss of generality.

Regarding Eq. (B.15), we proceed to express the probability distribution of the mixed signal-noise term. It follows from $W_n \sim \mathbb{C}\mathcal{N}(0, N_0)$ that

$$\begin{aligned}\lambda_{xw}^{k} &= \frac{1}{\sqrt{2}T_i} \sum_{n=-N+k}^{N} S_m\left(\frac{n}{T_i}\right) W\left(f_c + \frac{n-k}{T_i}\right)^* + S\left(\frac{n-k}{T_i}\right)^* W_m\left(f_c + \frac{n}{T_i}\right), \\ &\sim \sqrt{E_m^k} \cdot \mathbb{C}\mathcal{N}\left(0, \frac{N_0}{T_i}\right), \end{aligned} \tag{B.16}$$

where

$$E_m^k = \sum_{n=-N+k}^{N} \left| S_m\left(\frac{n}{T_i}\right) \right|^2 \cdot \frac{1}{T_i}. \tag{B.17}$$

The intended result is achieved as the probability distribution of the mixed signal-noise projection is described. The variance of λ_{xw}^k may be decomposed as the product of N_0/T_i, the energy of the integrated noise, and E_m^k, homologous to a fraction of the energy of the sent signal $s(t)$ – *cf.* Parseval's theorem. In an intuitive way, the mixed signal-noise projections are complex circularly-symmetric Gaussian variables with a variance equal to the product of the energies of the information and noise signals. Nevertheless, the probability distribution of mixed signal-noise projection on the 0-th branch is purely real and expressed differently,

$$\begin{aligned}\lambda_{xw}^{0} &= \frac{1}{\sqrt{2}T_i} \sum_{n=-N}^{N} S_m\left(\frac{n}{T_i}\right) W\left(f_c + \frac{n}{T_i}\right)^* + S_m\left(\frac{n}{T_i}\right)^* W\left(f_c + \frac{n}{T_i}\right), \\ &\sim \sqrt{2 \cdot E_m^0} \cdot \mathcal{N}\left(0, \frac{N_0}{T_i}\right). \end{aligned} \tag{B.18}$$

Distribution of received vectors: It has been shown in Chapter 6 that the channel of the considered transceiver can be expressed as

$$\lambda_r^k = H \cdot \lambda_m^k + 2\sqrt{H} \cdot \lambda_{xw}^2. + \lambda_{ww}^k. \tag{B.19}$$

In this appendix, we have derived the expressions and the probability distributions of the three projection terms in this equation. We synthesize these derivations in this paragraph to express the model of the communication channel. Finally for $k \neq 0$, the projections can be described by

$$\lambda_r^k = H \cdot \lambda_m^k + 2\sqrt{H \cdot E_m^k} \cdot w_k + \sqrt{2(2N + 1 - k)} \cdot z_k, \tag{B.20}$$

where w_k and z_k are circular-symmetric complex Gaussian variables, $w_k \sim \mathbb{C}\mathcal{N}(0, N_0/T_i)$ and $z_k \sim \mathbb{C}\mathcal{N}(0, N_0^2/T_i^2)$. For $k = 0$, the received projection is expressed by

$$\lambda_r^0 = H \cdot \lambda_m^0 + 2\sqrt{H \cdot 2E_m^k} \cdot w_0 + \sqrt{4(4N+2)} \cdot z_0 + 2(4N+2)\frac{N_0}{T_i}, \tag{B.21}$$

where w_0 and z_0 are real Gaussian variables, $w_0 \sim \mathcal{N}(0, N_0/T_i)$ and $z_0 \sim \mathcal{N}(0, N_0^2/T_i^2)$. Altogether, the communication channel of vector $\boldsymbol{\lambda}_r = (\lambda_m^0, \lambda_m^1, \cdots, \lambda_m^K)$ follows a $(K+1)$-dimensional complex circularly-symmetric Gaussian channel, except for projection on the 0-th branch which is real. To illustrate this channel, Figure 6.8 depicts the simulated and modeled distributions of received coordinates for different values of k in Chapter 6. We notice that the approximation of a Gaussian distribution is an efficient modeling close to the observations.

Appendix C

Résumé Étendu

Les travaux de thèse présentés dans ce manuscrit portent sur la *conception de la couche physique pour les futurs systèmes de communication sub-TeraHertz*. En d'autres termes, nous nous sommes intéressés à la définition des techniques de transmission et de réception des signaux radio pour les communications sans-fil dans les fréquences entre 90 et 300 GHz. Nous résumons ici brièvement les travaux de recherche menés ainsi que les résultats obtenus.

1 Introduction aux Communications Sub-TeraHertz

L'unique objectif de cette section est de répondre à la question suivante : pourquoi et comment les communications dans les fréquences sub-THz sont-elles envisagées pour les futures applications sans-fil ? Actuellement, les instituts de recherche et les entreprises industrielles consacrent d'importants efforts au développement des communications sans-fil dans les fréquence sub-TeraHertz. En effet, le spectre sub-THz, de 90 à 300 GHz, offre de larges bandes de fréquences disponibles qui pourraient être utilisées pour mettre en œuvre des services sans-fil haut-débit. Le spectre sub-THz représente ainsi une réelle opportunité de développer des communications haut-débit pour répondre aux exigences des futurs réseaux de communication. Les applications envisagées sont nombreuses et ambitieuses. Nous avons identifié trois scénarios principaux, représentatifs des différentes applications envisagées. Ces scénarios sont : les liaisons backhaul haute-capacité, les hot-spots haut-débit, et les communications inter-équipements. Ces trois scénarios tirent parti des grandes bandes de fréquences sub-THz pour déployer des services sans-fil haut-débit et sont décrits en Figure 1. Cependant, l'utilisation d'un nouveau spectre implique de nouveaux défis technologiques, notamment : des conditions de propagation difficiles, du bruit de phase important, des contraintes sur les convertisseurs à bande limitée, *etc.* Du fait de ces contraintes spécifiques, les technologies sans-fil classiques ne peuvent pas être transposées directement aux fréquences sub-THz. Des recherches supplémentaires sont donc menées pour concevoir des techniques de transmission performantes. L'optimisation de la couche physique pour les caractéristiques spécifiques des systèmes sub-THz est une tâche complexe. Le développement d'émetteurs-récepteurs sub-THz s'inscrit dans un paradigme de conception peu commun, proche de celui de la « dirty RF ». Dans le cadre de ce paradigme, notre approche peut être résumée comme suit : une conception conjointe des domaines analogique et numérique. Un des fondements de notre travail est de considérer les problèmes analogiques dans le cadre de la conception du traitement numérique des signaux. Cela permet de rendre les communications robustes aux fortes imperfections radiofréquences et ainsi d'améliorer significativement les performances. En d'autres termes, nous proposons une optimisation conjointe de l'architecture de l'émetteur-récepteur et des algorithmes de traitement du signal au regard des caractéristiques propres aux communications sub-THz – imperfections radiofréquences, conditions de propagation, *etc.*

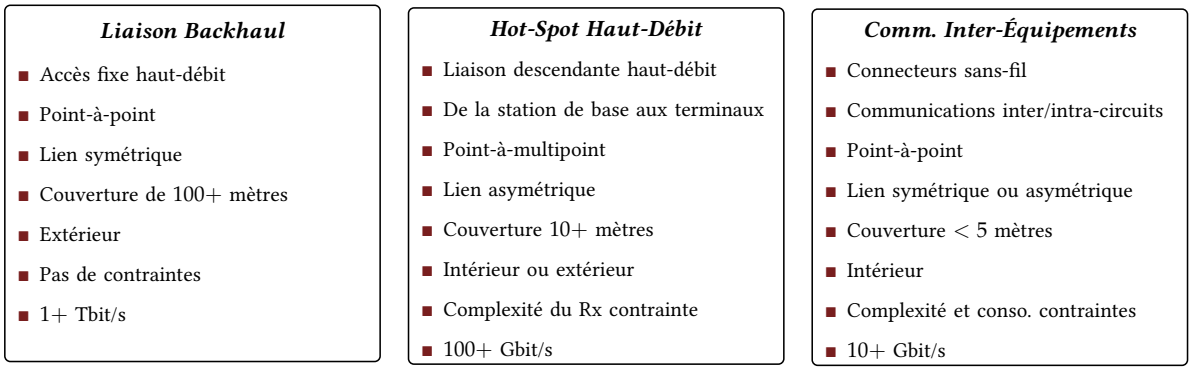

Figure 1 – *Principaux éléments descriptifs et indicateurs de performance des applications envisagées*

2 Optimisations des Émetteurs-Récepteurs Cohérents

Durant la première partie de cette thèse, nous avons étudié l'adaptation des technologies sans-fil existantes, les émetteurs-récepteurs cohérents, au spectre sub-THz. Ceci peut notamment être réalisé par l'optimisation du traitement du signal, c'est-à-dire des algorithmes de communication, afin d'améliorer les performances du système. Dans cette partie, nous nous sommes concentrés en particulier sur la réalisation de communications haut-débit en présence de fortes imperfections de phase. Les oscillateurs haute-fréquences sont peu stables et donc causent du bruit de phase important, ce qui dégrade fortement les performances de communication et limite le débit d'information. Le bruit de phase des oscillateurs est un des principaux défis technologiques amenés par la montée en fréquence et l'utilisation de bandes larges. Nous avons donc cherché à lever ce verrou technologique en concevant des algorithmes de traitements du signal adaptés et performants en présence de fort bruit de phase. Une application représentative des contributions de cette partie est le scénario de liaison backhaul haute-capacité. Les solutions proposées, conçues pour augmenter le débit de communication, peuvent également être utilisées pour assouplir les contraintes sur les composants radiofréquences.

2.1 Modélisation

Tout d'abord, nous avons étudié la modélisation des systèmes de communication sub-THz. Une modélisation efficace des imperfections radiofréquences est essentielle pour optimiser les algorithmes de la couche physique et améliorer les performances du système. Le canal de propagation a été décrit par un modèle en visibilité directe selon les résultats des campagnes de mesures récentes, ce qui est un modèle commun dans la recherche actuelle sur les systèmes de communication sub-THz. En particulier, nous nous sommes concentrés sur la sélection du modèle de bruit de phase pour les systèmes large bande et ainsi les communications sub-THz. Nous avons comparé deux modèles de bruit de phase : un modèle corrélé, précis mais complexe, et un autre non corrélé, analytiquement plus simple. Des simulations numériques ont été réalisées en considérant un bruit de phase réaliste correspondant à un oscillateur de l'état de l'art à 200 GHz. Nos résultats ont démontré qu'un processus gaussien non corrélé est un modèle de bruit de phase approprié pour les systèmes de communication sub-THz.

2.2 Algorithmes de communications optimisés

Sur la base du modèle de système proposé, nous avons ensuite étudié la démodulation optimale en présence de bruit de phase. Nous avons donc proposé un détecteur adapté, dérivé du critère de détection de maximum de vraisemblance. Il a été montré que l'utilisation d'un algorithme de démodulation optimisé, basé sur un détecteur conjoint amplitude-phase, conduit à des gains de performance significatifs

en présence de bruit de phase. Contrairement aux détecteurs de l'état de l'art, le démodulateur probabiliste proposé permet une mise en œuvre pratique simple avec des performances de démodulation optimales.

Par la suite, nous avons étendu l'optimisation des algorithmes de communication pour les canaux à fort bruit de phase aux niveaux du récepteur et de l'émetteur. Nous avons notamment décrit un schéma de modulation robuste au bruit de phase : la Polar-QAM. La modulation proposée est basée sur une analyse théorique des constellations optimales pour les canaux à bruit de phase et sur des considérations pratiques de mise en œuvre. La Polar-QAM est conçue pour améliorer le débit de données du système tout en conservant une mise en œuvre simple. Nous avons présenté l'analyse des performances de la modulation proposée en utilisant des outils analytiques et des simulations numériques, ce qui a permis de mettre en évidence les gains de performances par rapport aux modulations classiques et de l'état de l'art. Finalement, des stratégies d'adaptation de lien ont été présentées pour choisir le meilleur schéma de modulation et les meilleurs paramètres de la couche physique en fonction des conditions du canal.

2.3 Analyse des performances dans un scénario sub-THz

Nous avons aussi évalué les gains de performance des schémas de modulation et de démodulation proposés en utilisant des prédictions déterministes du canal, par tracé de rayons, dans un scénario backhaul. Ces simulations numériques modélisent un environnement de centre-ville (d'après le modèle 3D de San José, État-Unis d'Amérique). Les performances du système sont caractérisées pour une application de liaison backhaul haute-capacité en extérieur, qui pourrait être exploitée pour alimenter un réseau d'accès mobile très haut-débit. Les résultats des simulations numériques sont présentés par la Figure 2. Il a notamment été souligné que le débit de communication lors de l'utilisation de techniques de transmission conventionnelles est fortement limité par le bruit de phase. Au contraire, les solutions techniques que nous proposons permettent d'atteindre des débits d'information élevés même en présence d'un bruit de phase fort.

3 Proposition d'Architectures Dédiées

Dans la première partie de la thèse, nous avons développé une approche conventionnelle et incrémentale du développement des systèmes de communication sub-THz. Dans la deuxième partie de la thèse, nous développons une approche plus novatrice. Notre objectif est de proposer de nouvelles architectures d'émetteurs-récepteurs dédiées aux communications dans les fréquences sub-THz. En particulier, nous nous sommes concentrés sur la conception d'émetteurs-récepteurs de faible complexité basés sur la modulation et la détection d'enveloppe. Ce faisant, les émetteurs-récepteurs présentent une robustesse inhérente au bruit de phase et les architectures radiofréquences sont facilement réalisables même à très haute fréquence. Contrairement à la partie précédente, nous avons considéré plus que les optimisations logicielles pour atténuer les imperfections radiofréquences ; nous avons aussi évalué les considérations matérielles dès la conception du système. Les contributions de ces recherches ont des applications potentielles dans les scénarios sub-THz suivants : les hot-spots haut-débit et les communications inter-équipements.

3.1 Systèmes multi-antennaire avec récepteurs à détection d'énergie

Lorsque l'on considère l'utilisation d'émetteurs-récepteurs non-cohérents, le débit d'information est assez limité en raison des schémas de modulation impulsionnels. C'est pourquoi nous avons envisagé l'utilisation du multiplexage spatial non-cohérent dans les fréquences sub-THz afin de réaliser des communications haut-débit. Plus précisément, nous avons étudié la conception et l'analyse des performances des systèmes multi-antennaire utilisant des récepteurs à détection d'énergie pour les futures

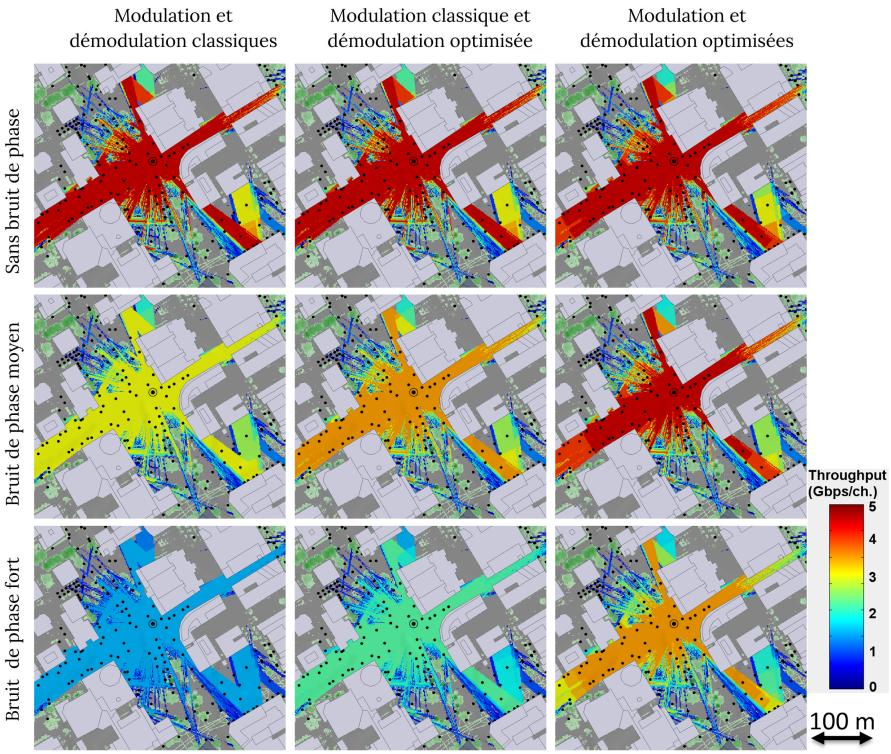

Figure 2 – *Cartes de débit pour un centre ville en présence de bruit de phase*

applications sub-THz. Dans le cas présent, l'interférence entre les canaux est forte et non-linéaire, ce qui représente un défi majeur pour mettre en œuvre le multiplexage spatial avec des émetteurs-récepteurs sub-THz non-cohérents. Comme le canal de communication est non-linéaire, les techniques conventionnelles ne peuvent pas être utilisées. Deux algorithmes de détection dédiés ont été proposés : un premier détecteur analytique et un second basé sur les réseaux de neurones. Nous avons également présenté les résultats d'une analyse des performances basé sur des simulations numériques modélisant un lien sans-fil dans les bandes sub-THz. Les principaux résultats des simulations sont présentés en Table C.1. Nos résultats ont démontré que les débits des systèmes sub-THz non-cohérents peuvent être efficacement augmentés en utilisant des architectures multi-antennaire et des récepteurs à détection d'énergie.

Table C.1 – *Résultats des simulations pour une application dans la bande D (145 GHz)*

Fréquence porteuse	f_c	145 GHz			
Débit des symboles	$1/T_s$	1 GHz			
Largeur de bande	B	2 GHz			
Distance Tx-Rx	d_0	10 m			
Gain d'antenne	g_0	32 dBi			
Nombre d'antennes	N	1	4	6	8
Débit de données	$\frac{N}{T} \cdot 0.9$	0.9 Gbps	3.6 Gbps	5.4 Gbps	7.2 Gbps
Puissance par antenne	$P_{\mathrm{A_{Tx}}}$	−31.8 dBm	−31.2 dBm	−30.4 dBm	−32.3 dBm

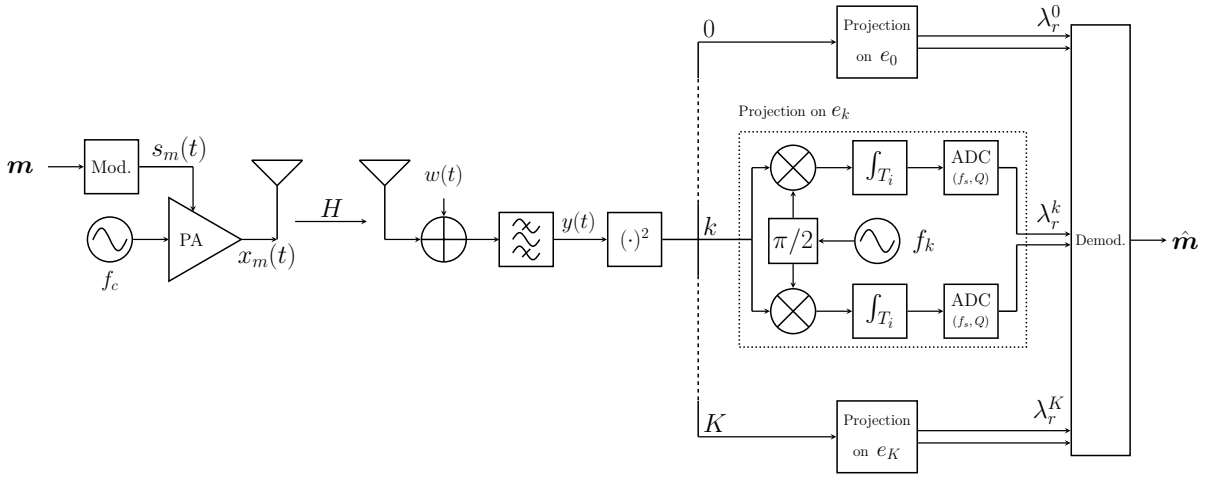

Figure 3 – *Schéma d'un émetteur-récepteur utilisant l'architecture de réception proposée RAFAE*

3.2 Parallélisation des récepteurs à détection d'enveloppe

L'utilisation de larges bandes de fréquences permet de réaliser des débits de communication élevés mais implique de fortes contraintes au niveau des convertisseurs analogiques-numériques, en particulier pour les systèmes embarqués ayant des couches physiques de faible complexité. Nous avons donc consacré une partie de nos recherches à la parallélisation de l'architecture des récepteurs sub-THz utilisant la détection d'enveloppe. Ce faisant, notre objectif a été d'assouplir les contraintes liées aux convertisseurs et leur fréquence d'échantillonnage. Nous avons présenté une nouvelle architecture de récepteur pour les communications sub-THz non-cohérentes, intitulée RAFAE (pour Receiver based on Analog Fourier Analysis of the Envelope). L'architecture du récepteur proposé est décrite par la Figure 3. Ce récepteur est conçu pour les communications haut-débit impulsionnelles avec des contraintes assouplies sur les convertisseurs. L'architecture proposée, contrairement aux récepteurs classiques, partitionne le traitement du signal lié à la démodulation entre les domaines analogique et numérique. L'utilisation d'une détection non-cohérente permet une robustesse inhérente au bruit de phase. De plus, la combinaison d'une projection analogique avec une détection multi-symbole permet de réduire la fréquence d'échantillonnage des convertisseurs. Les résultats des simulations numériques ont montré que des performances quasi optimales peuvent être obtenues avec des fréquences d'échantillonnage largement réduites.

Conclusion

Les recherches menées dans le cadre de cette thèse ont été orientées vers le développement de couches physiques performantes pour les futurs systèmes de communication sub-THz. Nous avons voulu répondre à la question de recherche suivante : comment concevoir des architectures et des algorithmes de communications pour faire face aux contraintes spécifiques des fréquences sub-THz ? Notre approche a consisté à concevoir conjointement les domaines analogique et numérique. En d'autres termes, nous avons étudié des optimisations conjointes de l'architecture radiofréquence et du traitement numérique du signal. Nos résultats ont montré que l'utilisation de techniques de transmission spécifiquement conçues pour les fréquences sub-THz permet à la fois d'augmenter le débit de communication et d'assouplir les contraintes sur les composants radiofréquences. En particulier, nous avons proposé dans en premier lieu des optimisations du traitement du signal pour les émetteurs-récepteurs cohérents dont la couche physique cible des efficacités spectrales élevées. Nous avons également conçu en second lieu des systèmes de communication dédiés utilisant des architectures non-cohérentes et

haut-débit. Ces architectures dédiées permettent de mettre en œuvre des couches physiques de faible complexité dans les fréquences sub-THz. Il est important de mentionner que le développement des systèmes sub-THz comble le fossé entre les systèmes de communication radiofréquence et optiques. Nous avons notamment observé que les systèmes sub-THz partagent des problématiques de conception communes aux systèmes radiofréquences et optiques. Pour conclure, nos contributions, des outils théoriques à la conception d'algorithmes et aux propositions d'architectures, ont pu être valorisées à travers différents types de publications : papiers de conférences, dépôt de brevet, et articles de journal.

Bibliography

[1] J. Proakis, *Digital Communications 5th Edition*, ser. McGraw-Hill series in electrical and computer engineering : communications and signal processing. McGraw-Hill, 2007.

[2] A. de Régulation des Communications Électroniques et des Postes, "Fréquences 5G : procédure d'attribution de la bande 3,4 - 3,8 GHz en métropole," June 2020.

[3] E. Faussurier, Y. Corre, and Z. Aslam, "Deliverable D1.1: Preliminary Regulation status," ANR project BRAVE, Tech. Rep., 2019.

[4] M. Saad, C. Bader, J. Palicot, Y. Corre, G. Gougeon, and D. Jean-Batiste, "Deliverable D1.0: Beyond 5G Wireless Tbps Scenarios and Requirements," ANR project BRAVE, Tech. Rep., 2018.

[5] N. Rajatheva *et al.*, "White Paper on Broadband Connectivity in 6G," 2020.

[6] ITU-T, "Guidelines for evaluation of radio interface technologies for IMT-Advanced," International Telecommunication Union, Geneva, Recommendation M.2135, 2009.

[7] C. Desset, P. Wambacq, Y. Zhang, M. Ingels, and A. Bourdoux, "Flexible power model for mm-wave and THz high-throughput communication systems," in *2020 IEEE 31st International Symposium on Personal, Indoor and Mobile Radio Communications*, 2020, pp. 1–6.

[8] F. F. Manzillo, A. Clemente, and J. L. Gonzalez-Jiménez, "High-gain D-band Transmitarrays in Standard PCB Technology for Beyond-5G Communications," *IEEE Transactions on Antennas and Propagation*, pp. 1–1, 2019.

[9] L. Pometcu and R. D'Errico, "Characterization of Sub-THz and mmWave Propagation Channel for Indoor Scenarios," in *12th European Association on Antennas and Propagation (EurAAP 18)*, Apr 2018.

[10] L. Pometcu and R. D'Errico, "Channel Model Characteristics in D-Band for NLOS Indoor Scenarios," *2019 13th European Conference on Antennas and Propagation (EuCAP)*, pp. 1–4, 2019.

[11] T. Xing and T. S. Rappaport, "Propagation Measurement System and Approach at 140 GHz–Moving to 6G and Above 100 GHz," in *2018 IEEE Global Communications Conference (GLOBECOM)*, Dec 2018.

[12] M. Eckhardt, T. Doeker, S. Rey, and T. Kürner, "Measurements in a Real Data Center at 300 GHz and Recent Results," in *13rd European Conference on Antennas and Propagation*, March 2019.

[13] T. S. Rappaport, Y. Xing, O. Kanhere, S. Ju, A. Madanayake, S. Mandal, A. Alkhateeb, and G. C. Trichopoulos, "Wireless Communications and Applications Above 100 GHz: Opportunities and Challenges for 6G and Beyond," *IEEE Access*, vol. 7, pp. 78 729–78 757, 2019.

[14] J.-B. Doré, Y. Corre, S. Bicais, J. Palicot, E. Faussurier, D. Kténas, and F. Bader, "Above-90GHz Spectrum and Single-Carrier Waveform as Enablers for Efficient Tbit/s Wireless Communications," in *25th International Conference on Telecommunications (ICT'2018)*, Saint-Malo, France, Jun. 2018.

[15] A. Ugolini, A. Piemontese, and T. Eriksson, "Spiral Constellations for Phase Noise Channels," *IEEE Transactions on Communications*, pp. 1–1, 2019.

[16] J. Park, S. Kang, S. V. Thyagarajan, E. Alon, and A. M. Niknejad, "A 260 GHz fully integrated CMOS transceiver for wireless chip-to-chip communication," in *2012 Symposium on VLSI Circuits (VLSIC)*, June 2012, pp. 48–49.

[17] H. Song, J. Kim, K. Ajito, M. Yaita, and N. Kukutsu, "Fully Integrated ASK Receiver MMIC for Terahertz Communications at 300 GHz," *IEEE Transactions on Terahertz Science and Technology*, vol. 3, no. 4, pp. 445–452, 2013.

[18] K. K. Tokgoz, S. Maki, S. Kawai, N. Nagashima, J. Emmei, M. Dome, H. Kato, J. Pang, Y. Kawano, T. Suzuki, T. Iwai, Y. Seo, K. Lim, S. Sato, L. Ning, K. Nakata, K. Okada, and A. Matsuzawa, "13.3 A 56Gb/s W-band CMOS wireless transceiver," in *2016 IEEE International Solid-State Circuits Conference (ISSCC)*, 2016, pp. 242–243.

[19] J. L. Gonzalez-Jimenez, C. Dehos, N. Cassiau, A. Siligaris, A. Clemente, R. D'Errico, V. Savin, Y. Durand, A. De Domenico, and D. Noguet, "Channel-bonding CMOS transceiver for 100 Gbps wireless point-to-point links," *EURASIP Journal on Wireless Communications and Networking*, vol. 2020, no. 1, p. 117, Jun 2020.

[20] G. Fettweis, M. Lohning, D. Petrovic, M. Windisch, P. Zillmann, and W. Rave, "Dirty RF: a new paradigm," in *2005 IEEE 16th International Symposium on Personal, Indoor and Mobile Radio Communications*, vol. 4, Sept 2005, pp. 2347–2355 Vol. 4.

[21] O. Tervo, T. Levanen, K. Pajukoski, J. Hulkkonen, P. Wainio, and M. Valkama, "5G New Radio Evolution Towards Sub-THz Communications," 2020.

[22] R. Krishnan, A. G. i Amat, T. Eriksson, and G. Colavolpe, "Constellation optimization in the presence of strong phase noise," *IEEE Transactions on Communications*, vol. 61, no. 12, pp. 5056–5066, December 2013.

[23] S. Verdú, "Spectral efficiency in the wideband regime," *IEEE Trans. Information Theory*, vol. 48, pp. 1319–1343, 2002.

[24] J.-B. Doré, B. Uguen, S. Paquelet, and S. Mallegol, "UWB Non-coherent high data rates transceiver Architecture and implementation," 06 2005.

[25] D. Morche, G. Masson, S. De Rivaz, F. Dehmas, S. Paquelet, A. Bisiaux, O. Fourquin, J. Gaubert, and S. Bourdel, "Double-Quadrature UWB Receiver for Wide-Range Localization Applications With Sub-cm Ranging Precision," *IEEE Journal of Solid-State Circuits*, vol. 48, no. 10, pp. 2351–2362, Oct 2013.

[26] S. Bicaïs and J.-B. Doré, "Design of Digital Communications for Strong Phase Noise Channels," *IEEE Open Journal of Vehicular Technology*, vol. 1, pp. 227–243, 2020.

[27] S. Bicaïs, J.-B. Doré, and J.-L. Gonzalez Jimenez, "On the Optimum Demodulation in the Presence of Gaussian Phase Noise," in *2018 International Conference on Telecommunications (ICT)*, June 2018.

[28] S. Bicaïs and J.-B. Doré, "Phase Noise Model Selection for Sub-THz Communications," in *2019 IEEE Global Communication Conference (GLOBECOM)*, December 2019.

[29] S. Bicaïs and J.-B. Doré, "Modèles de Bruit de Phase pour les Communications Sub-TeraHertz," in *XXVIIème Colloque francophone de traitement du signal et des images GRETSI 2019*, Lille, France, Aug. 2019.

[30] S. Bicaïs and J.-B. Doré, "Mitigation of Carrier Frequency Offset in a Sub-THz Channel Bonding Scenario," in *2019 IEEE 30th International Symposium on Personal, Indoor and Mobile Radio Communications (PIMRC Workshops)*, 2019, pp. 1–6.

[31] S. Bicaïs, J.-B. Doré, and J.-L. Gonzalez Jimenez, "Adaptive PSK Modulation Scheme in the Presence of Phase Noise," in *2018 Signal Processing Advances in Wireless Communications (SPAWC)*, June 2018.

[32] S. Bicaïs, J.-B. Doré, G. Gougeon, and Y. Corre, "Optimized Single Carrier Transceiver for Future Sub-TeraHertz Applications," in *2020 45th International Conference on Acoustics, Speech, and Signal Processing (ICASSP)*, Barcelona, Spain, May 2020.

[33] S. Bicaïs, J.-B. Doré, and J. L. Gonzalez Jimenez, "Digital High-Order Modulation Scheme Robust to Phase Noise," Patent, Mar. 2019.

[34] S. Bicaïs, J.-B. Doré, and V. Savin, "Design of MIMO Systems Using Energy Detectors for Sub-TeraHertz Applications," in *2020 IEEE 31st International Symposium on Personal, Indoor and Mobile Radio Communications (PIMRC)*, 2020, pp. 1–6.

[35] S. Bicaïs, A. Falempin, J.-B. Doré, and V. Savin, "Design and Analysis of MIMO Systems using Energy Detectors for Sub-THz Applications," *IEEE Transactions on Wireless Communications*, Submitted.

[36] S. Bicaïs, J.-B. Doré, and A. Falempin, "Neural Networks Based Demodulation for MIMO systems using Energy Detection Receivers," Patent, Jun. 2020.

[37] S. Bicaïs and J. Doré, "An Algebraic Framework for Digital Envelope Modulation," in *2019 27th European Signal Processing Conference (EUSIPCO)*, 2019, pp. 1–5.

[38] S. Bicaïs and J.-B. Doré, "Espaces de Hilbert pour les Modulations Numériques d'Enveloppe," in *XXVIIème Colloque francophone de traitement du signal et des images-GRETSI 2019*, Lille, France, Aug. 2019.

[39] S. Bicaïs, J.-B. Doré, and B. Miscopein, "Coherent Quadratic Receiver with Low Intermediate Frequency," Patent, Jan. 2020.

[40] S. Bicaïs and Doré, "Analog and Parallel Receiver Architecture for the Demodulation of Large-Bandwidth Signals," Patent, Mar. 2020.

[41] M. Voicu, D. Pepe, and D. Zito, "Performance and Trends in Millimetre-Wave CMOS Oscillators for Emerging Wireless Applications," *International Journal of Microwave Science and Technology*, vol. 2013, p. 6, 2013.

[42] G. Gougeon, Y. Corre, and M. Z. Aslam, "Ray-based Deterministic Channel Modelling for sub-THz Band," in *2019 IEEE International Symposium on Personal, Indoor and Mobile Radio Communications (PIMRC)*, Sep. 2019.

[43] M. Martalo, C. Tripodi, and R. Raheli, "On the information rate of phase noise-limited communications," in *2013 Information Theory and Applications Workshop (ITA)*, Feb 2013, pp. 1–7.

[44] A. Garcia Armada, "Understanding the effects of phase noise in orthogonal frequency division multiplexing (OFDM)," *IEEE Transactions on Broadcasting*, vol. 47, no. 2, pp. 153–159, 2001.

[45] C. Hager, A. G. i Amat, A. Alvarado, and E. Agrell, "Design of APSK Constellations for Coherent Optical Channels with Nonlinear Phase Noise," *IEEE Transactions on Communications*, vol. 61, no. 8, pp. 3362–3373, August 2013.

[46] G. J. Foschini, R. D. Gitlin, and S. B. Weinstein, "On the selection of a two-dimensional signal constellation in the presence of phase jitter and gaussian noise," *The Bell System Technical Journal*, vol. 52, no. 6, pp. 927–965, July 1973.

[47] M. R. Khanzadi, D. Kuylenstierna, A. Panahi, T. Eriksson, and H. Zirath, "Calculation of the Performance of Communication Systems From Measured Oscillator Phase Noise," *IEEE Transactions on Circuits and Systems I: Regular Papers*, vol. 61, no. 5, pp. 1553–1565, May 2014.

[48] H. Mehrpouyan, M. R. Khanzadi, M. Matthaiou, A. M. Sayeed, R. Schober, and Y. Hua, "Improving bandwidth efficiency in E-band communication systems," *IEEE Communications Magazine*, vol. 52, no. 3, pp. 121–128, March 2014.

[49] R. Krishnan, "On the impact of phase noise in communication systems - performance analysis and algorithms," Ph.D. dissertation, Chalmers University of Technology, 2015.

[50] A. Demir, "Computing Timing Jitter From Phase Noise Spectra for Oscillators and Phase-Locked Loops With White and 1/f Noise," *IEEE Transactions on Circuits and Systems I: Regular Papers*, vol. 53, no. 9, pp. 1869–1884, Sept 2006.

[51] S. Li, D. Fritsche, C. Carta, and F. Ellinger, "A 200-GHz Sub-Harmonic Injection-Locked Oscillator with 0-dBm Output Power and 3.5% DC-to-RF-Efficiency," in *2018 IEEE Radio Frequency Integrated Circuits Symposium (RFIC)*, June 2018, pp. 212–215.

[52] N. J. Kasdin and T. Walter, "Discrete simulation of power law noise [for oscillator stability evaluation]," in *Proceedings of the 1992 IEEE Frequency Control Symposium*, May 1992, pp. 274–283.

[53] T. Moon and W. Stirling, *Mathematical Methods and Algorithms for Signal Processing*. Prentice Hall, 2000.

[54] R. Krishnan, M. R. Khanzadi, T. Eriksson, and T. Svensson, "Soft Metrics and Their Performance Analysis for Optimal Data Detection in the Presence of Strong Oscillator Phase Noise," *IEEE Transactions on Communications*, vol. 61, no. 6, pp. 2385–2395, 2013.

[55] F. Tosato and P. Bisaglia, "Simplified soft-output demapper for binary interleaved COFDM with application to HIPERLAN/2," in *2002 IEEE International Conference on Communications. Conference Proceedings. ICC 2002 (Cat. No.02CH37333)*, vol. 2, 2002, pp. 664–668 vol.2.

[56] J.-H. Lee and H. Chung, "Exact and approximate log-likelihood ratio of M-ary QAM with two-time dimensions," *ICT Express*, vol. 5, no. 3, pp. 173 – 177, 2019.

[57] 3rd Generation Partnership Project (3GPP), "Overall Description Stage 2," Technical Specification Group Access Network 38.300, 12 2017, 2.0.0.

[58] S. M. Kay, *Fundamentals of Statistical Signal Processing: Estimation Theory*. Upper Saddle River, NJ, USA: Prentice-Hall, Inc., 1993.

[59] M. Düngen, "Crosstalk Mitigation Techniques for Digital Subscriber Line Systems," Ph.D. dissertation, Technischen Universität Hamburg-Harburg, 2016.

[60] F. Kayhan and G. Montorsi, "Constellation design for channels affected by phase noise," in *2013 IEEE International Conference on Communications (ICC)*, June 2013, pp. 3154–3158.

[61] J. Horton Conway and N. Sloane, *Sphere Packings, Lattices and Groups*, 01 1988, vol. 290.

[62] G. Forney, R. Gallager, G. Lang, F. Longstaff, and S. Qureshi, "Efficient Modulation for Band-Limited Channels," *IEEE Journal on Selected Areas in Communications*, vol. 2, no. 5, pp. 632–647, Sep 1984.

[63] M. Simon and J. Smith, "Hexagonal multiple phase-and-amplitude-shift-keyed signal sets," *IEEE Transactions on Communications*, vol. 21, no. 10, pp. 1108–1115, Oct 1973.

[64] A. Lapidoth, "On phase noise channels at high snr," in *Proceedings of the IEEE Information Theory Workshop*, Oct 2002, pp. 1–4.

[65] M. R. Khanzadi, G. Durisi, and T. Eriksson, "Capacity of SIMO and MISO Phase-Noise Channels With Common/Separate Oscillators," *IEEE Transactions on Communications*, vol. 63, no. 9, pp. 3218–3231, 2015.

[66] D. M. Arnold, H. . Loeliger, P. O. Vontobel, A. Kavcic, and W. Zeng, "Simulation-Based Computation of Information Rates for Channels With Memory," *IEEE Transactions on Information Theory*, vol. 52, no. 8, pp. 3498–3508, Aug 2006.

[67] M. A. Tariq, H. Mehrpouyan, and T. Svensson, "Performance of circular QAM constellations with time varying phase noise," in *2012 IEEE 23rd International Symposium on Personal, Indoor and Mobile Radio Communications - (PIMRC)*, Sep. 2012, pp. 2365–2370.

[68] Z. Liu, Q. Xie, K. Peng, and Z. Yang, "APSK Constellation with Gray Mapping," *IEEE Communications Letters*, vol. 15, no. 12, pp. 1271–1273, December 2011.

[69] F. Schreckenbach, N. Gortz, J. Hagenauer, and G. Bauch, "Optimization of symbol mappings for bit-interleaved coded modulation with iterative decoding," *IEEE Communications Letters*, vol. 7, no. 12, pp. 593–595, Dec 2003.

[70] S. Allpress, C. Luschi, and S. Felix, "Exact and approximated expressions of the log-likelihood ratio for 16-qam signals," in *Conference Record of the Thirty-Eighth Asilomar Conference on Signals, Systems and Computers, 2004.*, vol. 1, Nov 2004, pp. 794–798 Vol.1.

[71] A. Barre, E. Boutillon, N. Bias, and D. Diaz, "A polar-based demapper of 8psk demodulation for dvb-s2 systems," in *SiPS 2013 Proceedings*, Oct 2013, pp. 13–17.

[72] T. Yoshida, K. Matsuda, K. Kojima, H. Miura, K. Dohi, M. Pajovic, T. Koike-Akino, D. S. Millar, K. Parsons, and T. Sugihara, "Hardware-efficient Precise and Flexible Soft-demapping for Multi-Dimensional Complementary APSK Signals," in *ECOC 2016; 42nd European Conference on Optical Communication*, Sep. 2016, pp. 1–3.

[73] M. Zhang and S. Kim, "Efficient soft demapping for M-ary APSK," in *ICTC 2011*, Sep. 2011, pp. 641–644.

[74] B. Murmann. "ADC Performance Survey 1997-2019", [Online]. Available: http://web.stanford.edu/ murmann/adcsurvey.html.

[75] G. Gougeon, Y. Corre, S. B. M. Aslam, and J.-B. Doré, "Assessment of sub-THz Mesh Backhaul Capabilities from Realistic Modelling at the PHY Layer," in *2020 14th European Conference on Antennas and Propagation (EuCAP2020)*, March 2020.

[76] P. Ferrand, M. Maso, and V. Bioglio, "High-Rate Regular APSK Constellations," *IEEE Transactions on Communications*, vol. 67, no. 3, pp. 2015–2023, 2019.

[77] J. Groe, "Polar Transmitters for Wireless Communications," *IEEE Communications Magazine*, vol. 45, no. 9, pp. 58–63, September 2007.

[78] C. T. Chen, C. H. Hsiao, T. S. Horng, and K. C. Peng, "Wireless polar receiver using two injection-locked oscillator stages for green radios," in *2011 IEEE MTT-S International Microwave Symposium*, June 2011, pp. 1–4.

[79] E. Leitinger, B. C. Geiger, and K. Witrisal, "Capacity and capacity-achieving input distribution of the energy detector," in *2012 IEEE International Conference on Ultra-Wideband*, 2012, pp. 57–61.

[80] L. Jing, E. De Carvalho, P. Popovski, and A. O. Martinez, "Design and Performance Analysis of Noncoherent Detection Systems With Massive Receiver Arrays," *IEEE Transactions on Signal Processing*, vol. 64, no. 19, pp. 5000–5010, Oct 2016.

[81] G. K. Psaltopoulos, F. Troesch, and A. Wittneben, "On Achievable Rates of MIMO Systems with Nonlinear Receivers," in *2007 IEEE International Symposium on Information Theory*, June 2007, pp. 1071–1075.

[82] G. K. Psaltopoulos and A. Wittneben, "Diversity and spatial multiplexing of MIMO amplitude detection receivers," in *2009 IEEE 20th International Symposium on Personal, Indoor and Mobile Radio Communications*, Sep. 2009, pp. 202–206.

[83] S. Paquelet, L. . Aubert, and B. Uguen, "An impulse radio asynchronous transceiver for high data rates," in *2004 International Workshop on Ultra Wideband Systems Joint with Conference on Ultra Wideband Systems and Technologies. Joint UWBST IWUWBS 2004 (IEEE Cat. No.04EX812)*, May 2004, pp. 1–5.

[84] L. Barletta and G. Kramer, "On continuous-time white phase noise channels," in *2014 IEEE International Symposium on Information Theory*, June 2014, pp. 2426–2429.

[85] N. Farsad and A. Goldsmith, "Neural network detection of data sequences in communication systems," *IEEE Transactions on Signal Processing*, vol. 66, no. 21, pp. 5663–5678, 2018.

[86] N. Samuel, T. Diskin, and A. Wiesel, "Deep MIMO Detection," in *2017 IEEE 18th International Workshop on Signal Processing Advances in Wireless Communications (SPAWC)*, 2017, pp. 1–5.

[87] A. Elrharras, R. Saadane, M. Wahbi, and A. Hamdoun, "Hybrid architecture for spectrum sensing algorithm based on energy detection technique and artificial neural networks," in *2014 5th Workshop on Codes, Cryptography and Communication Systems (WCCCS)*, 2014, pp. 40–44.

[88] C. Fougstedt, K. Szczerba, and P. Larsson-Edefors, "Low-Power Low-Latency BCH Decoders for Energy-Efficient Optical Interconnects," *Journal of Lightwave Technology*, vol. 35, no. 23, pp. 5201–5207, Dec 2017.

[89] E. Nurvitadhi, Jaewoong Sim, D. Sheffield, A. Mishra, S. Krishnan, and D. Marr, "Accelerating recurrent neural networks in analytics servers: Comparison of FPGA, CPU, GPU, and ASIC," in *2016 26th International Conference on Field Programmable Logic and Applications (FPL)*, 2016, pp. 1–4.

[90] E. Nurvitadhi, D. Sheffield, Jaewoong Sim, A. Mishra, G. Venkatesh, and D. Marr, "Accelerating Binarized Neural Networks: Comparison of FPGA, CPU, GPU, and ASIC," in *2016 International Conference on Field-Programmable Technology (FPT)*, 2016, pp. 77–84.

[91] Agilent technologies, Inc., "Square Law and Linear Detection," Application Note 986, Tech. Rep., 1999.

[92] T. Fath and H. Haas, "Performance Comparison of MIMO Techniques for Optical Wireless Communications in Indoor Environments," *IEEE Transactions on Communications*, vol. 61, no. 2, pp. 733–742, 2013.

[93] M. H. Castañeda Garcia, M. Iwanow, and R. A. Stirling-Gallacher, "LOS MIMO Design Based on Multiple Optimum Antenna Separations," in *2018 IEEE 88th Vehicular Technology Conference (VTC-Fall)*, 2018, pp. 1–5.

[94] K. Kobayashi, T. Ohtsuki, and T. Kaneko, "Precoding for MIMO Systems in Line-Of-Sight (LOS) Environment," in *IEEE GLOBECOM 2007 - IEEE Global Telecommunications Conference*, 2007, pp. 4370–4374.

[95] K. Zhu, *Operator theory in function spaces.* New York etc.: Marcel Dekker, Inc., 1990, vol. 139.

[96] S. Paquelet and L.-M. Aubert, "A method for detecting UWB pulse sequences without generation of local pulses," Patent, 2004.

[97] G. Kolumban, M. P. Kennedy, Z. Jako, and G. Kis, "Chaotic communications with correlator receivers: theory and performance limits," *Proceedings of the IEEE*, vol. 90, no. 5, pp. 711–732, May 2002.

[98] A. W. Azim, A. Rullier, Y. Le Guennec, L. Ros, and G. Maury, "Energy Efficient M -ary Frequency-Shift Keying-Based Modulation Techniques for Visible Light Communication," *IEEE Transactions on Cognitive Communications and Networking*, vol. 5, no. 4, pp. 1244–1256, 2019.

[99] M. Pelissier and C. Studer, "Non-uniform wavelet sampling for rf analog-to-information conversion," *IEEE Transactions on Circuits and Systems I: Regular Papers*, vol. 65, no. 2, pp. 471–484, 2018.

[100] M. Saad, F. Bader, J. Palicot, A. C. A. Ghouwayel, and H. Hijazi, "Single carrier with index modulation for low power terabit systems," in *2019 IEEE Wireless Communications and Networking Conference*, April 2019.

[101] A. W. Azim, M. Chafii, Y. Le Guennec, and L. Ros, "Spectral and Energy Efficient Fast-OFDM with Index Modulation for Optical Wireless Systems," *IEEE Communications Letters*, pp. 1–1, 2020.

[102] O. Dabeer, J. Singh, and U. Madhow, "On the Limits of Communication Performance with One-Bit Analog-To-Digital Conversion," in *2006 IEEE 7th Workshop on Signal Processing Advances in Wireless Communications*, 2006, pp. 1–5.

[103] L. Landau, M. Dörpinghaus, and G. P. Fettweis, "1-Bit Quantization and Oversampling at the Receiver: Communication Over Bandlimited Channels With Noise," *IEEE Communications Letters*, vol. 21, no. 5, pp. 1007–1010, 2017.

[104] P. Dollard, "On the time-bandwidth concentration of signal functions forming given geometric vector configurations," *IEEE Transactions on Information Theory*, vol. 10, no. 4, pp. 328–338, October 1964.

[105] D. Gabor, "Theory of communication," *Journal of the Institution of Electrical Engineers*, vol. 93, pp. 429–441, November 1946.